Studies of Local Functional Network Connectivity in Cat Visual Cortex

Schmitz, Sarah Katharina

(2020)

DOI (TUprints): https://doi.org/10.25534/tuprints-00014188

TECHNISCHE
UNIVERSITÄT
DARMSTADT

MAX-PLANCK-GESELLSCHAFT

Studies of Local Functional Network Connectivity in Cat Visual Cortex

Studien lokaler funktioneller Netzwerkkonnektivität
im visuellen Kortex der Katze

vom Fachbereich Biologie
der Technischen Universität Darmstadt

zur Erlangung des Grades
Doctor rerum naturalium
(Dr. rer. nat.)

Dissertation

von Sarah Katharina Schmitz

Erstgutachter: Prof. Dr. Ralf A. W. Galuske
Zweitgutachter: Prof. Dr. Gordon Pipa

Darmstadt 2020

Schmitz, Sarah Katharina: Studies of local functional network connectivity in cat visual cortex
Darmstadt, Technische Universität Darmstadt
Jahr der Veröffentlichung der Dissertation auf TUprints: 2020
URN: urn:nbn:de:tuda-tuprints-141882
URL: https://tuprints.ulb.tu-darmstadt.de/id/eprint/14188
Tag der mündlichen Prüfung: 09.10.2020

Contents

List of Figures

List of Tables

List of Abbreviations

AP	action potential
BOLD	blood-oxygenation-level-dependent
CC	cross correlation / cross-correlogram
CORCONDIA	core consistency diagnostic
CTC	communication through coherence
EEG	electroencephalography
EPSP	excitatory postsynaptic potential
FFT	Fast Fourier Transform
fMRI	functional magnetic resonance imaging
GABA	gamma-aminobutyric acid
GLM	generalized linear model
IPSP	inhibitory postsynaptic potential
ISI	inter-spike interval
JSE	joint-spike event
KS test	Kolmogorov-Smirnov test
LFP	local field potential
LGN	lateral geniculate nucleus
LTD	long-term depression
LTP	long-term potentiation
MEG	magnetoencephalography
MI	modulation index
MT	middle temporal area
MUA	multi-unit activity
NX	NeuroXidence
PARAFAC	Parallel Factor Analysis
PCA	Principal Component Analysis
PFC	prefrontal cortex
PMLS	posteromedial lateral suprasylvian
pMS	posterior middle suprasylvian
PSTH	peri-stimulus time histogram
REM	rapid eye movement
SC	superior colliculus
SEM	standard error of the mean
SNR	signal-to-noise ratio
SPC	superparamagnetic clustering
STDP	spike-timing-dependent plasticity
SUA	single-unit activity
SWS	slow wave sleep
VLS	ventral lateral suprasylvian

Summary

Summary (English)

In the mammalian brain, network structures are apparent on multiple temporal and spatial scales.

While substantial knowledge is available about the action potential on the level of the individual cell, as well as about large-scale networks across brain areas, the intermediate level of local functional neuronal networks within one brain area has not been analyzed to the same extent. The advancement of multi-electrode recordings in the brain enables the analysis of functional connectivity between simultaneously recorded groups of neurons. With this, there is an increasing need for analysis approaches to study the characteristics of the recorded local functional networks.

In this context, the present study had two main goals: 1) the extension and development of analysis methods, and 2) the application of these methods to electrophysiological data in order to contribute to the knowledge in the field of local functional connectivity.

The data which were analyzed in this study had been collected as part of a cycle of studies on visual hemineglect. The study of neglect is closely linked to the study of feedback signals between areas in the visual system: electrophysiological signals were recorded from the primary visual area 18 in the anaesthetized cat, while a hierarchically higher area, the posterior middle suprasylvian (pMS) sulcus, was thermally deactivated. This deactivation silences the feedback signals from pMS to area 18. The deactivation was performed unilaterally – on the same (ipsilateral) and on the opposite (contralateral) hemisphere to the recording – as well as bilaterally.

The effect of the pMS deactivation was probed on multiple temporal and spatial scales: on the single-cell level, spike rates and tunings were assessed for both multi- and single-unit data. On the level of local functional network connectivity, multiple approaches were explored to extract different aspects of the deactivation effects. Parallel Factor Analysis (PARAFAC) was applied as a means to scan the effect of deactivation of pMS on cross-correlations between multi-units in area 18 over all recording sessions. PARAFAC proved to be a suitable approach to extract the deactivation effects. To the author's knowledge, this is the first application of PARAFAC to electrophysiological spike data.

Functional networks were created based on joint-spike events by application of "NeuroXidence", and effective connectivity was computed based on the application of a Generalized Linear Model (GLM) to the spike data.

Network connectivity was then assessed with a variety of graph theoretical measures. After excluding randomness (in the sense of Erdös-Rényi graphs), connection density was compared for short and long-range connections, and units with a similar or differing orientation or direction preference, respectively. Entire graphs were examined for similarity between different experimental conditions, based on a test using the Hamming distance.

Effects of the pMS deactivation on the local network structure in area 18 could be observed on all probed spatial and temporal scales, namely LFP and spike rates, as well as millisecond-precise synchrony based on NeuroXidence, and directed connectivity based on the GLM.

Overall, the results were in line with previous findings in the context of studies on the visual hemineglect in the anaesthetized cat: ipsi- and bilateral pMS deactivation led to lower activity and connectivity

levels as compared to the "warm" condition, while contralateral pMS deactivation left rates and coordinated activity largely unaltered. However, a large variability of the deactivation effects was observed.

In order to find a possible correlate for this variability, the data were divided into three subsets based on the level of gamma activity in the LFP prior to thermal deactivation of pMS. The group with the highest initial gamma power was observed to be the most dynamic and showed the largest effects during deactivation, both for rates and correlated activity. This raised the notion that the presence of low or medium initial gamma activity could be an indication that the global network was partially disconnected even before the deactivation of pMS, and for this reason did not exhibit the same extent of deactivation effects as compared to the "high initial gamma" group.

Thus it is concluded that global brain state bears a significant relevance for local networks and should be taken into account for any study of local connectivity in the brain.

Im Gehirn von Säugetieren werden Netzwerkstrukturen auf verschiedenen zeitlichen und räumlichen Skalen beobachtet. Während umfangreiches Wissen über das Aktionspotential auf dem Level der individuellen Zelle, ebenso wie über globale Netzwerke zwischen Hirnarealen, vorhanden ist, ist das intermediäre Level der lokalen funktionellen neuronalen Netzwerke innerhalb eines Hirnareals bisher weniger umfassend untersucht. Die Fortentwicklung von Multi-Elektroden-Ableitungen im Gehirn ermöglicht dabei die Analyse funktioneller Konnektivität unter simultan aufgenommenen Gruppen von Neuronen. Damit steigt der Bedarf nach Analysemethoden, um die Charakteristika der aufgenommenen lokalen funktionellen Netzwerke zu untersuchen.

In diesem Kontext hatte die vorliegende Studie vornehmlich zwei Ziele: 1) die Erweiterung und Entwicklung von Analysemethoden und 2) die Anwendung dieser Methoden auf elektrophysiologische Daten, um zum Wissen im Bereich der lokalen funktionellen Konnektivität beizutragen.

Die Daten, die der vorliegenden Dissertation zugrunde liegen, stammen aus einem Zyklus von Studien zum visuellen Hemineglekt, einem Phänomen, das beispielsweise als Folge eines Schlaganfalls auftreten kann, und bei dem der Patient eine Hälfte seines Gesichtsfeldes nicht mehr wahrnimmt. Die Studie des Neglekts ist eng mit der Erforschung von Feedback-Signalen zwischen Arealen im visuellen System verknüpft: Elektrophysiologische Signale wurden vom primären visuellen Areal 18 in der anästhesierten Katze abgeleitet, während ein hierarchisch höheres Areal, der posteromediale suprasylvische Sulkus (pMS), thermal, das heißt durch Kühlen, deaktiviert wurde. Diese Deaktivierung schaltet die Feedback-Signale vom pMS nach Area 18 aus. Die Deaktivierung erfolgte sowohl unilateral – auf derselben (ipsilateral) und auf der gegenüberliegenden (kontralateral) Hemisphäre – als auch bilateral.

Die Untersuchung des pMS-Deaktivierungseffekts erfolgte auf verschiedenen zeitlichen und räumlichen Skalen: Auf dem Niveau einzelner Zellen wurden Feuerraten und Orientierungs- sowie Richtungspräferenzen für Multi- sowie für Single-Units betrachtet. Auf dem Level der Netzwerk-Konnektivität wurden verschiedene Ansätze erprobt, um unterschiedliche Aspekte des Deaktivierungseffekts zu extrahieren. Die Anwendung der Parallelen Faktorenanalyse (PARAFAC) erfolgte mit dem Ziel, den Effekt der pMS-Deaktivierung auf die Kreuzkorrelation zwischen Multi-Units in Area 18 über alle Aufnahmesitzungen zu scannen. PARAFAC bewies sich hierbei als geeigneter Ansatz, die auftretenden Deaktivierungseffekte sichtbar zu machen. Nach dem Wissen der Autorin ist dies die erste Anwendung von PARAFAC auf elektrophysiologische Spike-Signale.

Funktionelle Netzwerke wurden auf der Basis von Joint-Spike-Events unter Verwendung der Methode "NeuroXidence" berechnet. Zur Bestimmung effektiver Konnektivität wurde ein Ansatz basierend auf einem Generalisierten Linearen Modell (GLM) gewählt.

Im Anschluss wurde die Netzwerk-Konnektivität mit einer Auswahl an graphentheoretischen Methoden untersucht. Nachdem Zufälligkeit (im Sinne von Erdös-Rényi-Graphen) ausgeschlossen werden konnte, wurde die Verbindungsdichte für kurze und lange Verbindungen sowie für Units mit ähnlicher und unterschiedlicher Orientierungspräferenz verglichen. Ganze Graphen wurden außerdem mit Hilfe eines auf der Hamming-Distanz basierenden Tests auf ihre Ähnlichkeit untersucht.

Effekte der pMS-Deaktivierung auf die lokale Netzwerkstruktur in Area 18 konnten auf allen räumlichen und zeitlichen Skalen, das heißt im LFP und den Feuerraten sowie in der millisekundengenauen Synchronität basierend auf NeuroXidence und der gerichteten Konnektivität basierend auf dem GLM, beobachtet werden. Die Ergebnisse sind dabei im Einklang mit früheren Erkenntnissen im Kontext der Studien zum visuellen Hemineglekt in der anästhesierten Katze: Ipsi- und bilaterale pMS-Deaktivierung führten im Vergleich zur "warm"-Bedingung zu niedrigeren Aktivitäts- und Korrelations-

niveaus, während kontralaterale Deaktivierung Raten und Korrelationen kaum veränderte. Allerdings zeigte sich eine hohe Variabilität der Deaktivierungseffekte.

Um ein mögliches Korrelat für diese Variabilität zu identifizieren, wurden die Daten in drei Untergruppen, basierend auf dem Niveau der Gamma-Aktivität im LFP vor der thermalen Deaktivierung, aufgeteilt. Die Gruppe mit der höchsten initialen Gamma-Power zeigte sich dabei als die dynamischste und wies die größten Veränderungen unter der Deaktivierung auf, sowohl für die Spikeraten, als auch für die korrelierte Spikeaktivität. Dies führte zu der Auffassung, dass das Vorhandensein niedriger oder mittlerer initialer Gamma-Aktivität ein Indikator dafür sein könnte, dass das globale Netzwerk bereits vor der pMS-Deaktivierung gestört war und aus diesem Grund im Vergleich zur "High Initial Gamma"-Gruppe nicht dasselbe Ausmaß der Deaktivierungseffekte zeigte.

Abschließend wird deshalb festgehalten, dass der Zustand des globalen Netzwerks im Gehirn einen maßgeblichen Einfluss auf die lokale Netzwerkstruktur in einzelnen Arealen hat und bei jeder Untersuchung von lokaler Konnektivität berücksichtigt werden sollte.

1 Introduction

> "The music of an orchestra is the harmonic sum of the music played by all of its individual members playing in a coherent fashion. Each instrument may follow a different individual tune, but in such a coherent way that the sum of the individual notes, the tunes played by all instruments, is music."
>
> Grinvald et al. (2003)

Like the musicians of the orchestra in Grinvald's quote, the individual players in the brain, the neurons, have to precisely interact to create an accurately tuned interplay. Only then will the organism be able to appropriately react to external stimuli, to feed, to procreate, and, ultimately, to survive. The ability to create this precise interaction is strongly dependent on the overall brain state: ongoing activity and attention level will determine whether certain stimuli are processed and ultimately consciously perceived, processed unconsciously, or even entirely neglected. These brain states reach from sleep and waking in the healthy animal to abnormal or pathological states, such as anaesthesia, or coma. The overall brain state influences the processing of information globally and locally, on the level of communication between areas of the brain to the level of single cells.

The present study was conducted in order to analyze the influence of a deactivation of feedback signals from one brain area on local activity in another hierarchically lower area and the dependency of this feedback influence on brain state. Moreover, this study contributes to the understanding of neuronal coding in the visual system in general as well as develop and extend analysis methods that can support further research in the challenging fields of neuronal networks and neural coding.

1.1 Oscillations and Brain States

The most obvious differences in behavioural state of a healthy animal can be observed between waking and sleeping. In addition, within the dichotomous states of waking and sleeping, there is a gradation of substates: in sleep, for example, substates like rapid eye movement (REM) sleep and slow wave sleep (SWS) can be distinguished. Likewise, there is also not just one "awake state", since while being awake an animal can be anything between highly alert and very inattentive and drowsy.

These behavioural states have been linked to differences in their cortical activity profile. REM sleep and SWS, for example, show very different oscillatory activity profiles, but also differences in large-scale network connectivity (**Stitt et al.**, 2017). With this, a cortical state, or "brain state", can be viewed as "a recurring set of neural conditions that is stable for a behaviourally significant period of time" (**Zagha and McCormick**, 2014). State switches can occur on very different time scales, from milliseconds (like up and down states in the barrel cortex of rats (**Luczak et al.**, 2007)) to hours or days (e.g. sleep, anaesthesia, and coma). The states may also overlap and change on a global and local level (**Zagha and McCormick**, 2014). States can hence be defined by assessing the behaviour of an animal, but also by determining the neuronal activity profile.

Typically, with extracellular electrophysiological recordings, as applied in this study, two aspects of the signal are of interest: the multi-unit spiking activity (MUA), for which the recorded signal is filtered for high frequency components to extract the action potential activity of single neuronal units, and the local field potential (LFP), the low-pass filtered signal (usually below 100 Hz), which represents a summation of dendritic potentials around the recording site (**Destexhe and Bedard**, 2013).

The separation into cortical states has typically been performed based on the level of oscillations, e.g. using the electroenecephalogram (EEG), or LFP, but also by spontaneous fluctuations in multi-unit spiking activity (**Schölvinck et al.**, 2015) and the extent of pupil dilation (**McGinley et al.**, 2015).

Since, in the present study, the level of gamma activity within a given time frame was utilized as brain state indicator, the focus shall first be set on the LFP signal.

1.1.1 Local field potential

The local field potential, a summation signal of extracellular currents, is usually separated into different frequency bands within which the oscillatory power can be measured (Table 1.1).

Table 1.1.: Frequency bands

Frequency band	Frequency range
Delta	0.5–4 Hz
Theta	4-8 Hz
Alpha	9-14 Hz
Beta	15-23 Hz
Low Gamma / "Gamma1"	24-48 Hz
High Gamma / "Gamma2"	52-90 Hz

Following the separation into frequency bands, the temporal relation between frequency bands can be assessed: in-sync oscillations between neuronal populations have been shown to facilitate communication between neuronal populations, while this does not apply for communication between populations that oscillate out of sync (**Fries**, 2005, 2015).

Beyond allowing for assessments of in or out of sync neural populations, specific frequency bands have been associated with certain cognitive states or functions (see e.g. **Gervasoni et al.** (2004)): oscillations in the delta frequency band are mainly linked to slow-wave sleep. Alpha oscillations, first described by **Berger** (1929), are prominent in the awake, relaxed brain and get stronger when the subject closes their eyes. Beta waves are mostly associated with the awake, conscious state. Cortical theta oscillations have been associated with active motor behaviour, but also REM sleep in rats, and drowsy states in humans. Oscillations in the theta band have also been studied in the hippocampus and, together with gamma oscillations, play a role in memory formation and recall and navigation (**Buzsáki**, 2005; **Hasselmo**, 2005; **Lisman**, 2010; **Buzsáki and Moser**, 2013). Gamma oscillations have been related with higher cognitive processes, such as working memory formation (**Lisman**, 2010), learning, multisensory integration, and attention (**Buzsáki**, 2006). They have also been proposed to play a crucial role in the solution of the binding problem (**Engel and Singer**, 2001). Gamma oscillations are present in the waking brain, but also during REM sleep (**Buzsáki**, 2006, p. 243). Gamma oscillations have been linked to feedforward processing, while oscillations in the beta (**Bastos et al.**, 2015; **Michalareas et al.**, 2016), but also the alpha frequency band (**van Kerkoerle et al.**, 2014) seemingly account for feedback signals.

Faster frequencies have been proposed to account for local activity, while slower frequencies were linked to long-range communication, although this reasoning has been questioned in more recent studies (**Fries**, 2015).

1.1.2 Action potentials and spike trains

Action potentials (APs), also referred to as spikes, are the means of information transmission between neurons. Even though deep knowledge about the action potential on the single-cell level has been collected (see e.g. **Kandel et al.** (2000, p.150 ff.), **Bean** (2007)), a thorough understanding of the principles of the neural code as such has yet to be achieved.

Neurons receive input from a large number, often many thousands, of other neurons. This input is mainly received via the dendrites, although other structures of the neuron, such as the soma or axon, can also form contacts with the presynaptic cell. The incoming potentials can be excitatory (EPSP[1]) or inhibitory (IPSP[2]), hence have a depolarising or hyperpolarising effect on the postsynaptic cell. The input of all these presynaptic neurons is integrated through temporal and spatial summation in the postsynaptic neuron and, if the threshold potential is reached, an action potential is triggered.

When questions on coding or information transmission are approached, spike signals are usually reduced to the timepoints at which an AP occurred, termed timestamps, leaving the researcher with a so-called spike train (see Fig. 2.5, p. 35). This is justified because it is assumed that action potentials follow an "all or nothing" principle. Hence, the waveform of the AP does not contribute to the information content that is processed.[3] The spike trains are then analyzed in order to characterize their temporal structure.

Many of the approaches towards obtaining a better insight into this challenging question take advantage of the possibility of simultaneous extracellular multi-electrode recordings (**Buzsáki**, 2004). Simultaneous extracellular multi-electrode recordings allow the activity in the local neuronal network around

---

[1] EPSP = excitatory post-synaptic potential

[2] IPSP = inhibitory post-synaptic potential

[3] However, it is known that for example during a burst, the shape of the action potential can change (Fee et al., 1996), leading to challenges for spike sorting procedures (Lewicki, 1998) (for details on spike sorting see section 4.2.6).

the electrode array to be characterized by not only describing activity at the single-electrode level, but also describing interactions between recording sites.

In the early stages of visual processing, representations of the visual field have been found to mirror certain properties of the environment. The retina and primary visual cortex, for example, have a retinotopic organization. Already as early as in the retina, visual input is integrated and encoded to enable further internal processing. In higher processing stages of the visual system, the match beween an external stimulus and its neural correlates becomes increasingly difficult.

In the present study, local neuronal networks were investigated in order to gain insight into the coding strategies in primary visual cortex, and the interactions among cells in different cortical states. These local networks were based on estimations of functional and effective connectivity (see also section 1.3), which can be derived through statistical computations of correlations or related directed connectivity measures.

In order to define and compute connectivity in neuronal networks, it is important to have a concept about how information is encoded, passed on, and processed in the brain. Only then is it possible to find meaningful measures of connectivity. The following chapter gives an overview of neuronal signals and potential coding mechanisms.

Potential coding strategies

The mechanisms of information processing in the brain are still under intense discussion. It seems very likely that action potential rates and temporal structure act conjointly in processing. However, a general principle, which describes and possibly separates the roles of rates and timing has not been identified.

Research on neural coding goes back to **Galvani** (1894, Orig.: 1791) and **Adrian and Zotterman** (1926). The latter discovered two important features of spikes when studying the stretch receptor in the frog's leg: first, the action potential frequency increased when the receptor was stretched more, and second, the waveform of the action potential did not change and was thus rated as not carrying any additional information. In many cases it can be observed that, if the intensity of a stimulus is increased, the rate of action potentials in the brain areas involved in the processing of this stimulus also increases (see **Kandel et al.** (2000, p. 421 ff.)). Hence, rates seem to carry at least part of the information about the stimulus. However, the nature of neural coding cannot be reduced to the simple relation "the higher the stimulus intensity, the higher the rate", but rather exhibits a more complex structure.

In addition, or alternatively, to spike rates, synchronous spikes occuring with millisecond precision and/or specific temporal sequences of spikes could matter to the brain (see e.g. **Singer** (1999a); **van Rullen et al.** (2005); **Jacobs et al.** (2009); **Uhlhaas et al.** (2009)).

Synchrony and millisecond-precise temporal patterns in spiking activity have been linked to several functional properties, and synchronisation can occur at multiple scales in time and space. Synchronisation can be observed between brain areas at the level of oscillations that become phase-locked, providing windows for communication between the respective areas (**Fries**, 2005). Synchrony can also be observed locally, i.e. on small spatial scales, between single cells or small groups of cells. Synchrony has been proposed to enable the binding of different stimulus features (**Milner**, 1974; **Grossberg**, 1976; **von der Malsburg**, 1981; **Treisman**, 1996; **Singer**, 1999a; **Engel and Singer**, 2001), although theories of temporal binding have been challenged (**Shadlen and Movshon**, 1999; **Treisman**, 1999).

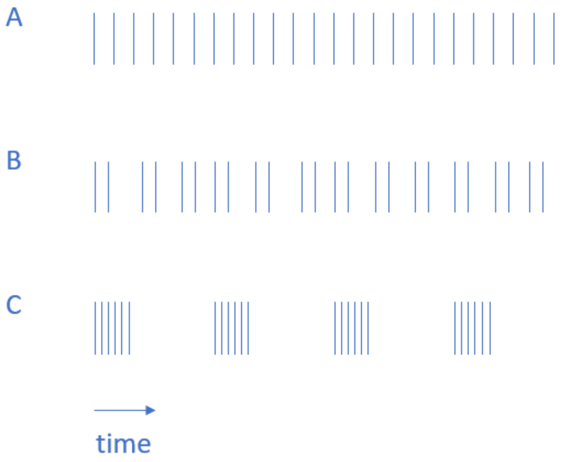

Figure 1.1.: Spiking variability. The depicted spiketrains, A, B, and C, are equivalent in a rate coding scheme, i.e. exhibit the same rate over the given time window, but show different temporal patterns. (A) exhibits regular spiking, while (c) shows bursts of spikes. Analogous, many other distributions of the same number of spikes over the same time interval are possible. The incorporation of temporal patterns largely increases the potential coding space as compared to a code that is purely based on spike rate.

Since the present study is concerned with local functional networks within a single area, the focus here will be put on the concept of local synchronisation.

Synchronized input of multiple cells may drive a target neuron through summation of the incoming EPSPs or IPSPs, which might not have been sufficient to reach the spiking threshold had the input not been synchronized. The same number of spikes thus can have a fundamentally different impact on the downstream neuron(s), depending on the timing of the individual spikes.

Both spatial and temporal summation of EPSPs can elicit a spike in the postsynaptic cell. Hence, both a faster succession of action potentials, as well as a precisely timed pattern of spikes from different cells, can drive or modulate the activity of a downstream neuron. The examination of the temporal structure of spike trains, i.e. sequences of action potentials, and the detection of correlations among the signals of multi-electrode recordings can thus provide fundamental insights into presumptive coding strategies, when compared to rate effects. In order to characterize the temporal structure in parallel recordings of spike trains, a number of measures can be applied in order to assess the flow of information among neurons, some of which produce directed networks (e.g. transfer entropy (**Schreiber**, 2000; **Vicente et al.**, 2011), general linear models (**Truccolo et al.**, 2005; **Okatan et al.**, 2005)), while others produce undirected networks (e.g. cross correlations, mutual information (**Shannon and Weaver**, 1949); NeuroXidence[4] (**Pipa et al.**, 2008)).

The famous statement that "neurons that fire together wire together" (**Shatz**, 1992) nicely summarizes the relevance of synchrony, or milli-second precise timing for that matter, for plasticity. Long-term potentiation (LTP) and depression (LTD) are crucially dependent on the relative timing of spikes (this is also referred to as spike-timing dependent plasticity (STDP) (**Bi and Poo**, 1998)). Synapses are strengthened when a presynaptic spike immediately precedes a postsynaptic spike (LTP), and they are weakened if the temporal order is reversed (LTD). While long-term plasticity, as the name suggests, will take several minutes to hours to be implemented, short-term plasticity occurs in the order of milliseconds to minutes. Effects that can occur are facilitation of the transmission at the synapse and post-tetanic potentiation (**Zucker and Regehr**, 2002).

---

[4] for details on NeuroXidence, see section 2.7.1

Furthermore, the brain uses a distributed code to represent different features of visual objects and needs to bind information from different features in order to perceive a compound impression of our surrounding world. Location and motion of an object are processed via the dorsal stream, while features for the identification of the object itself are processed via the ventral stream (see section 1.4).The separately processed information then has to be bound together in order to create a complete image of the environment. A candidate mechanism for the binding of previously segregated information is synchronisation of neuronal activity (**von der Malsburg**, 1981; **Singer**, 1999a). The temporal binding hypothesis, also referred to as "binding by synchrony", suggests that neurons coding for the same object are synchronously active within fractions of a second / millisecond, while - and this is equally important - cells coding for other objects are active at a slightly different point in time. This also stresses the role of inhibition and the importance of a precise coordination of activity. Linked with the hypothesis of binding by synchrony is the theory of assembly coding. In this context, Donald Hebb coined the term cell assembly, which he described as "a diffuse structure comprising cells in the cortex (...), capable of acting briefly as a closed system, delivering facilitation to other such systems" (**Hebb**, 1949, p. xix). György Buzsáki describes Hebbian assemblies as "a group of cells with excitatory connections whose synapses have been strengthened by coactivation and whose excitatory connections are stronger among themselves than with other nonmember neurons" (**Buzsáki**, 2006, p. 161). In contrast, Nancy Kopell and colleagues define assemblies as "subsets of pyramidal cells that fire approximately synchronously in a transient manner, whether or not those cells have recurrent excitatory connections" (**Kopell et al.**, 2010), or, in short, "a coactive neuronal population" (**Ainsworth et al.**, 2012). Thus, Kopell and colleagues do not necessarily assume direct excitatory connections among the assembly members. Both individual cells and populations of neurons have been demonstrated to be able to self-organize and exhibit zero time lag synchrony even over long distances and without direct synaptical connections (**Vicente et al.**, 2008). Therefore, and because of the applied analysis approaches in this study that are able to detect temporally correlated firing, but not the underlying anatomical structure, Kopell's definition shall be adopted here. The assembly hypothesis implicates the idea that simultaneous activity of the cells of an assembly could trigger or modulate activity in downstream neurons and might constitute an unambiguous image for the decoding units. This way, each synchronously active assembly could code for a specific stimulus feature, while individual cells could be part of different assemblies at different points in time. In consequence, the coding space becomes larger than for a pure rate code. Interestingly, assembly activity in the visual cortex has also been observed in the absence of a stimulus (**Grinvald et al.**, 2003). Note that, for the definition of an assembly on the basis of correlated firing, parallel recording techniques are necessary.

Spike coordination can be assessed on various timescales and the analysis of correlated activity is strongly dependent on the time window over which it is computed (see e.g. **Cohen and Kohn** (2011)). With this, it is desirable to isolate the effects on the different timescales whenever possible. In particular, slow variations in firing rate, even over trials, can have effects on measures dealing with millisecond-precise synchronisation of neuronal activity. The fluctuations themselves are inherent in brain activity (see **Arieli et al.** (1996); **Raichle** (2015)), and therefore cannot be abolished. However, with suitable methods it is possible to extract only the information concerning the designated timescale, discarding slower or faster components.

1.3 Cortical Networks and Graph Theory

Brain networks depict the connectivity structure between entities of the brain on different scales (**Bullmore and Sporns**, 2009; **Park and Friston**, 2013). They are being studied extensively, and novel methods are constantly being developed or adopted from other disciplines to promote the knowledge of the structural and functional organization among brain units. The terms connectome and connectomics, coined by Olaf Sporns and Patric Hagmann in 2005, have become set phrases in the context of brain connectivity research and have experienced a hype over the last decade.

Despite the limited amount of knowledge about network structures in the brain that is available today[5], a variety of research initiatives have set their goal in understanding, and even reproducing and simulating the wiring and functioning of the brain.[6] Although supported by governments and funded with millions of dollars, the reception of some of these approaches has been very critical and described as "radically premature" (**Peter Dayan** in The Guardian[7]), which seems justified, given that the general principles in network formation are still not known, nor are the relevant temporal and spatial scales. In addition, one might have ethical concerns when it comes to artificial intelligence systems.

In general, it is important to note that brain networks are influenced by topological, spatial, temporal, and functional aspects[8], and the choice of the related analysis parameters. Analysis can also focus on only one of these aspects, but all networks are subject to all of them. As the brain has been shown to process information in parallel on multiple scales or frequencies (**Akam and Kullmann**, 2014), it is likely that, also in the field of brain networks, multiple scales are relevant in parallel. The systematic combination of comprehensive approaches can thus be very helpful in order to understand the principles of network structure and function. So what principles have been identified to this day?

The study of the brain as a complex network is one of the key approaches in order to understand its operating principles: on the macroscale, the distinct areas of the brain constitute a network among themselves (see Fig. 1.2). The parcellation into areas is hereby based on the regional specialisation of certain parts of the brain. Hence, brain networks are modular, also on the microscale, where neurons in the brain and their (synaptic or functional) connections build a highly complex network, and on the mesoscale level among larger entities, like cortical colums.

Brain networks are also hierarchical (**Felleman and van Essen**, 1991; **Kaiser et al.**, 2010; **Markov and Kennedy**, 2013), whereby the term hierarchical can refer to a sequential processing of information, to the nesting of smaller elements that make up larger units (e.g. neurons form columns, columns form areas, areas form the brain; also referred to as a recursive or fractal organisation (**Sporns**, 2006)), or to temporal aspects (**Kaiser et al.**, 2010).

Many aspects of network architecture have shown to be universal, and have been observed over many very different fields of research (**Barabási**, 2009). However, there are distinctive features of the brain, when compared to other networks, e.g. its spatial restriction inside the skull, which acts as a constraint on network size and wiring. In addition, the nodes are not homogeneous: brain areas have different sizes, cell types, laminar organisation, and connectivity structures. Also on the level of single cells, cell labels (**Seung**, 2009), such as cell type, functional preferences, or laminar position, differ.

---

[5] The only organism whose connectome has been fully anatomically mapped is C. elegans, a small nematode with some 300 neurons and on average 14 connections per neuron (White et al., 1986; Achacoso and Yamamoto, 1991; Watts and Strogatz, 1998), see also http://wormwiring.org (page viewed on 16 July 2015), and close to whole-brain imaging at single-cell resolution has only been reported for the neonatal zebrafish (Ahrens et al., 2013).

[6] e.g. NIH Human Connectome Project, http://www.humanconnectomeproject.org, (viewed on 13 July 2015), Human Brain Project, https://www.humanbrainproject.eu (viewed on 13 July 2015), The Brain Activity Map Project (also "BRAIN Initiative") (Alivisatos et al., 2012)

[7] The Guardian, Monday 7 July 2014, available on http://www.theguardian.com/science/2014/jul/07/human-brain-project-researchers-threaten-boycott (viewed on 9 October 2014)

[8] Here, the term topological refers to graph theoretical measures, whereas spatial means the actual Euclidian distance of units in the brain.

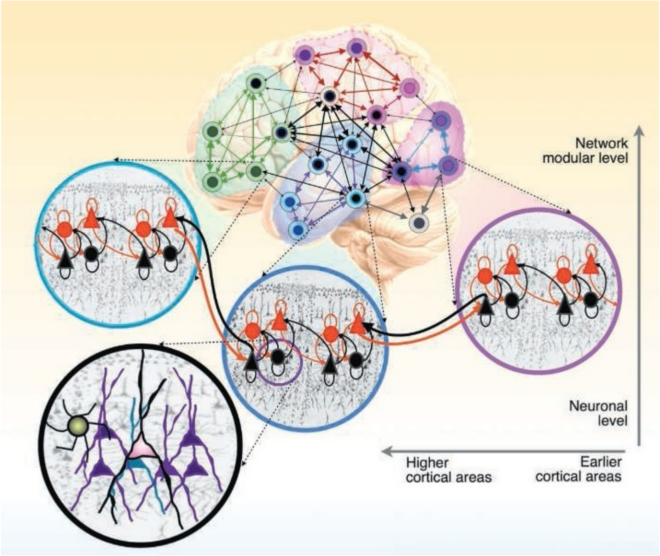

Figure 1.2.: Network scales. Network research in the brain can be conducted at several scales: at the neuronal level, between groups of neurons, or on the level of areas. Local networks constitute the basic building blocks that are linked internally and through feedforward and feedback connections (from Park and Friston (2013)) Reprinted with permission from AAAS.

In brain network analysis, typically, three types of connectivity are distinguished:

- structural = anatomical (physical, synaptic wiring between cells)
- functional = statistical (based on coherent or correlated activity)
- effective = causal (based on causality measures)

Functional and effective connectivity are computed using recorded neuronal activity without the knowledge about anatomical connectivity, although "structure always affects function" (**Strogatz**, 2001), or rather: structure constrains function (**de Costa and Martin**, 2013). Structural reconstructions in general fail to disclose the functional properties of the physical entities, while purely functional studies lack information about the underlying structural conditions. Thus, methods addressing structural and functional connectivity should be used in parallel, complementing each other's results. This, on the other hand, leads to the problem that anatomical structures have to be reliably matched to the observed functional properties, which can be a difficult endeavour. In addition, the time scales on which structural (order of minutes, hours, or longer) and functional (order of (milli-)seconds) networks are defined are fundamentally different. This further complicates the fusion of the two approaches. Therefore, only few studies provide parallel anatomical and functional approaches (e.g. **van den Heuvel and Sporns** (2013)), and also in the present study, the micro-anatomical structures cannot be provided.

Here, neuronal networks, based on electrophysiological recordings, will be interpreted in terms of graph theory (for an overview on the use of graph theory in brain research see **Sporns** (2011)). In the present approach, individual recording electrodes are set as nodes of a graph. The links of this graph are based on the functional connectivity between the nodes.

Information about the functional connectivity within a network can be obtained by calculating statistical dependencies between the signals of all possible pairs of electrodes. The observed functional connectivity determines the location of edges in the graph: if the observed statistical dependency between two nodes is significant (as determined by the applied method), an edge is inserted.

For more details on the methods and graph theoretical definitions, see section 2.8.

1.3.1 Graph analysis

As the experimental options in the context of multi-electrode recordings (as well as large-scale network measures like EEG[9], MEG[10] and fMRI[11]) are evolving, there is more and more complex data available which can be used to reconstruct functional neuronal networks. Consequently, the need for suitable tools to perform network analysis is increasing.

In addition to the analysis of graph measures, such as the clustering coefficient and the characteristic path length, two novel analysis approaches were developed in this context, which have been presented previously in the author's diploma thesis (**Schmitz**, 2009).

While the first method ("Test on Homogeneity") compares edge probabilities of graphs irrespective of the topology of the graph, the second approach tests whether the topology of two graphs composed of the same nodes, but different edge configurations for different experimental conditions, is different.

For the first approach, one first defines two disjoint sets of edges. This definition can be made based on experimental or physiological considerations, or should be research hypothesis driven. In this study, the partition of the set of edges was conducted in three ways: first, according to a neighbourhood relation dividing between local and distant connections, second, dividing between edges that link units with similar orientation preferences and those that do not, and third for edges between units with similar or different direction preferences. Subsequently, relative frequencies of edges in the two respective sets were compared.

The second approach ("Test on Hamming Distance") was developed to detect whether the same nodes in a graph are connected differently across two conditions. To test this, a metric similar to the one introduced by R. W. Hamming (**Hamming**, 1950) was used, thus called Hamming distance. The use of the Hamming distance as a measure for similarity between graphs has also been proposed by **Banks** (1994), **Butts and Carley** (2005), and **Berg and Lässig** (2004) (in their work referred to as pairwise mismatch). To construct an H_0 hypothesis and a hypothesis test, random Erdös-Rényi graphs were used as a reference.

For details on the procedures, please be referred to sections 2.10 and 2.11.

1.3.2 Types of networks

There is an ongoing debate about which general organizing principles the brain follows and what type of graph structure(s) it forms. Among the most common structures that are discussed are the random network, the scale-free network, and the small-world network. These network types need not be present exclusively, but can also partly be present simultaneously.

Random Networks

Random networks of the Erdös-Rényi (ER) type (**Erdös and Rényi**, 1959) have links that are all set independently with a certain probability. In a special case of the ER network, the Bernoulli network, links are set with the same probability.

It does not seem likely that the brain is randomly organized, as it is hard to imagine that a random structure could possibly solve the tasks that the brain has to cope with. However, even in very recent studies, this is still questioned: "The connectivity diagram of neocortical circuits is still unknown, and

---

[9] EEG = electroencephalography

[10] MEG = magnetoencephalography

[11] fMRI = functional magnetic resonance imaging

there are conflicting data as to whether cortical neurons are wired specifically or not" (**Fino and Yuste**, 2011). Even though there is piling evidence that wiring is extremely specific, one cannot take it for granted. Hence, the first step in graph theoretical analysis should be to check the networks for randomness. This can be especially important because with none of the methods that are availabe to this day it is possible to sample the complete brain network. Thus, even if the brain itself is not randomly organized, the sample drawn from it by the selected experimental method can be.

Scale-free Networks

A scale-free network is defined as a network that exhibits a power-law degree distribution, meaning a degree distribution wherein a few nodes in a given network have a large share of the inter-nodal connections while a large amount of nodes have relatively few connections, i.e. the degree distribution follows $P(k) \sim k^{-\gamma}$, where k the degree of a node and typically $2 < \gamma < 3$ (**Hildago and Barabási**, 2008). Many real-life networks have been shown to exhibit a scale-free structure, such as the world wide web (**Albert et al.**, 1999), and the network of scientific papers linked by citations (**Redner**, 1998). The feature of scale-free-ness arises through two fundamental mechanisms: growth and preferential attachment (**Barabási**, 2009).

Scale-free networks are particularly robust towards random attacks: if a random node is eliminated, chances are high that this is a sparsely connected one, leading to only minor effects on the global network structure. However, scale-free networks are vulnerable to targeted attacks onto so-called hubs, i.e. densely interconnected nodes. The average path length L in scale-free networks is rather small, it follows $L \sim \frac{log(N)}{log(log(k))}$ (**Hildago and Barabási**, 2008). While structural networks of mammalian brains seem to be connected in a scale-free manner, it is still in debate whether functional brain networks are (**Eguíluz et al.**, 2005; **Reijneveld et al.**, 2007). The ambiguity in results could be due to the fact that sub-networks of scale-free networks are not necessarily scale-free (**Stumpf et al.**, 2005).

Small-World Networks

In short, a small-world network (**Watts and Strogatz**, 1998) is a network with a particularly high clustering and a short average path length. The network amongst brain areas has been approved for small-world-ness in numerous studies (**Sporns and Zwi**, 2004; **Sporns and Honey**, 2006; **Bassett and Bullmore**, 2006). However, it has been argued that in dense networks like the large-scale brain network, this property is inherent, and thus expected (**Markov and Kennedy**, 2013), and is not even of any special interest, as the task of the brain is not simple message-passing (which would be facilitated by a small-world structure), but integration of information. For local brain circuits, however, the connectivity patterns are less well-known. Thus, in the context of microcircuits, probing the small-world characteristic might still yield valuable information. In fact, local networks have previously been shown to exhibit small-world properties (**Yu et al.**, 2008; **Gerhard et al.**, 2011), as well as the neuronal network of *C. elegans* (**Watts and Strogatz**, 1998), which also shows indications of a scale-free topology (**Barabási and Albert**, 1999).

In general, it holds that scale-free networks also exhibit small-world properties, but small-world networks are not necessarily scale-free (**Amaral et al.**, 2000).

1.4 The Cat Primary Visual Cortex

When photons falling on the retina are detected by photoreceptors, this chemical signal is transduced to an electrical one and fed into the visual system of the brain. After first processing steps in the retina, optical fibres run from the retina to the lateral geniculate nucleus (LGN) of the thalamus via the optical nerve.[12] From the LGN, visual information is relayed to layer IV of the primary visual cortex. Information is then further passed on via two different pathways: the ventral stream (also inferior temporal stream, or 'what' path), where information about the nature of the object(s) is processed, and the dorsal stream (also parietal stream, or 'where' path), which processes information about the position and velocity of objects in the visual field (**van Essen and Maunsell**, 1983). The posterior middle suprasylvian (pMS) cortex, one of the key areas in the context of the present study, is part of the dorsal stream and therefore plays a crucial role in motion processing.

The dataset that was assessed for the present study was recorded in area 18 (area occipitalis (**Otsuka and Hassler**, 1962; **Tretter et al.**, 1975)) of the cat primary visual cortex. In the cat, area 18, together with area 17, has been defined as a primary visual area (**Payne and Peters**, 2001, p.10).

Neurons in the primary visual cortex are selective for stimulus position, orientation and direction of motion, spatial and temporal frequency, binocular depth and colour (**Carandini**, 2012). Area 18 holds a retinotopic representation of the visual field (**Tusa et al.**, 1979). Neurons in this area have relatively large receptive fields and respond to rather rapid visual transients. They are highly orientation selective (**Hubel and Wiesel**, 1959), and most of the neurons also exhibit a pronounced direction selectivity (**Hubel and Wiesel**, 1965; **Tretter et al.**, 1975; **Orban et al.**, 1981b). Orientation selectivity is based on the shape of the receptive fields: while retinal and LGN receptive fields are round, mulitple LGN cells project to one simple cell in the primary visual cortex, resulting in combined receptive fields with elongated shapes (**Hubel and Wiesel**, 1962). As a result, these cells preferably respond to oriented stimuli that match the orientation of the receptive field. Complex cells receive input from several simple cells, consequently, their preferred orientation is dependent on the preferred orientation of the respective receptive fields, and they can additionally detect oriented movement.

The mammalian neocortex is organized in laminae, which run parallel to the surface. Area 18 shows six distinct layers (see Fig. 1.3). As mentioned before, the input from the thalamus first reaches layer IV and is then further transmitted to other layers.

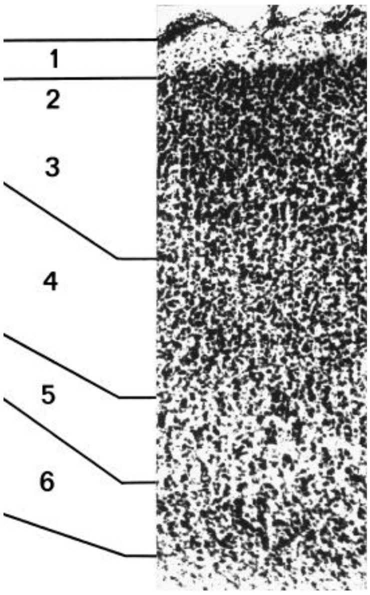

Figure 1.3.: Cortical Laminae. Cat area 18 exhibits six cortical laminae. Modified from Payne (1990).

---

[12] The retina also projects to the midbrain and the superior colliculus, where pupillary reflexes and eye movements are controlled, respectively.

Lorente de Nó (1949) first discovered that vertical connectivity in primary visual cortex is stronger than horizontal connectivity. **Hubel and Wiesel** (1962) investigated this fact further, discovering that cells with similar orientation preference are organized in a columnar fashion, running perpendicular to the surface, spanning all layers (see also **Mountcastle** (1997)). These so-called orientation columns cluster further into so-called orientation hypercolumns that contain orientation columns for all orientations. Together with colour blobs and ocular dominance columns, orientation columns are combined to form a hypercolumn, which includes, for a specific area of the visual field, all orientations, colours, and the information from both eyes.

While vertical connectivity amongst the neurons within a column is strong, columns are also interconnected via horizontal connections. Through these, information can be integrated over several millimetres of cortex. With this, columns with a similar tuning preference tend to be more densely interconnected than those with different preferences (**Gilbert and Wiesel**, 1989; **Engel et al.**, 1990).

Area 18 is highly connected to other brain regions (see Fig. 1.4). For the present study, the connection to the pMS cortex was of central interest. Area 18 sends information to pMS and, at the same time, receives feedback signals from that very same area. Roughly a third of afferent connections to area 18 originate from the LGN (34.8 %), while 26 % originate from the pMS cortex, namely PMLS, AMLS, and PLLS (**Payne and Lomber**, 2003). About 23 % of afferents come from areas 17 and 19, which, in turn, are indirectly influenced by the pMS cortex as well (see Fig. 1.5).

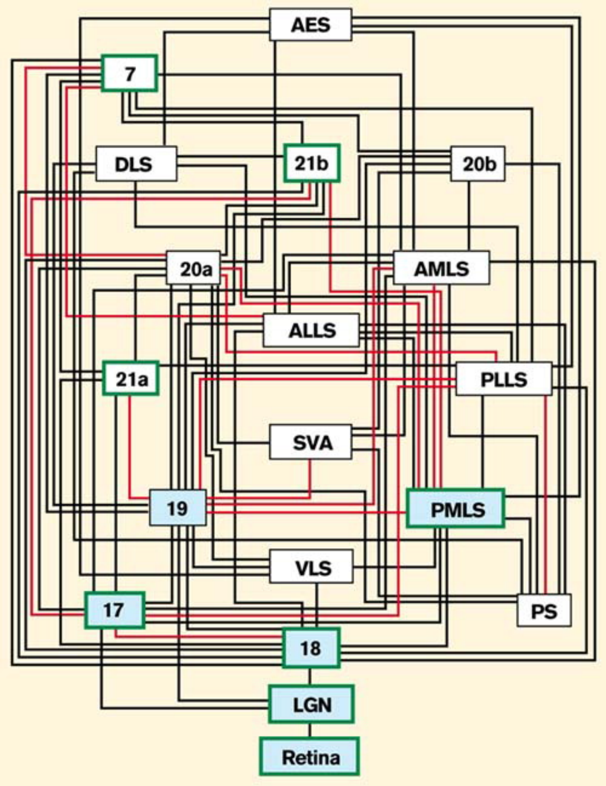

Figure 1.4.: Hierarchical connectivity in the visual system of the cat. Areas 17/18 are considered the first entry stage into the visual system after passing through the thalamus. However, the network amongst visual areas is highly reciprocal and processing can happen in separate streams in parallel. (red links: oriented connections, cyan: synchrony found in respective area, green border: synchrony found between areas; PMLS: posteromedial lateral suprasylvian area, AMLS: anteromedial lateral suprasylvian area, VLS: ventrolateral suprasylvian area, AES: anterior ectosylvian sulcus, SVA: splenial visual area, PS: posterior suprasylvian area, PLLS: posterolateral suprasylvian area, DLS: dorsolateral suprasylvian area, LGN: lateral geniculate nucleus) From Golledge et al. (1996).

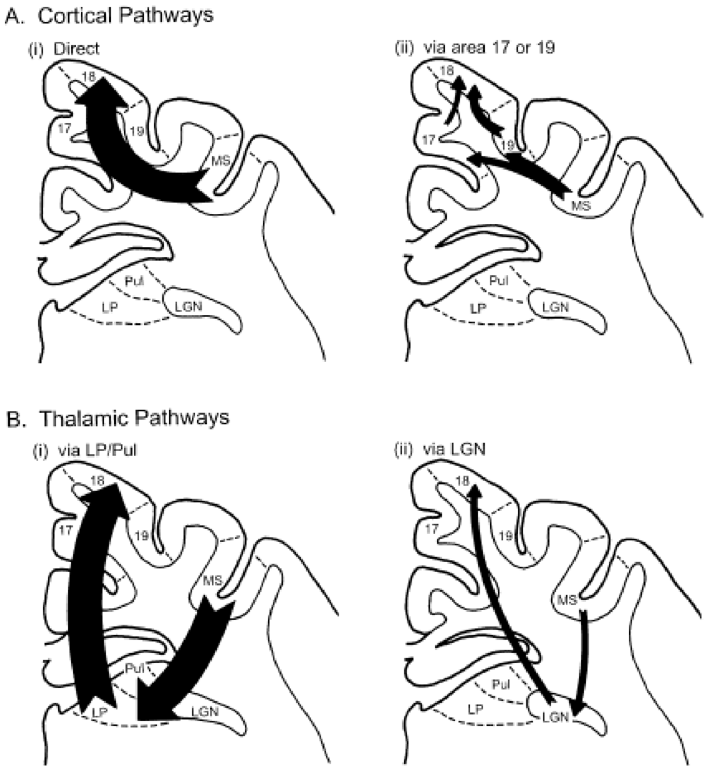

Figure 1.5.: Feedback signals to area 18. Area 18 receives direct and indirect feedback from the MS cortex, via (A) cortical and (B) thalamic pathways. MS = middle suprasylvian cortex; Pul = Pulvinar; LP = lateral posterior nucleus of the thalamus; LGN = lateral geniculate nucleus From Payne and Lomber (2003).

1.5 Hierarchies, Feedback Signals, and Visual Neglect

Whether you look at a scene from a comfortable chair in a café or talk to someone, you always have some (not necessarily conscious) expectation about what is going to happen next. People walking at a certain speed will not suddenly change their location or orientation and you can often predict the next couple of words someone is going to say. This indicates that the brain does not just react to external stimulation, but constantly builds and tests hypotheses about the environment.

While the classical view of information processing in the visual system, and the brain as a whole, was that of a serial bottom-up system, in which information is processed in a feedforward chain of hierarchically ordered stages (**Hubel and Wiesel**, 1965), it is now recognized that although sensory information is fed into the system in a feedforward manner, the pure feedforward model constitutes a strong simplification of the actual situation: processing is highly parallelized, and some of the fast processing times that are observed in the brain cannot be explained by feedforward connections alone (**Masquelier et al.**, 2011).

Most connections in the brain are reciprocal (**Symonds and Rosenquist**, 1984; **Felleman and van Essen**, 1991): while information is transferred up the hierarchy, the signal is modulated by feedback projections (**Sandell and Schiller**, 1982; **Mignard and Malpeli**, 1991; **Vanduffel et al.**, 1997; **Hupé et al.**, 1998; **Galuske et al.**, 2002; **Buschman and Miller**, 2007). More precisely, neuronal connectivity is organized using feedback, feedforward, and lateral connections. Feedforward connections usually originate in supragranular layers and target layer IV, while feedback connections rather originate in infragranular layers and terminate outside layer IV (**Felleman and van Essen**, 1991). Both of these types of connections are primarily excitatory (**Salin and Bullier**, 1995). Lateral connections are interconnections at the same hierarchical level, which occur throughout all layers (**Felleman and van Essen**, 1991).

The top-down influences mainly originate from prefrontal and parietal areas, however, there is no central control module, or "master" area that all information converges to or that could be seen as a general starting point for top-down signalling.

Roles of cortical feedback signals

It has been shown that feedback signals influence hierarchically lower areas depending on attention (**Salinas and Sejnowski**, 2001; **Zhang et al.**, 2014), expectation, and perceptual task (**Gilbert and Sigman**, 2007). Feedback signals enhance responses in lower areas, increase saliency and figure-ground segregation (**Hupé et al.**, 1998) and modulate receptive field properties (**Schwabe et al.**, 2006). They have been described to synchronize activity in hierarchically lower areas (**Engel et al.**, 2001; **Bal et al.**, 2000) and play a role in the manifestation of brain states by modulating intrinsic circuitry (**Gilbert and Sigman**, 2007). Whether feedback signals alone are able to drive a target neuron does not seem to be finally determined, with studies arguing in favour of (**Markov et al.**, 2014) and against this notion (**Vanduffel et al.**, 1997; **Hupé et al.**, 1998).

Feedback also plays a crucial role in the theory of predictive coding (**Rao and Ballard**, 1999): in this framework, feedback signals carry predictions about the expected sensory input, while feedforward signals carry the differences, or error signals, between the prediction and the actually received sensory input. This could be an efficient way for the brain to reduce the amount of redundant information (**Rao and Sejnowski**, 2002). The creation of predictions is likely supported by synchronous and oscillating activity (for a review see **Engel et al.** (2001)).

Neurons in primary visual areas respond selectively to certain spatial and temporal features of external stimuli, such as edges with a specific orientation, movement directions and speed, and colours. Moving up the hierarchy, more and more features are combined to form an increasingly complete picture (**Hubel and Wiesel**, 1965; **Felleman and van Essen**, 1991), also termed "vision at a glance" (**Hochstein and Ahissar**, 2002), which happens rapidly, but without exact examination of details. At the same time, feedback information provides "vision with scrutiny" (**Hochstein and Ahissar**, 2002) to enable the focusing on relevant information.

The area that was recorded from for the present study, area 18, receives direct feedback from the pMS cortex, which was deactivated during the experiments. It was previously shown that feedback signals from the pMS cortex strongly influence the formation of direction selectivity maps and sharpen orientation tuning in area 18 (**Galuske et al.**, 2002).

Visual neglect

A stroke can lead to severe, often life-threatening conditions. While many treatment approaches exist, the consequences for the communication among brain areas and the mechanisms of plasticity and restitution are not fully understood. For a thorough understanding of the flow of information and the effects of a disruption of this information flow, as it happens in case of a stroke, it can be of great help to dissect the neuronal code and the connectivity patterns between brain areas and neurons on the global and the local scale.

One possible consequence of a stroke is the so-called hemineglect (see e.g. **Rafal** (1994) for a short review of symptoms and pathophysiological mechanisms). In humans, a (visuospatial) neglect is most often caused by a lesion in the right parietal cortex. This results in the patient neglecting visual stimuli in the visual hemifield contralateral to the lesion.

In the cat, visuospatial neglect can be induced by unilateral deactivation of the posterior middle suprasylvian (pMS) cortex or the superior colliculus (SC) (**Payne et al.**, 1996). Deactivation can be performed via lesions (see e.g. **Müller** (2017)), thermal methods (cooling, see **Lomber et al.** (1999)) or pharmacological substances (see **Lomber** (1999)). Strikingly, bilateral deactivation of pMS cortex or parallel deactivation of one pMS and the contralateral SC leads to a restitution of normal behaviour ("Sprague effect"; (**Sprague**, 1966; **Lomber and Payne**, 1996; **Payne and Rushmore**, 2004)). For this reason, the neglect syndrome has been believed to be caused by disinhibition and a consequent hyperexcitation of the contralateral hemisphere (**Rushmore et al.**, 2006). The phenomenon has been shown not to involve blindness – also supported by the fact that neglect affects imaginary vision as well (**Bisiach et al.**, 1981) –, but rather be attention deficit. Recent evidence, however, points to the underlying deficit being a more complex network disconnection effect (**Bartolomeo**, 2007; **Barnes**, 2014; **Müller**, 2017).

In the dataset underlying this study, the pMS cortex was thermally deactivated to induce a visual neglect in the cat (see section 2.1). The effects of this disruption of the global brain network on the neural activity in the local subnetwork of area 18 are the subject of this thesis.

1.6 Purpose of the Study

The changes in activity of single neurons and the local field potential (LFP) in area 18 under similar experimental conditions as this dissertation work have been investigated previously (**Galuske et al.**, 2002; **Ebisch**, 2007), partly based on the same dataset as for the present dissertation (**Geider**, 2008; **Barnes**, 2014). However, neurons are neither isolated entities, nor does the compound activity of many neurons (as observed with methods with lower spatial resolution, such as EEG and LFP) occur in isolation of the activity in distant cortical locations. Rather, local neural activity is integrated in a complex global network, and only through concerted activity of this global network can complex tasks be solved. Therefore, the analysis of local functional networks performed in this work can provide important contributions to the resolution of research questions in neuronal signal processing and "close the gap" between single-cell and LFP analysis.

This thesis therefore starts off with the challenge of assessing the properties of local neuronal networks in a dataset recorded in cat area 18, while the posterior middle suprasylvian (pMS) cortex is thermally deactivated. The cells in deactivated pMS cortex, and hence the feedback signals to area 18, are thus silenced. This is assumed to alter the activity patterns in the recorded region, area 18.

In order to assess changes in network structure during the deactivation phases, methods that help define the links in the area 18 network are required, as well as methods that are able to disclose the network properties. Aspects that should be taken into account during such analyses are the suitability of the applied connectivity measure, the time windows used for correlation measures, the definition of the nodes of the networks, and the relevant spatial scales.

The goal of this study is the characterization of the functional properties of the recorded neurons under different experimental conditions. Particularly, the changes in interactions between (small groups of) cells are described. Spike rates, orientation and direction selectivity, and correlated activity among neurons are assessed, which are eventually used to create networks based on significantly correlated activity. To this end, methods and tests were developed, and used to ascertain and interrogate local functional networks.

The focus of this study will, however, not only be on the methods used and (further) developed through application to the datasets described below, but also on the interpretation of the results of the network analysis, as they pertain to the neurophysiology. With this, there are three levels of interest: 1) the changes in spiking activity and local network properties in area 18 during deactivation of pMS, 2) a more general characterization of the firing properties and network connectivity patterns of cells in V1/area 18, and 3) the even more general question of the principles of neuronal coding in the visual cortex, and the neocortex in general.

2 Material and Methods

In this chapter, the experimental and analytical methods that were used in the study are elucidated.

2.1 Experimental Procedures

The analysis methods described below were applied to a dataset obtained in a series of experiments concerning visual neglect. The analyses are based on electrophysiological action potential and local field potential recordings. The experiments were conducted at the Max Planck Institute for Brain Research, Frankfurt, Germany. All procedures were performed following the guidelines of the local authorities and overseen by a veterinarian.

Please note that the author did not perform the deactivation experiments, but was provided with the raw datasets after the recordings. Experiments were conducted by Boris Ebisch, Kirsten Geider, William Barnes, and Ralf Galuske. The same dataset has been analyzed with a different focus by **Kirsten Geider** (2008) and **William Barnes** (2014). These publications, as well as the doctoral thesis by **Boris Ebisch** (2007), also provide further details on the experimental procedures. Here, only a broad overview shall be given.

Data were collected in three anaesthetized male cats aged one and a half years, using an Eckhorn multi-electrode system (Thomas Recording, Germany) (Fig. 2.1). Sixteen custom-made tungsten electrodes were placed in area 18 of the cat's primary visual cortex, with a distance of 500 μm in the x-y-plane, but individually adjustable in cortical depth. Cooling probes, also known as *cryoloops* (**Lomber et al.**, 1999), were implanted in the pMS cortex to induce a visual hemineglect (**Payne et al.**, 1996).

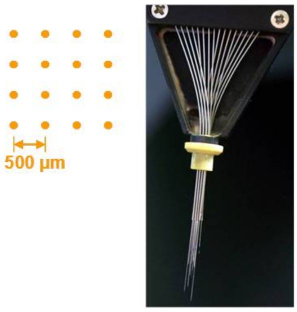

Figure 2.1.: Electrode matrix. The electrodes were placed in a 4x4 grid in a so-called "Eckhorn matrix", with an equal spacing of 500 μm in the 2D-plane, but each electrode was individually adjustable in depth with the aid of micro motors (photo by Matthias Munk).

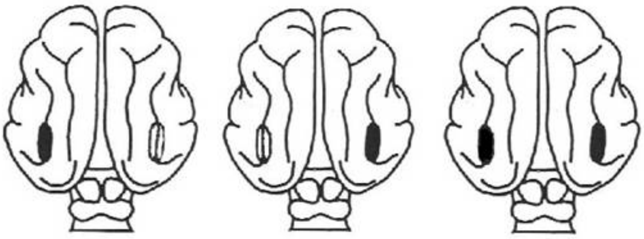

Figure 2.2.: Deactivation conditions. There were three possible deactivation conditions, as depicted in this figure. The deactivated area is shown in black, i.e. ipsilateral and bilateral deactivation is shown. Recordings were performed in the ipsilateral and contralateral area 18 on both hemispheres. Bilateral recordings were not performed. Modified from Lomber et al. (1999).

Electrophysiological signals were recorded in area 18, part of the primary visual cortex of the cat, while the ipsilateral, contralateral, or both pMS cortices were thermally deactivated (Fig. 2.2). For the deactivation, chilled methanol was pumped through the cryoloops. Figure 2.3 shows a schematic of the experimental setup.

Stimulation and recording protocol

The animal was visually stimulated with a black and white contrast square-wave grating, which was viewed by both eyes simultaneously. The grating was presented in four different orientations ($0°, 45°, 90°, 135°$), which moved in either of the two directions perpendicular to the bars of the grating. Hence, eight different stimulus conditions were possible (Fig. 2.4).

The order of occurence of the stimulus conditions was pseudo-randomized. Visual stimulation started with showing a grey screen for two seconds followed by one of the four differently oriented gratings remaining stationary for two seconds before the grating started moving for four seconds. Thus, one trial lasted for eight seconds.

Anaesthesia

Anaesthesia was induced by intramuscular administration of ketaminehydrochloride (ketamine 10%, 10 mg/kg body weight), xylacinehydrochloride (1 mg/kg body weight), and atropinsulfate (0,1 mg/kg body weight). For maintenance of anaesthesia, animals were artificially ventilated using a mixture of N_2O (ca. 70%), O_2 (ca. 30%), and halothane (1-1.2%). The concentration of O_2, CO_2, and halothane in inspiration and expiration was monitored closely throughout the experiment.

Multi-unit spike signal

In order to obtain spiking data, the signal was recorded with a sampling rate of 20-22 kHz and band-pass filtered (800-5000 Hz). Details on the analysis of the spike data are given below.

Local Field Potential

Parallel to the recording of the spike signal, a low-pass filter (120 Hz) was applied to the signal to obtain local field potential (LFP). This signal was digitized using a sampling rate of 1 kHZ. A Fast Fourier Transform (FFT) was applied to obtain the spectral composition of the signal. The power for different frequency bands between 4-90 Hz (see table 1.1, p. 16) was computed separately for further

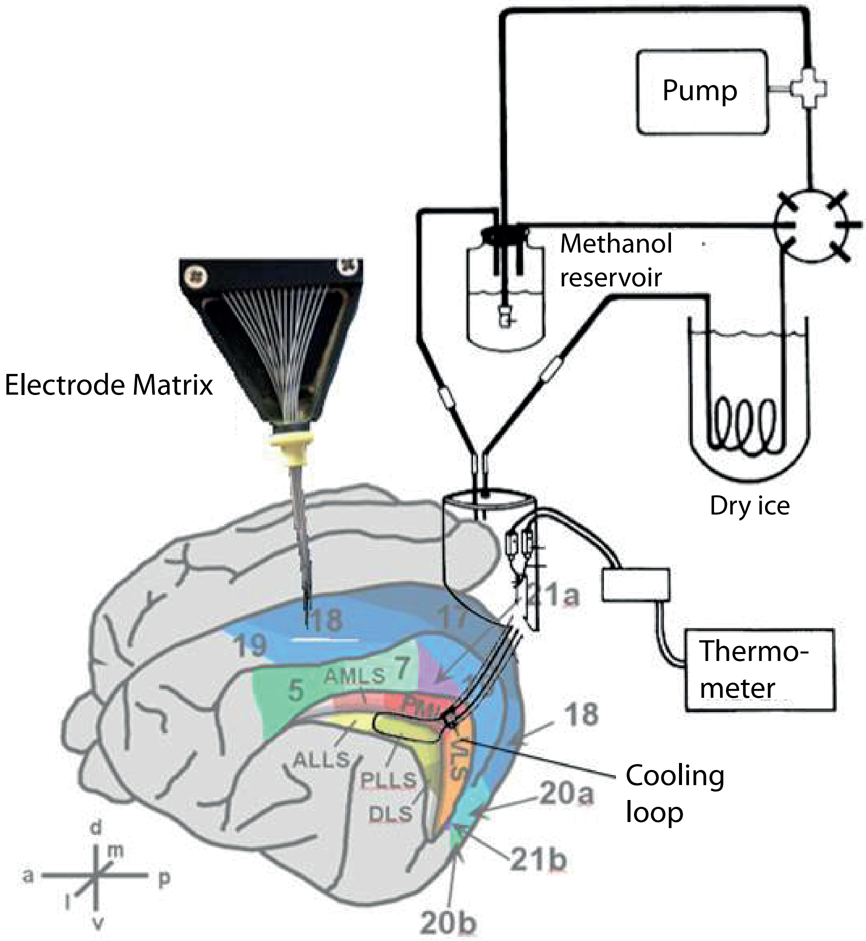

Figure 2.3.: Cooling circuit. The figure shows the position of electrodes and cryoloops in the cat's brain. Tungsten electrodes, operated using micro motors, were unilaterally placed inside area 18, while cooling probes were bilaterally placed into the pMS sulci. Methanol was cooled with dry ice and pumped through the circuit. The temperature at the cooling site was monitored and controlled by changing the velocity of the methanol flow. (Brain modified from Tusa et al. (1981); Galuske et al. (2002)[1], cooling circuit modified from Lomber et al. (1999), photo of electrode matrix by Matthias Munk.)

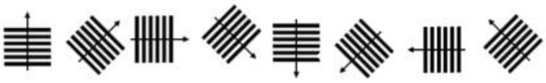

Figure 2.4.: Stimuli. A black and white square-wave grating was shown in four different orientations, and eight different moving directions.

analyis. With this, oscillations with a frequency of 50 Hz, i.e. of the European line noise, were omitted. Evoked and induced activity were calculated by computing the spectral composition of each trial and then averaging (induced activity), or averaging over all trials first and then applying the FFT (evoked activity), respectively.

2.2 Spike Detection

The first step in spike train analysis is the detection of spikes and the isolation of those from background noise (Fig. 2.5). In a lot of studies, spike detection thresholds are set online, i.e. during the recordings, and only the spike shapes around the values exceeding the thresholds are stored for further analysis. In the present study, the entire high-pass filtered signal was stored. This, of course, leads to larger data volumes, but bears the advantage that spike detection thresholds can be varied until the optimal value is found and variations depending on the choice of the threshold can be assessed.

Thresholds were chosen in two ways: for the multi-unit analysis, thresholds were set by visual inspection. For the single-unit analysis, the following criterion, suggested by **Quian Quiroga et al.** (2004) was applied:

$$Thr = 5\sigma_n, \qquad \sigma_n = median\left(\frac{|x|}{0.6745}\right) \tag{2.1}$$

Here, the median-dependent value σ_n is an estimate of the variation of the background noise, which is not as susceptive to rate fluctuations as the mean-based measure of standard deviation (**Quian Quiroga et al.**, 2004). Thus, the threshold is more robust against changes in noise level than thresholds that are based on the standard deviation of the signal. The so found thresholds were then used in the pre-processing before the application of the spike sorting procedure.

For the analysis of multi-unit activity (MUA), it was decided against automatic thresholds in the form of multitudes of the standard deviation, or σ_n for that matter, in order to avoid thresholds 'on the border' between two typical spike amplitudes. Thresholds were chosen by visual inspection of the raw data in Spike2 (version 4.01, Cambridge Electronic Design Limited, UK) of the first data set (first 56 trials for warm condition), checked using the following 128 trials for warm condition and, where necessary, adjusted. These thresholds were then kept constant for the course of one recording session to enable the comparison of rates between the deactivation conditions. Samples were taken from randomly selected parts of the session and checked to ensure that the thresholds were appropriate for the whole session. In ambiguous situations, the thresholds were set rather generously in order to be able to calculate correlations even for phases with only low amplitude spikes. This is also important because, despite action potential waveforms generally following the "all or nothing" principle and displaying the same shape, they can overlap with background activity and hence, amplitudes can vary slightly.

2.3 Spike Sorting

With spike sorting, action potentials can be assigned to separate single units, based on their waveform. Spike sorting requires three fundamental steps: first, the detection of spikes and isolation from the raw signal. This is usually accomplished by applying an amplitude threshold to the high-pass filtered multi-unit signal, as described in section 2.2. In a way, this already represents a form of spike sorting, especially if a distinct unit with considerably higher amplitude spikes than the other units can be isolated. Second, features of the spike waveforms are extracted that are then fed into a clustering algorithm. This step requires information about the waveform of the action potential. In this context, a high sampling frequency is beneficial, since the more information about the waveforms there is, the more sensitive and precise the classification will be. The third step is the classification of spikes into spikes originating from different cells. Ideally, each of the resulting clusters consists of the spikes fired by one cell.

Due to limitations in electrophysiological recordings and contamination with background "noise", the spiking of the cells close to the tip can never be completely described. A conservative decision in spike

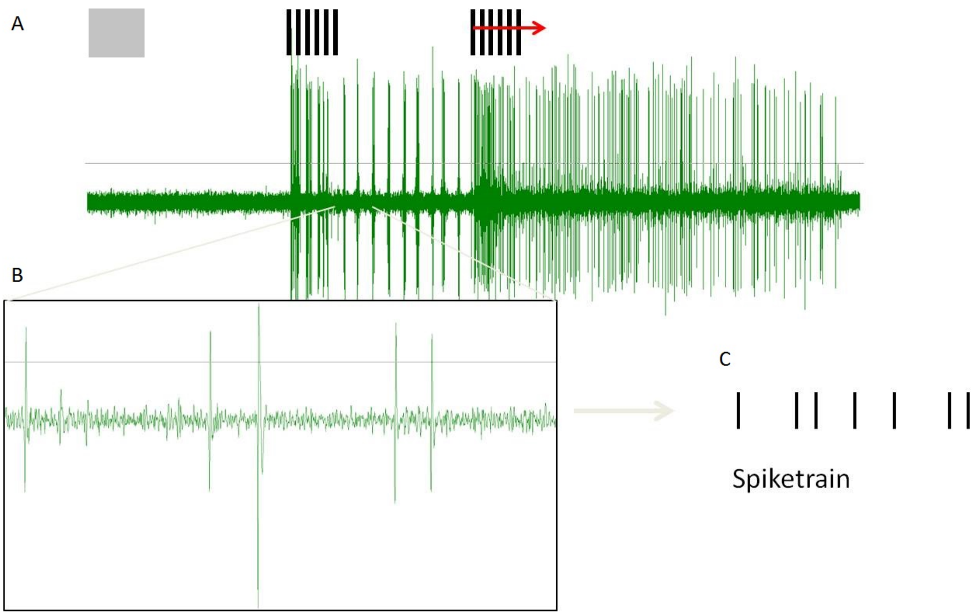

Figure 2.5.: Spike detection. (A) depicts the time course of an example trial from the dataset that is analyzed in the present study: during the first two seconds, a grey screen is shown to establish a 'baseline' activity. For the next two seconds, a static grating is shown, followed by a moving grating for four seconds. Both gratings evoke strong responses in cells that are tuned to the respective orientation and/or direction of the grating. (B) shows an enlarged section of the trial shown in (A); the spikes are clearly separable from the background activity. (C) For spike detection, individual events are isolated by thresholding and the timestamps are stored as a spiketrain.

selection, i.e. a tendency to leave ambiguous spikes out of the analysis rather than including them, can lower the percentage of the detected spikes further (though only slightly, if the spike sorting was of high quality), but will avoid contamination of the spiketrains with spikes of other units. This principle was followed here.

From the vast range of available spike sorting algorithms, "WaveClus"[2], developed by **Quian Quiroga et al.** (2004), was selected. With this algorithm, spikes are extracted from the raw spike signal first, applying an automatic threshold (see Eq. 2.1). Feature extraction is performed using a wavelet transform. Clusters are then identified by superparamagnetic clustering (SPC, **Blatt et al.** (1996)).

An example for the spike sorting procedure and the criteria for the identification of different clusters is shown in Fig. 2.6.

One of the goals of this study was to show the impact of spike sorting on the networks compared to networks resulting from multi-unit signals. To examine the effect of using the sorted signal rather than the multi-unit signal, spike sorting was performed on a subset of the data, namely all sessions for which all three deactivation conditions (ipsi-, contra-, and bilateral cooling) were available.

2.4 Orientation and Direction Tuning

Orientation and direction tunings for each single and multi-unit were determined. The orientation tuning index (OI) was calculated based on the rate-stationary phase during stimulation with the moving grating. Responses to opposite directions were added, the results were extended to the whole circle,

---

[2] The MATLAB code for WaveClus is freely available on http://www.vis.caltech.edu/~rodri/Wave_clus/Wave_clus_home.htm, page last viewed on March 31st, 2016.

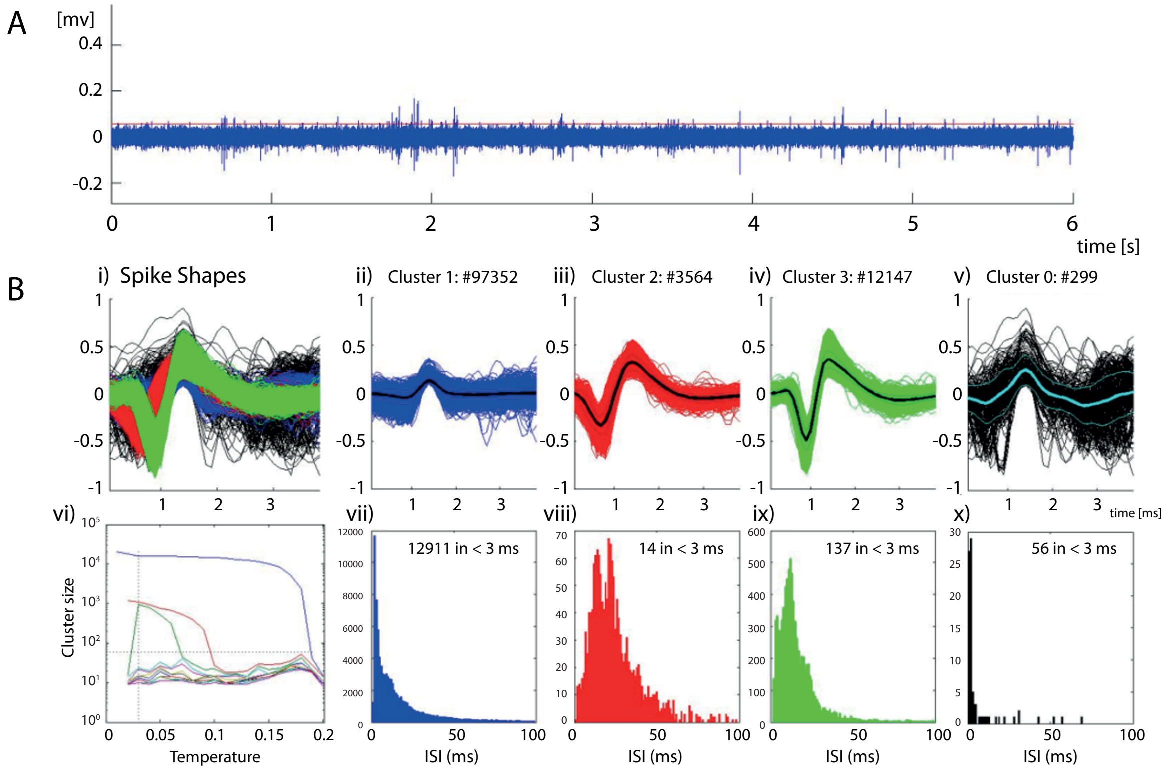

Figure 2.6.: Spike Sorting Example. The figure shows a screenshot of the application of WaveClus for an example session from experiment 121007 (session 20T, see appendix). (A) shows an extract of the spike signal (blue), with the automatic amplitude threshold set by WaveClus (red line). (B) shows the detected spikes and clusters as follows: i) Spike shapes of all detected spikes, superimposed and aligned at the point of threshold crossing; ii)-iv) Extracted clusters with mean spike waveform (black line); v) Cluster 0 ("trash cluster"), which contains all spikes that were not assigned to any cluster. The spikes of this "cluster" were excluded from the subsequent analysis; vi) Temperature for the SPC (see Quian Quiroga et al. (2004)), which was selected such that the resulting clusters were large, and as clearly separated as possible; vvi)-x) Inter-spike interval distributions for each cluster. In this example, it shows that Cluster 1 is not as clean as Clusters 2 and 3, which only exhibit very few spikes in an interval of 3 ms after the preceding spike (13% in Cluster 1, as compared to 0.3% in Cluster 2 and 1.1% in Cluster 3).

and the vector average was computed. Afterwards, the angles were scaled back to 180° to obtain the respective orientation, such that

$$OI \in \quad]-90,...,90] \subset \mathbb{R} \tag{2.2}$$

The direction tuning index (DI) was calculated by determining the preferred stimulus direction (PD) of the unit, i.e. the one that lead to the response with the largest number of spikes. Then, the number of spikes in the response for the opposite direction (non-preferred direction, NPD) was calculated. The direction index was then computed following **Orban et al.** (1981b):

$$DI = \frac{PD - NPD}{PD} \in [0,...,1] \subset \mathbb{R} \tag{2.3}$$

For later analysis, for each possible pair of units it was determined whether they shared a similar orientation and/or direction preference. For orientation, this was done by comparing the preferred orientation +/- 15°. For directions, units were viewed as sharing a similar direction preference, if the preferred direction was the same for both units.

2.5 Cross Correlation

As the basis for the Parallel Factor Analysis (see section 2.6), pairwise *cross correlation* values were used. Cross correlation is a widely used method for the detection of correlated activity between spike trains and has regained interest with the development of multi-electrode devices and the resulting possibilities concerning network analysis. Cross correlation between two spike trains was calculated using the MATLAB function `xcorr`. The computed cross correlation values were rate-corrected using a jitter correction (for details see section 2.6).

2.6 Parallel Factor Analysis (PARAFAC)

In order to get a first grasp of the effects of the thermal pMS deactivation on correlated activity in area 18, a screening method was required. It was decided to use *Parallel Factor Analysis* (PARAFAC) (**Hitchcock**, 1927; **Harshman**, 1970; **Carroll and Chang**, 1970), a method that is frequently used in chemometrics, but has so far not been well developed for electrophysiological data.

PARAFAC provides a clear and quickly assessible visualisation of the changes in correlation, with the advantage that a whole cycle of warm-cool-rewarm conditions is accessible at a glance. The results can be used to assess the correlation level during the baseline condition (i.e. no deactivation), physiological effects caused by the deactivation, and also to identify sessions with an unusual correlation profile. PARAFAC should then ideally be followed by further analysis methods, possibly also using several measures for correlated activity, to thoroughly describe the dataset. This is why, for the first coarse look at the data, the definition of correlation was kept fairly general (see definition of κ_{sync} in equation 2.6), and was refined in later analysis steps.

An article about the application of PARAFAC to neurophysiological data by the author of this thesis and colleagues was published in *Frontiers in Neuroinformatics* (**Schmitz et al.**, 2015). Parts of the publication are presented in the next chapter, followed by some additional comments and analyses. The following passages in italics are taken from the publication by **Schmitz et al.** (2015)[3].

---

[3] Contributions to the publication Application of Parallel Factor Analysis (PARAFAC) to electrophysiological data by Schmitz et al. (2015):

- Sarah Katharina Schmitz wrote the paper, designed the analysis, contributed to the implementation in MATLAB, performed the analysis, selected the results to be presented, and developed the discussion.
- Philipp P. Hasselbach developed the program code (with support by Marcelo Nakano Daniel and Stephan Wirsing), assisted in the design of the analysis and in writing the methods section.
- Ralf A. W. Galuske and Boris Ebisch performed the experiments.
- Ralf A. W. Galuske, Gordon Pipa, and Anja Klein helped with the design of the analysis and the interpretation of the results.

*"**The PARAFAC Model***

PARAFAC is based on a mathematical model that represents the interactions of the dimensions in which the input data is to be analyzed. In order to carry out PARAFAC, the analysis dimensions have to be defined first. Each input value can then be related to an index for each of the dimensions. Assuming N = 3 dimensions, for example, x_{ijk} *identifies the measured value for index i in the first dimension, j in the second dimension and k in the third dimension. In our case, the three dimensions are constituted by three experimental variables: electrode pair, stimulus, and repetition / trial. The correlation values* κ_{sync} *are obtained by the procedure explained [below] and used as an input into the three-dimensional array. They are placed at the location corresponding to the experimental condition they were obtained for (electrode pair x stimulus x repetition / trial).*

PARAFAC is now used to model this input array. Let F denote the number of so-called components and define so-called loading matrices A, B, and C of dimensions $I \times F$, $J \times F$ *and* $K \times F$ *and with elements* a_{if}, b_{jf} *and* c_{kf}, *respectively, and the modelling error* ε_{ijk}. *The general model used by PARAFAC to represent the input data is then given by (**Bro**, 1997)*

$$x_{ijk} = \sum_{f=1}^{F} a_{if}\, b_{jf}\, c_{kf} + \varepsilon_{ijk}. \tag{2.4}$$

A graphical illustration of the model is given in Fig. 2.7.

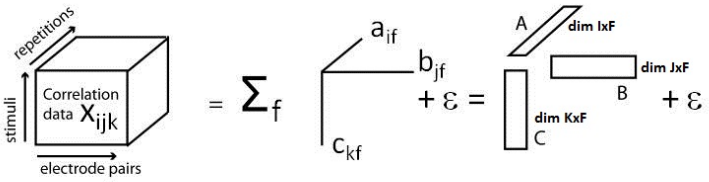

Figure 2.7.: Illustration of the PARAFAC model. The three-dimensional array containing the cross correlation information for each electrode pair, stimulus, and repetition, is decomposed into a sum of products of three factors, called loadings, which build up the loading matrices A, B, and C. Modified with permission from Miwakeichi et al. (2004).

PARAFAC thus constrains the interactions between the different dimensions to the complete multiplicative interaction. The loading vectors are determined by minimizing the modelling error ε_{ijk}. *This minimization can be carried out using the alternating least squares (ALS) approach, for example. ALS iteratively determines the loading matrices A, B, and C by the following algorithm (**Bro**, 1997):*

1. *Choose the number of components, F (on the choice of F see next paragraph)*
2. *Initialize B and C*
3. *Estimate A from X, B, and C by least squares regression to minimize the square of the model error*
4. *Estimate B likewise*
5. *Estimate C likewise*

6. *Repeat from 3) until the algorithm converges (indicated by only little changes in fit or loadings)*

*The choice of the number F of components is difficult and no technique giving clear values has been identified yet. If F is chosen too small, not all effects in the input data can be identified. If F is chosen too large, however, noise is modeled increasingly and the existing effects in the data will be modeled by correlated components. Different approaches for estimation of the best value for F exist (**Bro**, 1997). The approach taken in this work was to increase the number F of components until the decrease in the residual error decayed significantly. The model with the optimal number of components was then determined to be the one which was able to explain the highest amount of variance without any of the components being correlated. The quality of the analysis results of multilinear variation strongly depends on the preprocessing of the input data. Possible preprocessing strategies are centering and scaling (see (**Bro**, 1997)): Centering removes a non-zero mean from the data. A complete centering of the input data in all dimensions can be achieved by taking the result of the previous centering and center it in the next dimension. Scaling adjusts the variations in each of the dimensions to comparable magnitudes. Note that in contrast to centering, subsequent scaling of several modes is problematic since scaling one mode affects the scaling of other modes as well as the centering of the same mode. For this reason, centering should be carried out after scaling. Iterative approaches that can achieve a scaling of all modes are available (**Bro**, 1997). In this study, the data were centered in all dimensions. No scaling of the data was carried out.*

Synchrony and oscillatory synchrony

Two different metrics were established in order to quantify the degree of synchrony and oscillatory synchrony. Since both phenomona are identified using the correlogram, both metrics are based on the correlogram.

Spike trains were stored as binary vectors with sampling frequency resolution. Ones occurred where a sample value exceeded the chosen threshold and the sample before did not. For the calculation of cross correlations, a binning of 2 ms was introduced.

For the synchrony measure, the cross correlogram λ_{xy}^{raw} of the spike trains $\mathbf{x}$ and $\mathbf{y}$ of two multi-units in the analysis window T was computed:

$$\lambda_{xy}^{raw}(\tau) := \sum_{t \in T} x(t) y(t+\tau). \tag{2.5}$$

To correct for rate induced chance coincidences, we normalized the correlograms to the firing rate. To this end, the spikes in the spike trains were convolved with a 'jitter kernel' and the resulting cross correlogram was subtracted from the raw correlogram λ_{xy}^{raw}. To implement a computationally efficient jitter correction, we rely on convolution with a homogeneous filter with entries $\frac{T_{\text{sample}}}{T_{\text{jitter}}}$, with T_{sample} the time interval between two samples, which corresponds to jittering the spike train randomly within a time interval of $T_{\text{jitter}} = 6$ ms. The jittered spike train $\tilde{x}$ was thus obtained from spike train x according to $\tilde{x} := K * x$, where $*$ denotes the convolution. A correlogram was then computed from the two convolved spike trains and subtracted from the original correlogram, to obtain the normalized correlogram $\lambda_{xy} := \lambda_{xy}^{raw} -$

> *λ_{xy}^{jitter}. The convolution approach is equivalent to the random drawing of jitter times from a uniform distribution (following the Wiener-Khinchin theorem, see also (**Pipa et al.**, 2008)).*
>
> *The degree of synchrony was measured by the largest positive peak in the normalized correlogram within a window of size $T_{\text{sync}} = 5$ ms around a lag of zero. The synchrony metric κ_{sync} is thus defined as follows. Let $\kappa = \max_{l, l \in [-5 \text{ ms}, 5 \text{ ms}]} \lambda_{xy}(l)$. Then,*
>
> $$\kappa_{\text{sync}} := \begin{cases} \kappa, & \text{if } \kappa \geq 0 \\ 0 & \text{else.} \end{cases} \tag{2.6}$$
>
> *In addition to the synchrony measure, we looked at the oscillatory synchrony between the spike trains. The degree of oscillatory synchrony can be determined by considering how much energy is contained in the oscillations of the correlogram in a chosen frequency range. To this end, the correlogram λ_{xy} was subjected to an N-point Discrete Fourier Transform (DFT) (**Oppenheim et al.**, 1997), in order to extract the frequencies of interest. The oscillatory synchrony κ_{oscsync} was then set as the relative power of the signal in a chosen frequency range between $f_{\min}$ and $f_{\max}$:*
>
> $$\kappa_{\text{oscsync}} := \frac{\sum_{m=f_{\min}}^{f_{\max}} DFT^2_{\lambda_{xy}}(m)}{\sum_{n=0}^{N-1} DFT^2_{\lambda_{xy}}(n)}. \tag{2.7}$$
>
> ### *Validation*
>
> *The verification of the results obtained with the PARAFAC model of (5) was achieved by carrying out so-called split-half experiments (**Harshman and Lundy**, 1994). To this end, the set of input data is split into two halves and PARAFAC is carried out for both halves independently. The model is considered to be applicable if the results gained from both halves are similar. In this work, several split-half experiments were carried out, splitting the input data set into odd and even trials.*
>
> ### *PCA*
>
> *We use the trilinear PARAFAC model because we assume the data to be (at least) trilinear. To show that a bilinear model, such as principal component analysis (PCA), is not adequate in this context, we also decomposed the correlation matrices using PCA and compared the results. PCA is a widely used technique. An introduction can be found in **Jolliffe** (2002). In order to make the data array accessible for PCA, it was unfolded into a two-dimensional structure."*

PCA

There are several aspects in validating a model, comprising *computational*, *statistical*, and *explanatory* validation (see (**Bro**, 1998), p. 99). Split-half experiments (see section "Validation" in (**Schmitz et al.**, 2015)) were applied and residuals and the ***core*** ***con***_sistency_ ***dia***_gnostic_ (CORCONDIA) (**Bro and Kiers**, 2003) were evaluated. Explanatory validation, meaning the appropriateness of the model for the data at hand and the research question, will be covered in the discussion section (see section 4.1.1).

Finding the optimal number of components for the model is non-trivial and can be facilitated by experience and prior knowledge about the data ((**Bro**, 1998), p. 110).

While for PCA the loading matrices are always orthogonal to each other, this is not the case for PARAFAC. As a consequence, correlated loadings can occur. If this correlation is "high" (positive or negative correlation > 0.8 (**Field and Graupe**, 1991) or > 0.9 (**Kruskal**, 1989)), degenerate solutions emerge. In general, correlations lower than this seem to be common in real data and do not present the PARAFAC algorithm with problems. Degenerate solutions are thus present, if there are "high correlations (...) in all three modes between the loadings of two or more components" (**Field and Graupe**, 1991). If this is the case, the Nway toolbox (**Andersson and Bro**, 2000) issues a warning, which was used as a stopping criterion in the search for the optimal number of components and thus to avoid degenerate solutions.

As a further criterion in the search for the optimal PARAFAC solution, the *core consistency diagnostic*, or CORCONDIA (**Bro and Kiers**, 2003) was applied. It is defined as

$$\text{core consistency} = 100\left(1 - \frac{\sum_{d=1}^{F}\sum_{e=1}^{F}\sum_{f=1}^{F}\left(g_{def} - t_{def}\right)^2}{F}\right), \tag{2.8}$$

where F the number of components in the PARAFAC model, $\underline{\mathbf{G}}$ the Tucker3[4] core array and $\underline{\mathbf{T}}$ a binary array with ones on the superdiagonal, and zeros otherwise (for more details see (**Bro**, 1998; **Bro and Kiers**, 2003)). The CORCONDIA thus assesses how well the Tucker3/PARAFAC core fits the assumptions of the PARAFAC model. CORCONDIA values above 90 indicate that the data is indeed trilinear, whereas values around 50 and below indicate that the model includes both trilinear and non-trilinear variation and therefore is not appropriate (**Bro and Kiers**, 2003).

CORCONDIA cannot find *the* most appropriate model, but it can tell the researcher that the model does not overfit. However, "by assuming that noise is not trilinear (...), it follows that the valid model with the highest number of components must be the one to choose." ((**Bro**, 1998), p. 120). According to this rule, the model with the highest number of components that reached a CORCONDIA value of larger than 70-75 was selected. With this, it is worthwhile to note that models with only one factor always have a CORCONDIA of 100.

2.7 Computation of Network Connectivity

Information about the functional connectivity within a network can be obtained by calculating statistical dependencies between the signals of all possible pairs of electrodes. To accomplish this, several methods are available, some of which produce directed networks (e.g. transfer entropy (**Schreiber**, 2000; **Vicente et al.**, 2011), general linear models (**Truccolo et al.**, 2005; **Okatan et al.**, 2005)), while others produce undirected networks (e.g. cross correlations, mutual information (**Shannon and Weaver**, 1949); NeuroXidence (**Pipa et al.**, 2008), as used in this study). The observed functional connectivity determines the location of edges in the graph: if the observed statistical dependency between two nodes is significant, an edge is inserted.

---

[4] The Tucker model is a three-way extension of well-known two-way decomposition methods, such as factor analysis and principal component analysis. It is closely related to PARAFAC; for details see (Tucker, 1966) and section 4.1.1.

Here, the recorded spike data were subjected to three analysis approaches in order to extract functional (cross correlation, see section 2.5; NeuroXidence, see section 2.7.1) and effective connectivity (Generalized Linear Models, see section 2.7.2). All these approaches were exerted to all possible electrode pairs, partly to the MUA and partly to the SUA data. The three measures were used to complement each other as they extract different aspects of potential communication between neurons on different time scales.

An overview of the methods and the criteria for the detection of links in the networks are listed in Table 2.1.

Table 2.1.: Overview on the applied connectivity measures. Two measures, namely NeuroXidence (NX) and Generalized Linear Modeling (GLM) were applied in the detailed network analysis. Cross correlation (CC) was used as a basis for the PARAFAC analysis.

Method	Nodes	Criterion for links	Type of connectivity	Model type
CC	MUA	no threshold used; computed CC value was used as basis for PARAFAC algorithm	functional connectivity/ undirected	parametric
NX	MUA	NeuroXidence p-value (excess of JSEs) < 0.05, time windows*: $\tau_r = 15$, $\tau_c = 5$ * see section 2.7.1 for details	functional connectivity/ undirected	non-parametric
GLM	SUA	Likelihood of H_1 model (auto + cross history) larger than of H_0 model (only auto history)	effective connectivity/ directed	parametric

2.7.1 NeuroXidence

Cross correlation, which was used as a basis for the PARAFAC analysis, is a well established method, which, however, fails if correlations do not occur frequently (**Singer**, 2009). Hence, the use of a more sensitive correlation measure was indicated.

To this end, the NeuroXidence method (**Pipa et al.**, 2008) was applied to the MUA data in order to detect synchronous spiking, so-called *joint-spike events* (JSEs).

NeuroXidence is a non-parametric approach, which has the advantage that the non-appropriate assumption of a Poisson distribution is avoided: other methods used for the same purpose often assume that the spike trains, or rather their inter-spike intervals (ISIs), are Poisson distributed. This, however, is most often a false assumption; the non-Poissonity of most ISI distributions is based on the neurons' refractory times.

The NeuroXidence approach was designed to test for the rate against assembly hypothesis, i.e. the idea of coding solely via the frequency of spikes in a population ("rate coding") against the precisely coordinated activity of groups of cells in the order of milliseconds ("assembly coding", see also section 1.2). NeuroXidence corrects for rate changes and thus only shows effects of synchronous events (**Pipa et al.**, 2008). Another advantage is that, when applying the NeuroXidence algorithm, the size of the analysis window is not restricted, because the statistical test incorporates the full autostructure of the data, which, for this reason, does not have to be stationary (**Pipa et al.**, 2008).

The NeuroXidence algorithm utilizes surrogate data, which are constructed by trial shuffling and subsequent shifting of spike trains, in order to separate induced from evoked activity and destroying the millisecond-precise cross-structure between the spike trains of different cells, respectively (**Pipa et al.**, 2008). The surrogate dataset thus has the same auto-structure as the original data, but all cross-structure effects on a millisecond level have been removed.

The algorithm requires two parameters, τ_c, the temporal precision of the temporal cross-structure, typically between 1-10 ms, and a slower timescale τ_r, corresponding to the scale of the rate coding, with $\tau_r = \eta \cdot \tau_c$, $\eta > 1$. The parameters used in the NeuroXidence algorithm were set to $\tau_c = 5$ and $\tau_r = 15$. NeuroXidence was applied to all possible pairs of MUA spike trains of all electrodes. P-values below 0.05 were considered as significant and formed the basis for the construction of the graph theory analysis, since edges were inserted into the graphs between the nodes corresponding to those electrodes.

2.7.2 Generalized linear model

The methods to construct the networks that were described so far (i.e. NeuroXidence and Cross Correlation) are limited in the sense that it is not possible to extract a directed information flow from correlations or synchronous activity. In order to be able to detect directed effects[5], also termed *effective* connectivity, a complementary approach was required. To implement this idea, an approach in the context of Generalized Linear Modelling (GLM) (**Nelder and Wedderburn**, 1972; **McCullagh and Nelder**, 1989), more precisely the point process-GLM framework (see (**Truccolo et al.**, 2005)) was selected.

Generalized Linear Models are generalizations of linear regression. Instead of a normal distribution, distributions of the exponential family can be selected. Here, in order to model the spiking probabilities at time t, a Bernoulli GLM was applied, since the selection of a bin size of 1 ms resulted in either 1 or 0 spikes per bin.

The approach followed the idea of Granger Causality (**Granger**, 1969): the spiking activity of a unit A at time t was predicted in the null model H_0, using the rate and auto-history of spiking of that same unit. For the alternative model H_1, again the spiking of unit A was predicted, but now the spiking history of another unit B was added to the model. If the H_1 model was better able to describe the observed spiking of unit A than the H_0 model, a causal influence of unit B on unit A was deduced.

The following description of the GLM approach for the characterization of effective connectivity is based on the description by **Gerhard et al.** (2011). There, however, instead of the activity of a single unit, the ensemble activity was considered in the cross-history term.

Spike trains can be represented as a point process, i.e. a series of spike times. Such a point process is completely characterized by its conditional intensity function $\lambda(t|H_t) = \lim_{\Delta \to 0} \frac{P[N(t+\Delta)-N(t)=1|H_t]}{\Delta}$, with $N(t)$ the number of events in the interval [0,t], and H_t the history (**Daley and Vere-Jones**, 2003).

---

[5] Note that, by considering directed connectivity, the number of possible connections, and thus the adjacency matrices become larger, since now neurons A and B can be connected by two edges (A $\rightarrow B, B \rightarrow A$).

With this, for a Bernoulli GLM, the probability of spiking in a small time interval of bin size Δ is

$$\lambda(t|H_t)\Delta = \frac{1}{1+exp(-h)}, \tag{2.9}$$

with $h = \beta_A + g_{hist_A}(t) + g_{hist_B}(t)$. Here, β_A depicts the baseline spike rate of unit A, g_{hist_A} the auto-history term of spiking of unit A, and g_{hist_B} the cross-history term of spiking of unit B.

Hence, rewriting the equation

$$h = \log \frac{\lambda(t|H_t)\Delta}{1-\lambda(t|H_t)\Delta} = \beta_A + g_{hist_A}(t) + g_{hist_B}(t) \tag{2.10}$$

The model filters were based on cubic B-splines. A spline of order n is a piecewise polynomial function of degree $n-1$, i.e. for cubic splines $n = 4$. Every spline function can be built by a linear combination of B-splines (which, for this reason, is short for *basis splines*).

With this, the following model represents the H_0 hypothesis for neuron A at time t, with a constant term for the baseline spike rate of A and a term for the auto-history:

$$H_0 := \log \frac{\lambda_A(t|H_t)\Delta}{1-\lambda_A(t|H_t)\Delta} = \sum_{i=1}^{m_{rate}} \alpha_i \cdot B_i^{rate}(t) + \sum_{j=1}^{m_A} \sum_{t_n^A<t} \beta_j \cdot B_j^{hist_A}(t-t_n^A), \tag{2.11}$$

where $\{t_n^A\}$ are the spike times of unit A, and B_i^{rate} and $B_j^{hist_A}$ are the basis functions, with m_{rate} and m_A the number of B-splines applied for rate and auto-history of A, respectively.

For each experimental condition (deactivation condition, stimulus phase, stimulus direction) the MATLAB function `glmfit` was used to fit a model for each neuronal unit, including the rate and auto-history of the unit.

The model parameters α_i and β_j were subjected to a maximum likelihood (ML) estimation and the resulting ML values α_i^{ML} and β_j^{ML} were then fixed for the construction of the H_1 model.

The model for the H_1 hypothesis was built by adding the contribution of the spiking history of a second unit B to the current model:

$$H_1 := \log \frac{\lambda_{AB}(t|H_t)\Delta}{1-\lambda_{AB}(t|H_t)\Delta} = \sum_{i=1}^{m_{rate}} \alpha_i^{ML} \cdot B_i^{rate}(t) + \sum_{j=1}^{m_A} \sum_{t_n^A<t} \beta_j^{ML} \cdot B_j^{hist_A}(t-t_n^A) + \sum_{k=1}^{m_B} \sum_{t_n^B<t} \gamma_k \cdot B_k^{hist_B}(t-t_n^B), \tag{2.12}$$

with $\{t_n^A\}$ the spike times of unit A, and $\{t_n^B\}$ the spike times of unit B. The parameter γ_k again was estimated using maximum likelihood estimation.

The goodness of fit was then measured using the log-likelihood $log(L(H))$ of the models H_0 and H_1, i.e. if the log-likelihood of the H_1 model was larger than the log-likelihood of the H_0 model, a directed edge from unit B to unit A was added into the respective network. This step was repeated for all remaining units, so that an H_1 model was constructed for each pairwise relationship of unit A to any available other unit. The above steps were then performed for all available units to create a directed network.

Figure 2.8 shows examples of the model components.

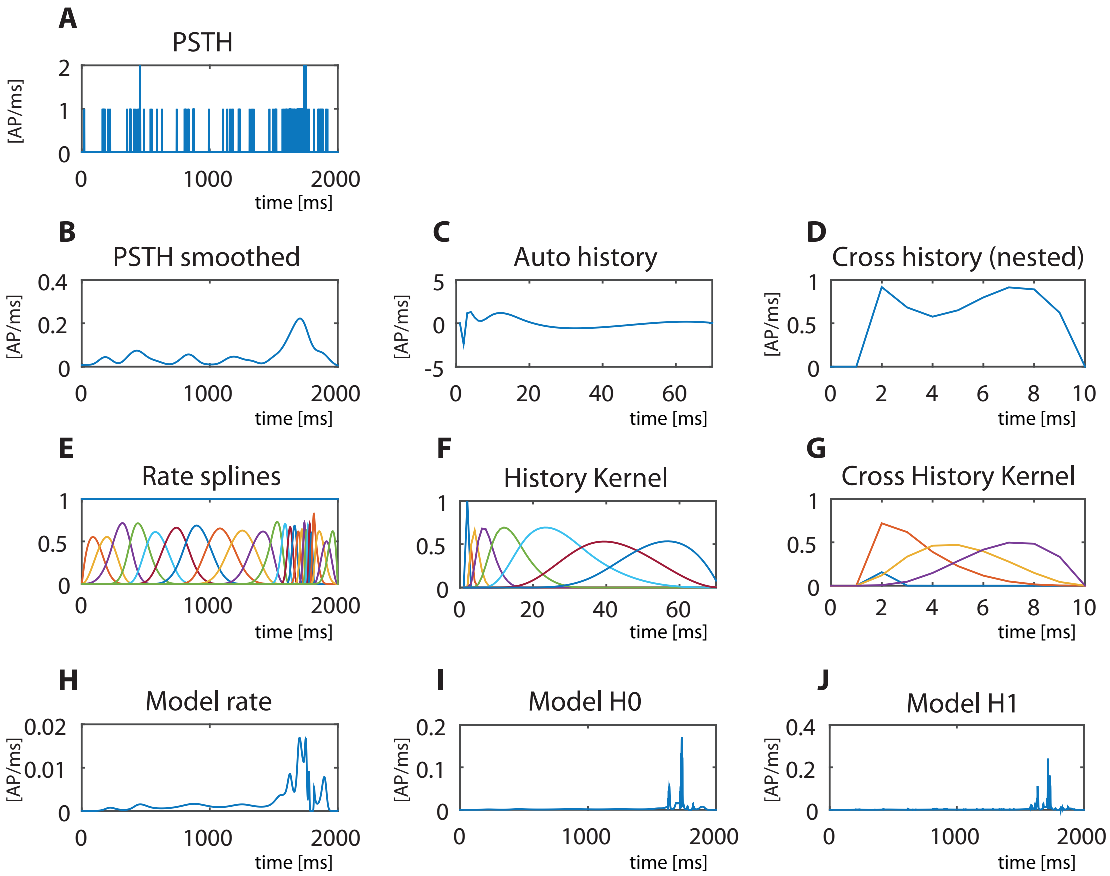

Figure 2.8.: Example for GLM model & parameters: (A) Peri-stimulus time histogram (PSTH) of the recorded spikes in the analysis window, binned (1 ms); (B) Smoothed PSTH, i.e. PSTH from (A) convolved with a Gaussian kernel; (C) Auto history; (D) Cross history; (E) Splines used to model the rate; (F) Splines used to model the auto-history; (G) Splines used to model the cross history; (H) GLM model for rate only; (I) GLM model including rate and auto-history; (J) GLM model including rate, auto-history, and cross-history

2.8 Graph-Theoretical Analysis of Networks

In order to properly define the network properties, some general graph theoretical definitions are required: a *graph* $G = (V, E)$ is an ordered pair of sets, where V is a set of *vertices*, or *nodes*, and $E \subseteq K := \{\{i, j\} \mid i \neq j,\ i, j \in V\}$ is a set of *edges*, i.e. links between the nodes. The nodes can be labeled with an index $i = 1, \ldots, n$. By x_{ij}, the edge between nodes i and j is denoted. A graph can be described by an $n \times n$ - *adjacency matrix* A with entries $a_{ij} = 1$ if egde x_{ij} is present in the graph and $a_{ij} = 0$ otherwise. A graph is called *directed* if there is a distinction between x_{ij} and x_{ji}, else it is called *undirected*. In the latter case the associated adjacency matrix is symmetric. The *size* $|E|$ of a graph is the number of possible edges. For undirected, binary graphs it can be derived from $|E| = \frac{|V|(|V|-1)}{2}$. For a directed graph $|E| = |V|(|V|-1)$.

If the analyzed networks are large enough and the number of graphs is sufficient, it may be advisable to first test whether the observed graphs are random graphs.

Two kinds of random graphs were used to construct the H_0 hypothesis: in a *Bernoulli graph* the edges X_{ij} are inserted independent of each other with probability p_{ij}. The *Erdös-Rényi graph* represents a special case of a Bernoulli graph; in this case all edges are inserted with the same probability p.

In order to assess randomness, two characteristic features of Erdös-Rényi graphs can be used: the distribution of the number of edges and the *degree distribution*.

In Erdös-Rényi graphs the number of edges is binomially distributed. Therefore, the empirical distribution of the number of edges should be tested against the H_0 model distribution, which in this case is a binomial with parameters $\binom{n}{2}$ and $\hat{p}$. The parameter $\hat{p}$ is the maximum likelihood estimator for the edge probability and can be estimated using the relative frequency of edges in the N empirical graphs:

$$\hat{p} = \frac{\sum_{\{i,j\}\in E} x_{ij}}{N}. \tag{2.13}$$

Note that, as opposed to measures like the degree distribution, it is not possible to obtain the distribution of the number of edges from an individual graph.

The Kolmogorov Smirnov test (KS test) can be used to test the hypothesis. Other statistical tests are applicable as well, but using a non-parametric test, and comparing the entire distribution combines a high sensitivity with a high statistical robustness. Another advantage is that the KS test can also be applied if sample sizes are small (as opposed to the χ^2 test for example, (**Massey**, 1951)).

The question whether a graph is an Erdös-Rényi graph can also be assessed by analysis of the degree distribution. This approach is, in contrast to the analysis of the distribution of the number of edges, also applicable to an individual network. The degree distribution in Erdös-Rényi graphs for $n \to \infty$ follows a Poisson distribution with parameter $\lambda = p(n-1)$, so the respective Poisson distribution constitutes the null hypothesis for the test. For a poisson distributed random variable X, $E(X) = Var(X)$ holds. Thus, the empirical degree distributions can be checked for poissonity by comparing expected value and variance.

2.10 Test on Homogeneity of Edge Probabilities

The tests described in 2.9 were not able to reveal a clear picture about the randomness of our graphs, due to small sample sizes. Therefore, different approaches that can also be applied in the case of small sample sizes were employed to look for specific structures within the graphs. The first question is, whether the graph might be a Bernoulli graph with two disjunct sets of edges holding two different edge probabilities. The respective disjoint subsets of the set of edges that are assumed to have different edge probabilities can be chosen in many different ways. One might want to assess differences in the edge probabilities based on topological features (e.g. distance), cell types, tuning preferences or other properties of the nodes that are relevant in a given context.

To design a hypothesis test that is able to answer the question posed in the preceding paragraph, let us first consider a single graph.

Let N_1 and N_2 be the number of possible edges in the two subsets of the set of edges E: E_1, representing a specific type of links, and E_2, representing all other links. It shall be checked whether one of these types of links is stronger represented than the other, relative to the maximum possible number of links in the respective sets. The null hypothesis again is that the graph is an Erdös-Rényi graph with edge probability p. For the test, p is estimated by equation (2.13).

A suitable test statistic for the comparison of edge probabilities for two distinct subsets of edges is

$$T := T_1 - T_2 \tag{2.14}$$

with

$$T_1 = \frac{1}{N_1} \sum_{\{i,j\}\in E_1} x_{ij} \qquad \text{and} \qquad T_2 = \frac{1}{N_2} \sum_{\{i,j\}\in E_2} x_{ij}. \tag{2.15}$$

Under the null hypothesis $N_1 \cdot T_1$ is binomially distributed with parameters N_1 and p. Likewise, $N_2 \cdot T_2$ is binomially distributed with parameters N_2 and p. To obtain a critical value c, an upper bound for the alpha error (false positive) is required. The null hypothesis is rejected if $|T| > c$. The upper bound for the alpha error can be estimated according to $\sup_p P_p(|T| \geq c) \leq \alpha$. One possibility to obtain an alpha error is to use *Chebyshev's inequality* (**Georgii**, 2007):

$$P(|X - E(X)| \geq c) \leq \frac{Var(X)}{c^2} \tag{2.16}$$

gives only a very coarse estimation. The critical value for one graph found with *Chebyshev's inequality* is

$$c_1 = \sqrt{\left(\frac{1}{N_1} + \frac{1}{N_2}\right)\frac{1}{\alpha}}. \tag{2.17}$$

If a number of l graphs are considered together this term expands to

$$c_l = \sqrt{\left(\frac{1}{l \cdot N_1} + \frac{1}{l \cdot N_2}\right)\frac{1}{\alpha}}. \tag{2.18}$$

An alternative – and more sensitive – estimation can be obtained using *Hoeffding's inequality* (**Hoeffding**, 1963):

$$P\left(\left|\frac{1}{n}X - p\right| \geq \varepsilon\right) \leq 2 \cdot e^{-2n\varepsilon^2}, \tag{2.19}$$

with $X := \sum_{\{i,j\}\in E} X_{ij}$ binomially distributed, $\varepsilon > 0$, $n \geq 1$ and $0 < p < 1$. This inequality yields more precise estimates, but the calculation of the critical value is not possible analytically, and, thus, has to be performed numerically.

If a set of l graphs is considered,

$$P(|T_1 - T_2| \geq c) \leq P(|T_1 - E(T)| \geq \frac{c}{2}) + P(|T_2 - E(T)| \geq \frac{c}{2}) \overset{Hoeffding}{\leq} 2e^{-2lN_1(\frac{c}{2})^2} + 2e^{-2lN_2(\frac{c}{2})^2} = \alpha \tag{2.20}$$

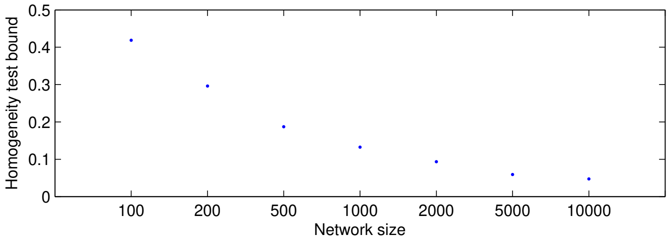

Figure 2.9.: Scaling of the bound with network size. The values were calculated for the two edge subsets each building up 50% of the graph, and equal weighting.

holds. Computation of the critical value c is not straightforward, but can be obtained by finding the roots of

$$f(c) := e^{-2lN_1(\frac{c}{2})^2} + e^{-2lN_2(\frac{c}{2})^2} - \frac{\alpha}{2}. \tag{2.21}$$

The critical bound can be further improved by using a convex combination other than dividing the influence of the sets N_1 and N_2 in half:

$$f(c) := e^{-2lN_1(\lambda c)^2} + e^{-2lN_2((1-\lambda)c)^2} - \frac{\alpha}{2}, \qquad \lambda \in [0,1]. \tag{2.22}$$

The critical value c will be smallest for the infimum of (2.22) over $\lambda \in [0,1]$. Finding the derivative of the continuous function (2.22) and rewriting shows that this value can be obtained by solving

$$e^{2lN_2(1-\lambda)^2c^2-2lN_1\lambda^2c^2} = \frac{N_2}{N_1}\frac{(1-\lambda)}{\lambda}, \tag{2.23}$$

which has to be performed numerically.

Figure 2.9 shows how the bound scales with network size.

If more than two sets of edges are compared to each other, a correction for the alpha error has to be applied because of a cumulation of the alpha error due to multiple comparisons. One way to accomplish this is the use of the Bonferroni correction (**Miller**, 1991), i.e. replacing α by $\frac{\alpha}{\text{number of tests}}$.

2.11 Test on the Similarity of Graphs Using the Hamming Distance

After assessing the similarity of subsets of edges, the topologies of different realizations of a graph as a whole should be compared. Thus, in contrast to the previous method that can also be used for individual graphs, here, two or more graphs are required. The only prerequisite for this analysis is that the graphs are made up of exactly the same nodes. The different realizations of a graph can either originate from repeated trials with the same experimental conditions, or be derived from different conditions, depending on the research question.

The Hamming distance between two graphs X and Y is calculated as follows:

$$d_h(X,Y) := \sum_{\{i,j\}\in K} |X_{ij} - Y_{ij}| \quad \in \{1, ..., \binom{n}{2}\}. \tag{2.24}$$

Edge probabilities can again be estimated using equation (2.13).

In the following, the statistical test with the null hypothesis that the graphs are Erdös-Rényi graphs with a certain probability p is described. However, the test can be extended to the application of Bernoulli graphs with different probabilities for subsets of the set of edges.

The Hamming distance between two Erdös-Rényi graphs is binomially distributed with parameters $\binom{n}{2}$ and $2p(1-p)$. For a set of more than two graphs the following assertions hold:
Let $G := \left\{X^1, X^2, \dots, X^l \mid X^i \in \{0,1\}^{|K|}\right\}$ be a set of l graphs with the same nodes. Let the edges be independently Bernoulli-distributed with the same probability p for each edge, and the edges of the complete graph be numbered, $k = 1, \dots, \binom{n}{2}$. Let $M = (m_{ik}) \in \{0,1\}^{l \times \binom{n}{2}}$ be a matrix that carries information about the actual realizations of edges in the graphs X^i. Let $m_{ik} = 1$ if and only if edge k appeared in graph i and $m_{ik} = 0$ otherwise. Let S_k be the k-th column of M. Let $Z_k = \sum_{i=1}^{l} m_{ik} \in \{0, \dots, l\}$ be the random variable that describes the frequency of occurrence of ones in S_k.

The concept of the Hamming distance is now generalized to the distance $d_h(S_k)$ inside a column of the matrix M. The Hamming Distance in S_k can thus be calculated as follows:

$$d_h(S_k) := \sum_{\substack{i,j \in \{1,\dots l\} \\ i<j}} d_h(X^i_{vw}, X^j_{vw}) \tag{2.25}$$

$$= Z_k(l - Z_k) \tag{2.26}$$

$$= \binom{l}{2} - \left[\binom{Z_k}{2} + \binom{l - Z_k}{2}\right]. \tag{2.27}$$

The expected value of the Hamming Distance in S_k is

$$E(d_h(S_k)) = E\left(\sum_{\substack{i,j \in \{1,\dots,l\} \\ i<j}} d_h(X^i_{vw}, X^j_{vw})\right)$$

$$= \sum_{\substack{i,j \in \{1,\dots,l\} \\ i<j}} E(d_h(X^i_{vw}, X^j_{vw})) \tag{2.28}$$

The Hamming distance for one edge between two graphs equals 1 if and only if an edge is present in only one of the graphs. The probability for this to happen is $p(1-p)$, or $(1-p)p$, respectively. Thus, (2.28) can be rewritten as

$$E(d_h(S_k)) = \sum_{\substack{i,j \in \{1,\dots,l\} \\ i<j}} 2p(1-p)$$

$$= \binom{l}{2} 2p(1-p). \tag{2.29}$$

The expected value for the sum of the Hamming distances between all pairs of graphs in G can be calculated as

$$E(d_h(G)) = \sum_{k \in \{1,\dots,\binom{n}{2}\}} E(d_h(S_k)). \tag{2.30}$$

$$= \binom{n}{2} E(d_h(S_k)) \tag{2.31}$$

$$\overset{(2.29)}{=} \binom{n}{2}\binom{l}{2} 2p(1-p). \tag{2.32}$$

Let h be a realization of $d_h(S_k)$. As the probability that a given edge occurs exactly z times in the l graphs is binomially distributed, for the single probabilities of $d_h(S_k)$

$$P\left(d_h(S_k) = h\right) = \sum_{\substack{z \in \{0,\dots,l\} \\ z(l-z)=h}} P\left(Z_k = z\right) = \sum_{\substack{z \in \{0,\dots,l\} \\ z(l-z)=h}} \binom{l}{z} p^z (1-p)^{l-z} \tag{2.33}$$

holds, with $h \in \{0,\dots,\binom{l}{2}\}$.

Also, the variance of $d_h(S_k)$ can be specified:

$$Var(d_h(S_k)) = \sum_{h=0}^{\binom{l}{2}} (h - E(d_h(S_k)))^2 \, P\left(d_h(S_k) = h\right). \tag{2.34}$$

To test whether the Hamming distance between the analyzed graphs in set G is significantly smaller than in a group of Bernoulli graphs with the same probabilities for the edges, the test statistic T_H is introduced. T_H is required to be approximately normally distributed. This can be achieved by demeaning and normalizing the variance using

$$\mu := \frac{N_1 E(d_h(S_k))_1 + N_2 E(d_h(S_k))_2}{\binom{l}{2}} \tag{2.35}$$

and

$$\sigma := \sqrt{\frac{N_1 Var(d_h(S_k))_1 + N_2 Var(d_h(S_k))_2}{\binom{l}{2}^2}}. \tag{2.36}$$

Here, $d_h(S_k))_1$ and $d_h(S_k))_2$ denote the Hamming distances for a column of M in the subsets of edges E_1 and E_2, respectively. All $d_h(S_k)$ are independent and identically distributed. In addition, variance and expected value can be derived, so the normal approximation is justified, and

$$T_H := \frac{H_{emp} - \mu}{\sigma} \tag{2.37}$$

with H_{emp} the mean empirical Hamming distance between graphs in the examined set, is thus normally distributed with zero mean and variance equal to 1.

For the normal approximation, the number of edges per subset should be large enough ($n \geq 30$, (**Sullivan**, 2008)) to achieve a reasonably good approximation. However, if this constraint is not met, the test can, for example, also be carried out using bootstrap procedures (**Efron and Tibshirani**, 1993).

2.12 Network Measures

In addition to the spike rate and tunings as well as the methods introduced in section 2.8, the following measures were computed and compared for the different experimental conditions (see Table 2.2).

Table 2.2.: Graph theory measures.

Parameter	Definition
degree (per node)	$k = \sum_j a_{ij}$ where $a_{ij} \in \{0, 1\}$
degree distribution	$P(k) = \frac{N(k)}{\sum N(k)}$, where $N(k)$ the number of nodes with degree k
characteristic path length	$L = \frac{\sum_i \sum_j L_{i,j}}{N(N-1)}$, where $L_{i,j}$ the shortest path between nodes i and j
clustering coefficient (per node)	$C = \frac{2e_i}{k_i(k_i-1)}$, where e_i the number of edges connecting the nearest neighbours of node i

For the calculation of graph theory measures the Brain Connectivity Toolbox (**Rubinov and Sporns**, 2010) was utilized.

2.13 Statistics and Further Remarks

Depending on the structure of the dataset in question, suitable statistical tests were applied to evaluate statistical significance of the results. The respective tests are stated with the corresponding sets of results in chapter 3.

For some analyses, instead of calculating increase and decrease in percentage, a so-called Modulation Index (MI) was calculated, which is defined as follows (example given for spike rate):

$$MI := \frac{R_c - R_b}{R_c + R_b}, \qquad MI \in [-1, ..., 1] \tag{2.38}$$

with R_c the rate during deactivation and R_b the baseline rate during the "warm" condition.

Analyses were performed using custom scripts written in MATLAB (The Mathworks, Inc., Natick, MA).

3 Results

Data from three experiments, 101007, 121007, and 112807, were subjected to the analyses described in the methods chapter. For the multi-unit analysis, sessions from all three experiments were included. In this context, a session is defined by the position of the electrode array in the tissue: every time the position was altered, a new session started. Of these sessions, some were not complete in the sense that they did not cover all possible deactivation conditions (ipsi-, contra-, and bilateral). For the single-unit analysis, spike sorting methods were applied to 16 sessions in total, 8 from experiment 101007 and 8 from experiment 121007 (see table 3.1). All these "SUA" sessions comprised a full cycle of all possible deactivation conditions. An overview of the recording sessions can be found in appendix A.

Table 3.1.: An overview over the numbers of sessions and graphs used for analysis.

Cat /Experiment	No. sessions (total)	No. of sessions MUA/NX	No. of graphs MUA/NX	No. of sessions SUA/GLM	No. of graphs SUA/GLM
101007	13	12	2048	8	1792
121007	14	14	2112	8	2240
112807	14	14	896	0	0
total	41	40	5056	16	4032

The neglect during unilateral deactivation of the pMS cortex, as well as the restitution in behaviour during bilateral deactivation, and for the rewarmed tissue, were tested in an arena experiment similar to the one described by **Payne et al.** (1996) in the awake animal prior to the recordings. The results showed that a decrease in temperature below 10 °C led to the expected behavioural deficit, confirming the correct placement of the cooling probes for all hemispheres except one: in 112807, the cooling probe on the right hemisphere was not functional. Hence, for 112807, only the left pMS cortex could be inactivated, leading to a lower number of sessions in this experiment, since neither right unilateral, nor bilateral pMS inactivation were possible.

3.1 Parallel Factor Analysis (PARAFAC)

The multi-unit spike data was separated into subsets according to sessions and deactivation conditions and a cross correlation value was calculated for each possible pair of neurons. The resulting arrays of cross correlation values were then subjected to the PARAFAC algorithm. In this section, a selection of results of this analysis is presented.

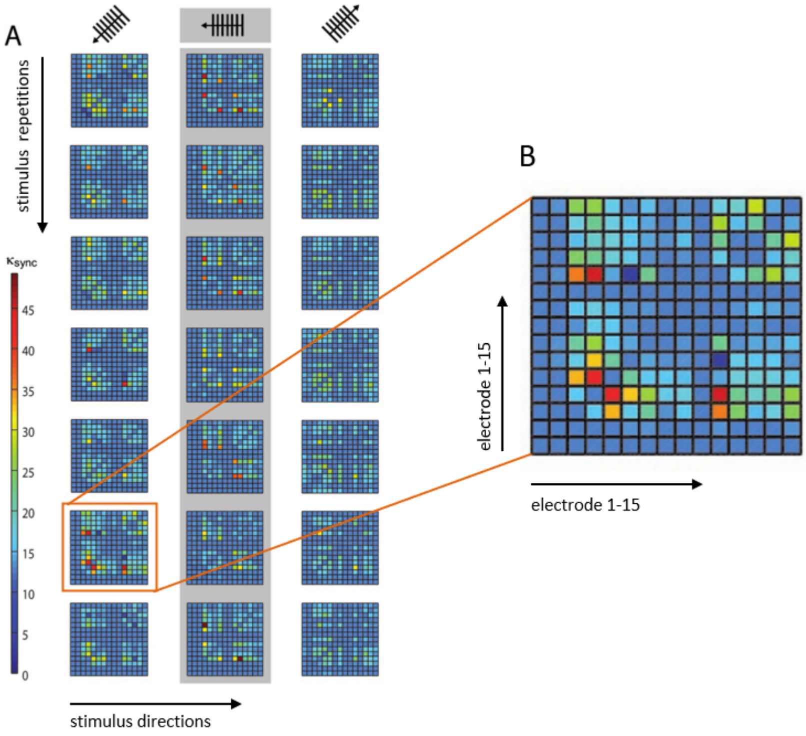

Figure 3.1.: Visualization of κ_{sync}. (A) κ_{sync} was calculated for all electrode pair, for each of the eight different stimulus direction, and for each repetition of each of these stimulus conditions separately. (B) Each of the small plots shows the synchrony measure κ_{sync} (see equation 2.6, p. 40) colour-coded and plotted for each electrode pair.

Figure 3.1 acts as an auxiliary figure to explain the visualization of the level of synchrony calculated as κ_{sync} in (**Schmitz et al.**, 2015) that was fed into the PARAFAC algorithm (see Fig. 3.2).

The following text in italics and the figures referred to in this section are taken from **Schmitz et al.** (2015).

> *"To demonstrate the application of PARAFAC to multiunit spiking data, we applied the algorithm to an example dataset obtained in the experiment described above. PARAFAC was carried out in MATLAB (The Mathworks, Inc., Natick, MA) using the N-way toolbox developed by Andersson and Bro ((**Andersson and Bro**, 2000), available at http://www.models.life.ku.dk/nwaytoolbox/). Figure 3.2A illustrates the synchrony measure, κ_{sync}, for one experimental session (three stimulus directions are shown).*
>
> *The first 21 repetitions of each stimulus were thus recorded without deactivation, repetitions 22-42 correspond to the phases of thermal deactivation of pMS and repetitions 43-63 show the results for the rewarm condition. In each of the subplots of Fig. 3.2A, the 15 recording channels are shown on x-and y-axis (one channel in the 4x4 grid was not working and was not included in the analysis). Each square in the subplots represents the strength of correlation (κ_{sync}) for the respective pair of recording channels. The figure provides an illustrative representation of the synchrony effects in the spiking data. It clearly shows that the signals of certain groups of neurons are correlated only for the presentation of certain stimuli. Furthermore, it can be observed that this structure is maintained over time. After examination of the correlation plots, we chose a 3D PARAFAC with the dimensions electrode pair, stimulus*

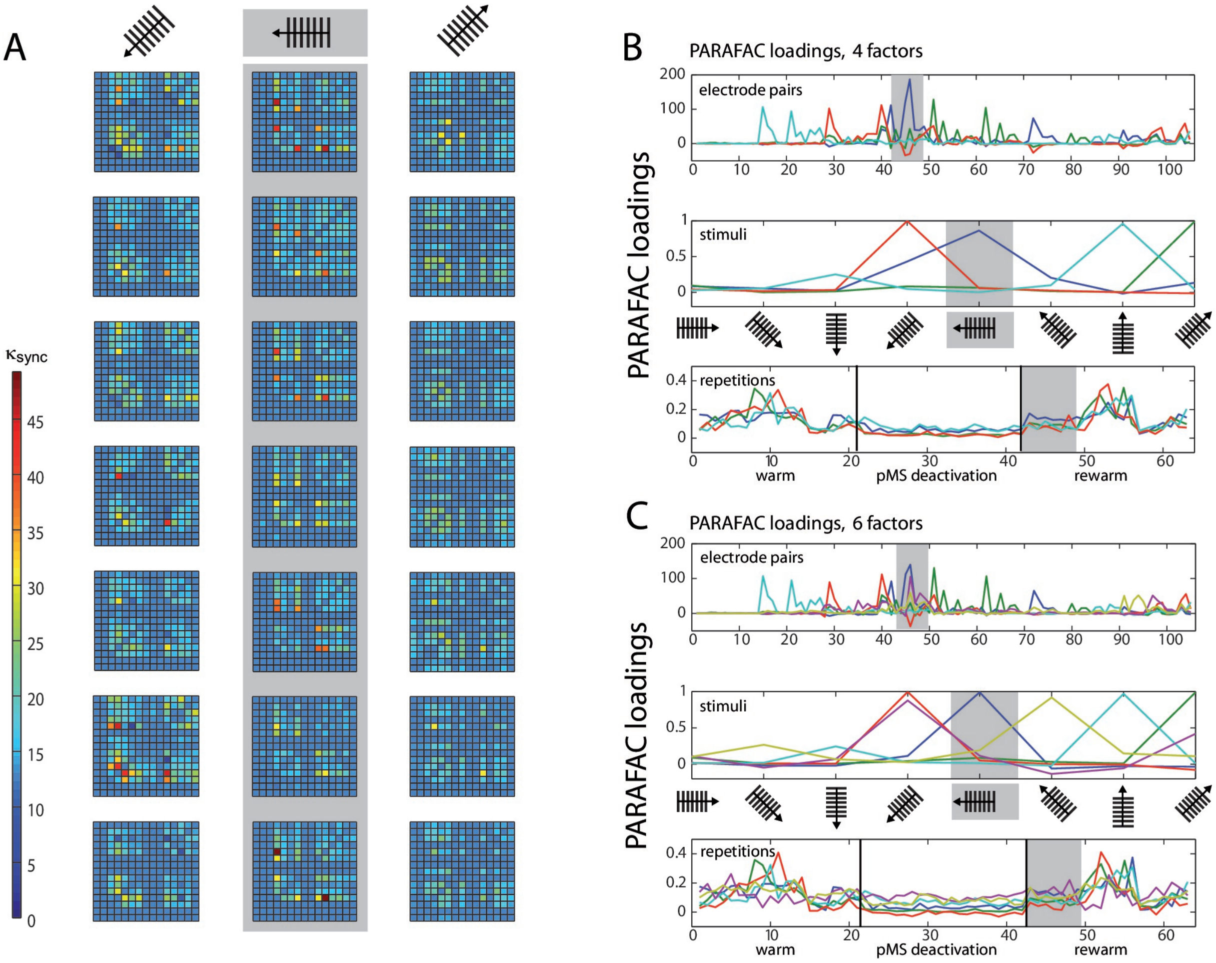

Figure 3.2.: PARAFAC visualization. (A) depicts the κ_{sync} measure for the three stimuli with the highest correlated activity. For each stimulus, seven repetitions are shown. κ_{sync}, expressing correlation strength, is colour-coded, see colour bar. The correlations correspond to repetitions 43-49 (rewarm phase) in (B) and (C) (see grey shaded areas). The values $\kappa_{sync}(electrodepair, stimulus, repetition)$, are subject to the PARAFAC analysis. (B) shows the results of a 3D PARAFAC analysis for the choice of the dimensions electrode pairs, stimulus directions and repetitions of the stimulus in a session with bilateral pMS deactivation. The algorithm was carried out with four factors. (C) shows the PARAFAC result for a calculation with six factors for the same dataset as in (B). Note that for each factor, a new aspect of the correlation structure becomes visible, as contributions of new electrode pairs and stimuli emerge. The plots are to be interpreted in the following way: Values from the original array containing the values of κ_{sync} for the three conditions electrode pair, stimulus and repetition are factorized into loadings for a number of factors that is chosen beforehand. To obtain the original values (but for a small error), the loadings for one factor are multiplied and then added over all factors. Loadings belonging to the same factor are marked in the same colour. The dark blue factor in the third panel of (B) has the highest loading values for this phase. The electrode pairs and stimuli for which this finding holds are the ones whose dark blue factor also takes high loading values. This points to the fact that stimulus 5 (vertical grating, movement to the left) leads to the highest correlation values during this phase of the experiment, mostly for electrode pairs 45 and 72 (upper panel). The pairs emphasized by the PARAFAC loadings are the same ones that repeatedly show high correlation values in (A), but their contribution is much more easily accessible using the PARAFAC visualisation. To help with reading the plot, let us consider another example, concentrating on the light blue curve: As written in the top left corner of the plot, this panel depicts the influence of the electrode pair. Hence, correlation is high for e.g. electrode pair no. 15 (but also no. 21, for example). In order to find out if this is true for a specific stimulus, one should check the middle panel: here, it is shown that the effect is most prominent for the grating moving upwards. To get an idea of the time course of this effect, examine the lower panel of stimulus repetitions. This indicates that the high correlations were mainly observed in the middle of the warm and rewarm conditions (here, the loading values are high), e. g. especially for the tenth repetition. This procedure can be applied for the other factors as well, there is no order of importance.

and repetition. The input data was centered in all dimensions. No scaling of the data was carried out. The measures based on normalized cross correlation data for all possible pairs of electrodes in the array were fed into the PARAFAC algorithm to obtain the multidimensional analysis results.

3.1.1 Synchrony

The PARAFAC algorithm revealed the influence of electrode pairs and stimuli on the correlations and showed its behaviour over time, since the stimulus repetitions were considered in an extra dimension. Fig. 3.2 shows the result of the PARAFAC analysis. The optimal number of factors was chosen as the highest number of factors with no correlated ones and resulted in numbers of 4 to 6.

The loadings can be interpreted as the strength of influence on the correlation for the respective electrode pair, stimulus condition and time point: The higher the loading value, the stronger the influence of the respective feature on the correlation.

The correlation values in Fig. 3.2A correspond to repetitions 43-49 in Fig. 3.2B and C. A comparison of these corresponding parts shows that the same effects can be observed in both ways of presentation. This becomes especially clear when the focus is put on the dark blue PARAFAC component in Fig. 3.2B for repetitions 43-49. The component clearly reflects the strong peaks in Fig. 3.2A for the respective stimulus.

Separate analyses were carried out taking into account the distance between the electrodes. For this purpose, the electrodes in a homogenously spaced 4×4 *grid with grid size* d_{grid} *were divided into two sets, the set of neighbouring pairs and the set of remote pairs. With* (x_i, y_i) *the position of electrode i, two electrodes are called neighbouring nodes if*

$$\sqrt{(x_1 - x_2)^2 + (y_1 - y_2)^2} \leq \sqrt{2} d_{grid} \tag{3.1}$$

holds. Any two electrodes fulfilling this constraint are referred to as neighbouring pairs, all other electrode pairs are termed remote pairs. In the case of a 4 × 4 grid of electrodes, this results in 42 neighbouring pairs and 78 remote pairs.

We found a strong influence of pMS deactivation on the strength of correlations for both ipsi- and bilateral deactivation (see Fig. 3.3). For these conditions, loading values for the deactivation phase were considerably lower than for the warm phases. Also, the variation in the warm phases was higher, indicating a more dynamic correlation pattern. This effect could already be observed in the spontaneous activity before stimulus onset (results not shown).

During contralateral deactivation of pMS (see Fig. 3.3), the effect was much weaker, showing that the activity in area 18 was almost not affected by the deactivation of contralateral pMS.

3.1.2 Oscillatory synchrony

In order to analyze the measured data with respect to its oscillatory synchrony properties, the oscillatory synchrony measure $\kappa_{oscsync}$ *was used as input data for the PARAFAC algorithm*

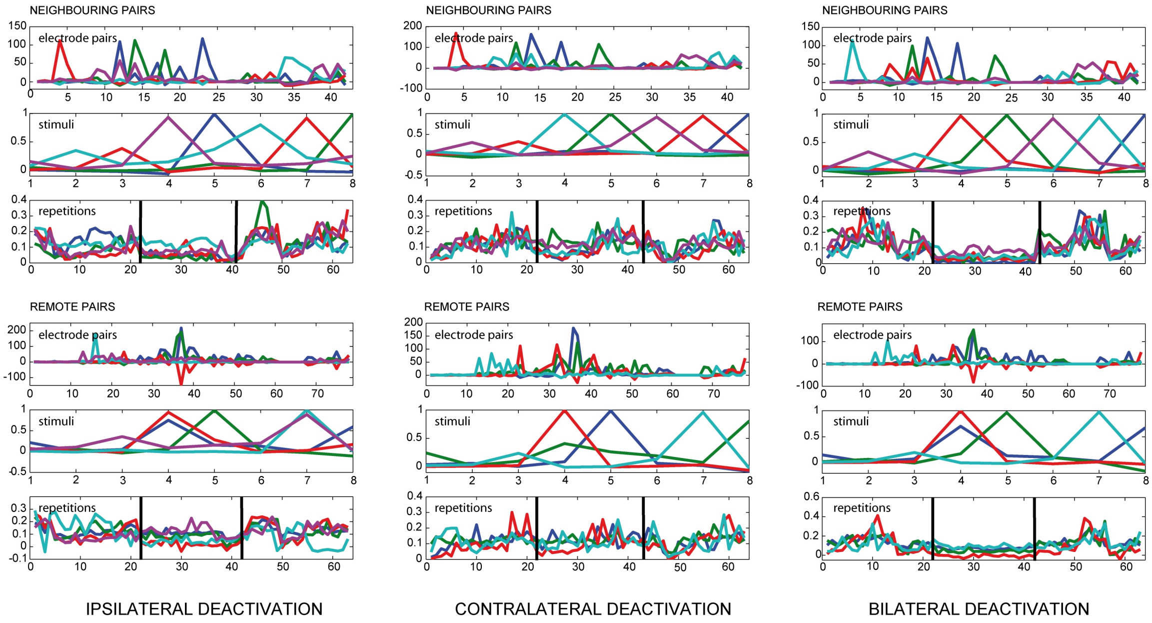

Figure 3.3.: Results of PARAFAC for local and remote connections. The figure shows the results of a PARAFAC analysis for all deactivation conditions. The electrode pairs were split into neighbouring and remote pairs according to the neighbourhood condition defined in equation (3.1). If one looks at the loading values for the repetitions, illustrating the time course of the observed correlations, the deactivation effect is visible for ipsilateral deactivation and even more pronounced during bilateral deactivation, depicted by a decrease in the PARAFAC loading value. During ipsi-and bilateral deactivation the variance for the PARAFAC loading values also decreases, indicating a network behaviour which is less dynamic. During contralateral deactivation the course of the correlations does not seem to change substantially.

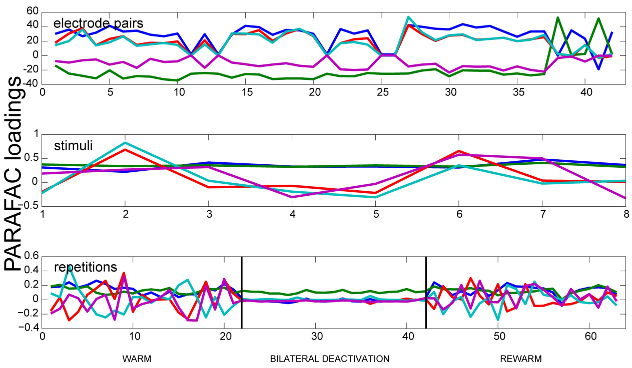

Figure 3.4.: Results of PARAFAC for the Oscillatory Synchrony measure. Results of a PARAFAC analysis using the oscillatory synchrony measure is shown for a phase of spontaneous activity. Only neighbouring electrode pairs are shown. The bilateral deactivation of the pMS cortex has a strong effect on the correlations, which can be clearly observed when looking at the deactivation phase in the lower panel.

(Fig. 3.4). For this measure the deactivation effects were most prominent during spontaneous activity. For frequencies between 1-10 Hz the deactivation effect could only be observed for bilateral deactivation. Here, it leads to a severe decrease of correlations. The correlations return to initial values in the rewarm phase. For the low gamma frequency range (30-50 Hz), the deactivation effect can also be seen during ipsilateral deactivation of pMS, and it is most pronounced during bilateral deactivation. In both frequency ranges, PARAFAC very soon developed correlated factors. For the oscillatory synchrony, the highest value for the variance explained by the model reached levels of 50 % (for the results shown in Fig. 3.4). This value increases when the number of factors F is increased. However, as already mentioned above, the factors become correlated under these conditions.

3.1.3 Validation

As a control for the appropriateness of PARAFAC for our data, we performed split-half experiments in which the data set was divided into odd and even trials. Fig. 3.5 shows an example of the results for the data shown in Fig. 3.2 . The results show that the method works equally well on both newly created data sets: The loadings are similar and also the variation explained by the model was similar in both cases (71.26 and 70.17 % respectively). Consequently, the PARAFAC model of (5) was considered to be applicable.

3.1.4 PCA

The results of the PCA showed two distinct features: 1) The phases of pMS deactivation are not very prominent (see Fig. 3.6) A high number of principal components is needed until a reasonable proportion of the total variance is explained. We showed that, for our example data set, with four and six PARAFAC components, the model is able to explain 70.07%, respectively 76.26% of the variance in the data. In comparison, 17 PCA components were needed to reach 70% of cumulated variance."

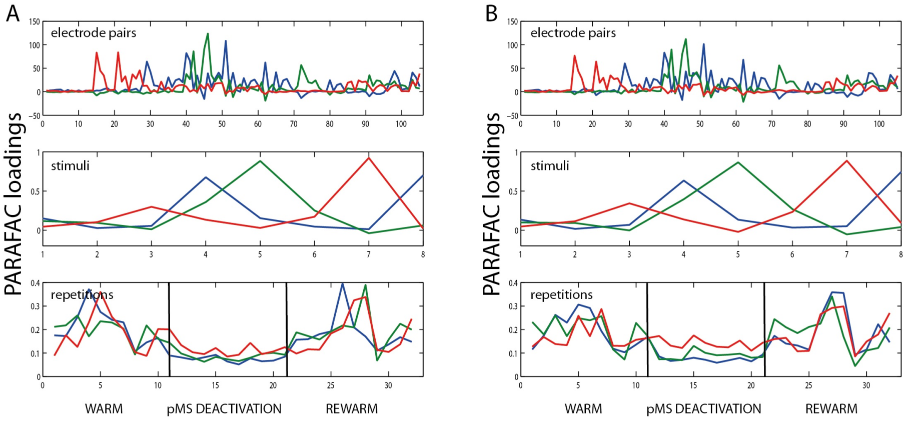

Figure 3.5.: Example for split half validation. The figure shows the results of PARAFAC analysis of the bilateral deactivation data shown in Fig. 3.2, split into two halves. The similarity of the plots indicates that it is justifiable to use PARAFAC in this context.

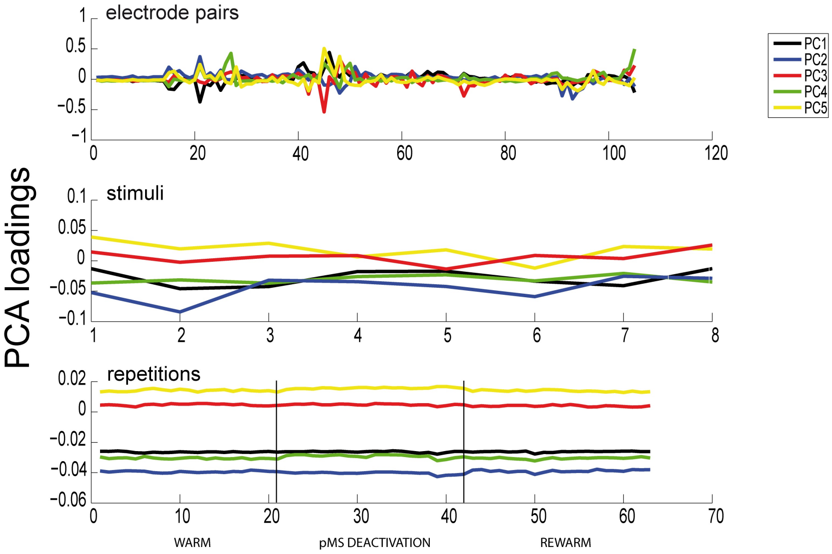

Figure 3.6.: Results of PCA. Here we show the results of a PCA for the same dataset as previously analyzed with PARAFAC (see Fig. 3.6). All 105 electrode pairs are shown. It can be observed that PCA is able to extract the same correlated pairs as PARAFAC, but the changes in correlations over time are not captured. Hence, the deactivation effect is not apparent in any of the panels.

3.1.5 Further validation of PARAFAC

To take a closer look at the choice of the number of components, for the example dataset shown in **Schmitz et al.** (2015), further information was retrieved to support the decision: the residual matrices for 4 and 6 components were calculated. The patterns of the residual matrices for 4 and 6 components turned out to be similar, but residuals are generally higher for 4 components (sum of squares of residuals for 4 components: 102892.11; for 6 components: 81614.76). At the same time, the explained variance is higher for 6 components (76.26 %) than for 4 components (70.07 %). In addition, the core consistency diagnostic (CORCONDIA) value, indicating the validity of the model, was calculated. Here, in contrast to what is indicated by the residuals and the amount of variation explained, it shows that the 4-component

Table 3.2.: CORCONDIA values for electrode pair number 45, repetitions 43 and 49. Comp. = Components; Rep. = Repetition number. Values were rounded to four decimal points, highest values are marked in green.

		Stim 1	Stim 2	Stim 3	Stim 4	Stim 5	Stim 6	Stim 7	Stim 8
4 Comp.	Rep. 43	0.6654	1.1230	-0.2119	1.2762	18.2052	3.8341	0.2002	-0.4074
6 Comp.	Rep. 43	1.4406	1.0929	0.3754	5.1795	17.3600	4.1063	-0.0259	1.3341
4 Comp.	Rep. 49	0.6625	1.0317	-0.1809	1.5534	16.7887	3.5437	0.0752	-0.2844
6 Comp.	Rep. 49	1.3064	0.9486	0.3428	5.4251	14.9597	3.5437	-0.0845	1.4520

model (CORCONDIA = 93.77) is more suitable than the 6-component model (CORCONDIA = 19.01). Hence, following the CORCONDIA criterion, the 4-component model should be preferred over the 6-component model.

Furthermore, the relevant values for electrode pair No. 45 and repetitions 43 and 49 were extracted (see Table 3.2). It is noticeable that the residuals for stimulus 5 (the one shown in the middle panel in A) are much larger than for all other stimuli. This is likely due to the high original correlation values for this stimulus.

3.1.6 PARAFAC results

PARAFAC was utilized as a screening method to gain an overview of the deactivation effects. Overall, the PARAFAC algorithm was able to extract the effects that the pMS deactivation had on the correlated firing in area 18. With this, the deactivation effect showed to be very distinct for some sessions, but not as prominent for others; in some cases large differences in the cross correlation structures for the different deactivation conditions could be observed, while in others, the effects were much less pronounced. The following section shows a selection of typical PARAFAC results, covering examples for each deactivation condition.

Synchrony measure

Ipsilateral deactivation (example: session 27T[1]) led to a reduction in correlation strength and variance for all stimulus phases (i.e. spontaneous activity, stationary stimulus, moving stimulus; see Fig. 3.8), but mostly during spontaneous activity (Fig. 3.8a). A second example (session 5S) again shows a decrease in the variance of correlation for the spontaneous activity (Fig. 3.12a), but the effects are not clearly visible for stationary and moving stimulus (Fig. 3.12b,c). For contralateral deactivation (example: session 10T), the results were not as pronounced. During spontaneous activity, the activity looked roughly the same over the warm/cooling/rewarm cycle (Fig. 3.9a), during the stationary and moving stimulus, a slight increase in activity could be observed (Fig. 3.9b,c). Bilateral deactivation (example: session 23T) led to a clear decrease in correlated activity for all stimulus phases, up to being almost extinct during spontaneous activity, and then a rebound in activity for the rewarmed phase (Fig. 3.10a). This trend is similar for the phases of stationary and moving stimulus, but not as pronounced. A second example for bilateral deactivation (session 28T) shows a similar pattern (Fig. 3.11).

Oscillatory synchrony measure

Fig. 3.7 shows two examples of the PARAFAC loadings for the oscillatory synchrony measure. In these

---

[1] For the session numbering, please be referred to the appendix, pp. 141.

examples, the oscillatory synchrony was computed for lower (1-10 Hz) and higher (30-50 Hz) frequencies during spontaneous activity, i.e. the relative power between 1-10 Hz, and 30-50 Hz, respectively, was extracted from the correlogram as defined in equation 2.7 (p. 40). While a decrease in variability of oscillatory synchrony is only visible for higher frequencies (Fig. 3.7D), variability of oscillatory synchrony clearly decreases during bilateral pMS deactivation for both low and high frequencies (Fig. 3.7C,F). Hence, also the oscillatory synchrony measure is clearly affected when the pMS cortex becomes inactive and the effect is reverted once the tissue rewarms (Fig. 3.7C,F).

Since the focus in this thesis was put on measures based on millisecond-precise spiking, the oscillatory synchrony measure was not looked into further, but this could be worthwhile in future studies.

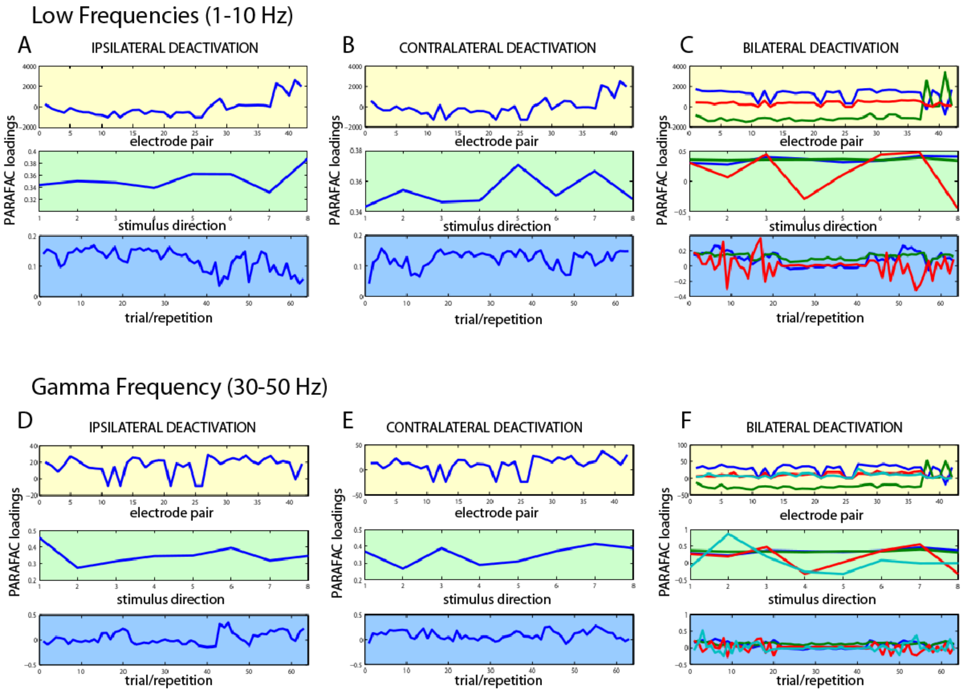

Figure 3.7.: The plots show an example for the pMS deactivation effects on the oscillatory synchrony measure for the lower frequencies (1-10 Hz) and the gamma frequency band (30-50 Hz) during phases of spontaneous activity. While the low frequencies are mainly affected by bilateral deactivation (C), the activity in the gamma band is also reduced during ipsilateral deactivation (D, F).

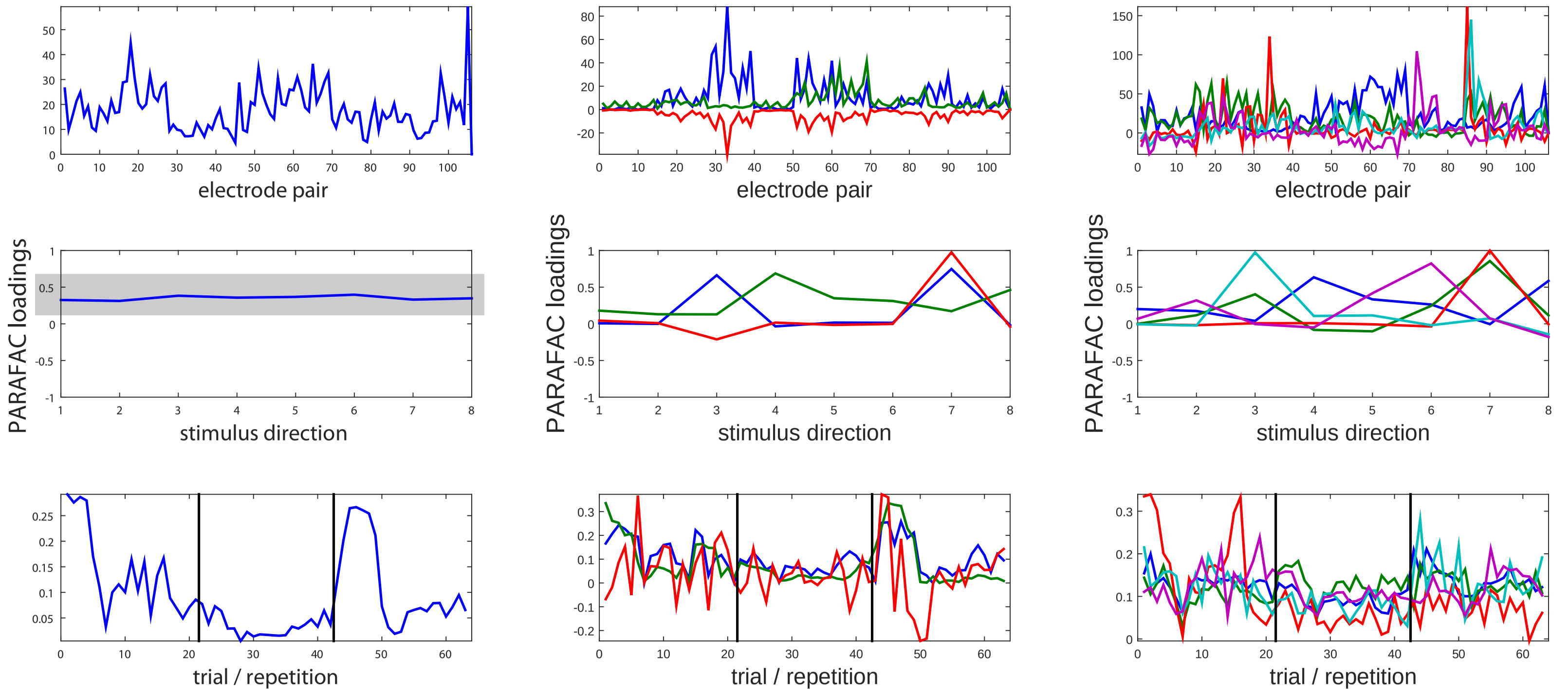

(a) Spontaneous activity

(b) Stationary stimulus

(c) Moving stimulus

Figure 3.8.: PARAFAC loadings for experiment 121007, session 27T (right hemisphere, ipsilateral pMS deactivation). The panels (a), (b), and (c) show the PARAFAC loadings for spontaneous activity, static stimulation, and moving stimulation, respectively. PARAFAC models were computed with 1-8 factors, and the optimal number of factors was chosen as the one for which the PARAFAC model showed the highest value of explained variance. Only the optimal number of factors is shown here. Each of the coloured lines depicts one factor that yielded from the PARAFAC analysis. Within each of the panels a, b, and c, the same colour refers to the same factor. The absence of variance in the loading for stimulus direction in (a) confirms that PARAFAC is able to extract the information that there is no stimulus-dependent fluctuation during spontaneous spiking activity. A reduction in correlated activity during thermal deactivation is visible for all phases of the trial (spontaneous / static / moving). Remarkable features are highlighted in grey.

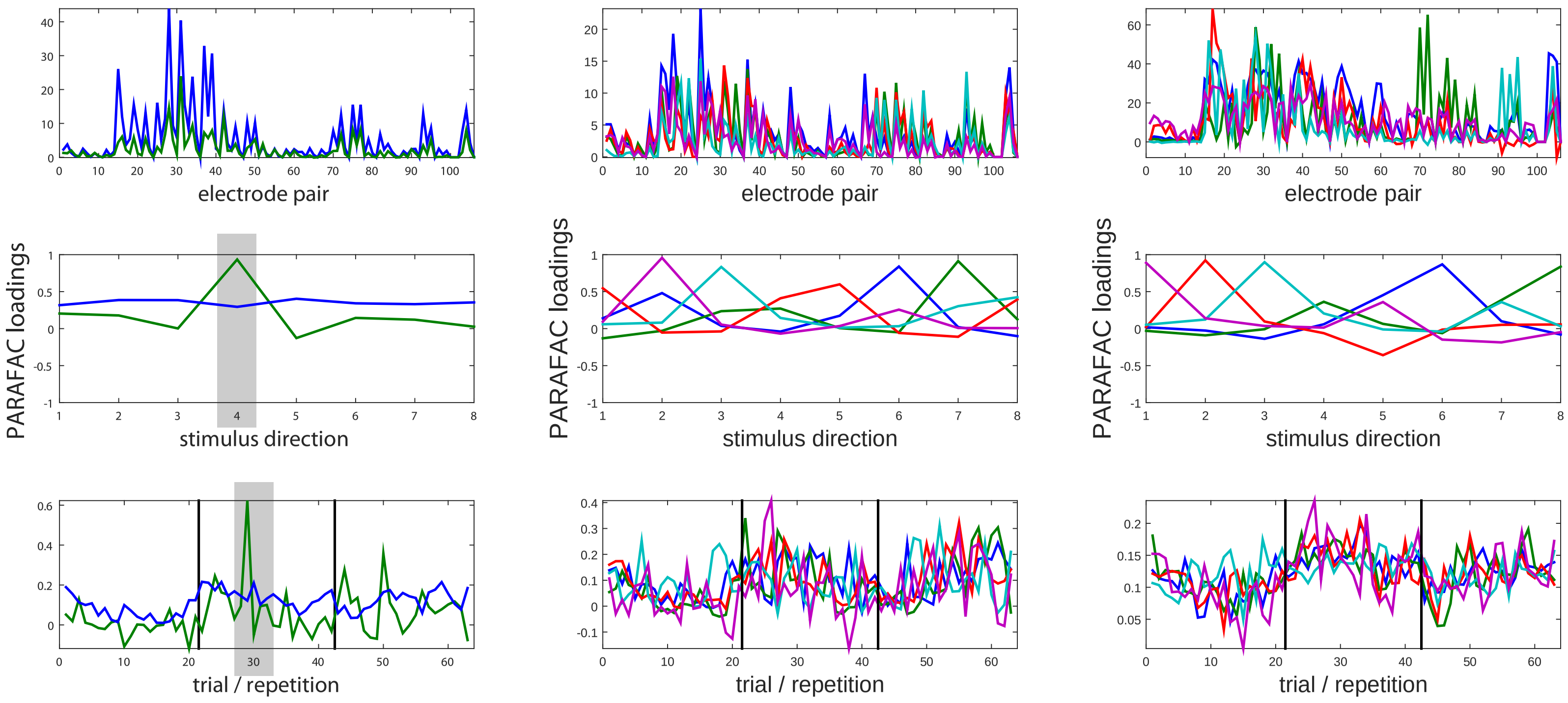

(a) Spontaneous activity

(b) Stationary stimulus

(c) Moving stimulus

Figure 3.9.: PARAFAC loadings for experiment 121007, session 10T (left hemisphere, contralateral pMS deactivation). The panels (a), (b), and (c) show the PARAFAC loadings for spontaneous activity, static stimulation, and moving stimulation, respectively. PARAFAC models were computed with 1-8 factors, and the optimal number of factors was chosen as the one for which the PARAFAC model showed the highest value of explained variance. Only the optimal number of factors is shown here. Each of the coloured lines depicts one factor that yielded from the PARAFAC analysis. Within each of the panels a, b, and c, the same colour refers to the same factor. In this example of contralateral pMS deactivation, no pronounced change in correlated activity during deactivation is visible. It also shows that PARAFAC can be applied to identify artefacts, as can be seen in (a) for stimulus direction (stimulus 4) and trial/repetition (trial 29). Remarkable features are highlighted in grey.

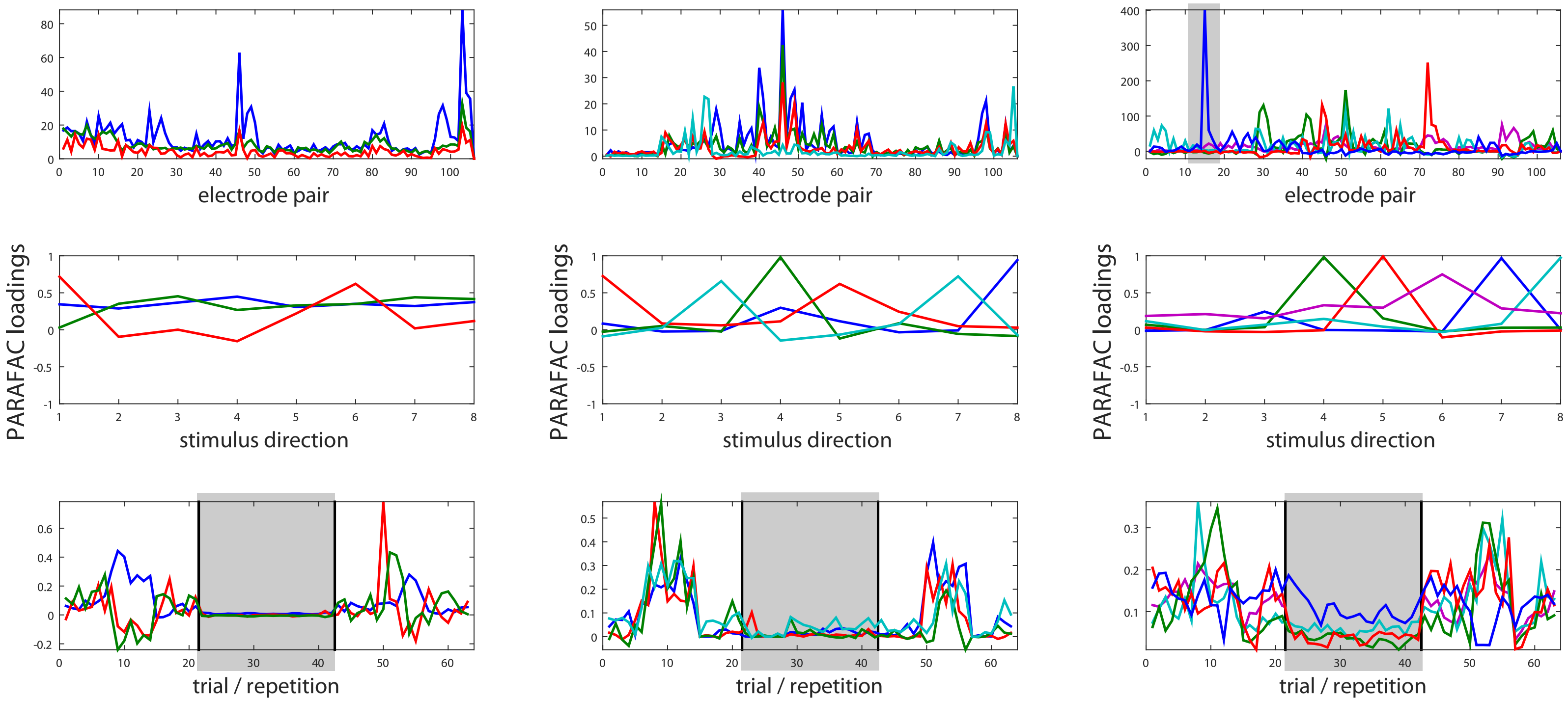

(a) Spontaneous activity

(b) Stationary stimulus

(c) Moving stimulus

Figure 3.10.: PARAFAC loadings for experiment 121007, session 23T (right hemisphere, bilateral pMS deactivation). The panels (a), (b), and (c) show the PARAFAC loadings for spontaneous activity, static stimulation, and moving stimulation, respectively. PARAFAC models were computed with 1-8 factors, and the optimal number of factors was chosen as the one for which the PARAFAC model showed the highest value of explained variance. Only the optimal number of factors is shown here. Each of the coloured lines depicts one factor that yielded from the PARAFAC analysis. Within each of the panels a, b, and c, the same colour refers to the same factor. In this example for bilateral pMS deactivation, a clear decrease in correlated activity during all phases of the trial can be observed, close to extinction during spontaneous activity, but rebounding when the cortex is rewarmed (a). Some electrode pairs show very high correlation, such as e.g. pair no. 16 during moving stimulation, which corresponds to the electrodes 2 and 4. Remarkable features are highlighted in grey.

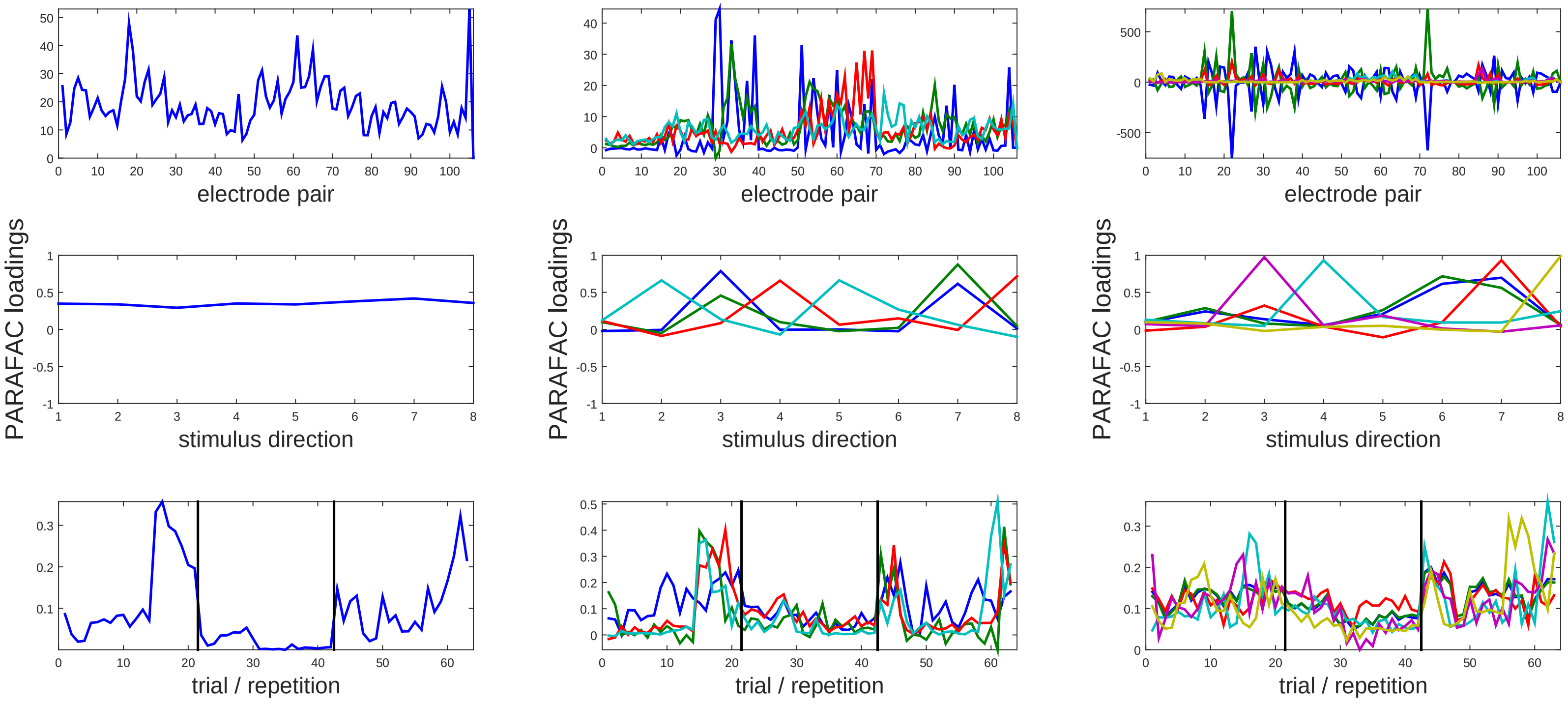

(a) Spontaneous activity (b) Stationary stimulus (c) Moving stimulus

Figure 3.11.: PARAFAC loadings for experiment 121007, session 28T (right hemisphere, bilateral pMS deactivation). The panels (a), (b), and (c) show the PARAFAC loadings for spontaneous activity, static stimulation, and moving stimulation, respectively. PARAFAC models were computed with 1-8 factors, and the optimal number of factors was chosen as the one for which the PARAFAC model showed the highest value of explained variance. Only the optimal number of factors is shown here. Each of the coloured lines depicts one factor that yielded from the PARAFAC analysis. Within each of the panels a, b, and c, the same colour refers to the same factor. Again, during bilateral deactivation a remarkable increase in correlated spiking could be observed, which was most pronounced during spontaneous activity.

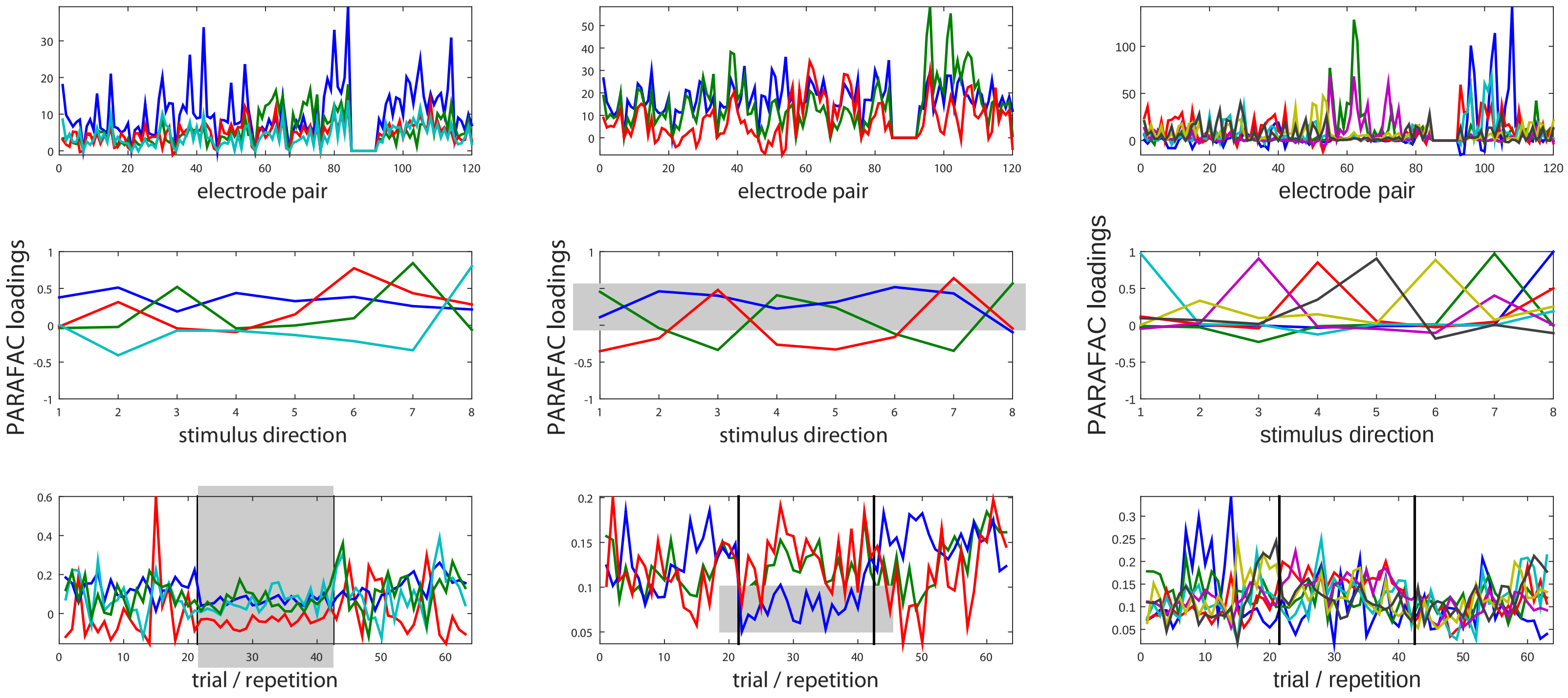

(a) Spontaneous activity

(b) Stationary stimulus

(c) Moving stimulus

Figure 3.12.: PARAFAC loadings for experiment 112807, session 5S (left hemisphere, ipsilateral pMS deactivation). The panels (a), (b), and (c) show the PARAFAC loadings for spontaneous activity, static stimulation, and moving stimulation, respectively. PARAFAC models were computed with 1-8 factors, and the optimal number of factors was chosen as the one for which the PARAFAC model showed the highest value of explained variance. Only the optimal number of factors is shown here. Each of the coloured lines depicts one factor that yielded from the PARAFAC analysis. Within each of the panels a, b, and c, the same colour refers to the same factor. In this example of ipsilateral deactivation, a decrease in strength and variability in cross correlation was observed during thermal deactivation for spontaneous activity. During presentation of the static grating, there was a general decrease, which was not stimulus-dependent (blue component). During presentation of the moving grating, no clear effect is visible. Remarkable features are highlighted in grey.

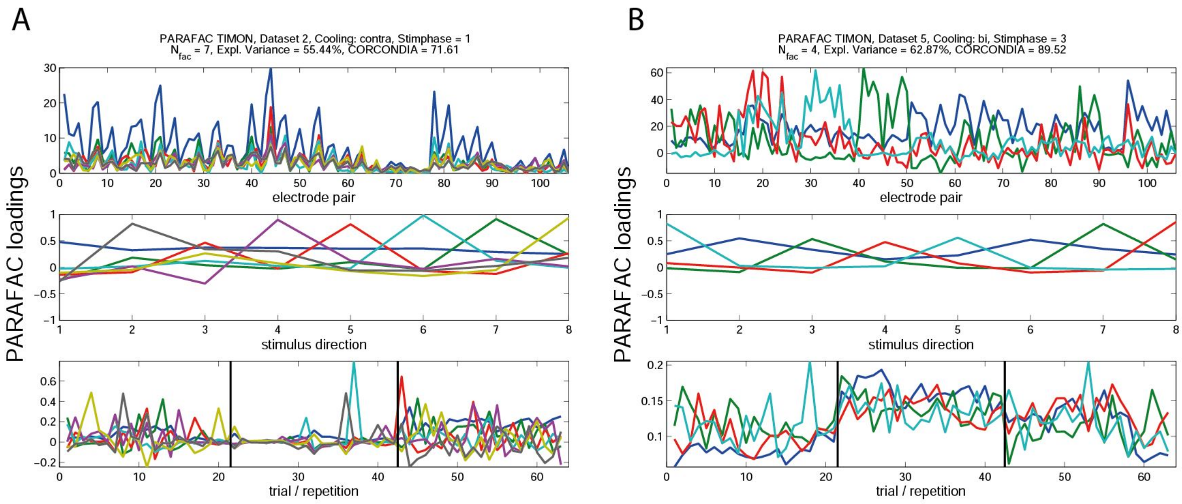

Figure 3.13.: Selected examples that deviate from the "typical" PARAFAC observations. The panels (a), (b), and (c) show the PARAFAC loadings for spontaneous activity, static stimulation, and moving stimulation, respectively. PARAFAC models were computed with 1-8 factors, and the optimal number of factors was chosen as the one for which the PARAFAC model showed the highest value of explained variance. Only the optimal number of factors is shown here. Each of the coloured lines depicts one factor that yielded from the PARAFAC analysis. Within each of the panels a, b, and c, the same colour refers to the same factor. A) Decrease in variability during contralateral pMS deactivation, spontaneous activity. B) Increase in correlations during bilateral pMS deactivation, moving grating.

In contrast to the "typical" observations described above, some sessions showed deviations from those. Fig. 3.13 shows two of these examples. In the cases depicted here, contralateral deactivation led to a decrease in correlations, while bilateral deactivation resulted in an increase in cross correlation values.

In order to further investigate the possible reasons for the observed deviations, the local field potential (LFP) signal was analyzed (see section 3.2).

3.1.7 CORCONDIA I

CORCONDIA values were calculated for all sessions of the three experiments (Fig. 3.14). Since the PARAFAC model is not nested, a new calculation was performed for every number of factors, i.e. the factors are calculated anew and in parallel. This results in the fact that a model with a higher number of factors does not have to have a lower CORCONDIA value than a model with less factors. This phenomenon could especially be observed for models for phases of spontaneous activity (Fig. 3.14). The optimal number of factors showed to lie below six with a tendency towards higher values during visual stimulation as compared to phases of spontaneous activity.

3.2 Analysis of the Local Field Potential

The LFP signal of this dataset had been assessed previously (**Geider**, 2008; **Barnes**, 2014). However, in these studies, only the averaged activity over all experiments of this series of experiments (3 cats) was presented. Here, the effects in the LFP signal were first considered for each experiment separately. This became necessary after the apparent variability between experiments that was observed with the previously applied methods. The application of the Fast Fourier Transfor (FFT) to the LFP signal as a well-established method was utilized in order to collate the variability found in the spike signals with the

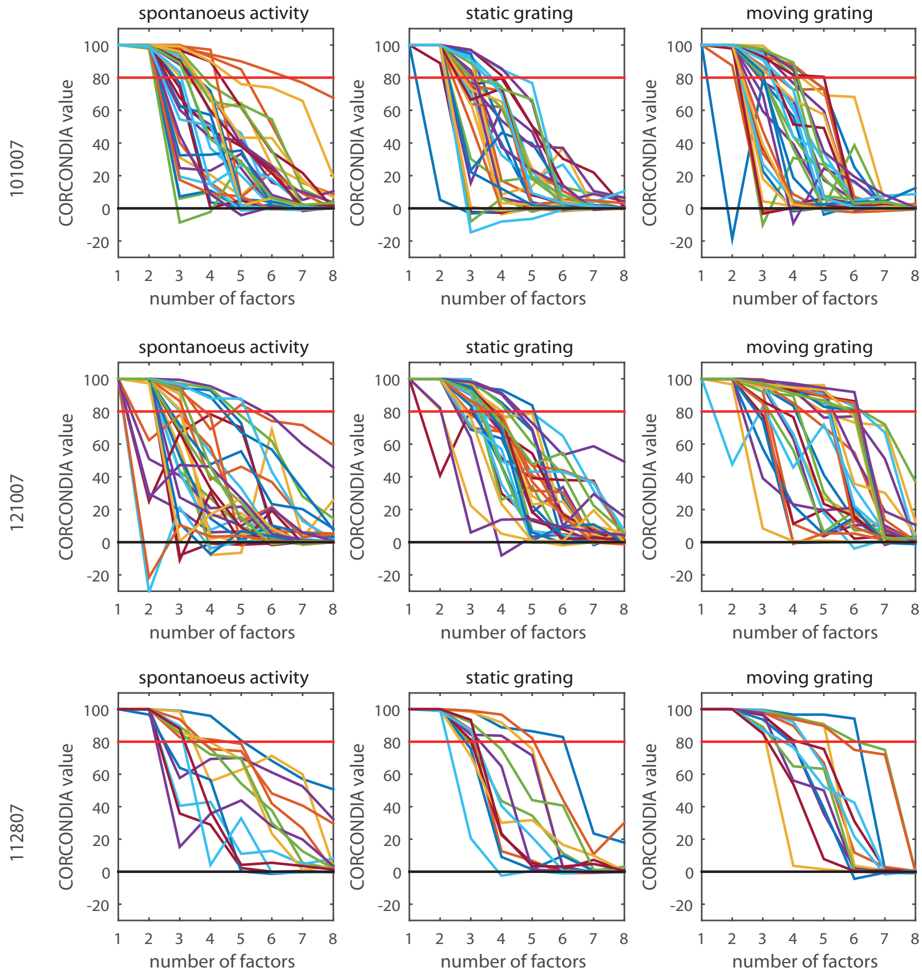

Figure 3.14.: CORCONDIA values for all three experiments. The figure shows the CORCONDIA value for each session and each number of factors that was calculated. One colour depicts one session. The red line marks the recommended value of "(well) below 80", at which the model should be discarded. Thus, in most cases, the optimal model consisted of 2-6 factors. (101007: n=32, 121007: n=33, 112807: n=14)

potential variability in the FFT spectra of the three experiments. Figures 3.15-3.17 show the resulting LFP spectra.

The observed variability between the datasets is supported by effects that were observed in the LFP signal: there was a marked difference in initial power for the warm condition in the three cats (see Fig. 3.15). This could particularly be observed during phases of spontaneous activity and presentation of the static grating. When the pMS cortex was deactivated ipsi- or bilaterally, the absolute power was approximately at the same level for 101007 and 112807, but higher for 121007. As a result, the difference between power for warm vs. ipsilateral and bilateral deactivation, respectively, differed for the three cats.

The mean absolute LFP power for the different frequency bands is depicted in Fig. 3.18. Although the sessions group around a similar median value, there are differences in initial power for all frequency bands, with the largest variation in high gamma power. Based on this observation, the individual sessions were separated into three different groups according to the initial "Gamma2" power (52-90 Hz). A Kruskal-Wallis test confirmed the validity of this separation ($p < 0.0001$, corrected for multiple comparison; see Fig. 3.19). All subsequent analyses were performed for the three resulting groups separately.

3.3 CORCONDIA II

After the separation of the data into groups depending on the initial level of gamma oscillations, a closer look was taken on the number of components of the PARAFAC models. Based on the CORCONDIA values, the most suitable model was determined for each session and the number of factors for this best-suited model was determined. As the most suitable model, the model with the highest number of factors that still had a CORCONDIA value larger than 75 was selected. Then, the number of factors were compared for all stimulus phases for the three gamma groups. The results are shown in Fig. 3.20.

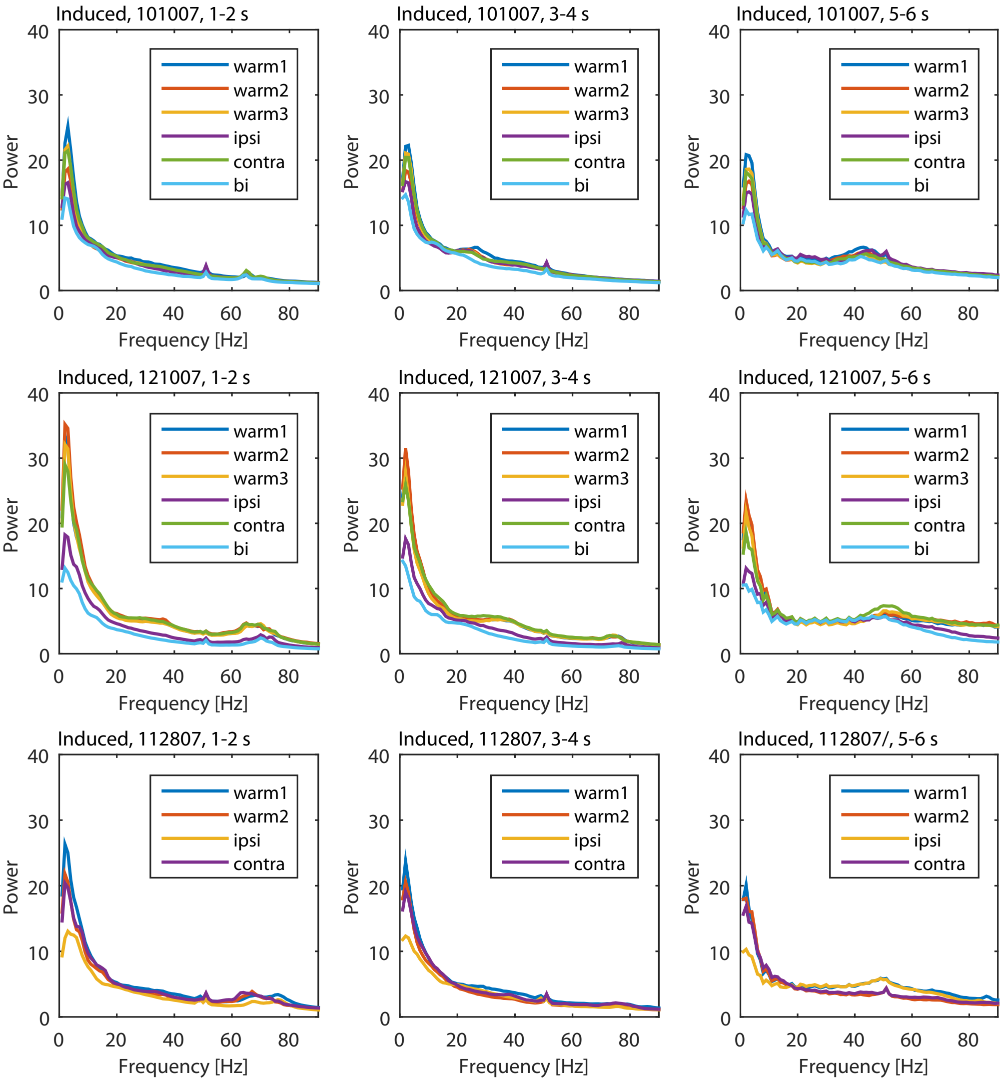

Figure 3.15.: Induced LFP activity. For all experiments, a clear drop in overall oscillation power is visible during ipsi- and bilateral deactivation (where applicable). In fact, oscillation power reaches a very similar level during ipsilateral pMS deactivation although the initial power for the warm and rewarm condition deviates. This deviation is most pronounced for the spontaneous activity phase for 121007 as compared to the other two experiments. Note: the above signal has not been cleaned from the 50 Hz line noise, which is still visible. (101007: n=5376, 121007: n= 5544, 112807: n= 2352)

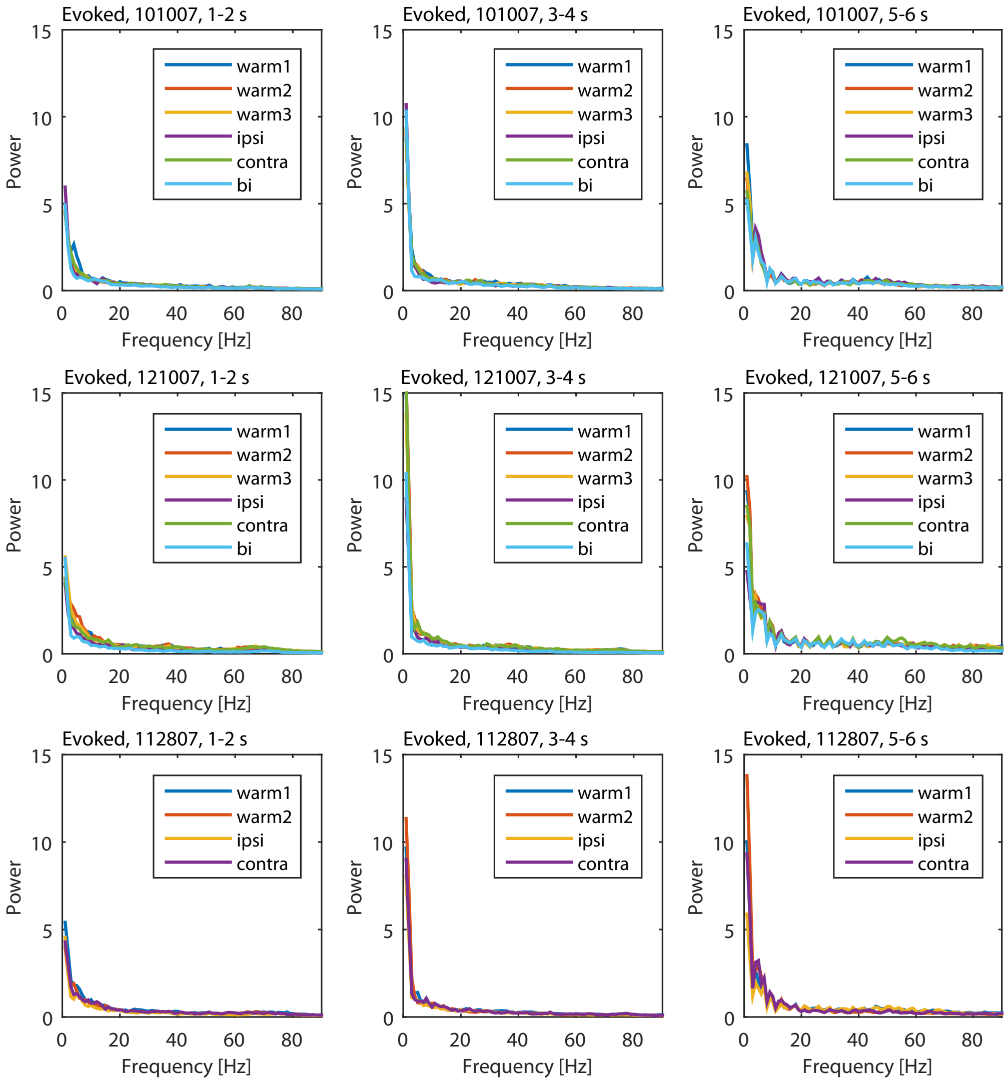

Figure 3.16.: Evoked LFP activity. Differences between experiments are not as pronounced as for induced activity. However, power is slightly higher in the theta band for experiments 121007 and 112807 as compared to experiment 101007, this effect is most pronounced during the stimulation with a moving grating. (101007: n=5376, 121007: n= 5544, 112807: n= 2352)

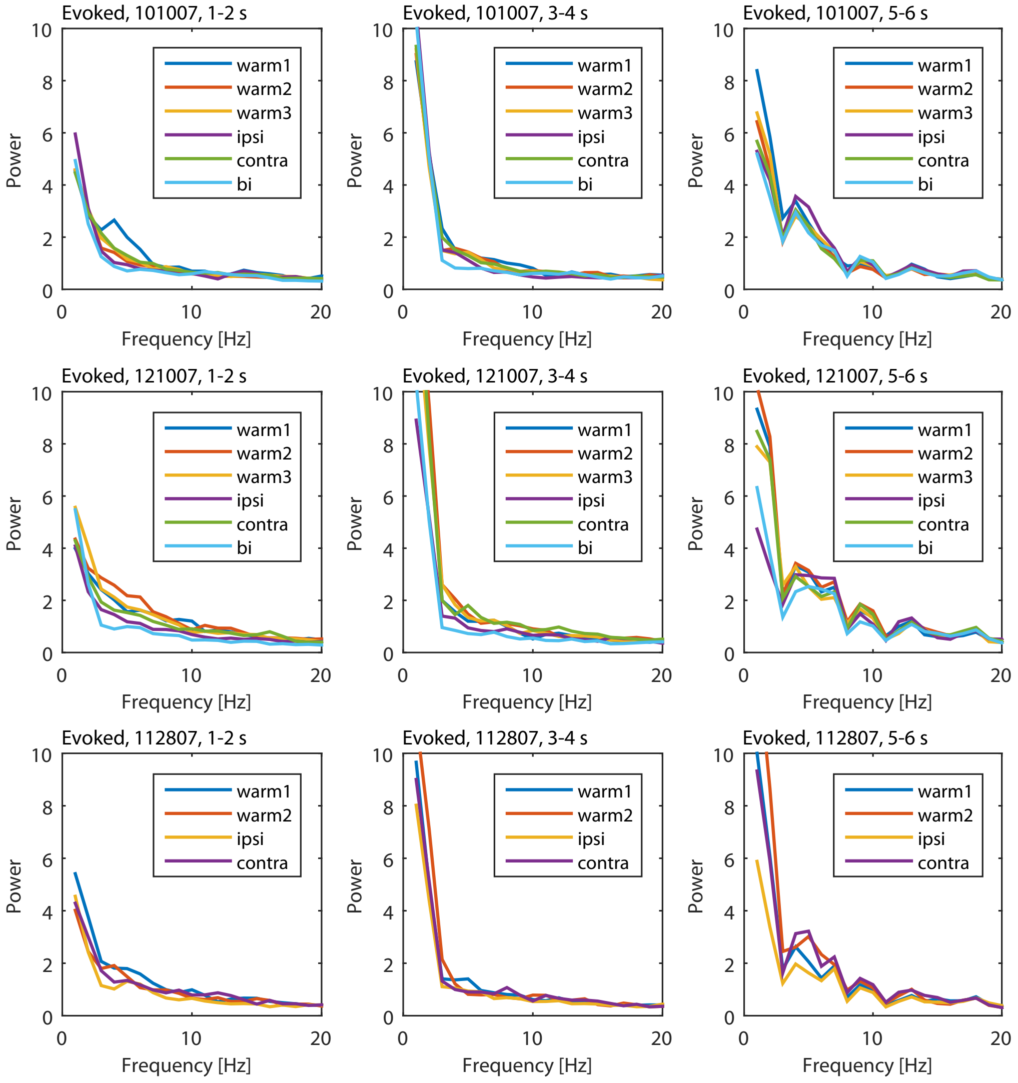

Figure 3.17.: Evoked LFP activity (0-20 Hz). Differences between experiments are not as pronounced as for induced activity. However, power is slightly higher in the theta band for experiment 121007 and 112807 as compared to experiment 101007, this effect is most pronounced during the stimulation with a moving grating. For better visibility of the differences in lower frequencies, the displayed frequency range was restricted to 0-20 Hz. (101007: n=5376, 121007: n= 5544, 112807: n= 2352)

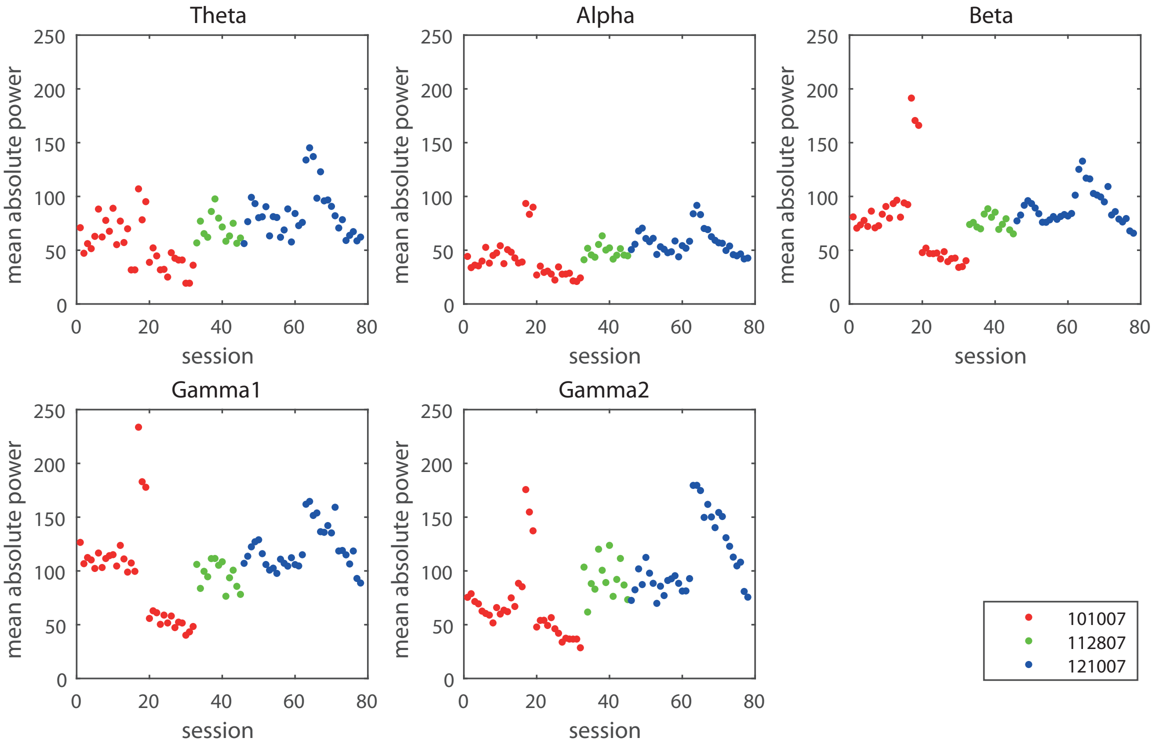

Figure 3.18.: LFP Power. Induced power was calculated for the theta (4-8 Hz), alpha (9-14 Hz), beta (15-23 Hz), low gamma ("gamma1", 24-48 Hz) and high gamma ("gamma2", 52-90 Hz) band. Only "warm" trials were included to gain an impression of the baseline activity for the respective session. The figure shows data for the three experiments in red (101007), green (112807), and blue (121007).

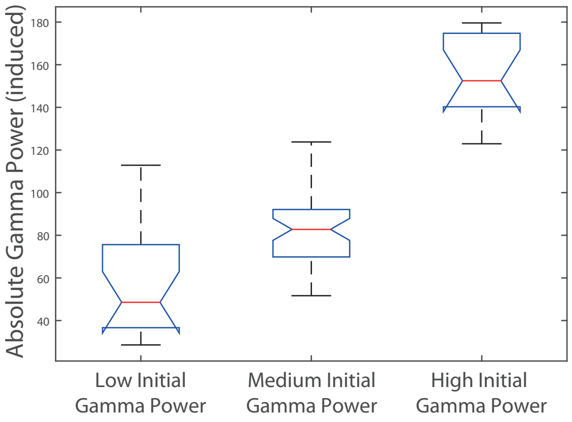

Figure 3.19.: Gamma groups. Based on the initial gamma2 power for the warm condition (see Fig. 3.18), the sessions were separated into three groups: "Low Initial Gamma" (6 sessions), "Medium Initial Gamma" (30 sessions), and "High Initial Gamma" (5 sessions). The gamma power in the groups is significantly different ($p = 4.5908 * e^{-10}$, Kruskal Wallis test, corrected for multiple comparison).

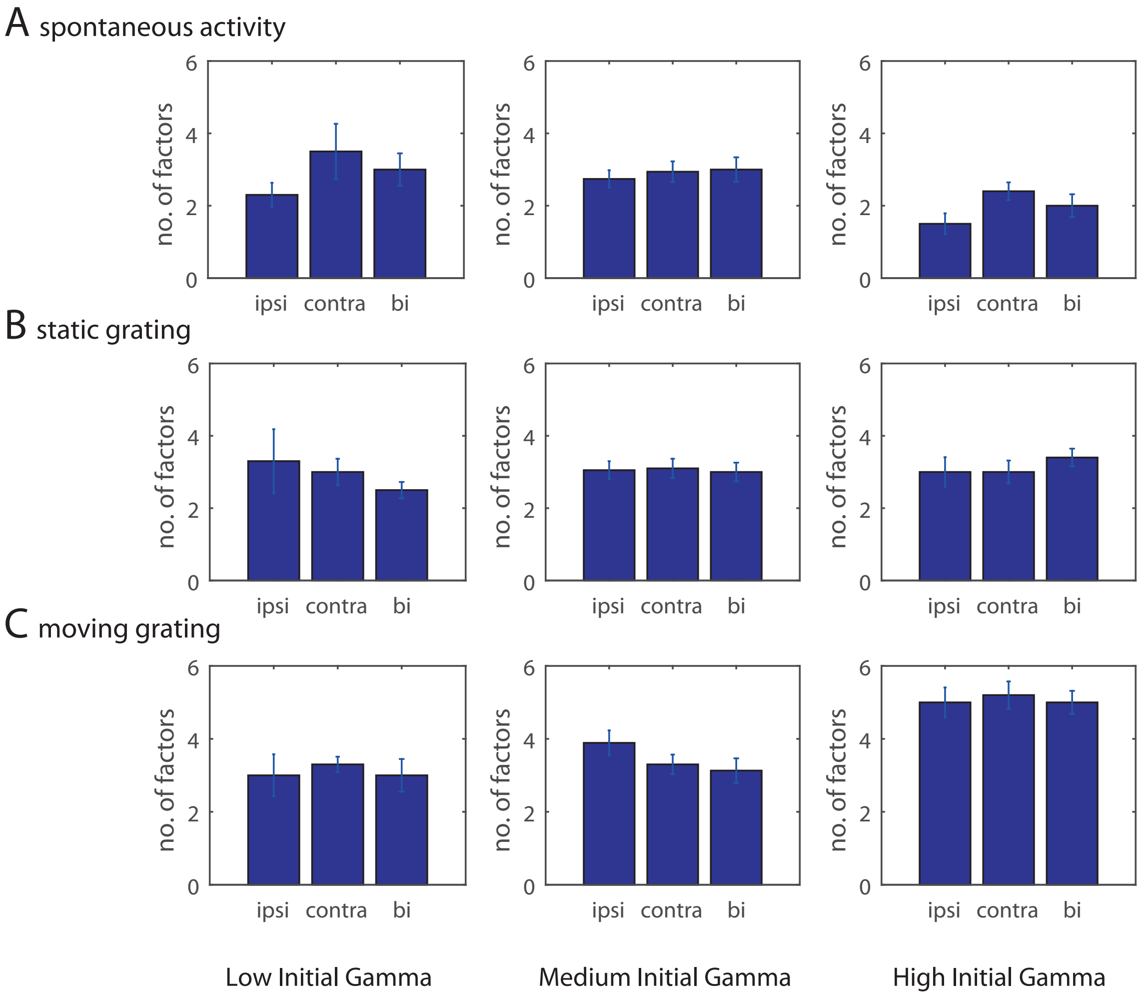

Figure 3.20.: PARAFAC components. Number of PARAFAC components for models with CORCONDIA values larger than 75, separated by stimulus phases, deactivation conditions, and initial gamma power. (A) Spontaneous activity, (B) Static grating, (C) Moving grating. Overall, no dependency between the number of PARAFAC components and the deactivation condition could be observed. The number of PARAFAC components turned out to be lowest for models for spontaneous activity for the High Initial Gamma group and were highest for models for moving grating, again for the High Initial Gamma group. Error bars are SEM. (Low Initial Gamma: $n_{ipsi} = 24$, $n_{contra} = 48$, $n_{bi} = 48$; Medium Initial Gamma: $n_{ipsi} = 152$, $n_{contra} = 136$, $n_{bi} = 112$; High Initial Gamma: $n_{ipsi} = 32$, $n_{contra} = 40$, $n_{bi} = 40$)

3.4 Spiking Activity and Tuning Properties

As a first step, spiking activity was extracted from the raw signal for all experiments and tuning preferences and spike rates were computed. The results are displayed in the following sections.

3.4.1 Electrode positions

Due to the removal of the electrodes prior to sacrificing the animal, ducts caused by the penetration of the tissue could not be reliably identified. Hence, the exact laminar position of the recording electrodes could not be determined. However, the electrode depths were estimated using the initial recording positions from the first session, as noted in the study protocol. Based on the depths of the cortical laminae as shown in Table 3.3.

Table 3.3.: Depth of cortical layers in area 18, based on laminar depths as given in Mitzdorf and Singer (1978).

Layer	Cortical depth
II	200-470 μm
III	470-850 μm
IV	850-1180 μm
V	1180-1560 μm
VI	1560-1770 μm

Based on these values, an estimated layer was assigned to each electrode position (see Fig. 3.21).

3.4.2 Spike sorting

As specified above, spike sorting was applied to sixteen sessions, eight of experiments 101007 and 121007 each. The results of the automatic spike sorting using WaveClus were manually adjusted to obtain the clearest separation of units.

The sorting process yielded around 25-40 units per session (see table 3.4).

Table 3.4.: Number of single-units that resulted from the spike sorting for the sorted sessions.

Experiment	Session	No. units /nodes	No. edges /graph size		Experiment	Session	No. units /nodes	No. edges /graph size
101007	1	30	870		121007	1	31	930
101007	2	33	1056		121007	3	27	702
101007	3	25	600		121007	4	26	650
101007	4	29	812		121007	7	36	1260
101007	7	29	812		121007	9	29	812
101007	9	28	756		121007	10	30	870
101007	13	31	930		121007	12	37	1332
101007	14	28	756		121007	14	34	1122

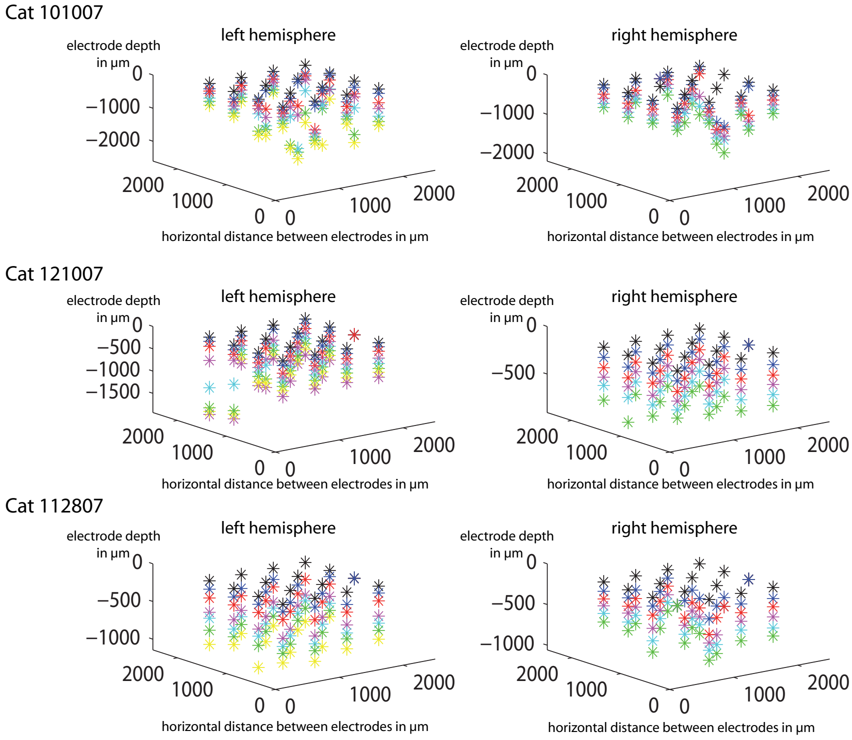

Figure 3.21.: Electrode depths for all sessions. The figure shows the depths of the electrodes for the two hemispheres of all three experiments. Positions belonging to the same session have the same colour. Electrodes were moved deeper into the tissue starting from the topmost position (black).

3.4.3 Spike rates

In order to obtain an impression on overall spiking activity, PSTHs (peri stimulus time histograms) were calculated for both the set of single- and multi-unit data.

For multi-unit spiking activity (Fig. 3.22), even though thresholds were chosen quite liberally, i.e. rather lower than higher, the average rates turned out to be very low. Still, the overall picture shows that for the phases of spontaneous activity and during the presentation of the static grating, bilateral pMS deactivation has a strong impact on the spiking activity in area 18, lowering the spike rates. The presentation of a moving stimulus, on the other hand, is strong enough to bring the rates back to the approximate level of spiking activity for the warm condition.

Spike rates were determined for all single units that were used in the analysis (16 sessions, 483 units) and compared for the different deactivation conditions (Fig. 3.23). The results of this analysis are shown in Fig. 3.23. Changes were calculated per unit and then averaged.

Contralateral stimulation only had a negligible effect on MUA spike rate throughout all sessions and all phases of the trial. Bilateral deactivation led to a drop in spike rates in all three groups for spontaneous activity and static stimulation, however, for the moving stimulus the activity returned to the level of the warm condition for the Low and Medium Initial Gamma groups. Ipsilateral deactivation led to different patterns of spiking rates for the three groups; with causing an increase in rates for static and moving stimulation for the Low Initial Gamma group, a decrease for spontaneous activity and static stimulation for the Medium Initial Gamma group and a decrease throughout all stimulus phases for the High Initial Gamma group. Except for the Low Initial Gamma group, the described changes were strongest during spontaneous activity.

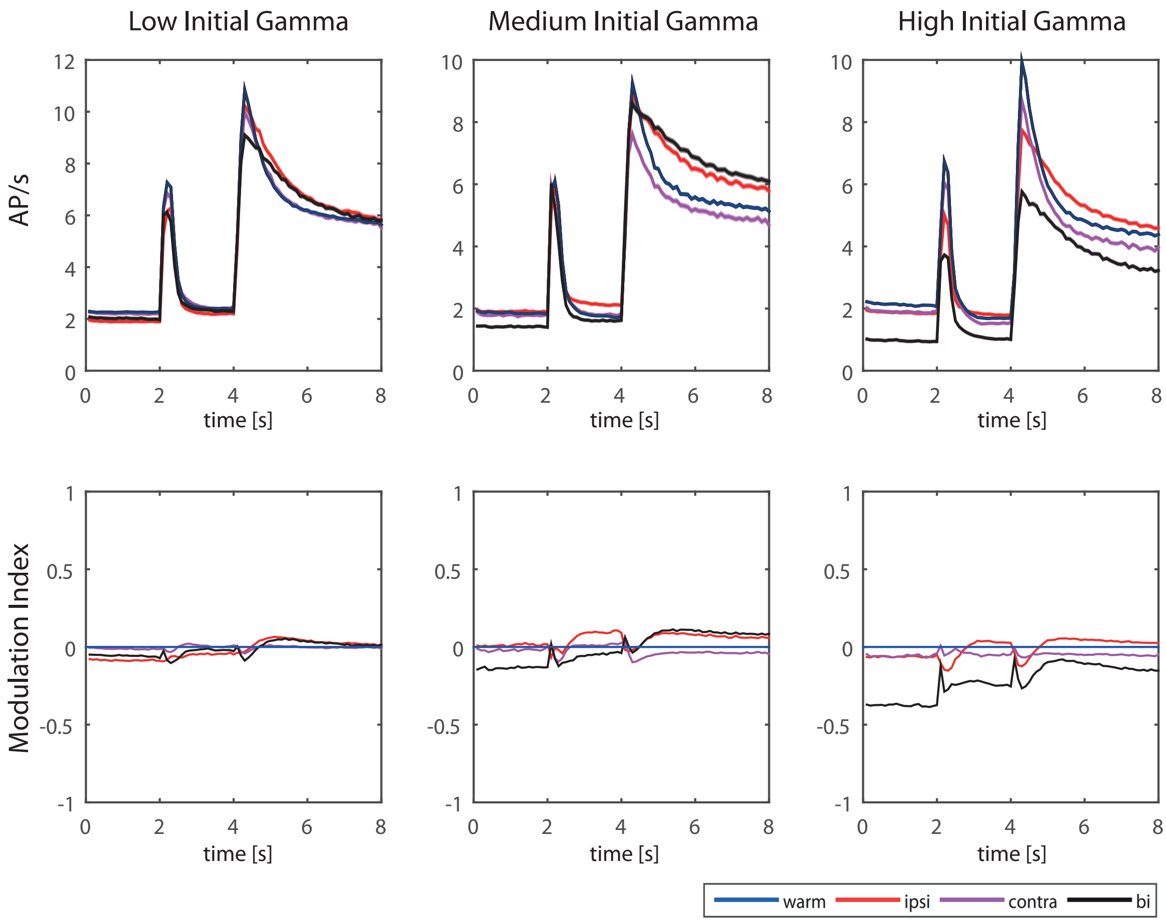

Figure 3.22.: Spike Rates MUA. Multi-unit spike rates were calculated for the Low, Medium, and High Initial Gamma groups. The figure shows the peri-stimulus time histogram (PSTH), i.e. the mean spike rates (+/- SEM) in the upper panels and the Modulation Index in the lower panels. The deactivation effect is strongest for bilateral deactivation for both the Medium and High Initial Gamma groups. For the Low Initial Gamma group, the deactivation only has little effect on the spike rate for all conditions over the whole trial. For the Medium Initial Gamma group, spike rates even show an increase during ipsilateral pMS deactivation for the static grating (2-4 s) and during ipsi- and bilateral pMS deactivation for the moving grating (4-8 s). (Low Initial Gamma: $n_{warm}=94064$, $n_{ipsi}=24192$, $n_{contra}=37632$, $n_{bi}=32256$; Medium Initial Gamma: $n_{warm}=59072$, $n_{ipsi}=21504$, $n_{contra}=18672$, $n_{bi}=18800$; High Initial Gamma: $n_{warm}=64480$, $n_{ipsi}=24192$, $n_{contra}=21488$, $n_{bi}=18784$)

In order to get a more complete view, Tables 3.5 and 3.6 show the warm spike rates for both multi- and single-unit activity. From Table 3.5, there is no consistent trend as to which of the gamma groups exhibits the highest spike rates. For single-unit activity (Table 3.6), note that the High Initial Gamma group exhibits the highest mean warm spike rates for each phase of the trial (i.e. spont/stat/mov), but variability is very high.

Table 3.5.: Spike rates warm, MUA. The table shows the mean spike rates for the multi-unit activity in AP/s +/- standard deviation (Total number of trials: Low Initial Gamma: n=94064; Medium Initial Gamma: n=59072; High Initial Gamma: n=64480).

	Low Initial Gamma	Medium Initial Gamma	High Initial Gamma
spont	2.26 AP/s +/– 6.66	1.84 AP/s +/– 3.78	2.10 AP/s +/– 4.51
stat	2.41 AP/s +/– 6.74	1.76 AP/s +/– 3.98	1.69 AP/s +/– 4.40
mov	6.52 AP/s +/– 8.73	5.82 AP/s +/– 7.75	5.16 AP/s +/– 6.50

Table 3.6.: Spike rates warm, SUA. The table shows the mean spike rates for the single-unit activity in AP/s +/- standard deviation. Analysis is based on mean spike rates for 15 sessions, comprising 76 units for Low Initial Gamma, 267 units for Medium Initial Gamma, and 96 units for High Initial Gamma. Mean spike rate was calculated per session for each unit before calculating the standard deviation, such that Low Initial Gamma: n=608; Medium Initial Gamma: n=2670; High Initial Gamma: n=960. (Total number of trials: Low Initial Gamma: n=102144; Medium Initial Gamma: n=448560; High Initial Gamma: n=161280)

	Low Initial Gamma	Medium Initial Gamma	High Initial Gamma
spont	2.68 AP/s +/– 4.90	3.87 AP/s +/– 7.34	8.41 AP/s +/– 13.04
stat	4.18 AP/s +/– 6.41	3.56 AP/s +/– 5.71	5.50 AP/s +/– 6.80
mov	15.75 AP/s +/– 15.11	16.55 AP/s +/– 21.25	21.07 AP/s +/– 20.13

Table 3.7.: Spike Rates MUA. The table shows the percentage change of spike rates for all gamma groups and deactivation conditions compared to the "warm" condition. Increases (blue) and decreases (red) are colour-coded for easier readability.

MUA		Low Initial Gamma [perc. change]	Med. Initial Gamma [perc. change]	High Initial Gamma [perc. change]
ipsi	spont	-16.0 %	3.4 %	-11.5 %
	stat	-8.6 %	21.1 %	6.8 %
	mov	11.5 %	18.7 %	10.6 %
contra	spont	-2.7 %	-3.2 %	-10.4 %
	stat	0.8 %	2.9 %	-9.9 %
	mov	0.6 %	-7.2 %	-8.8 %
bi	spont	-11.3 %	-23.1 %	-54.9 %
	stat	-3.7 %	-8.3 %	-38.5 %
	mov	9.3 %	24.2 %	-16.9 %

Table 3.8.: Spike Rates SUA. The table shows the percentage change of spike rates for all gamma groups and deactivation conditions compared to the "warm" condition. Increases (blue) and decreases (red) are colour-coded for easier readability.

SUA		Low Initial Gamma [perc. change]	Med. Initial Gamma [perc. change]	High Initial Gamma [perc. change]
ipsi	spont	8.6 %	-42.5 %	-69.1 %
	stat	34.0 %	-5.4 %	-54.8 %
	mov	44.4 %	16.2 %	-31.4 %
contra	spont	17.4 %	-3.3 %	-10.5 %
	stat	24.7 %	14.7 %	3.1 %
	mov	16.4 %	14.4 %	7.7 %
bi	spont	-21.0 %	-53.4 %	-83.9 %
	stat	-11.4 %	-29.0 %	-63.2 %
	mov	8.8 %	12.8 %	-37.8 %

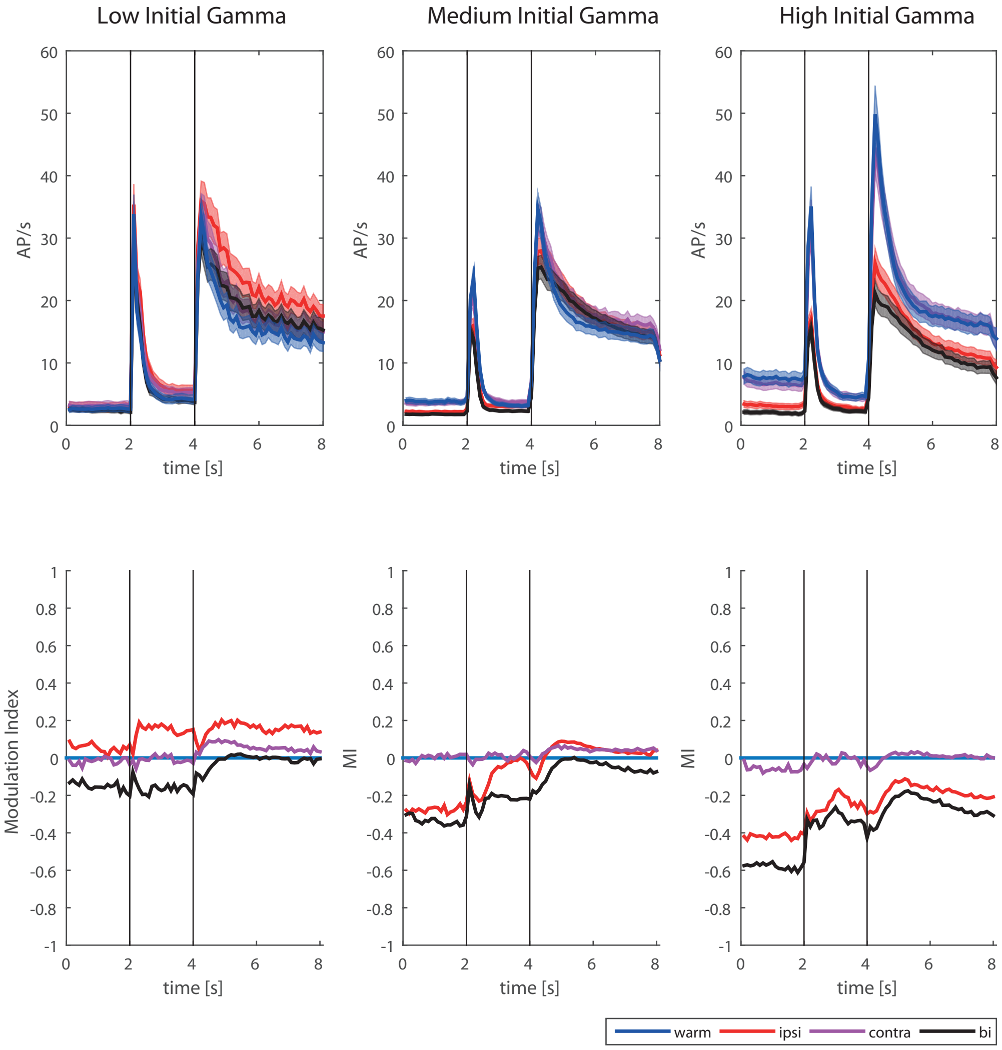

Figure 3.23.: Spike Rates SUA. Single-unit spike rates were calculated for the Low, Medium, and High Initial Gamma groups. The figure shows the peri-stimulus time histogram (PSTH), i.e. the mean spike rates (+/- SEM) in the upper panels and the Modulation Index in the lower panels. For the Low Initial Gamma group (left panel), bilateral pMS deactivation led to a decrease in spike rates, which was diminished once the moving stimulus appeared. Ipsilateral deactivation even led to an increase, especially during static, as well as moving stimulation. For the Medium Initial Gamma group (middle panel), both ipsi- and bilateral deactivation led to a decrease in spike rates, but this effect fades with stronger stimulation, in particular for ipsilateral deactivation. For the High Initial Gamma group (right panel), ipsi- and bilateral deactivation lead to a distinctive drop in spike rates, which stays in effect, even with strong visual stimulation. Contralateral deactivation led to almost no change in spike rate for all three groups. (Low Initial Gamma: $n_{warm/ipsi/contra/bi}$=608; Medium Initial Gamma: $n_{warm/ipsi/contra/bi}$=2670; High Initial Gamma: $n_{warm/ipsi/contra/bi}$=960)

A pre-analysis had shown that the spike sorting procedure separated multi-units into single units with partly deviating orientation and direction preferences[2]. Fig. 3.24 shows one example of these units: here, one multi-unit splits up into four single units, which show different orientation and direction preferences.

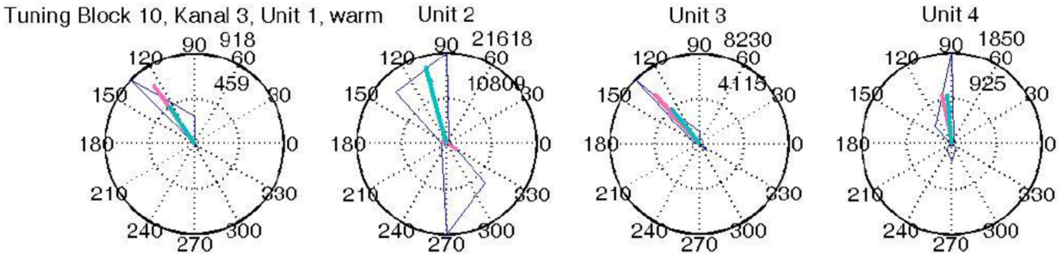

Figure 3.24.: Spike Sorting - Effect on Tuning Properties. An example of the resulting units after spike sorting: Stimulus directions are depicted radially. The dark blue curve shows the number of spikes that were fired for the respective stimulus direction. The number on the top right marks the maximum number of spikes for one of the directions. The light blue arrow points in the direction of the preferred orientation, it will only take values between 0 and 135. The preferred stimulus direction is pointed towards by the pink arrow. For the depicted channel, 4 Units could be identified, which show clearly distinct orientation and/or direction preferences, respectively.

Since within a multi-unit, the actual preferences of the single units might be concealed or distorted by the interplay of units, the effects of the pMS deactivation on tuning preferences were assessed based on the single unit data. For each unit, the tuning curve during the non-inactivated "warm" state as well as the ipsi-, contra- and bilateral deactivation conditions was computed.

However, MUA tuning curves were computed as a control (see example in Fig. 3.25). The similarity of the tuning curves over the different layers indicates that the electrode was moved through an orientation column, i.e. perpendicular to the surface.

Fig. 3.26 depicts the changes in tuning specificity during the warm condition and the pMS deactivation conditions for all three Gamma groups. In general, the Medium Initial Gamma group showed the lowest tuning strength as compared to the other sets. For the High Initial Gamma group the highest specificity values were measured. Direction tuning significantly decreased during ipsi- and contralateral deactivation, but not during bilateral deactivation; here, the specificity did not show any significant change. Orientation tuning specificity significantly decreased for the Medium Initial Gamma group for all three deactivation conditions and also for the Low Initial Gamma group during ipsilateral deactivation. For the High Initial Gamma group, no significant change in orientation tuning specificity was observed.

Fig. 3.27 shows the correlation between the initial strength of tuning and the change in tuning specificity caused by the pMS deactivation. Tuning strength was measured by the direction index (DI) (see equation 2.3, p. 36). For both orientation and direction tuning a least squares regression was performed and the correlation coefficients, c_{dir} and c_{ori}, together with the corresponding p-values, p_{dir} and p_{ori}, were computed.

A reduction in tuning specificity was observed throughout, and the stronger the initial strength, the stronger was the observed change. In all but one case (contralateral deactivation for the Medium Initial Gamma group) the change in direction selectivity was greater than the change in orientation selectivity.

---

[2] For more details see Lisa Henß's bachelor's thesis (Henß, 2012)

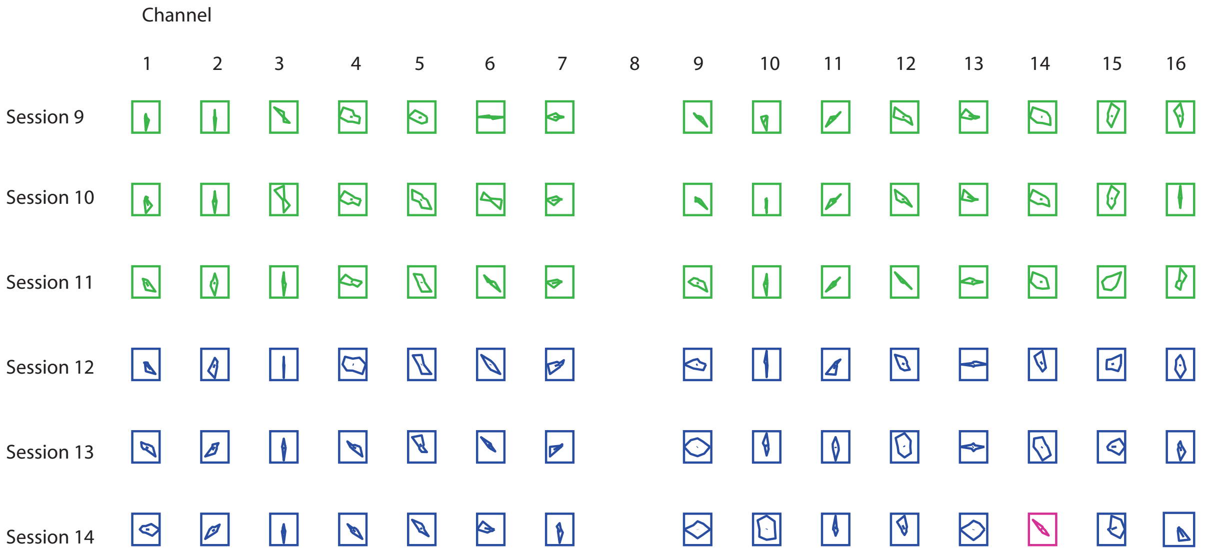

Figure 3.25.: MUA tuning curves. MUA tuning curves are shown for each session for experiment 121007, right hemisphere. The electrode was moved deeper into the tissue with each session so that a similarity of the tuning curves throughout the sessions indicates that the electrode being moved through an orientation column (estimated laminae are colour-coded: blue: layer II/III, green: layer IV, magenta: layer V; electrode 8 was defective and therefore excluded from the analysis).

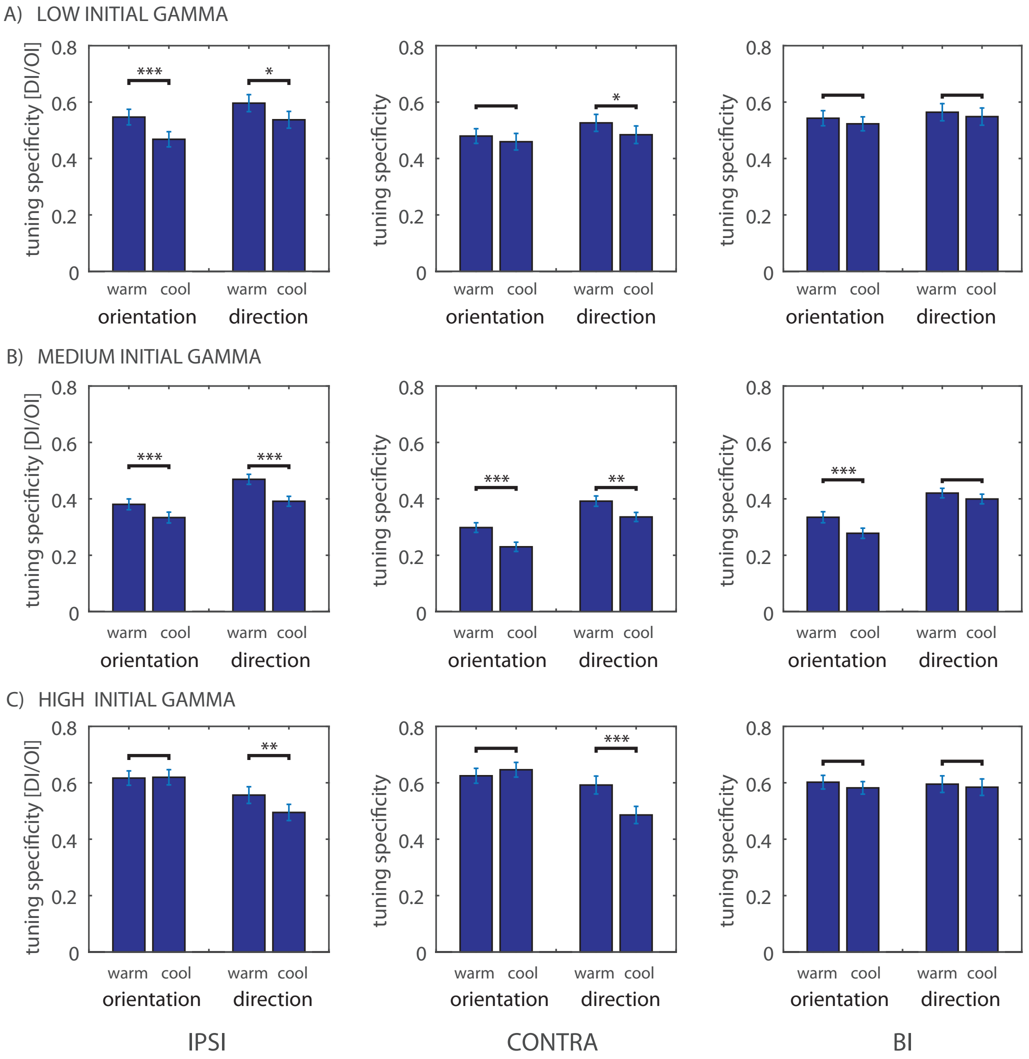

Figure 3.26.: Tuning Specificity, SUA. The figure shows the differences in tuning specificity between the warm and cool condition for all Gamma groups and deactivation conditions, for both orientation and direction tuning. (Wilcoxon signed rank test, ***: $p<0.01$, **: $0.01<p<0.05$, *: $0.05<p<0.1$; errorbars are SEM; Low Initial Gamma: $n_{warm/ipsi/contra/bi}=76$; Medium Initial Gamma: $n_{warm/ipsi/contra/bi}=267$; High Initial Gamma: $n_{warm/ipsi/contra/bi}=96$)

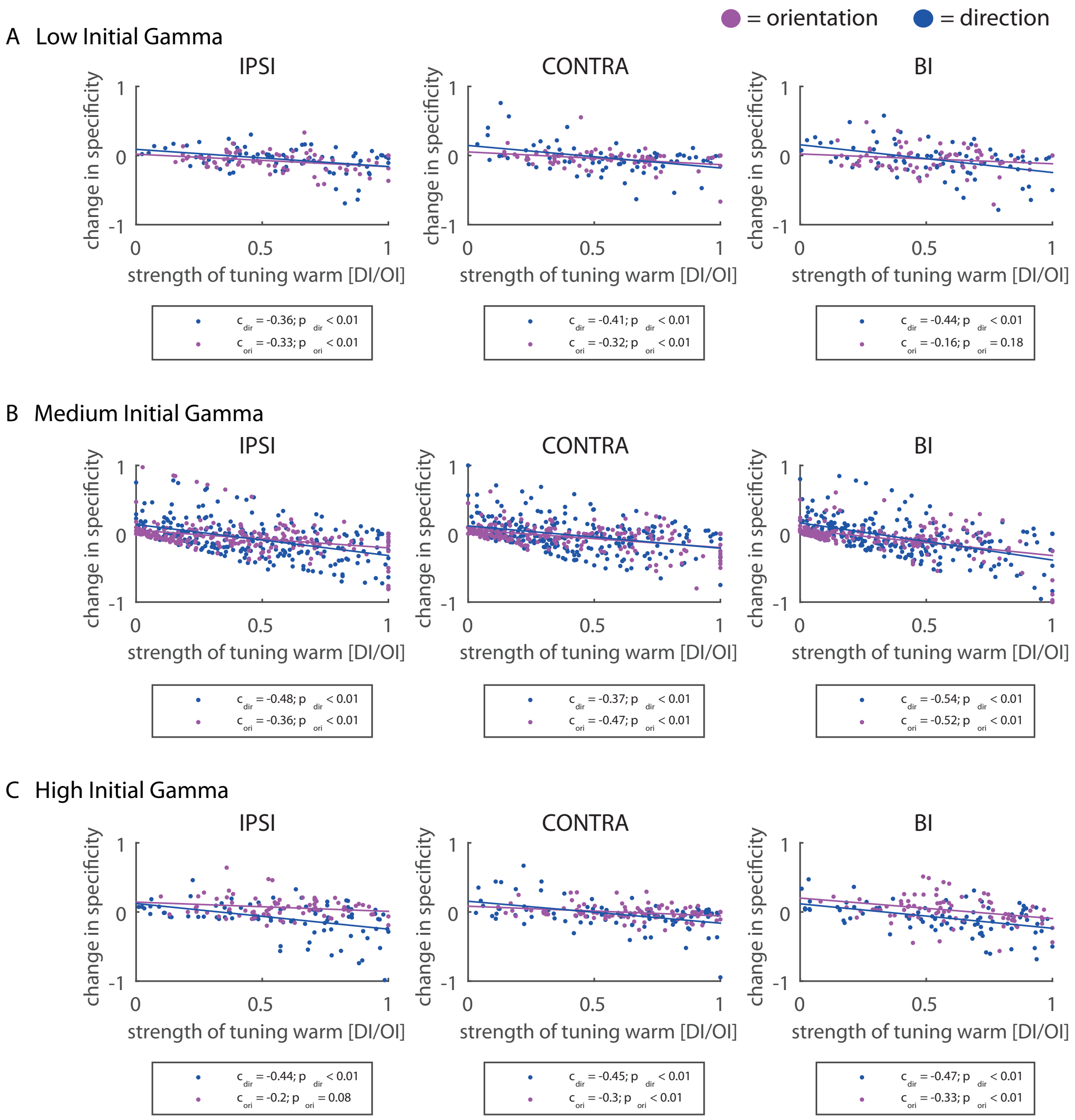

Figure 3.27.: Changes in tuning specificity, SUA. The figure shows scatter plots of the initial strength of tuning specificity, measured by the direction index, DI (see eq. 2.3), for both orientation and direction tuning. The lines depict the least squares regression for the respective dataset, with the correlation coefficients(c_{dir} and c_{ori}, respectively) and corresponding p-value (p_{dir} and p_{ori}). (A) Low Initial Gamma Power, (B) Medium Initial Gamma Power, (C) High Initial Gamma Power.

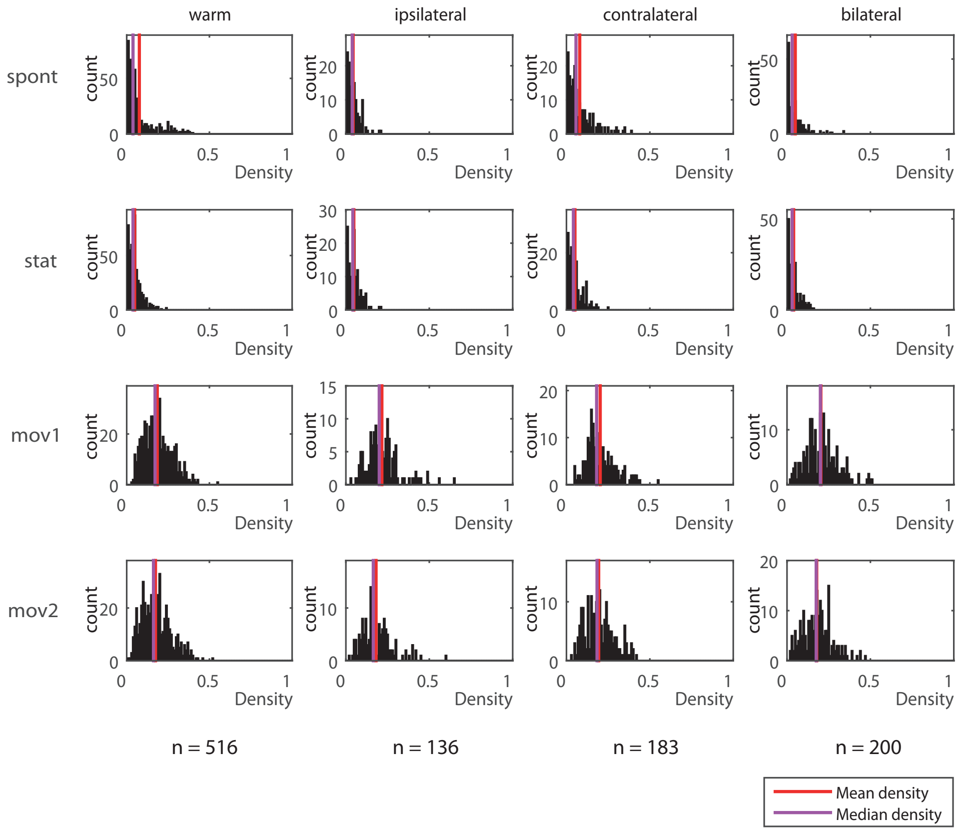

Figure 3.28.: Graph Densities, NeuroXidence I. Histograms for the networks that were calculated based on NeuroXidence. In general, the density showed to be similar for spontaneous activity and the static stimulus, and higher for moving, so that the level of correlation/no. of JSEs increases with stronger stimulation. Data are pooled for all experiments and initial gamma levels. The empirical distributions significantly differed from the expected binomial distributions for same-sized random networks (KS test of empirical distribution, $p < 1 \cdot 10^{-29}$ for all cases; binomial distributions not shown).

3.5 Network Analysis Based on NeuroXidence

The NeuroXidence method was applied to the multi-unit spiking activity. For networks with 16 nodes (i.e. the size of the electrode array) the graph size will be 120. Since channel 8 was non-functional in experiments 121007 and 112807, the number of nodes was reduced to 15, and the corresponding graph size to 105.

Two approaches were applied in order to check the graphs for randomness: probing the density of the networks, and their degree distribution.

Density of Networks

A split-half procedure was applied for the tests, i.e. data were divided in two equally sized subsets to compute the edge probability on one half of the data and use the second half to test the distribution of the number of edges. The tests showed no indication that the graphs were random (Fig. 3.28).

Degree distribution

Figures 3.29-3.31 show the degree distributions for the graphs based on the NeuroXidence analysis. None of the distributions resembles the expected distribution for random networks. Overall, higher degrees could be observed for stronger, i.e. the moving, stimulation, and for the warm condition. For the moving warm and moving bilateral deactivation conditions, the distributions are smoothest, exhibiting a power-law shape.

The graphs were also statistically tested for poissonity, i.e. checked for possible randomness. The parameter λ for the Poisson distribution was estimated from one half of the data and the test was performed on the remaining half. The p-values for these tests are also given in Figs. 3.29-3.31.

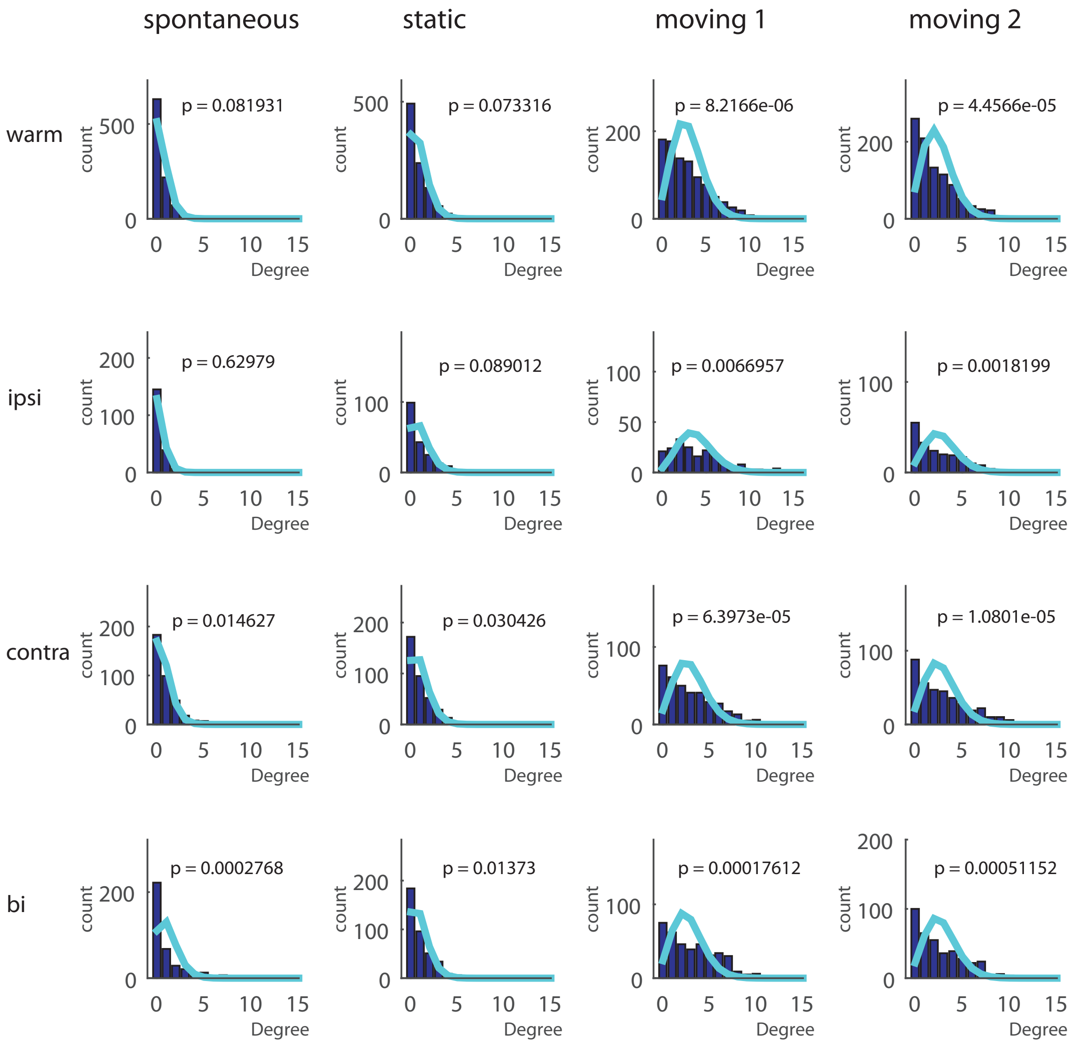

Figure 3.29.: Degree Distributions Low Initial Gamma. Degree distributions for the networks based on NeuroXidence for all deactivation conditions and stimulus phases. Histograms are shown in dark blue, the light blue line depicts the expected degree distribution for random networks of the same size. The p-values are given for the test on Poissonity (see section 2.9).

The results of the test of poissonity differ slightly for the three datasets. For the Low Initial Gamma set, the null-hypothesis of the graphs being random could not be excluded for spontaneous activity and static stimulus, for warm and ipsilateral deactivation (Fig. 3.29). For the Medium Initial Gamma set,

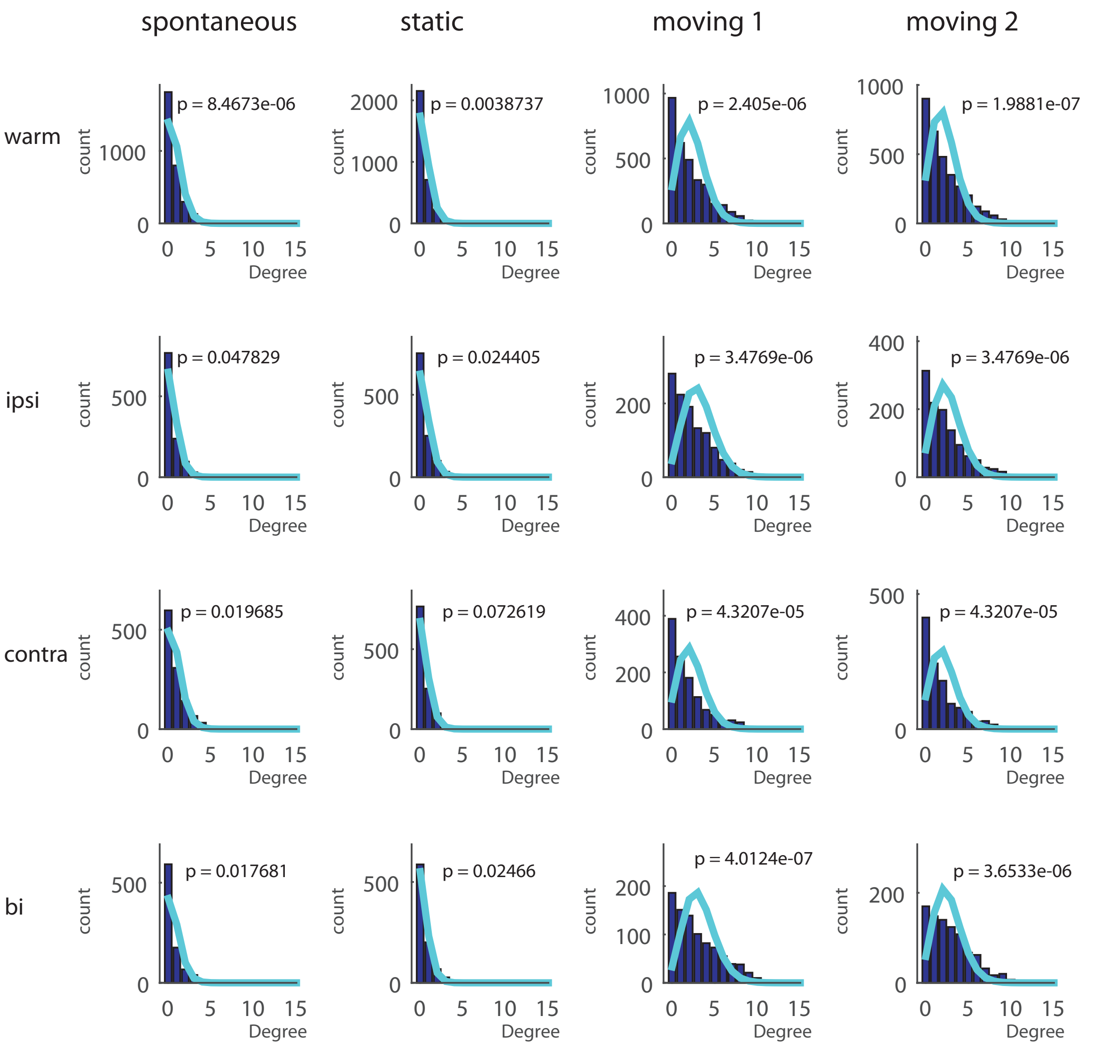

Figure 3.30.: Degree Distributions Medium Initial Gamma. Degree distributions for the networks based on NeuroXidence for all deactivation conditions and stimulus phases. Histograms are shown in dark blue, the light blue line depicts the expected degree distribution for random networks of the same size. The p-values are given for the test on Poissonity (see section 2.9).

the null hypothesis was only kept for static stimulation during contralateral deactivation. For the High Initial Gamma set, the null hypothesis was rejected for all cases except the spontaneous activity and static grating phases during ipsi- and bilateral pMS deactivation, and also for contralateral deactivation during static stimulation (Fig. 3.31).

During moving stimulation, the graphs showed no indication of being random in any of the sets.

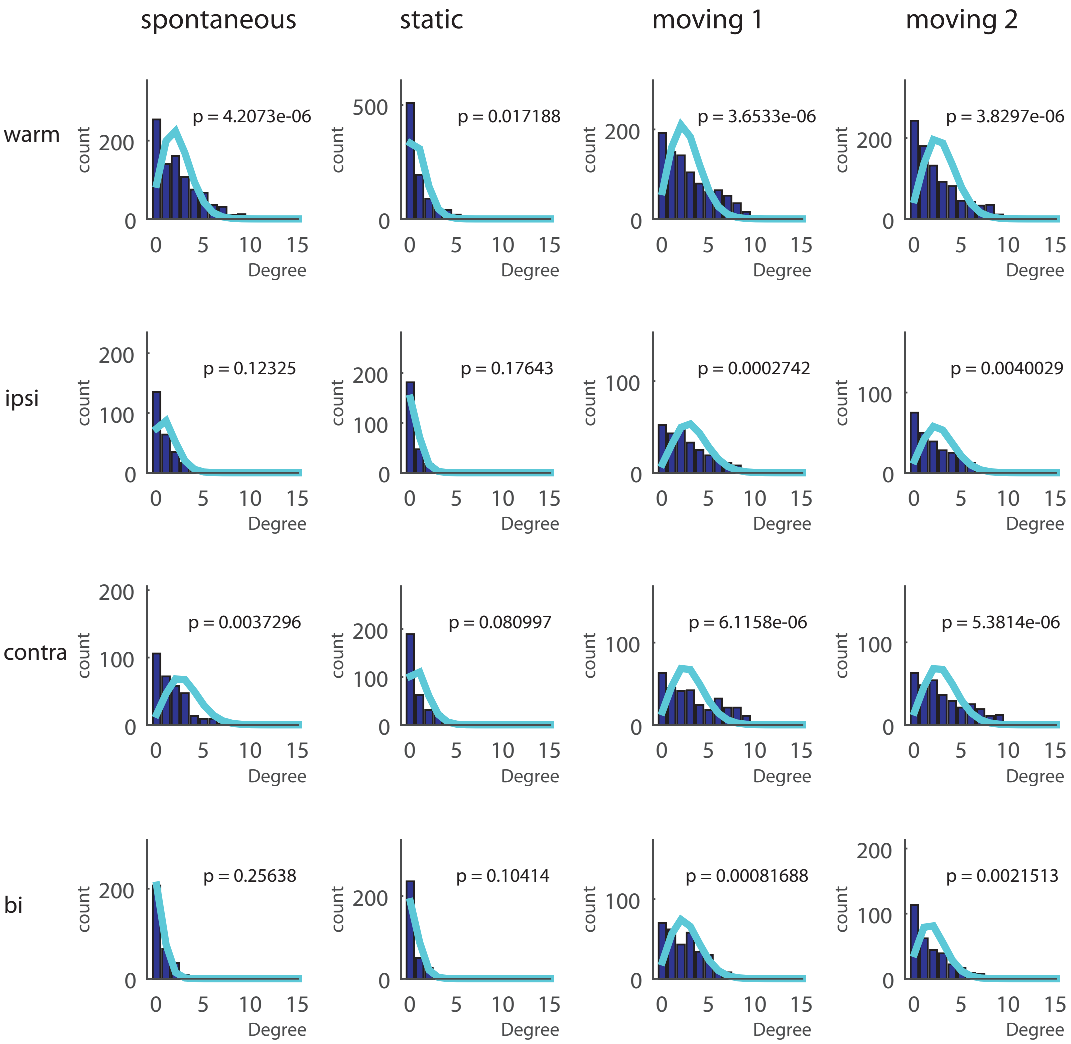

Figure 3.31.: Degree Distributions High Initial Gamma. Degree distributions for the networks based on NeuroXidence for all deactivation conditions and stimulus phases. Histograms are shown in dark blue, the light blue line depicts the expected degree distribution for random networks of the same size. The p-values are given for the test on Poissonity (see section 2.9).

The test on homogeneity, proposed in (**Schmitz**, 2009) and described in section 2.10, was compared with the χ^2 test on homogeneity, and the exact Fisher test.

Both the Exact Fisher Test and the Test on Homogeneity are based on a fourfold contingency table of the following form:

	local (or 'similar tuning')	remote (or 'differing tuning')
connected		
not connected		

Figure 3.32 shows a comparison of the sensitivity of the three tests. The χ^2 test showed to be the most sensitive, followed by the Exact Fisher test. The 'Test on Homogeneity' turned out to be the most conservative test.

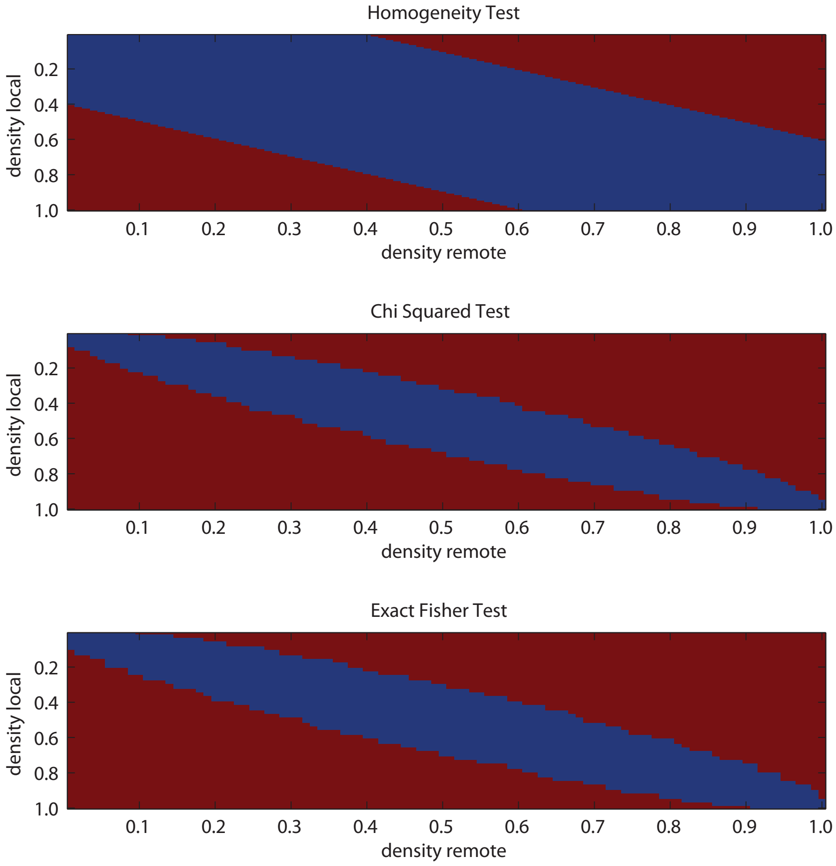

Figure 3.32.: Test comparison. Comparison of the sensitivity of 'Test on Homogeneity', χ^2 test and Exact Fisher test with the assumption of 42 "local" and 78 "remote" edges. Red indicates significant difference of x and y value, blue non-significant differences. Asymmetry is due to the different sample sizes of local and remote edges. Note that the Fisher test is less sensitive than the χ^2 test for medium connection densities in both subsets.

Since the χ^2 test is not applicable when the entries in the fields of the contingency table are not sufficiently large, overall the Fisher test is preferred over the χ^2 test although it is slightly less sensitive.

In the next sections, results of the Exact Fisher Test and the Test on Homogeneity are shown in order to provide two approaches with different levels of sensitivity. This way, a dependance of the results on the significance level can be disclosed and potentially different aspects of the deactivation effects can be shown.

3.7 Results Based on NeuroXidence

The network generation based on NeuroXidence (NX) resulted in a total of 5056 graphs:

experiment	number of graphs
101007	2048
121007	2112
112807	896

3.7.1 Homogeneity of edge probabilities

The homogeneity of edge probabilities was assessed applying both the Test on Homogeneity (see section 2.10) and the Exact Fisher Test. With this, the spatial and functional organisation of the network connectivity can be analyzed. To this end, the set of links in the graphs was separated in three ways: first, between local vs. remote edges (following the neighbourhood criterion given in equation 3.1), second, between links connecting units with similar orientation preferences and those with different orientation preferences, and third, between links amongst units with the same preferred direction as compared to different direction preferences. Results are shown in Figures 3.33-3.35.

For experiments in the Low Initial Gamma group, activity is distance-dependent mainly for the warm condition, and again for bilateral pMS deactivation, but only during stimulation with a moving grating. Overall, orientation preference seems to be the dominant factor. Only for the orientation preference did the Test on Homogeneity detect any significant differences at all. This is interesting, since orientation preference can be explained by purely feedforward-based models.

For experiments in the Medium Initial Gamma group, physical distance between the nodes units becomes more relevant.

For experiments in the High Initial Gamma group, distance is very relevant; for the warm condition, local connections are dominant in all tested networks. For spontaneous activity, the percentage of graphs with local dominance decreases, but when the stimulation gets stronger, again, almost all graphs show a local dominance, even for the deactivation conditions. Stimulus orientation is relevant especially for the warm condition. However, this is not picked up by the Test on Homogeneity, indicating that the dominance is not particularly strong. However, in contrast to the Low and Medium Initial Gamma, now direction preference also comes into play. Units with the same direction preference are preferably connected during the warm condition, but are highly affected by pMS deactivation: for ipsi- and bilateral deactivation, the number of graphs with a dominance of connections between units with a similar direction prefence is much lower; none of them is picked up by the Test on Homogeneity.

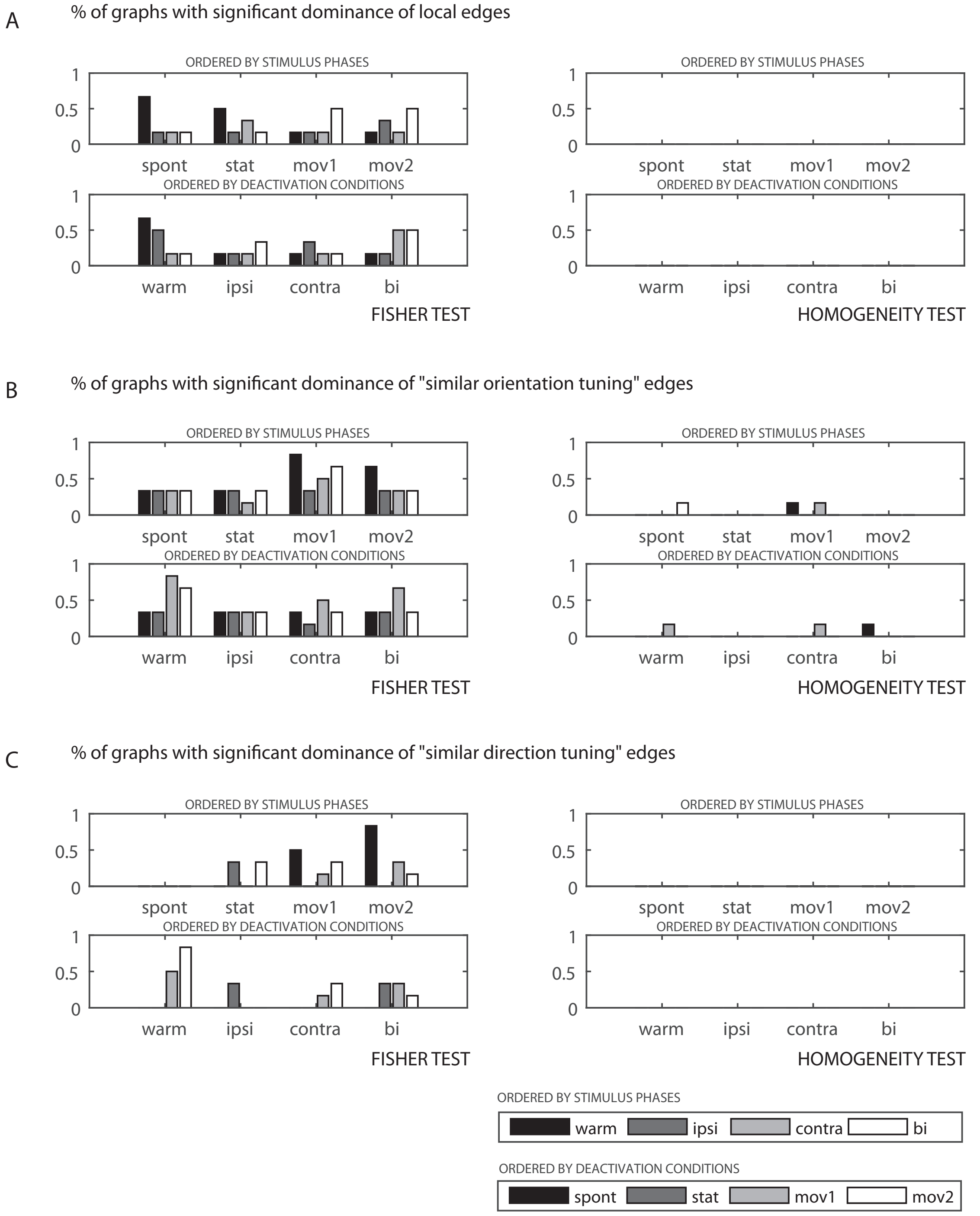

Figure 3.33.: Results of the Homog and Fisher tests, NeuroXidence, Low Initial Gamma. The figure shows the percentage of graphs for which a dominance of (A) edges for local connections, (B) edges between units with similar orientation preference and (C) edges between units with similar direction preference. (A) Distance shows to be most relevant during spontaneous activity and static stimulation for the warm condition. In addition, it becomes of importance for strong moving stimulation during bilateral deactivation. (B) Similar orienation tuning shows to be most relevant for moving stimulation during the warm condition. (C) Similar direction tuning becomes most dominant for the warm condition during moving stimulation. In total, orientation tuning was found to be the most relevant predictor for connectivity in the Low Initial Gamma group. There were no occurrences of the "remote" or different orientation/direction groups being dominant over the local, same orientation or same direction preference groups, respectively. (Analysis based on 6 sessions / 96 graphs)

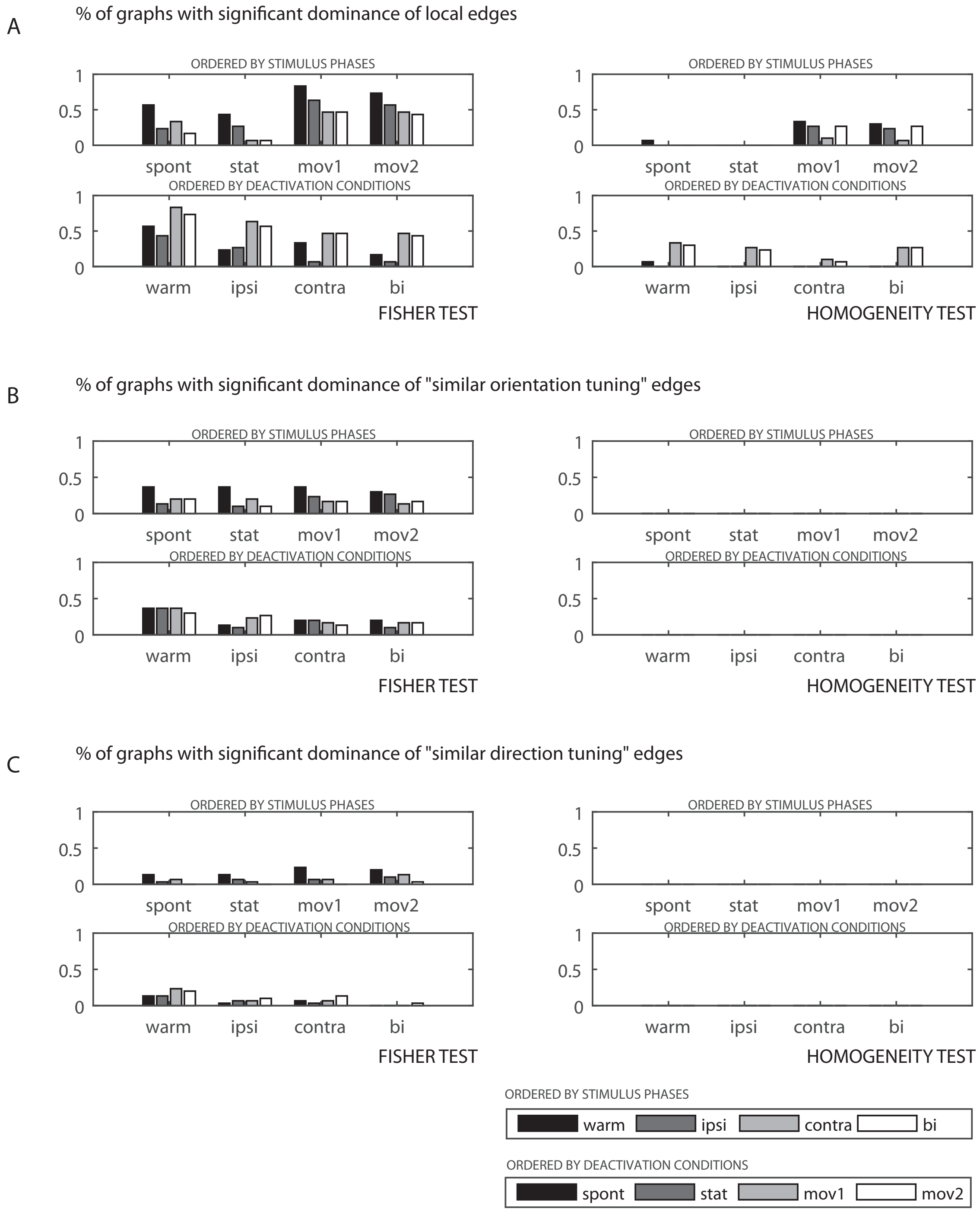

Figure 3.34.: Results of the Homog and Fisher tests, NeuroXidence, Medium Initial Gamma. The figure shows the percentage of graphs for which a dominance of (A) edges for local connections, (B) edges between units with similar orientation preference and (C) edges between units with similar direction preference. (A) Dominance of local connections as opposed to remote connections can be observed for all stimulus and deactivation conditions, but is highest for the warm condition and during moving stimulation. (B) Similar orientation tuning shows to be a weaker predictor for connectivity as compared to distance. The influence is highest for the "warm" condition. (C) Similar direction tuning shows to have the lowest influence on connectivity as compared to distance and orientation tuning. It is highest for the warm phase, specifically during moving stimulation. In total, distance was found to be the most relevant predictor for connectivity in the Medium Initial Gamma group. (Analysis based on 30 sessions / 480 graphs)

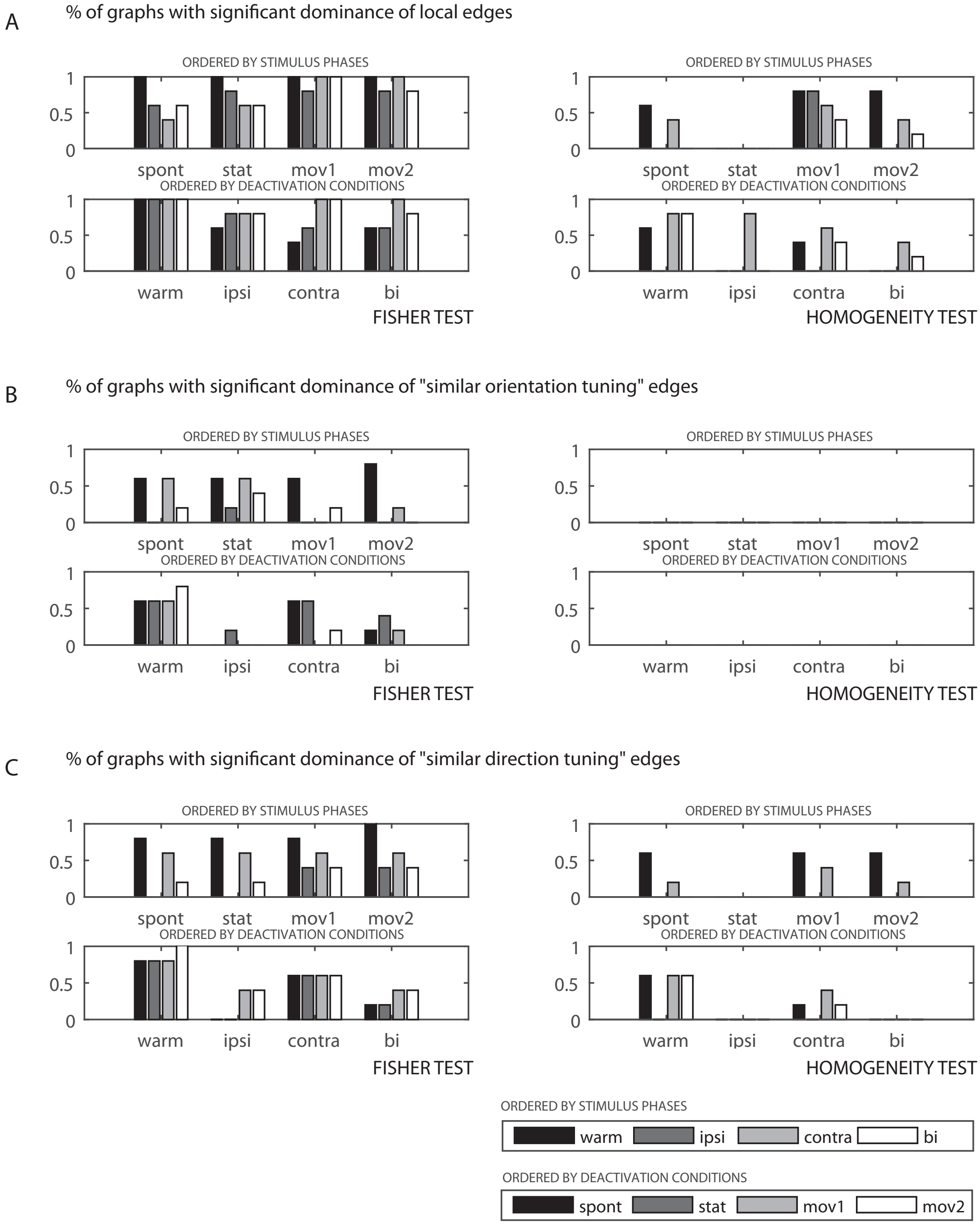

Figure 3.35.: Results of the Homog and Fisher tests, NeuroXidence, High Initial Gamma. The figure shows the percentage of graphs for which a dominance of (A) edges for local connections, (B) edges between units with similar orientation preference and (C) edges between units with similar direction preference. (A) Local connections were dominant in almost all networks, in particular for the warm condition, where, when tested using the Fisher test, all networks turned out express a dominance of local edges. The Test on Homogeneity also detected the dominance of local edges. Interestingly, this dominance was least prominent for the static grating phase. (B) Similar orientation tuning was less influential. Most significant dominances were observed for the warm condition and contralateral deactivation, at least during spontaneous activity and static stimulation. (C) Similar direction tuning showed to be a predictor for connectivity, especially for the warm phase and during contralateral deactivation. In total, distance and direction tuning were found to be the most relevant predictor for connectivity in the High Initial Gamma group. (Analysis based on 5 sessions / 80 graphs)

3.7.2 Similarity of graphs

All subsets of graphs were subjected to the assessment of similarity using the Hamming distance test as described in section 2.11. The results are shown in Fig. 3.36.

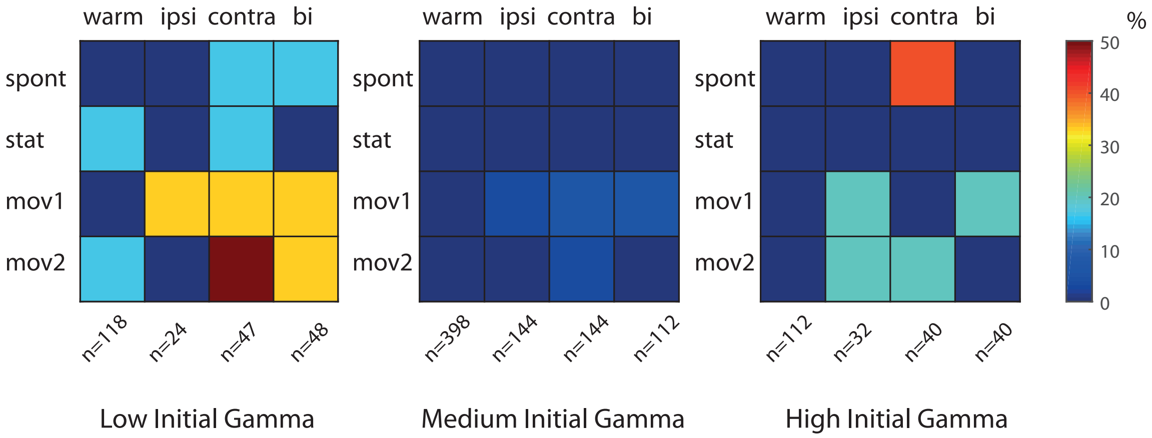

Figure 3.36.: Hamming distance (NeuroXidence). The figure shows a metaanalysis of the Hamming distance results. Depicted is the percentage of cases with a significantly low Hamming distance between graphs for the same conditions, i.e. strong similarities among these networks, following the analysis with the test on the similarity of graphs using the Hamming distance as described in section 2.11. The observed percentages are colour-coded (see colourbar on the right).

Notably, the networks turned out to be most similar for the Low and High Initial Gamma groups, but considerably less for the Medium Initial Gamma group. Within the Low and High Initial Gamma groups, the similarity is strongest during presentation of the moving grating, but not exclusively, as can be seen for example for contralateral deactivation during spontaneous activity for the High Initial Gamma group.

Density

For the warm condition, density showed a gradual increase from spontaneous activity, over stimulation with a static grating, to stimulation with a moving grating (see Fig. 3.37). During phases of spontaneous activity, density was highest for the High Initial Gamma group, and for this condition actually almost reached a similar level to the density during the presentation of a moving stimulus. For the High Initial Gamma group, during ipsi- and bilateral deactivation, density was found to be lower than for the warm condition and during contralateral deactivation. This trend was also observed for other conditions, e.g. spontaneous activity for the Medium Initial Gamma group. However, it was not consistent and for other conditions, such as the "mov1" window for the Medium Initial Gamma group, an opposite effect was observed.

Clustering Coefficient

The clustering coefficient was determined per graph, i.e. the clustering coefficient was computed per node and then averaged for each graph, and the resulting values were compared between the different experimental conditions. Fig. 3.38 shows the results of this analysis. The clustering coefficient turned out to be lowest during spontaneous activity, taking a value of 0 in many cases, which could be in parts due to overall low edge densities and consequently small connected components in the graphs. This is especially visible for ipsilateral deactivation in the Low Intial Gamma group. For the High Initial Gamma group, a similar pattern to the density effects could be observed for spontaneous activity and the static grating phase. However, this effect disappears for the moving grating. Overall, the effects were quite varied over all Gamma groups and stimulus phases and no clear trend could be extracted.

Characteristic Path Length

Results for the characteristic path length for the graphs obtained with the NX method are depicted in Fig. 3.39. In general, the characteristic path length turned out to lie below 3. Overall, again the effects showed a high variation. The highest median values were observed for the phase of the moving stimulus, while for the High Initial Gamma group, similar levels were actually obtained during spontaneous activity for the warm condition and during contralateral deactivation. During spontaneous activity, a significant decrease of the characteristic path length was observed during ipsi- and bilateral deactivation. This trend was also observed for the phase of the static stimulus and the later phase of the moving stimulus, as well as for the Medium Initial Gamma group during spontaneous activity, although not significant for all comparisons. With this, it should be noted that there is a dependency between the maximum possible characteristic path length and the overall level of connectivity (as measured by the density).

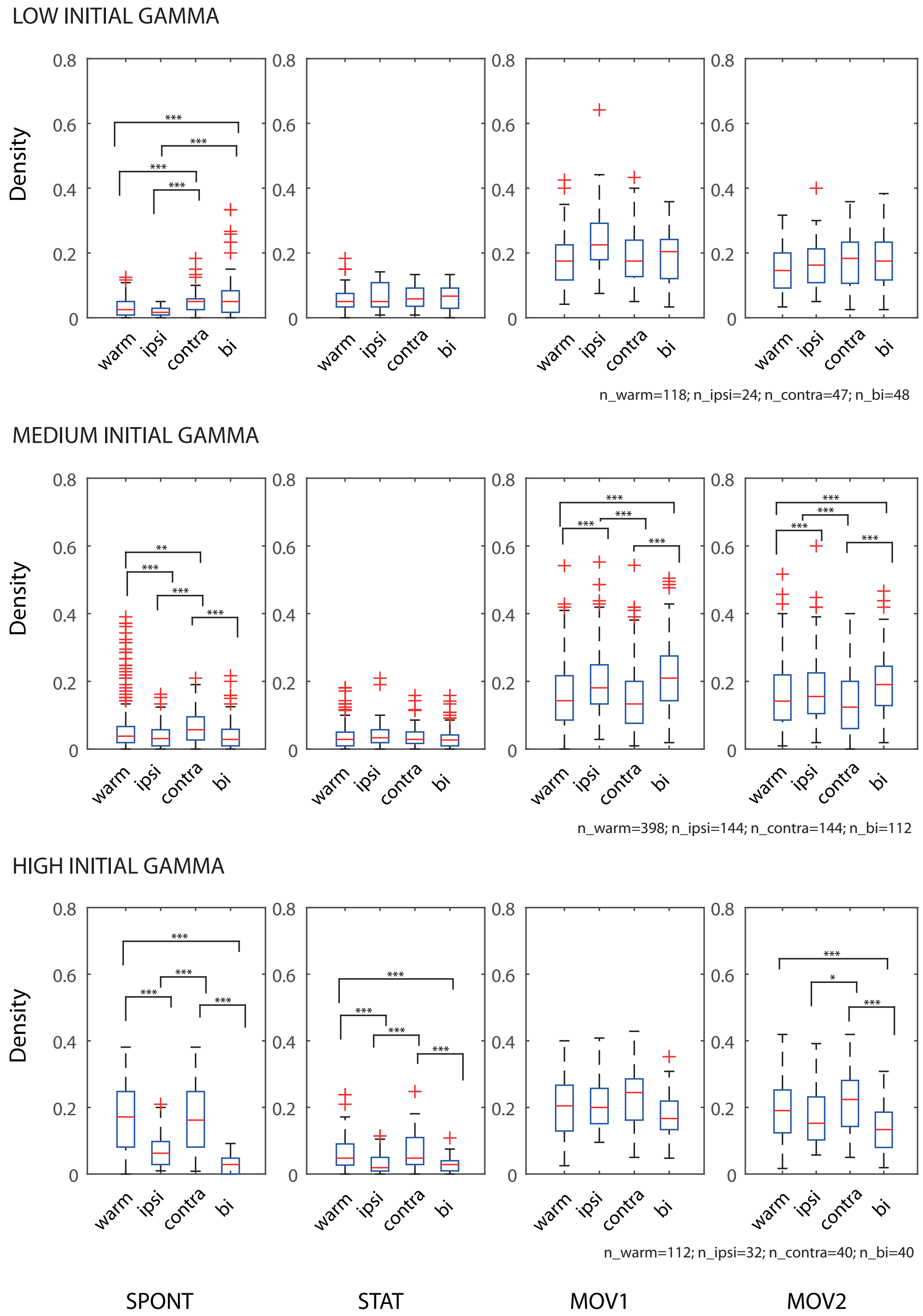

Figure 3.37.: Graph Densities, NeuroXidence II. The figure shows the graph densities for graphs based on the NeuroXidence analysis, for each deactivation condition. In general, it can be observed that the stronger the stimulus, the higher the density, independent of the deactivation condition. Especially for the warm condition during the phase of spontaneous activity it can be observed that the density is highest for the High Initial Gamma group. Interestingly, for the first phase of the moving stimulus for bilateral deactivation, there is no significant difference in the density between the three Gamma groups. (Kruskal Wallis test, ***: $p<0.01$, **: $0.01<p<0.05$, *: $0.05<p<0.1$; Boxplots show the median (red line), 25th/75th percentile (outer lines of boxes), most extreme data points not considered outliers (whiskers), and the outliers (+).)

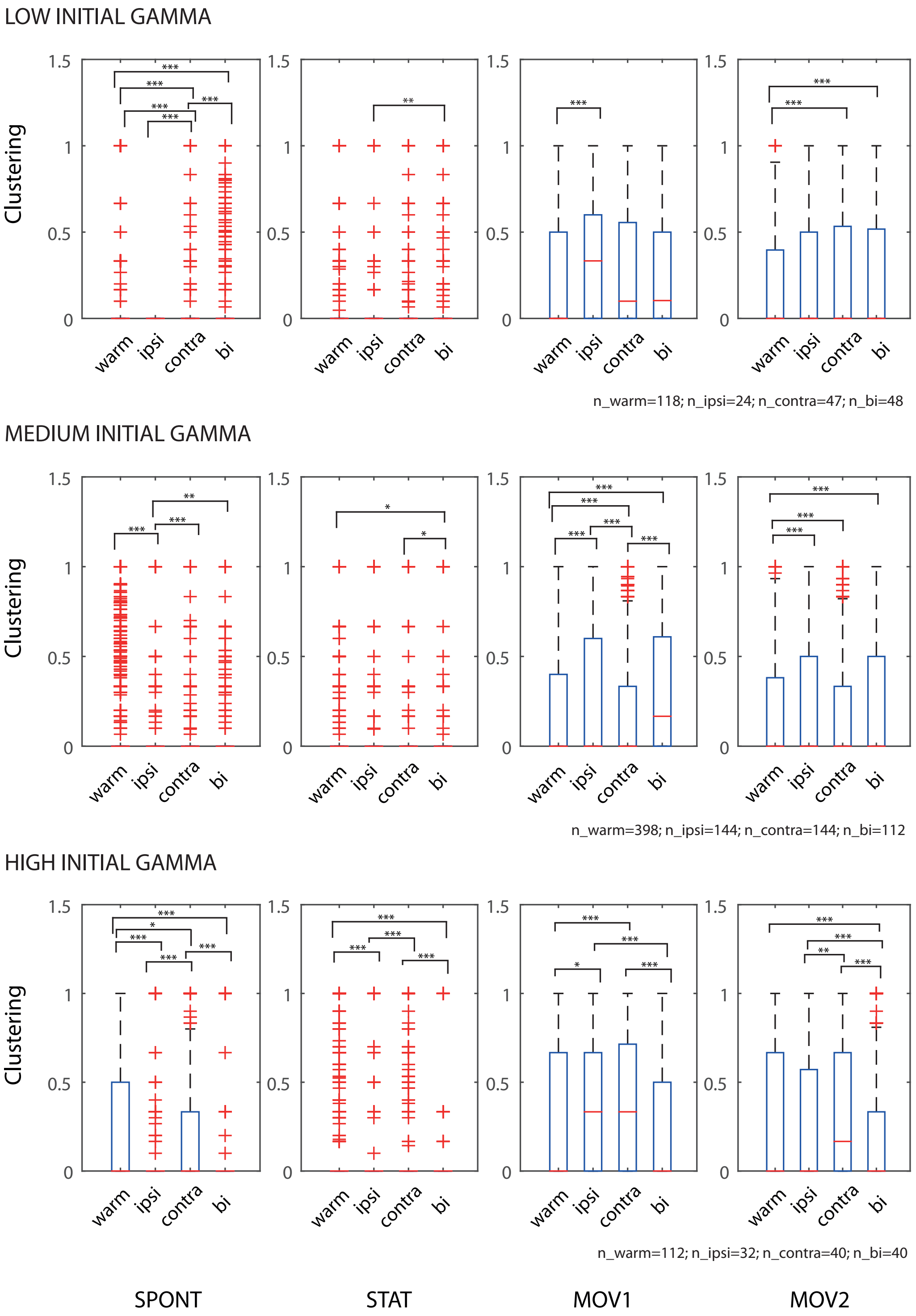

Figure 3.38.: Clustering Coefficient, NeuroXidence. The figure shows the clustering coefficients for the graphs based on the NeuroXidence analysis for all deactivation conditions. In general, it can be observed that clustering gets higher with stronger stimulation. The highest clustering coefficients can be observed for the Low Initial Gamma group for ipsi- and bilateral deactivation, and for ipsi- and contralateral deactivation for the High Initial Gamma group. Note that for the graphs based on spontaneous activity and static grating, the majority of values for the clustering coefficient is close to zero, this is ahy only the outliers are visible. (Kruskal Wallis test, ***: $p<0.01$, **: $0.01<p<0.05$, *: $0.05<p<0.1$; Boxplots show the median (red line), 25th/75th percentile (outer lines of boxes), most extreme data points not considered outliers (whiskers), and the outliers (+).)

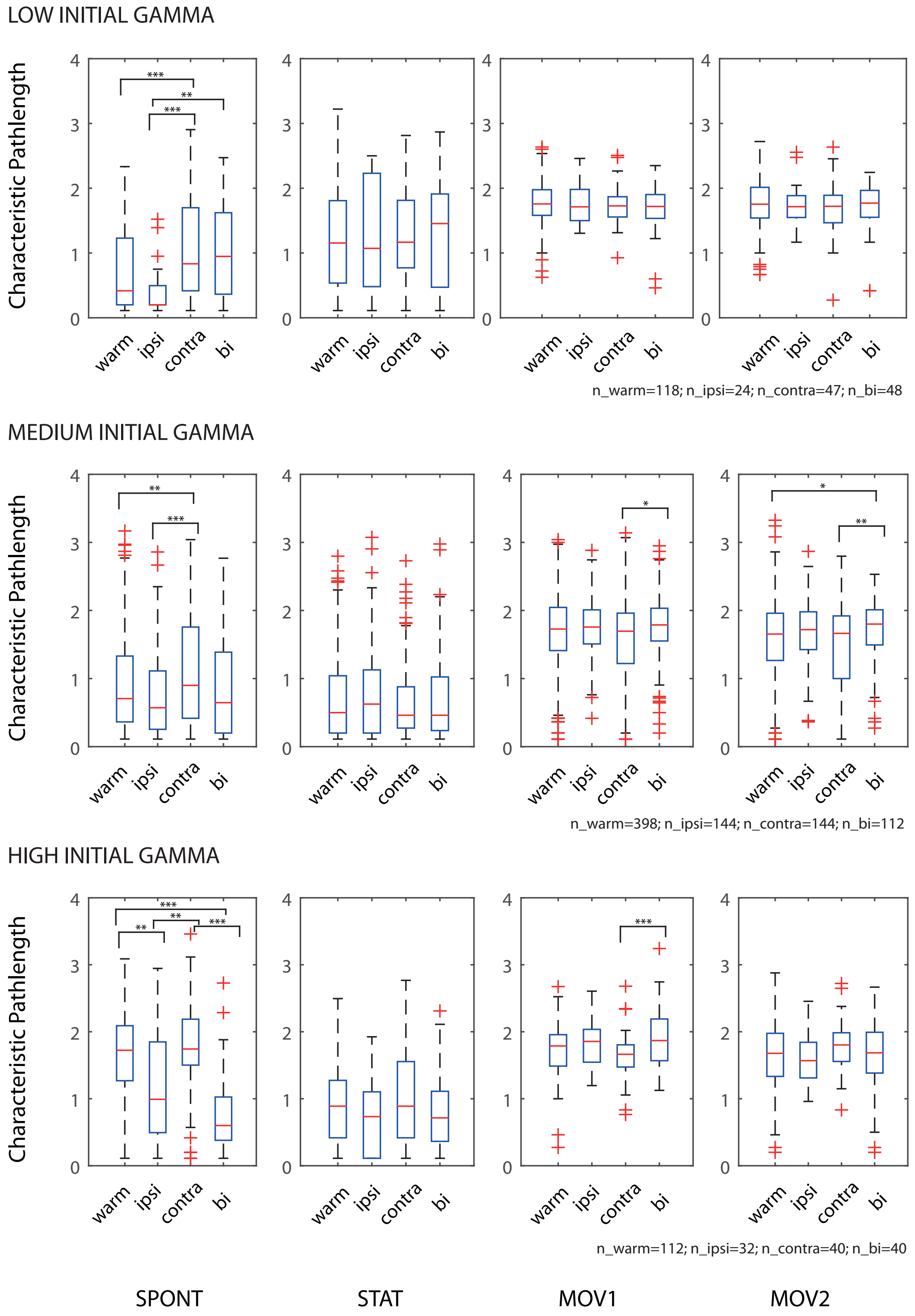

Figure 3.39.: Characteristic Path Length, NeuroXidence. The figure shows the characteristic path lengths for the graphs based on the NeuroXidence analysis for all deactivation conditions. It can be observed that the characteristic path length gets higher with stronger stimulation and is highest for Low Initial Gamma, ipsi- and bilateral, and also for ipsilateral deactivation for High Initial Gamma. (Kruskal Wallis test, ***: $p<0.01$, **: $0.01<p<0.05$, *: $0.05<p<0.1$; Boxplots show the median (red line), 25th/75th percentile (outer lines of boxes), most extreme data points not considered outliers (whiskers), and the outliers (+).)

The log-likelihood was calculated for models with a variety of parameter settings. The log-likelihoods closest to zero were determined and thus, suitable model parameters were found. After careful consideration of various combinations of parameters, the model parameters were set to the values given in Table 3.9.

Table 3.9.: Model parameters for GLM

Parameter	tested values	optimal value
Percentage of training data	50%, 70%	70%
Auto-history	30 ms, 70 ms	70 ms
Cross-history	5 ms, 10 ms	5 ms
History knot number	3	3
Knot rate	0, 5, 10, 15, 20	15

The analysis was applied to the sorted spike data of eight complete sessions of each of the experiments 101007 and 121007. The result were directed networks, which were then further examined using graph theory methods as described in sections 2.8-2.13.

3.8.1 Similarity of graphs

Fig. 3.40 shows the results of the analysis of the Hamming distance between the GLM graphs as described in section 2.11. Results were obtained for all links and then separately for links connecting nodes with a similar orientation or direction preference, respectively. For the Low Initial Gamma group, graphs showed high similarities for various experimental conditions. For the Medium Initial Gamma group, the overall similarities were lower, but spanned over all conditions. For the High Initial Gamma group, graph similarities turned out to be highest during spontaneous activity (and static gratings for the warm condition); for the moving grating, no significantly similar graphs were detected.

3.8.2 Graph measures GLM

Density, clustering coefficient and characteristic path length were also calculated and analyzed for the graphs based on the GLM approach.

Density

Densities for the graphs based on GLM turned out to lie on a similar level of around 0.4-0.6 for the three Gamma Groups (see Figs. 3.41-3.42). However, a tendency towards the density dropping for ipsi- and bilateral deactivation could be observed. This trend was apparent for all stimulus phases for the High Initial Gamma group, but also partly showed for the Low and Medium Initial Gamma groups (see e.g. Low Initial Gamma, spontaneous activity, and Medium Initial Gamma, static stimulus), though it was not as consistent. The meta analysis that was performed on the single graphs shows these effects for the High Initial Gamma group even more clearly (Fig. 3.43).

Clustering Coefficient

The clustering coefficient for the GLM graphs showed similar tendencies as the density, i.e. a decrease of

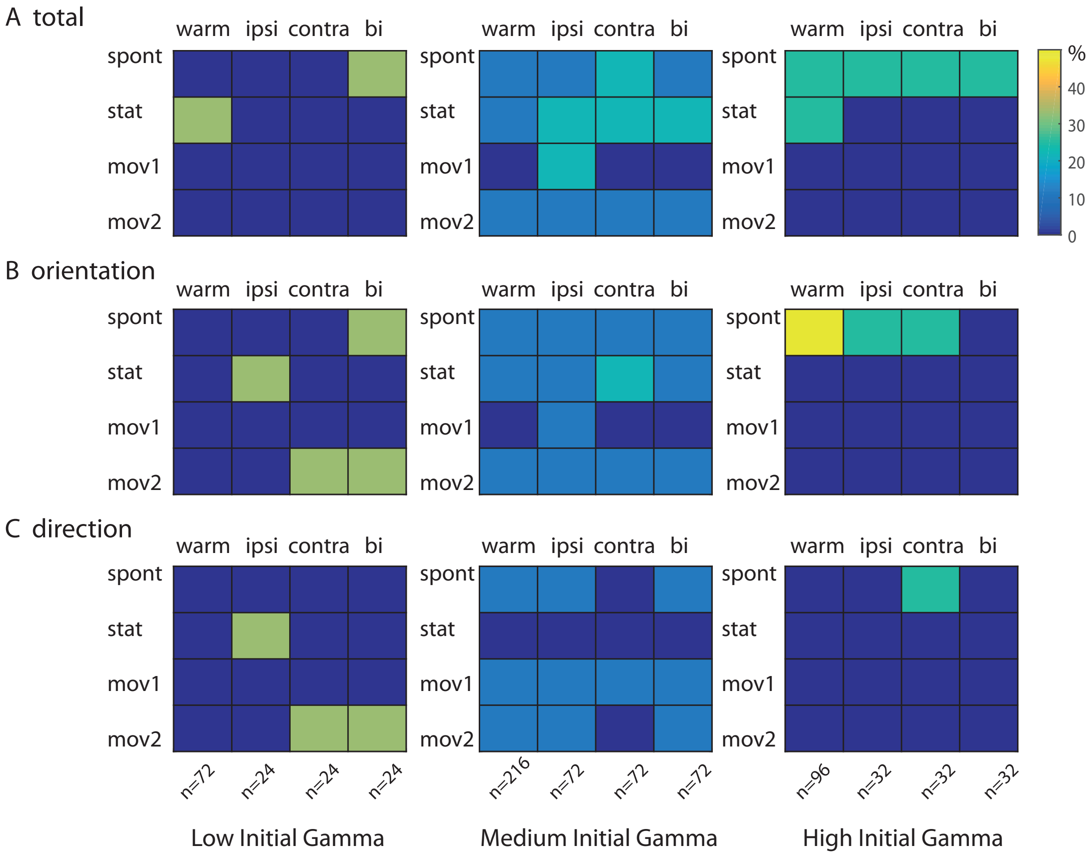

Figure 3.40.: Hamming distance (GLM). The figure shows the percentage of cases with a significantly low Hamming distance between graphs for the same conditions, i.e. strong similarities among these networks. (A) shows the results for the whole graphs, (B) shows the results for the subset of edges with similar orientation tuning and (C) shows the results for the subset of edges with similar direction tuning. Over all conditions, the graphs of the Medium Initial Gamma group show the most similarities, spanning all experimental conditions. However, the highest similarities were observed for single conditions in the Low Initial Gamma and High Initial Gamma groups; for the High Initial Gamma group mainly during phases of spontaneous activity (see right pane), while for the Low Initial Gamma group, highest similarity was observed for various experimental conditions (see left pane).

clustering was observed for ipsi- and especially bilateral deactivation for the High Initial Gamma group and in parts for the Low and Medium Initial Gamma groups, though not as pronounced (Figs. 3.44-3.45).

Characteristic Path Length

Characteristic path length for the GLM graphs showed an opposite trend as compared to density and clustering, i.e. an increase for ipsi- and bilateral deactivation (Figs. 3.46-3.47). This is in contrast to the NeuroXidence results on characteristic path length. Possible implications are discussed in section 4.1.5.

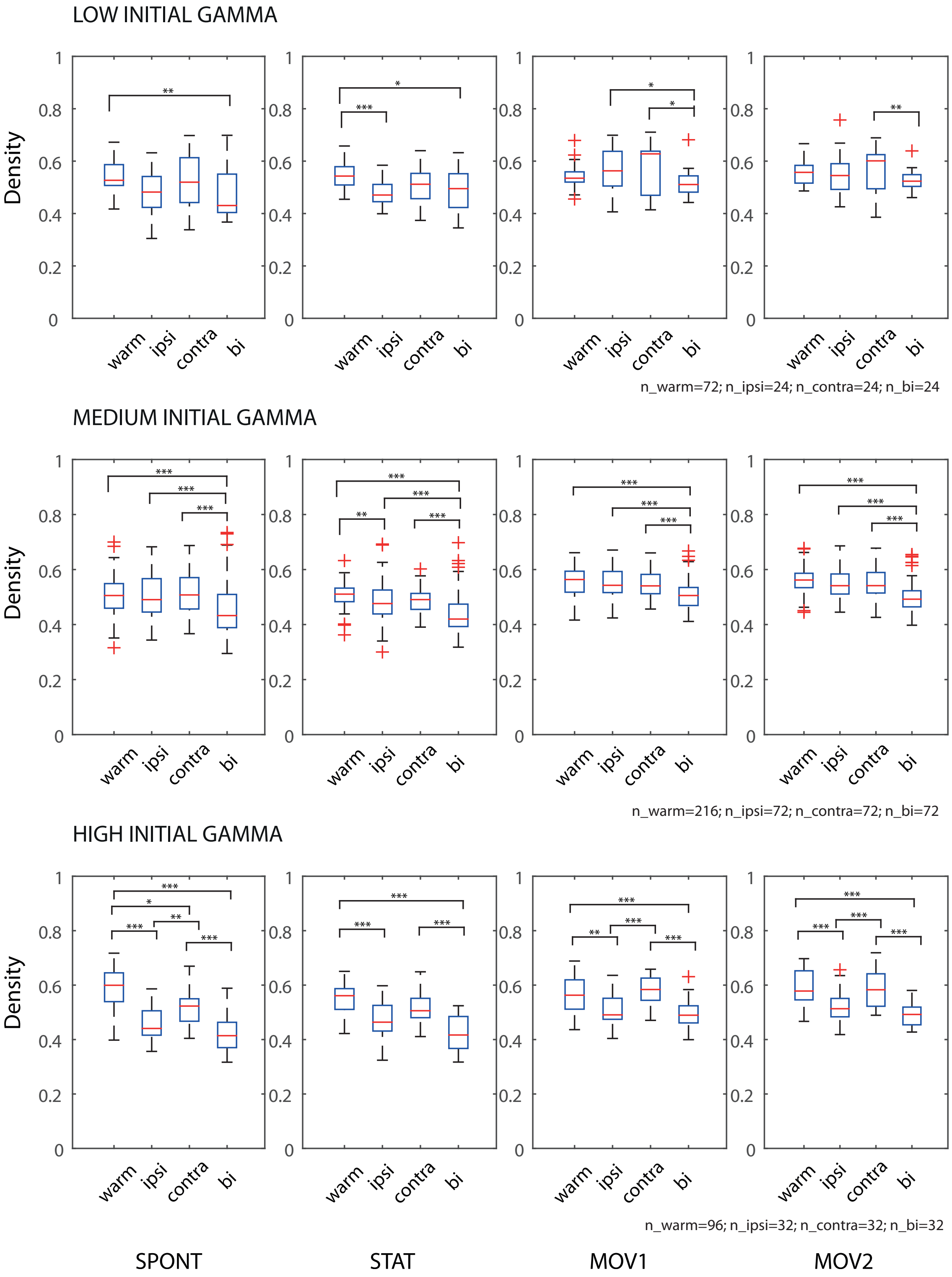

Figure 3.41.: Density, GLM, 5 ms cross-history. Densities were calculated for all GLM graphs and averaged for each experimental condition and Gamma Group. Densities turned out to lie around a similar percentage for all conditions; still, significant differences between conditions could be observed. Moving stimulation increased the graph density for all experimental conditions as compared to spontaneous activity and static stimulation. (Kruskal Wallis test, ***: $p<0.01$, **: $0.01<p<0.05$, *: $0.05<p<0.1$; Boxplots show the median (red line), 25th/75th percentile (outer lines of boxes), most extreme data points not considered outliers (whiskers), and the outliers (+).)

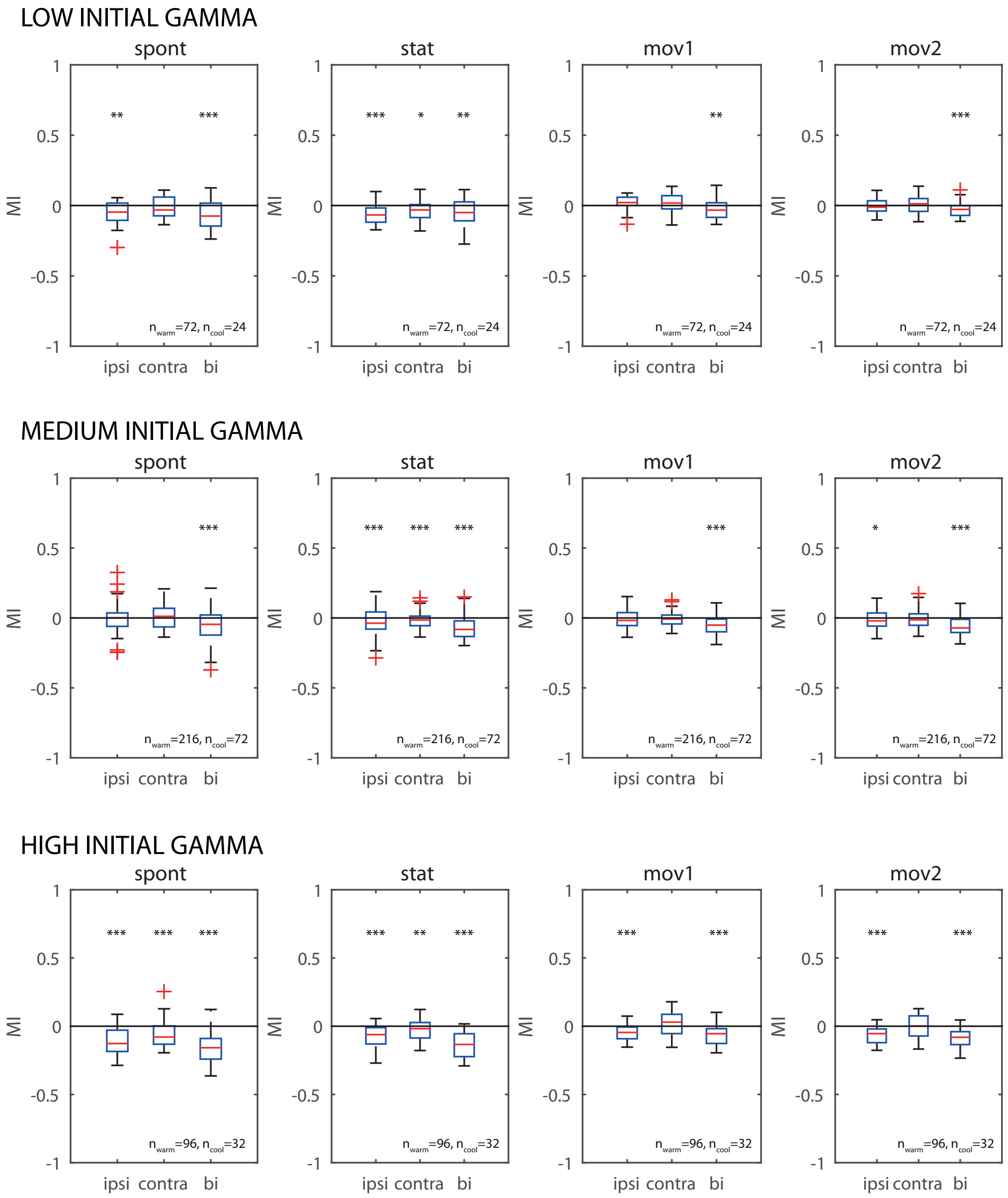

Figure 3.42.: Density, GLM, 5 ms cross-history. Modulation Index of Densities for the GLM graphs, i.e. comparison of the density for each deactivation condition to the density during the warm condition. (Kruskal Wallis test, ***: $p<0.01$, **: $0.01<p<0.05$, *: $0.05<p<0.1$; Boxplots show the median (red line), 25th/75th percentile (outer lines of boxes), most extreme data points not considered outliers (whiskers), and the outliers (+).)

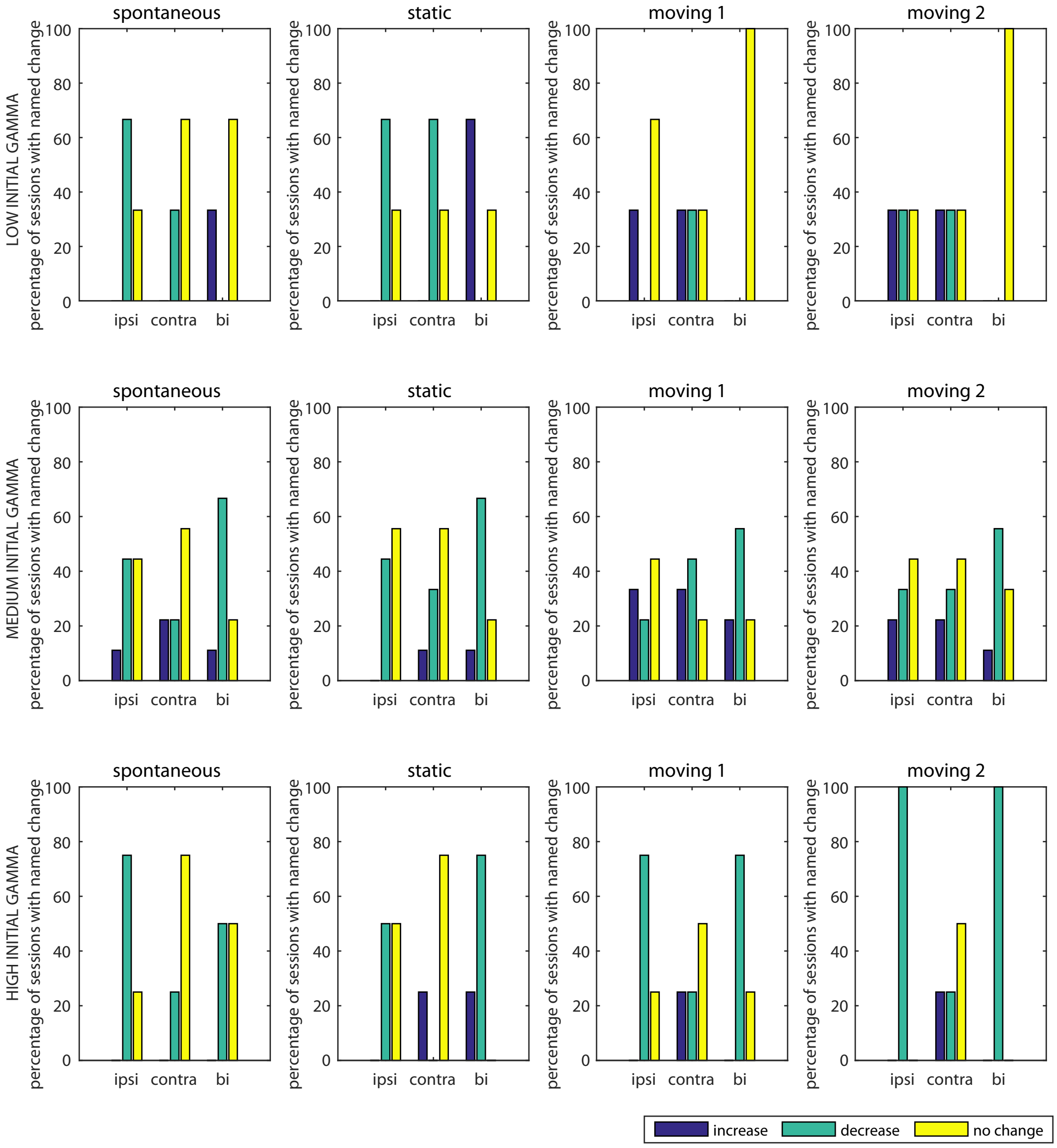

Figure 3.43.: Changes GLM Density. The figure shows a meta analysis of the changes in graph density based on the 16 sessions that were included in the analysis for the networks based on GLM, separated by Gamma groups. The percentages of sessions that showed an increase, decrease, or no significant change, were captured. Note that results were most consistent in the High Initial Gamma group. (Low Initial Gamma: n=3; Medium Initial Gamma: n=9; High Initial Gamma: n=4)

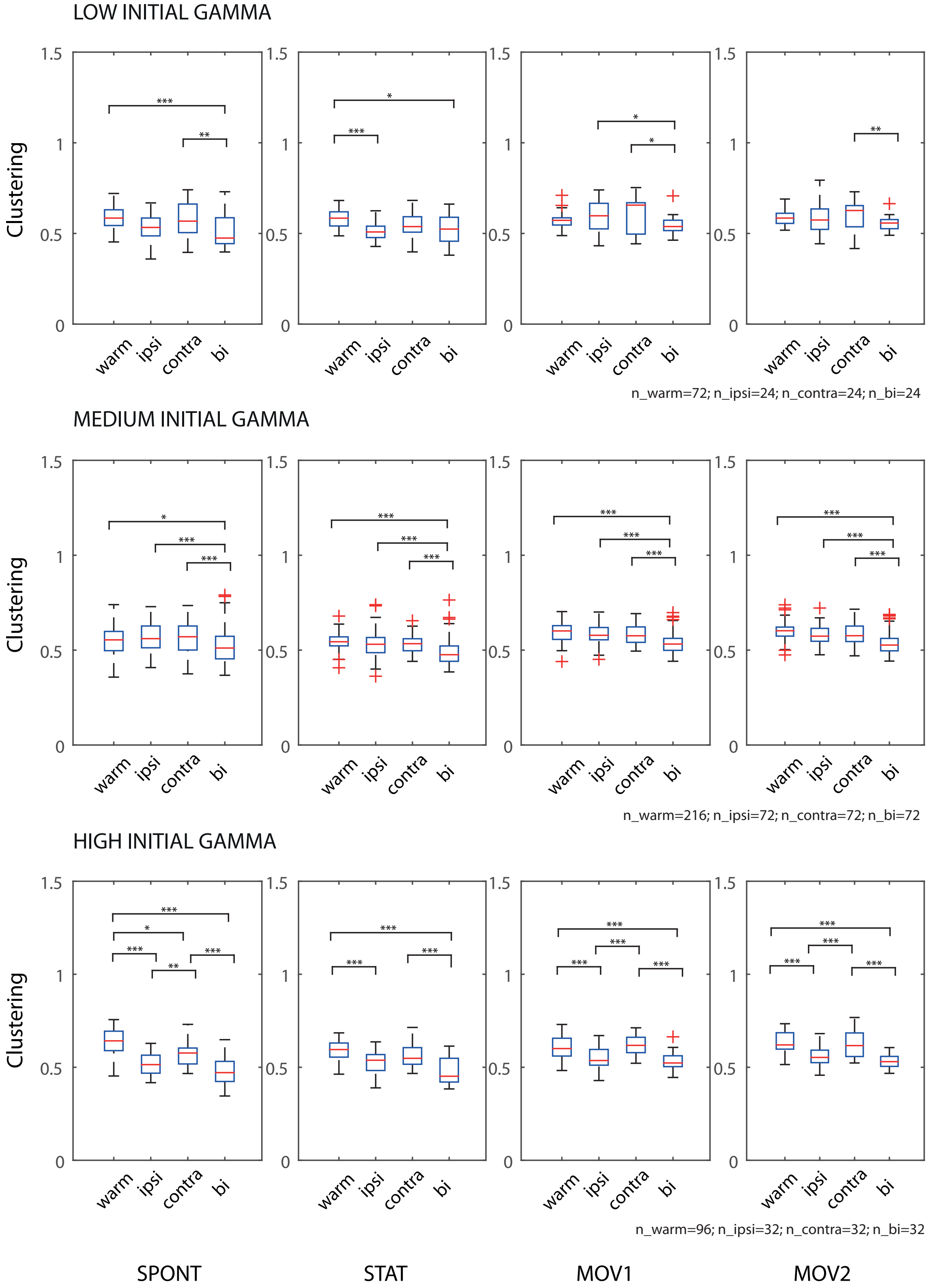

Figure 3.44.: Clustering Coefficient, GLM, 5 ms cross-history. Clustering coefficients were calculated for all GLM graphs and averaged for each experimental condition and Gamma Group. The clustering coefficient tended to increase with stronger stimulation. (Kruskal Wallis test, ***: $p<0.01$, **: $0.01<p<0.05$, *: $0.05<p<0.1$; Boxplots show the median (red line), 25th/75th percentile (outer lines of boxes), most extreme data points not considered outliers (whiskers), and the outliers (+).)

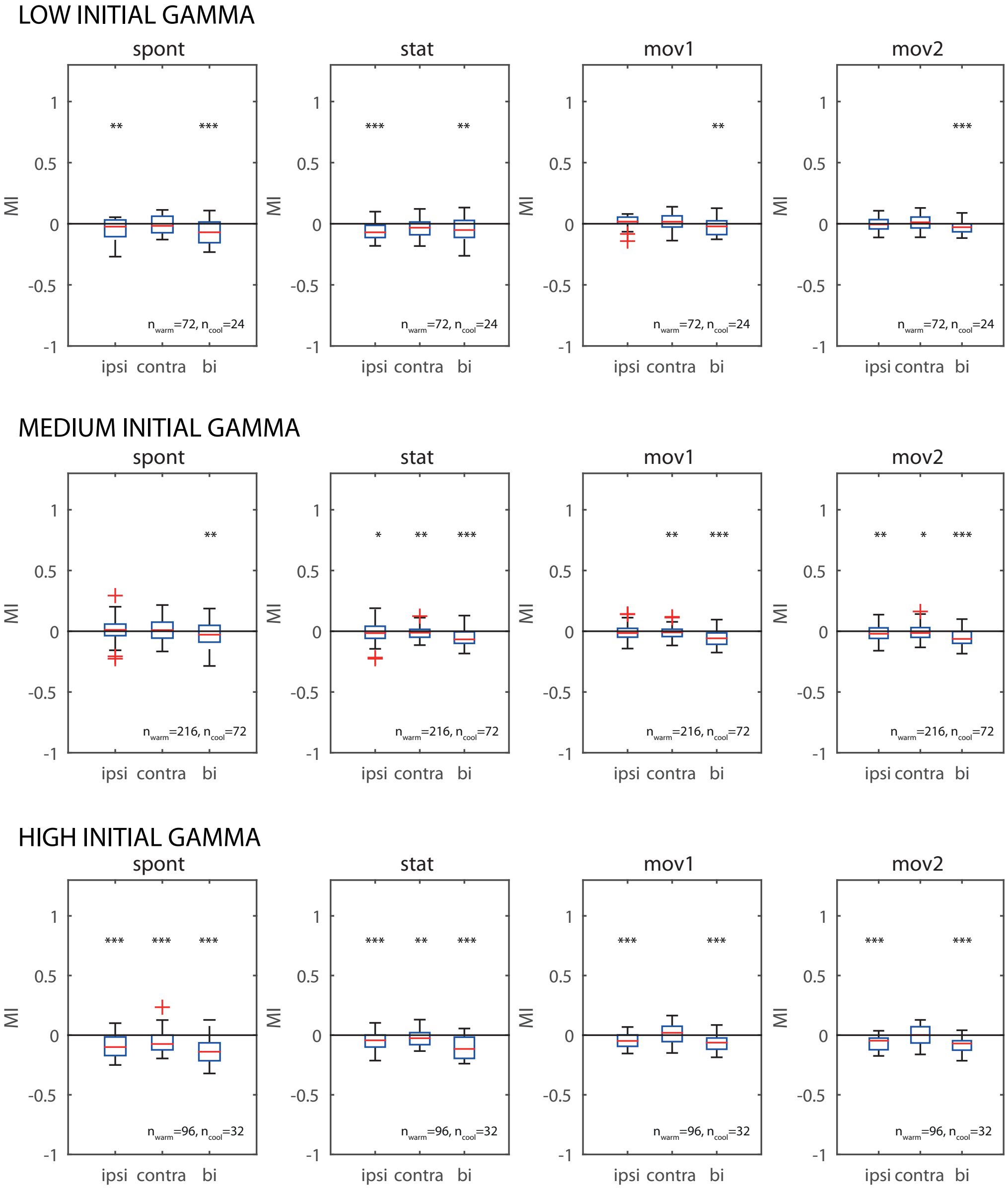

Figure 3.45.: Clustering Coefficient, GLM, 5 ms cross-history. Modulation Index of the clustering coefficient for the GLM graphs, i.e. comparison of the clustering coefficient for each deactivation condition to the clustering coefficient during the warm condition. (Kruskal Wallis test, ***: $p<0.01$, **: $0.01<p<0.05$, *: $0.05<p<0.1$; Boxplots show the median (red line), 25th/75th percentile (outer lines of boxes), most extreme data points not considered outliers (whiskers), and the outliers (+).)

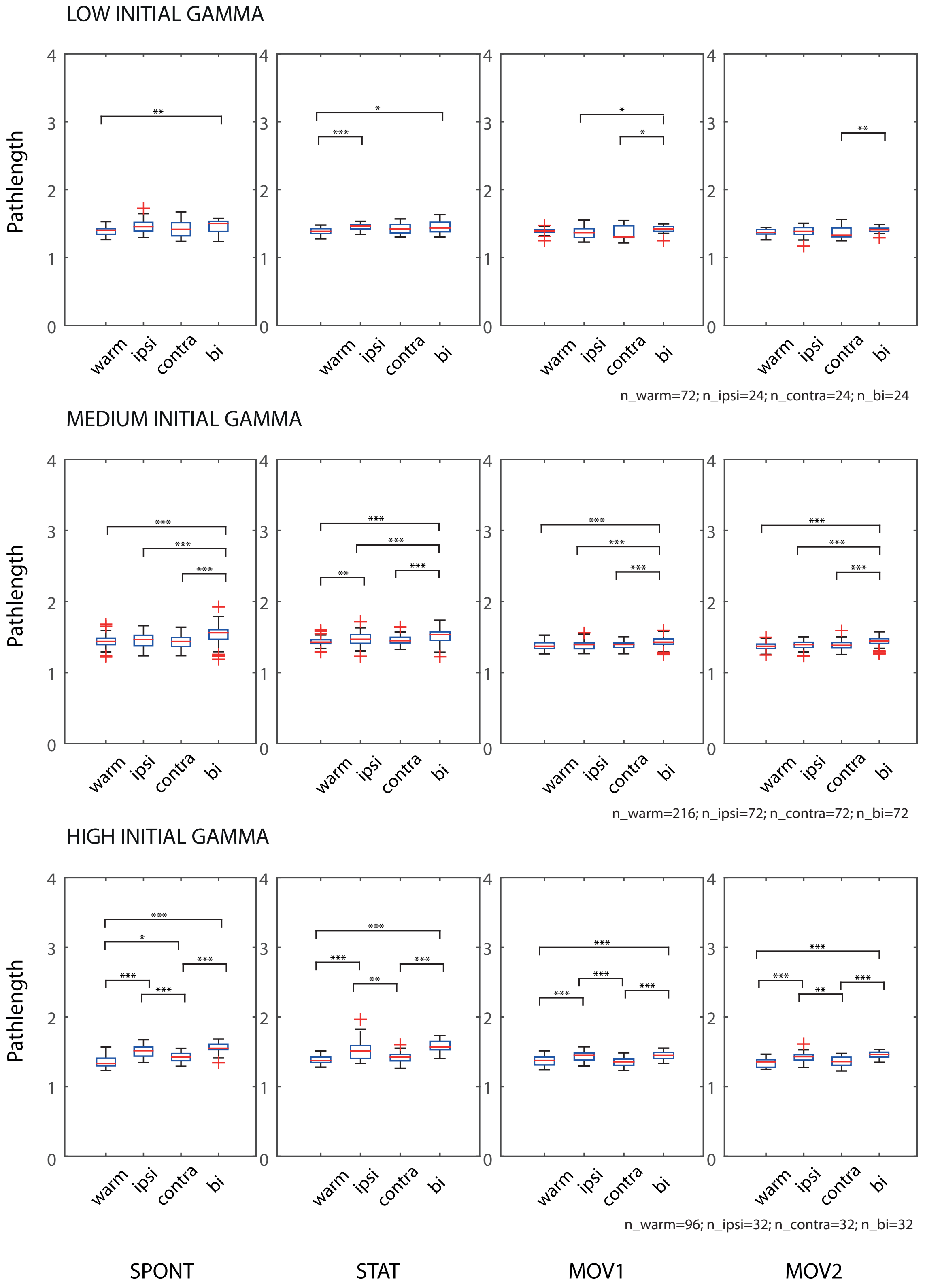

Figure 3.46.: Characteristic Path Length, GLM, 5 ms cross-history. Characteristic path lengths were calculated for all GLM graphs and averaged for each experimental condition and Gamma Group. The characteristic path length tended to decrease with stronger stimulation. (Kruskal Wallis test, ***: $p<0.01$, **: $0.01<p<0.05$, *: $0.05<p<0.1$; Boxplots show the median (red line), 25th/75th percentile (outer lines of boxes), most extreme data points not considered outliers (whiskers), and the outliers (+).)

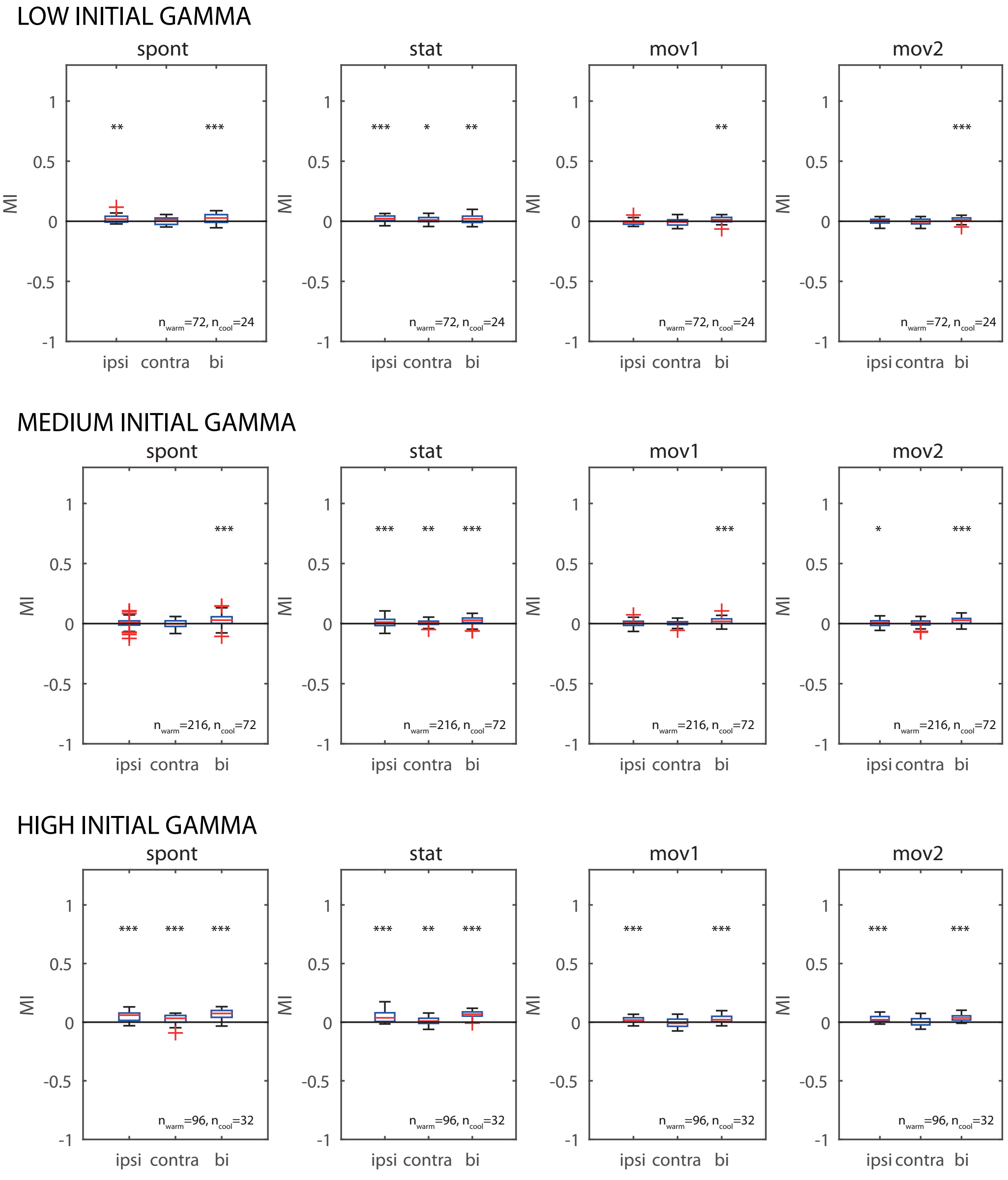

Figure 3.47.: Characteristic Path Length, GLM, 5 ms cross-history. Modulation Index of the characteristic path length for the GLM graphs, i.e. comparison of the characteristic path length for each deactivation condition to the characteristic path length during the warm condition. (Kruskal Wallis test, ***: $p<0.01$, **: $0.01<p<0.05$, *: $0.05<p<0.1$; Boxplots show the median (red line), 25th/75th percentile (outer lines of boxes), most extreme data points not considered outliers (whiskers), and the outliers (+).)

After the final experiment, the animals were euthanised and perfused with paraformaldehyde. The brain tissue was dissected and prepared for histological analysis in order to assess the positions of cooling probes and electrodes (see Figures 3.48 and 3.49). The electrode traces that were found indicated that all electrodes had been placed in area 18. The histological inspection of the tissue also confirmed that there were no damages caused by the surgery, and no apparent abnormalities (**Geider**, 2008; **Henß**, 2012).

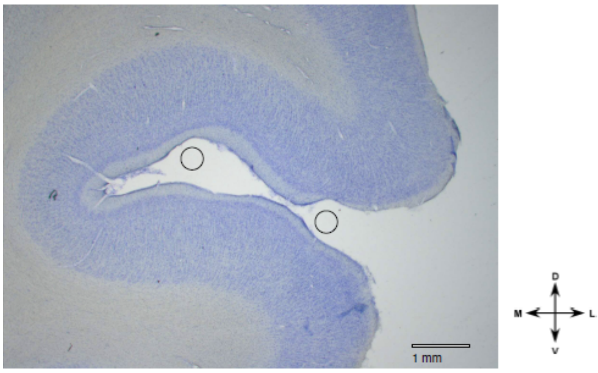

Figure 3.48.: Histology I. The figure shows a coronal slice of the right pMS sulcus of cat 101007. The circles indicate the position of the cooling probe. The tissue at these locations is slightly dented, but no injuries were discovered. (Histological analysis by Kirsten Geider.)

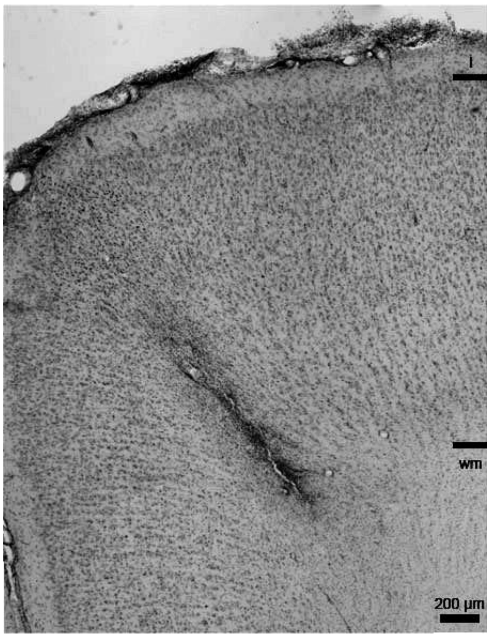

Figure 3.49.: Histology II. The figure shows an example of a Nissl-stained brain slice of experiment 121007, viewed under the light microscope, showing a lesion caused by one of the electrodes. The electrode trace is located in area 18, on the Gyrus lateralis, close to the 17/18 border. I = border to layer I, wm = border to white matter (Histological analysis by Lisa Henß.)

4 Discussion

I would like to start this discussion chapter with a central finding:

> **Finding:**
> Deactivation of the pMS cortex leads to changes in local network activity in area 18.

While this might seem trivial, it is actually worth mentioning that, despite relatively small sample sizes, remarkably clear effects could be extracted from the data.

In this discussion, these effects shall be interpreted not only in relation to current knowledge of neuronal processing, but also in the context of the methods with which the effects have been derived.

4.1 Summary of Results and Interpretation

First, the results shall be summarized and interpreted.

4.1.1 PARAFAC results

Parallel Factor Analysis based on cross correlations between the activity of multi-units was applied as a first step in probing the level of correlations in the recorded network, as opposed to rates alone. In fact, in the present study, PARAFAC was applied to electrophysiological data for the first time. In this context, PARAFAC was applied as a scanning method in order to retrieve an overview on the trends that pMS deactivation caused. Details can and should be extracted with other methods afterwards.

The application of the PARAFAC method to cross correlation values proved it to be able to extract relevant information from the data. Changes in activity during pMS deactivation could be clearly identified.

All in all, the following trends were observed: 1) less correlated activity during spontaneous activity and static stimulation conditions as compared to moving stimulation, and 2) lower correlated activity during ipsi- and bilateral pMS deactivation relative to warm, while contralateral pMS deactivation led to a similar pattern as for the "warm" condition, and sometimes even slightly higher levels of cortical activity relative to warm. During spontaneous activity, no fluctuations between the directions of the stimulus gratings were visible. For the stationary phase, it could often be observed that there were similar effects for stimuli of the same orientation that moved in opposite directions (which are actually identical during the stationary phase). These observations are in line with previous results obtained from LFP studies (**Ebisch**, 2007) and further affirm that the PARAFAC method extracts true effects from the data:

Finding:
PARAFAC is able to extract deactivation effects on the level of cross correlations.

However, these effects turned out not to be consistent over all sessions; some largely deviated from the pattern described above (see examples in Fig. 3.13), indicating that internal activity might affect the evoked response. The possible reasons and implications of these differences will be discussed in section 4.4. On the other hand, the observation of outliers also shows that PARAFAC can be suitable in the detection of artefacts (see e.g. Fig. 3.9).

Methodological considerations

PARAFAC is not the only method that can be useful in the analysis of multi-dimensional datasets. The immediate competitors are Principal Component Analysis (PCA) and a related method referred to as "Tucker3" (**Tucker**, 1966).

Let us first look at a comparison of PARAFAC to PCA (**Schmitz et al.**, 2015):

> *"In contrast to PARAFAC, PCA is not a multilinear but a bilinear decomposition (**Smilde and Doornbos**, 1991). If applied to multi-dimensional data, PCA requires unfolding of the multidimensional data array to a two-dimensional matrix. Unfolding easily causes overfitting since the two-dimensional structure of the model does not correspond to the underlying structure of the data. Furthermore, PARAFAC applies a less complex model (as compared to PCA), which features easier and clearer interpretation. In particular, the uniqueness of the solutions of PARAFAC has to be emphasized in this context, since this is in strong contrast to the solutions obtained with PCA, which provide rotation invariance (**Bro**, 1997). The choice of PARAFAC as the decomposition technique is also supported by the principle of parsimony ((**Seasholtz and Kowalski**, 1993); also 'Occam's razor'), which recommends to use the least complex model that is capable of capturing the desired information.*
>
> *Concerning the determination of the solutions, more effort has to be spent when using PARAFAC instead of PCA. This is mainly due to two reasons. First, the determination of the number of components required for the PARAFAC is not trivial and requires effort prior to the actual determination of the solution. Second, obtaining the solution of the PARAFAC using the alternating least squares (ALS) algorithm is computationally more complex than the projection applied in PCA. In addition, it has to be kept in mind that with PARAFAC, the solutions obtained for different number [sic] of components are independent, such that changing the number of components requires the recalculation of the complete solution."*

Looking at the relation of PARAFAC and Tucker3, PARAFAC is essentially a constrained version of Tucker3 (see Fig. 4.1). Thus, any data set that can successfully be modeled with PARAFAC can also be modeled with Tucker3. In addition, results of TUCKALS3 (alternative least squares algorithm for Tucker3 (**Kroonenberg and de Leeuw**, 1980)) are harder to interpret than PARAFAC results: as for PCA, the components found by TUCKALS3 have rotational freedom, which further complicates the interpretation (**Kiers**, 1991). Also, PARAFAC does not impose assumptions on the data, as, for example, statistical independence of the components.

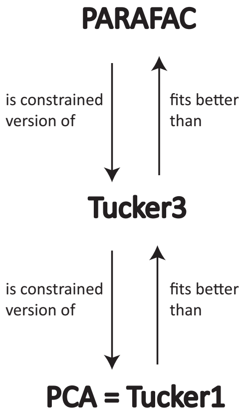

Figure 4.1.: Comparison of the PARAFAC model with its immediate competitors (see Kiers (1991); Bro (1997)).

With PARAFAC it was possible to extract the key features in the level of correlations in the spiking activity, as shown in Fig. 3.2, p. 55. This can be taken as an indication that PARAFAC yields plausible results and is applicable as a screening method in the present context. Since PARAFAC was able to provide a clear and quick overview of the effects of pMS deactivation on the correlations in area 18, it did not seem useful to consult Tucker3 in addition, and it was concluded that PARAFAC was the most suitable method in the present case.

In **Schmitz et al.** (2015), this reasoning has been elaborated on further (within the quote, the Figure references have been adjusted to match the numbering in this thesis):

> *"Since PARAFAC applies a truly multilinear model (**Bro**, 1997), it is a well suited decomposition technique for data that can be factorized. In our experiments, stimulus condition and repetition can be assumed to be independent, such that they can be factorized. Thus, PARAFAC can be expected to be suitable for data analysis in the scope of our study. The results of the analysis of correlation effects in action potential data, as shown in Fig. 3.2 B and C, support this reasoning. They show that PARAFAC allows to easily assess the correlation effects in the data and to represent the relevant dependencies much more compact than more elementary analysis techniques, such as the evaluation of plain spike rates or correlations as shown in Fig. 3.2 A. Thus, PARAFAC proves to be a good choice to reveal the structure contained in the experimental data and to enable the assessment of the functional relation between the recorded groups of neurons as well as the influence of different stimulus conditions and time structure.*
>
> *(...)*
>
> *One prerequisite for the use of the ALS algorithm is a normal distribution of the model error* ε_{ijk}*. However, this could not be held for our dataset, therefore the validity of our analysis has to be tested. To this end, split-half experiments were carried out. The results are shown in Fig. 3.5. The results show that despite an error distribution that deviates from the normal distribution, the PARAFAC results obtained with the ALS algorithm are stable and meaningful. For further analysis of the sensitivity of the PARAFAC solution with respect to the error distribution, a bootstrapping procedure (**Efron and Tibshirani**, 1993) that works with two different sets of errors is suggested: One set is obtained by randomly drawing error values*

from the empirical distribution of errors as they actually occurred in the PARAFAC analysis. The second set of errors is obtained from a Gaussian distribution that is fitted to the empirical distribution of the empirical errors. The errors from both sets are added to the original data and a PARAFAC analysis is carried out for the two data sets. The sensitivity of the PARAFAC algorithm to the distribution of the error can then be determined by comparing the solutions of PARAFAC obtained from the two data sets.

To summarize, PARAFAC is proposed in this work as a technique to analyze action potential recordings. The proposal is made based on the properties of PARAFAC and the properties of the data. The application of PARAFAC for the proposed purpose is verified in this work and the analysis results support the reasoning. A comparison with other relevant approaches is drawn and the differences between PARAFAC and other approaches are discussed. Furthermore, the specific requirement of PARAFAC concerning the normal distribution of the analysis error is discussed and the effect of an error distribution that deviates from the normal distribution on the analysis performance is evaluated. It is shown that the proposed analysis approach is valid also for a non-normal distribution of the analysis error. For a more detailed analysis of the sensitivity of the analysis, a bootstrapping approach is proposed.

Discussion of Results

*Even though this is a very methodological contribution we would like to illustrate how far this unique combination of different methodological approaches may help to reveal the neuronal basis of brain states. It should be emphazised that we only analyzed a randomly selected set of data from these experiments in order to examine to what extent the application of PARAFAC could help to better describe brain states and their transition. Unilateral deactivation of pMS cortex is linked to the neurological syndrome of visual neglect, an attentional deficit with impairment in motion, spatial, and attentional processing in one half of the visual field (**Lomber**, 2001). Bilateral pMS deactivation, by contrast, leads to a remarkable restitution of behaviour (**Lomber and Payne**, 1996). Our PARAFAC analysis is able to reveal distinct effects of the deactivation of the pMS cortex on correlated activity in area 18 (see Fig. 3.3, left and right columns, middle parts of bottom panels): during ipsi-, and even more during bilateral pMS deactivation, the strength of correlated activity in area 18 decreases. This is in accordance with our expectations, as unilateral deactivation of the pMS cortex eliminates the strong feedback input from pMS to the ipsilateral area 18 (**Symonds and Rosenquist**, 1984). However, while the feedback input from the ipsilateral pMS is missing, the affected primary visual area still gets feedforward input from LGN and also lateral input from its non-affected contralateral homotopic area and the contralateral pMS (**Segraves and Innocenti**, 1985).*

When the middle panels of Fig. 3.2B and 3.2C are examined, the analysis seems to allocate the factors in such a way that each factor depicts the situation for one distinct stimulus condition. For each of the stimuli, a certain pattern of correlated electrode pairs emerges, i.e. a different network is observed. In Fig. 3.2C, with the 6th factor (shown in magenta), another set of correlated electrode pairs that is present when a diagonally left/downwards moving stimulus is presented, becomes visible. The same electrode pairs are also correlated for the stimulus moving in the opposite direction, and a slight anticorrelation can be observed for the perpendicular stimulus. The bottom panels show the time course of effects, indicating a *larger trial-to-trial variability during the warm phases as compared to the ipsi- and bilateral deactivation sequences and similar variability for the warm condition and contralateral deactivation (see Fig. 3.3). Hence, each stimulus produces a distinct network activity, but all of those networks become less variable during the ipsi- and bilateral deactivation phases.*

*The neuronal correlate of visual neglect has been proposed to be based on an imbalance of activity between hemispheres, which, presumably among other effects, leads to a disinhibition of areas in the non-affected hemisphere, which in turn leads to further inhibition of the already attenuated area (**Payne and Rushmore**, 2004). This is in accordance with the low level of correlated activity in ipsilateral area 18 (relative to the deactivation) and the observed correlation level in the contralateral area 18, which resembles the 'warm' condition. When both pMS cortices are deactivated, as in the 'bilateral deactivation' condition, the input from the contralateral areas is also reduced. Hence, the degree of correlated activity in area 18 is further lowered. In addition to the strength of correlation, the trial-to-trial variability is also diminished (see Fig. 3.3, right column). This could indicate a less dynamic neuronal network, operating on a lower activity level, which is less able to adapt to and process new stimulus inputs than the normally functioning visual network. However, the lower but balanced correlation level seems to enable at least some functions that are impaired by unilateral deactivation: Behavioural studies indicate that during bilateral deactivation of pMS cortex, the animal is still able to complete simple orienting tasks, while it encounters problems with more abstract tasks, such as the so-called 'landmark-discrimination task', in which the cat is asked to choose between two wells, one of which contains food, the correct side of the well being cued by one of six equally spaced landmarks, three left and three right of the midline (**Lomber and Payne**, 2000). Thus, although the animal is able to successfully complete some tasks, which may be owed to the restored equilibrium of activity levels in both hemispheres, there is an impairment of cognitive functions. Figure 3.4 shows that a strong decrease in the variation of correlated activity is even present in the spontaneous activity before stimulus onset, indicating a different processing mode of the respective neuronal network (see bottom panel, deactivation phase). As these are only speculations based on a very preliminary analysis of only a part of the dataset, these findings and conclusions have to be validated on the full database from these experiments. Also, further analyses should be conducted to examine the detected effects in greater detail. Nevertheless, PARAFAC proved to be a highly sensitive and helpful tool to identify relevant changes in neuronal processing modes on a multi-dimensional scale which open the window for a more targeted analysis of brain states linked to perceptual (and other) performance."*

4.1.2 Separation of data based on gamma activity

The analysis of some recording sessions showed effects that match the ones previously observed in LFP analysis (ipsilateral deactivation leads to decrease in activity, contralateral deactivation leads to no change or a slight increase, bilateral deactivation again leads to decreased activity; see Figs. 3.8-3.12; cf. **Ebisch** (2007); **Geider** (2008)), but these effects were not apparent in all sessions (see Fig. 3.13). From this level of detail, there is an indication that the activity evoked by the stimulus was similar (see Fig. 3.17), but the initial state (as shown in Fig. 3.15) was not. This observation led to the question about the reason for these deviations. One possibility could be a difference in the initial brain state. Therefore, a way to define this brain state had to be identified. From previous studies, the level of gamma activity deemed a suitable candidate. Based on this idea, all sessions were grouped based on their initial gamma amplitudes during the warm condition. Subsequent analyses were then performed separately for three groups (Low / Medium / High Initial Gamma Power; see Fig. 3.19, p. 73).

With this, it should be kept in mind that the separation based on gamma activity is only one of many possible options to split up the data. Other possible criteria include LFP power in other frequency bands, or the initial spike rate during the warm condition, which might have led to a different assignment of sessions to the individual groups.

Further, it is visible that especially the Low and High Initial Gamma groups are biased towards individual experiments. This is partly due to the approach that was taken with the separation, because sessions recordings from the same hemisphere were generally kept in the same group. Only extreme outliers were then re-assigned to other groups. Experiment 121007, which is mainly represented in the High Initial Gamma group also had the highest signal-to-noise ratio for the spike signal, so that signal quality also might have had an impact here. Thus, even though the separation into the three groups was statistically justified based on the rank (see Fig. 3.19), a larger sample size could mend these issues.

4.1.3 Spike rates

For multi-unit activity, warm spike rates were at a similar level for all three Gamma groups for all phases of the stimulus (see Fig. 3.22, Table 3.5). As expected, the rates were highest during presentation of a moving stimulus. Interestingly, though at similar levels, the observed rates were highest for the Low Initial Gamma group. For single-unit activity, considerable differences in spike rates were observed between the different Gamma groups (Fig. 3.23, Table 3.6), with the rates being highest for the High Initial Gamma group for all stimulus phases. One thing to consider with these observations is that many trials exhibited very low spike rates of zero or close to zero, while at the same time the spike rates showed very high variability (see standard deviations in Tables 3.5 and 3.6).

During pMS deactivation, again, the spike rates calculated for multi- and single-unit activity showed a slightly different behaviour (see Figs. 3.22-3.23 and Tables 3.7-3.8): for the multi-units, there was a clear decrease in rates for bilateral deactivation in the High Initial Gamma group, which also reflected in the Medium Initial Gamma group (though not as pronounced) and was absent for the Low Initial Gamma group. For the single-units, the Low Initial Gamma group showed a decrease in single-unit rates for bilateral deactivation, but an increase for ipsilateral pMS deactivation. For the Medium and High Initial Gamma groups, a clearer picture emerged, with a decrease in rates for ipsi- and bilateral deactivation, which was especially visible for spontaneous activity and during static stimulation. For the Medium Initial Gamma group, the single-unit rates went back to the level of the warm condition once the moving stimulation started, while for the High Initial Gamma group, the rates never returned to the level of the warm condition, even for the phases of moving stimulation (see Fig. 3.23). The observations for the Medium and High Initial Gamma group fit previous observations for the LFP (**Ebisch**, 2007; **Geider**, 2008; **Barnes**, 2014), i.e. decreased activity during ipsi- and bilateral deactivation, and a similar, or even increased activity level during contralateral deactivation. The deviance of the Low Initial Gamma group could be due to the general impairment of the network for this condition. Activity levels and initial connectivity seem so low for this group that meaningful information processing cannot be attained. Therefore, a further manipulation of the network by deactivation pMS might lead to no or little changes, and could also increase the weight of input signals from other areas, which in turn might have led to the observed slight increase in rates for the ipsilateral deactivation condition.

4.1.4 Tuning properties

In many cases, a striking similarity in the shape of the tuning curve throughout the layers was observed, indicating that the electrode was moved through an orientation column, i.e. perpendicular to the surface. This observation supports the estimations of electrode depths and layers, as this can only be sufficiently accurate when the electrodes are moved vertically (an example for the tunings and estimated laminae is shown in Fig. 3.25).

Overall, the tuning selectivity, i.e. the vector strength for the preferred stimulus orientation and direction, respectively, was strongest for the High Initial Gamma group and lowest for the Medium Initial Gamma group. The strength of both orientation and direction selectivity were found to be reduced by pMS deactivation: with ipsilateral, but also contralateral pMS deactivation, a significant decrease in direction selectivity was observed for all Gamma groups. During bilateral pMS deactivation, no significant change in direction tuning was observed. Orientation selectivity in the Medium Initial Gamma group decreased for all deactivation conditions, while for the Low Initial Gamma group a significant decrease was only observed during ipsilateral pMS deactivation. For the High Initial Gamma group, no significant changes in orientation selectivity were observed.

The maintenance of direction selectivity during bilateral pMS deactivation is surprising, since the pMS cortex was described as an important contributor to the manifestation of direction selectivity **Galuske et al.** (2002). On the other hand, in the awake animal, a restitution in behaviour can be observed when pMS is deactivated in both hemispheres (**Lomber and Payne**, 1996), which could be related to this effect: other areas might take over functions that had previously been covered by the pMS cortex and the equilibrium in activity between the hemispheres might play a crucial role in this context (**Payne and Rushmore**, 2004).

Interestingly, orientation selectivity slightly increased for ipsi- and contralateral deactivation for the High Initial Gamma group. This could be a hint that the influence of the pMS cortex that might have sent corrective signals before, modulating the sensory signal already at the level of the primary visual cortex, is lacking, and with this, the feedforward impact gets stronger, resulting in a more stimulus-driven system.

4.1.5 Network properties

The methods that were introduced in this study provide an efficient way to discover structural patterns in neuronal networks. By first selecting sets of edges according to research question driven criteria, the homogeneity test enables the researcher to quickly assess differences of edge probabilities between different sets, while the Hamming distance test constitutes a powerful tool for the evaluation of similarity between networks defined by edge sets, either within the same experimental condition or between different conditions. Both tests, homogeneity and Hamming, are easily applicable to various kinds of networks, not only in the context of brain research. It is obvious that the larger the networks, the more reliable the test results will be. However, also for small networks, as in our example, the methods provide reasonably reliable results.

Homogeneity

Looking at the results on the homogeneity of edge probabilities (Figs. 3.33-3.35), it becomes clear that the number of graphs with more local than distant links clearly outweighs the number of graphs with more distant than local links. This is most pronounced for the phase of the moving stimulus. Similarly, there are, in total, more graphs with a higher density among the units with a similar orientation preference as compared to those among units with different orientation preferences. Thus, with the application of the network analysis approaches to a sample data set, it was possible to reproduce a number of fundamental findings: the results of the analysis on homogeneity of edge probabilities suggest that spatial proximity is a better predictor for functional connectivity than common orientation preference, as it has been described by **Engel et al.** (1990) and **Braitenberg and Schüz** (1998). These findings are also in line with the assumption that the brain has a small-world property with a high local clustering, but relatively few long-range connections (**Watts and Strogatz**, 1998; **Sporns and Zwi**, 2004; **Gerhard et al.**, 2011).

Looking at the different "Gamma groups" separately, the effects separate as well: for Low Initial Gamma Power (Fig. 3.33), spatial proximity and orientation preferences are the main indicators for connectivity. For Medium Initial Gamma Power (Fig. 3.34), spatial proximity becomes even more dominant than it was observed for the Low Initial Gamma Power group. For High Initial Gamma Power (Fig. 3.35), spatial proximity is even more strongly linked to the strength of connectivity between the units in the network than it became apparent for the other two Gamma groups. Stimulus direction preference shows a strong relation to the connection probabilites for High Initial Gamma Power. This is mainly apparent during the warm condition and only slightly reduced during contralateral deactivation (this effect is not apparent in the Low and Medium Initial Gamma groups). Interestingly, this observation also holds for the spontaneous activity and static grating phases, but is in these cases completely diminished with ipsilateral deactivation. This indicates that feedback primes these connections between units of similar direction preference, even in the absence of a stimulus. This priming disappears when the feedback from the ipsilateral pMS cortex is eliminated.

Since the Neuroxidence algorithm eliminates the influence of rate variations and only exhibits the effect of synchronous firing events, all effects that were observed were due to changes in synchrony. This means that there were some effects in the structure of the synchronisation patterns, while there was no change in firing rate. This supports the hypothesis that information in the brain is encoded by synchronously active cell assemblies.

Hamming Distance

A significantly small Hamming Distance indicates a strong resemblance between the compared graphs, revealing the existence of characteristic structures in the observed networks. During spontaneous activity and presentation of the stationary stimulus, the networks were sparse, which made it difficult to statistically assess their features. Also, the variability among the networks was high in these phases. Accordingly, for most cases of spontaneous activity, the Hamming distance was not significantly small. **Kenet et al.** (2003) showed that even if the eyes are not exposed to any visual stimulus, specific activity structures can be observed in visual cortex, which resemble stimulus-induced activity patterns. However, from the observations presented here, these spontaneous structures seem to become severely disrupted by the deactivation of feedback from pMS.

For the moving stimulus, fixed structures emerged, indicated by smaller Hamming distances among the networks obtained under this condition. Since the stimulus is dynamic in this phase, new incoming information has to be constantly processed. Thus, the workload for the visual areas is higher as compared to the other stimulation conditions. Assuming the validity of the assembly hypothesis, a higher degree of synchrony among the cells belonging to the same assembly would be expected in this case. The small Hamming distance for this phase indicates the repeated synchronous activity of the same groups of neurons, again speaking in favour of the assembly hypothesis.

When interpreting the Hamming distance one should bear the following in mind: a small Hamming distance could be due to the fact that two networks with a certain number of edges are very similar, but also that the two networks might only show a few number of connections at all. Thus, the results should be interpreted relative to the total number of edges. However, also the absence of an edge holds information and should possibly even be valued as much as the presence of an edge.

Density

For both the NeuroXidence and the GLM approach, decreases in density were observed for both ipsi- and bilateral deactivation, which is in line with the changes in gamma power under the same conditions, as observed in previous studies of the LFP (**Ebisch**, 2007; **Geider**, 2008; **Barnes**, 2014) (see sections 3.7.3 and 3.8.2). These differences in density were most pronounced for phases of spontaneous activity.

The graphs constructed on the basis of NeuroXidence results exhibited densities up to 30 %, while the graphs constructed on the basis of results from GLM analysis showed densities between around 40-60 %. Though densities around 50 % could be seen as suspicious and pointing to a random assignment of links in the network, significant differences between experimental conditions could be extracted from the data: densities decreased during ipsi- and bilateral deactivation as compared to the warm condition, and especially for the High Initial Gamma group, this effect was very consistent.

It is important to note that graph density did not follow the same trends as the spike rate and sometimes even showed diametrical effects. This is, for example, visible for the High Initial Gamma group, for MUA rate vs. network density based on NeuroXidence: for static and moving grating, an increase in spike rate was observed during ipsilateral deactivation (Fig. 3.22). The graph density, in contrast, decreased for these conditions (Fig. 3.37). Similarly, for single-unit spike rates vs. network density based on the GLM, it was observed that for the Low Initial Gamma group, spike rates increased during ipsilateral deactivation for the phases of spontaneous activity and static stimulus (Fig. 3.23), but graph densities decreased (Fig. 3.41). This confirms that the functional and effective connectivity measures applied here to determine the density extracted effects that are independent from the rate.

Clustering Coefficient

The clustering coefficient showed similar tendencies for the NeuroXidence and GLM apporaches (see sections 3.7.3 and 3.8.2). However, for the graphs based on the NeuroXidence analysis, the median clustering coefficients were very low, often at 0. There was no clear overall trend for the deactivation effects. This could be due to the fact that the graphs based on the NeuroXidence analysis only exhibited densities up to 20-30 % and, as a consequence, the graphs were not fully connected. For this reason, the low clustering coefficients might at least partly be due to a sampling effect, caused by spatial subsampling of the selected cells, and the size of the correlation windows. With this, some actually existing connections might not be detected. The graphs constructed on the basis of the GLM analysis exhibit higher densities overall and thus might form fully connected graphs, so that the analysis of the clustering coefficient is able to pick up the tendencies towards weaker clustering during ipsi- and bilateral deactivation, especially for the moving stimulus.

Characteristic Path Length

For calculating the characteristic path length, different definitions can be found in the literature, some of them setting $L_{ij} := \infty$ for two nodes i and j that are not connected. In this case, for any graph that is not completely connected, the average path length will be infinite. Thus, as the initial probing of the networks already showed that many graphs exhibited disconnected components, L_{ij} was set to ∞ for any two disconnected nodes i and j, but not considered for the computation of the average path length. With this, it should be noted that many connections do not exist in the graphs. Since the computation of the characteristic path length only considers existing connections, these missing links are skipped. This could lead to a bias in the analysis and result in higher observed characteristic path lengths than actually present in the underlying network.

For the analysis based on NeuroXidence, the characteristic path length behaved in a similar way to the density and the clustering coefficient (see section 3.7.3). This is actually counter-intuitive, but again might be due to the sampling issues described above.

For the GLM graphs, the characteristic path length increased for ipsi- and bilateral deactivation (see 3.8.2), which fits the expectation and can be viewed as a further validation of the analysis approach, even with the observed densities of around 50 %. Here, in contrast to the NX analysis, the density might be high enough to allow for a better assessment of the deactivation effect on the characteristic path length.

Longer path lengths during pMS deactivation might aggravate information processing on the local network level and disturb the accuracy in the timing of action potentials, which could be one reason for the impairments that can be observed during neglect.

Summary

The analyses in this study were performed on different levels of granularity (from coarse to detailed):

- LFP
- MUA rates and tunings
- MUA cross correlations / PARAFAC
- MUA / networks based on NeuroXidence
- SUA rates and tunings
- SUA / networks based on GLM

It is likely that multiplexing is present in the brain, meaning that information processing might happen at multiple time scales and frequencies in parallel. Depending on the selected methods and analysis windows, the measures at hand will usually only extract information on a certain time scale. In order to identify the relevant time scales that the system is operating at, it is advisable to probe multiple measures at different temporal and spatial scales, this is why multiple methods were applied here.

While the NeuroXidence approach yielded results based on binary, undirected networks, the GLM method was utilized in order to obtain information about directional information flow. It was shown that plausible effects could be extracted from the datasets, confirming that the application of both approaches is suitable in this context.

The analysis of the networks based on the GLM approach revealed a tendency that with increasing stimulation strength (from a blank screen to a moving high contrast grating), the observed density and clustering coefficient increased and the average path length decreased. Therefore, a stronger stimulus leads to a higher level of correlated activity. At the same time, the graph-theoretical distances are shortened. This might facilitate signal propagation and increase processing speed, because a lower number of synapses must be overcome to reach the next unit of cells.

However, due to the length of the cross-history window, the effect that is extracted by the GLM method might partly be a population effect, linked to the LFP, because within the selected integration window of 70 ms, global rate changes might be captured. This could lead to the relatively high density of links, but at the same time conceal more specific effects.

Both the NeuroXidence method and the GLM models are rate-corrected, and, therefore, comparable. Still, the two approaches did not yield the exact same results, for example with regards to the characteristic path length. However, with both approaches, significant results could be obtained, which were in line with previous studies. Possible reasons for these deviances are the differences in the probed time scales and the fact that NeuroXidence observes joint-spike events, i.e. synchronous activity of pairs of units, while the GLM approach focuses on temporal patterns and considers the direction of information flow within the network. These two measures might actually behave differently, so that it is not necessarily expected that congruent observations are made.

4.2 Validation and Limitations of Methods

In the following sections the advantages and limitations of the applied experimental and analytical methods are described in order to outline which questions can be answered and the treatment of which questions would require further advancements or alternative methods.

4.2.1 The cat as the model organism

The cat is one of the mostly used model organisms for research of the visual system. Reasons for this are the similarities with the human visual system, such as the similar eye position and resulting angle of the visual field, and the columnar organization of the visual cortex, as well as mechanisms of visual motion perception (**Orban et al.**, 1981b). Moreover, the position of the visual areas (area 18, for example, is located right at the top of the brain) makes them easily accessible for electrophysiological recordings, and for optical imaging. In addition, cats are relatively easy to handle in behavioural experiments, and are able to perform complex tasks.

4.2.2 Visual stimulation

Visual stimulation was performed using black and white whole-field gratings, which, being high in contrast and stimulating both eyes simultaneously, presented a very strong stimulus for the neurons. Inherently, gratings have a spatial and temporal frequency component, but these were not varied during the experiments, neither were contrast, color, and distance to the monitor, which were set to values that had been proven to be suitable for studies of signal processing in area 18 (see e.g. **Vögler** (2014); **Barnes** (2014)), such as the applied stimulus velocity of 16 °/s. Preferred velocities in area 18 vary (**Orban et al.**, 1981a), so that the velocity might not have been optimal for each of the recorded cells. However, this is not very likely, since the recordings were always performed in the very central part of the visual field, in which the chosen parameters are optimal. In addition, in the present study, orientations and directions of the grating were chosen in discrete steps, which might have lead to a non-optimal congruency of the presented stimuli with the receptive fields for some of the recorded neurons. Nevertheless, the applied stimuli cover a variety of scenarios and enable detailed studies of functional features of the recorded cells.

The use of cooling probes leads to very large areas being deactivated. A surface temperature of 2-3 °C leads to the deactivation of all cortical layers (**Lomber et al.**, 1999). Since the cooling probes were placed inside the sulcus, it can be assumed that the neuronal activity on both sides of the probe was shut off. The exact extent of the deactivation is difficult to control, because the spread of the cold into the tissue depends on various factors, such as size of the probe, position relative to blood vessels, etc. In general, it is assumed that neuronal activity extending 2-3 mm from the surface of the probe is ceased.

The switch between activation and deactivation should not be understood as being dichotomous: in the transition area between cooled and non-cooled tissue, at around 20 °C, hyperactivation occurs (**Brooks**, 1983; **Volgushev et al.**, 2000). If present in PMLS, this activity boost could be passed on to the connected neurons in area 18 via feedback connections, leading to a local increase in activity. It has also been stated that an increase in temperature by 1 °C leads to an increase of conduction velocity by 5% (**Waxman**, 1980). Hence, cooling induces no simple on/off situation, but exhibits a more complex pattern. This also has to be considered in particular in connection with the impact of anaesthesia, which is further discussed in section 4.4.

The deactivation of pMS not only leads to the inhibition of direct feedback towards area 18. In addition, several other feedback pathways are affected (e.g. PMLS → area 17 → area 18, PMLS → VLS[1] → area 18, etc.; see also Figure 1.5, p. 27).

The correct position of the cooling probe was validated by examination of the awake behaving animal in a perimetry task prior to the final experiment. These tests showed that one of the probes could not elicit a visual neglect (right probe in experiment 112807). Other than that, no signs of a displaced cooling probe, nor signs of any undesired lesions caused by the surgery were detected. Nevertheless, a deviance in size of the cooling probe or a positioning in a slightly different angle could have led to deactivation of a larger area than desired.

In contrast to lesioning of brain areas, thermal deactivation has many advantages: first and foremost, the deactivation is reversible. For this reason, the animal can "serve as its own control" (**Lomber**, 1999), because comparisons between an uninfluenced baseline condition and thermal deactivation phases are possible. Switching between deactivated and activated state can be conducted within minutes. This also leads to a high number of repeated trials and with the number of trials, statistical power increases.

With short deactivation sessions that lasted around 30 minutes, it can be assumed that long-term plasticity does not occur. Signalling mechanisms following cell death that would trigger repair mechanisms or alter long-term plasticity mechanisms (as in the case of an ischemic stroke (**Calabresi et al.**, 2003; **Stein et al.**, 2015), or chemically induced lesions, see e.g. **Müller** (2017)) are not activated, because the cells are not damaged. Structural plasticity usually only occurs after days (see Figure 4.2). However, there might be short-time changes in synaptic strength, which can occur on the order of milliseconds to minutes (for a review see **Zucker and Regehr** (2002)).

Since long-term plasticity occurs on a scale of hours or days, this could be relevant in the context of the whole experiment. The plasticity might not be due to the inactivation alone, but the visual system might have adapted to the stimulus. The continuous decrease in gamma power during the timecourse of the experiment in the right hemisphere of experiment 121007 (see Fig. 3.18) might give an indication of some kind of adaptation over time.

---

[1] VLS = ventral lateral suprasylvian areas

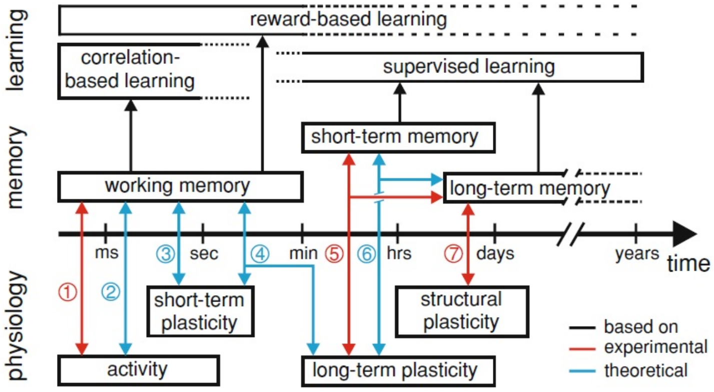

Figure 4.2.: Timescales of plasticity mechanisms. From Tetzlaff et al. (2012).

4.2.4 Sampling issues

When recording and investigating electrophysiological activity, one is always confronted with several types of (sub-)sampling and choices of parameters that affect the outcome of the analysis, because the relevant temporal and spatial scales are not known. These parameters can be determined through testing, with the help of previous studies, or based on models of neuronal networks, but are far from being obvious. Hence, parameters have to be estimated, which, of course, can lead to dead ends or suboptimal parameter choices. Also, parameters might perfectly work within the context of a chosen model, but might not reflect the situation that is present in the brain. As current recording methods do not have access to the "whole" network, neither on the temporal, nor on the spatial scale, the complete brain network cannot be fully captured and described.

However, based on the results obtained in this study, the following statement can be made:

Finding:
Changes in activity are detectable on the local network level despite restrictions due to sampling issues.

In the following sections, some of the sampling issues and choices of parameters will be discussed.

Definition of nodes and edges

In network analysis, one of the fundamental steps in the creation of the networks is to define the nodes of the networks of interest (**Papo et al.**, 2014).

In the present study, the nodes in the networks under investigation were set to be either multi-units, i.e. a handful of neurons around the electrode tip, or 'single-units', still not necessarily only one neuron, but clean clusters, characterized by a typical spike waveform and an ISI distribution with very few spikes having a temporal distance below 1 ms (which should be fulfilled because of the refractory period between action potentials).

Analogous to the nodes in *peer-to-peer (P2P)* computer networks, the nodes of the networks here are considered to be equal. In reality, however, this might not be the case. The heterogeneity of cell types, sizes, and other features could not be captured. Particular nodes might play a more crucial role in the actual underlying network than others, which cannot necessarily be evaluated with the analytical methods that were applied here. A description of the cell types thus could further improve the understanding of the functional connectivity patterns between different cell types in cat primary visual cortex and provide information about the interaction between excitatory and inhibitory neurons.

Still, the uniform sampling of nodes guaranteed a random selection of nodes among the cells within the same cortical layer, i.e. with supposedly very similar connectivity patterns, so the abstraction of an homogenous network is somewhat justified.

Similar to the definition of nodes, the definition of edges is crucial. Here, edges were defined in multiple ways: first, by calculation of the cross correlation, second, by the computation of an excess of joint-spike events between the units (NeuroXidence), and third, by the directed influence of the spiking of one unit towards another (GLM).

One obvious consequence of the sampling issues is the fact that due to the use of thresholds for the selection of links, the networks in this study rarely consisted of only one connected component. This, in turn, hampers, for example, the analysis of the characteristic path length in these binary graphs, since only the existing links will be taken into consideration.

The choice of functional connectivity measures as a basis of the study of assemblies, as applied in this study, is supported by the fact that "cooperativity of neuron firing is a readily demonstrated phenomenon, and can be used as a defining indicator of neural assemblies and assembly processes" (**Gerstein et al.**, 1989).

The applied methods operate on slightly different timescales (5 ms for the correlation windows for the κ_{sync} measure of PARAFAC and for the NX analysis, and also for the cross-history window for GLM, but here also taking up to 70 ms of the auto-history into account), and thus detect slightly different aspects of the coordinated firing, namely joint spiking in the millisecond range (NX) as opposed to directed connectivity (GLM). This in turn leads to differences in the resulting networks. In this regard, there is not one "local functional network", but the resulting network will always depend on the time scales and methods that were selected for the computation of correlated activity. In this sense, "analytical sampling" occurs as well, which is governed by the choice of analysis methods. It could be mitigated by applying multiple timescales and alternative methods in addition to the ones that have been applied here (see suggested options in the outlook section, p. 136ff) in order to obtain further details about the network properties.

Spatial sampling

Area 18 is described to span a surface of 60-80 mm^2 (**Tusa et al.**, 1979; **Albus and Beckmann**, 1980). With the electrode array used in the experiments of this study, 2.8 - 3.8 % of the area was covered. Hence, a better coverage of the area with larger areas and more recording sites would be desirable.

In 1 mm^3 of cortex, there are around 100.000 neurons. Spike sorting yields up to a handful of single units per electrode, often less, so that with a small number of electrodes, the network is highly undersampled (see Fig. 4.3).

One issue with this is that the networks become – seemingly – disconnected, which can be problematic for some network measures, like the shortest path length, which might become infinite, although anatomically and functionally, there is a path connecting these units in the actual network, but it is not sampled. Likewise, other network measures, like the degree, can get distorted (**Levina and Priesemann**, 2017; **Wilting and Priesemann**, 2018).

For the current data, this means that measures like density, clustering, and degree might be underestimated. However, these values could actually also be lower, if probed for the entire network. For the

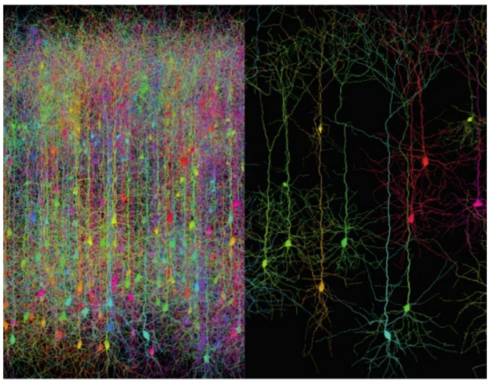

Figure 4.3.: Spatial sampling. From the entire local anatomical network (left), electrophysiological recordings only pick up a subset of the cells in the vicinity of the electrodes (right) From Wilting and Priesemann (2018).

shortest path length, the calculated values determine an upper bound, since additional links to nodes that were not sampled can only shorten the path length.

However, simply due to space restrictions, it is impossible to sample the whole circuit with electrodes that are inserted into the tissue, so that new experimental approaches are needed. Nevertheless, due to redundancy and population coding mechanisms, knowledge about each single neuron might not be necessary (**Priesemann et al.**, 2013).

Cell types

Very likely, with extracellular recordings, as used in the experiments that constituted the basis for this study, only the signals of large excitatory neurons can be separated from the background activity. Such neurons are mainly pyramidal neurons and spiny stellates, which together make up 80 % of the neurons in the cat primary visual cortex. Hence, a large proportion of cells can potentially be recorded from. However, there are many other neuronal cell types involved in signal processing in area 18, constituting the remaining 20 % (chandelier cells (layers 2/3 and 5), large basket cells (layers 2-6), double-bouquet cells (layer 2/3), and neurogliaform cells (all layers) (**Payne and Peters**, 2001)), which all are *inhibitory interneurons*. Their alternative name "local circuit neurons" depicts their important role in local circuit computation, since without inhibition there is no precise coordination. Inhibition in the cat is typically as selective as excitation (**Isaacson and Scanziani**, 2011). Hence, obtaining knowledge about the behaviour of inhibitory cells during the trials could be extremely insightful.

Temporal sampling

With sampling rates of around 20 kHz, the waveform of the spikes can be traced sufficiently well. However, spikes were later binned into windows of 1 ms, so that spikes with a temporal distance shorter than this could not be separated. In addition, precisely synchronous spikes of multiple cells that are picked up by the same electrode will superimpose and likely be regarded as outliers because of the resulting shape.

On a different note, the strength of correlation strongly depends on the timescale that is used for analysis (**Smith and Kohn**, 2008; **Schulz et al.**, 2015). In combination with conduction velocities and the distance between the points of interest, the spatial configuration also has to be taken into account in order to find the optimal correlation windows for analysis. As it has been suggested that information between brain areas might be carried via multiple oscillation frequencies in parallel, a phenomenon also referred to as multiplexing (**Akam and Kullmann**, 2014), information could be processed on multiple time scales at the same time also on the level of single cells.

It should be noted that, while a larger window size may be beneficial if spatio-temporal patterns shall be investigated, smaller window sizes are more appropriate for the study of synchronous patterns. In the present study, spike coordination was assessed within a window of 5 ms. Although the exact timescales for synchronous spiking input are still unknown, they have been estimated to lie around a few tens of, or even just a few milliseconds (**Cohen and Kohn**, 2011), and similar window sizes have proven suitable in other studies: temporal coordination on the order of ≤ 10 ms, as also described as crucial by **Singer** (2009), has been observed in monkeys, particularly in *M. mulatta* (ventral prefrontal cortex, window size: 3 ms (**Pipa and Munk**, 2011); caudal auditory cortex, window size: 5 ms (**Kayser et al.**, 2010)), and *Cebus apella* (primary visual cortex, window size: 5 ms (**Maldonado et al.**, 2008)), mouse (primary visual cortex, window size: 3-11 ms (**Mao et al.**, 2001)), and rat (visual cortex slice, window size: 5 ms (**Gansel**, 2014)). The reliability of spike timing has also been identified to be optimal in a window of 2-5 ms (**Galán et al.**, 2008). The choice of the window sizes is further supported by the fact that temporal summation of EPSPs occurs within approximately 1-15 ms (**Bear et al.**, 2008, p.138).

Another issue with temporal sampling is that the graphs are viewed as static, although connectivity patterns are likely dynamic and the analysis of the network dynamics over time could yield useful information.

Common input

Common input from an unobserved source towards the recorded units might be the most important source of errors in the type of analysis that is presented here. The problem with unobserved common input is inherited from the spatial subsampling discussed above. If information about all units in the network was available, it would be possible to separate direct and indirect inputs.

Influences of common input can potentially be time lagged or occur with zero time lag, but if the two units under investigation are under influence of a common source of activation, this common input will have an impact on correlation histograms and similar measures (see **Ostojic et al.** (2009)).

Although there are some approaches that indicate that spurious interactions can be detected and assigned to their "latent confounders" (**Elsegai et al.** (2015), see also **Quinn et al.** (2011)), the problem of common input has been described as being "not a theoretical one" (**Bastos and Schoffelen**, 2016), and can only be overcome by sampling all nodes of a network.

Concerning the present study, it is very likely that the applied recording techniques were not able to capture possible sources of common input, be it intra- or inter-areal cortico-cortical projections, or inputs from the thalamus. In particular, the feedback-providing units in the pMS cortex were not recorded. Consequently, simultaneous recordings in the pMS cortex, especially in PMLS, could be of great help in order to assign the observed interactions to the corresponding feedback-sending units.

But even if the number of recorded units could be increased, the exhaustive sampling of activity on the cellular level in a mammal is still far from reality. In addition, if recordings from each cell were available, the researchers would also be faced with computational issues that arise from the amount of data.

In summary, the existence of spurious correlations caused by common input cannot be excluded.

4.2.5 Experimental factors

Although the experimental setup was carefully planned and scrutinized, and several physiological parameters were constantly monitored throughout the experiment, there are still possible sources of variability that are hard to control. In addition, the experimental setup does, in some ways, create a rather artificial situation: the animal is kept under anaesthesia over a period of days, the stimulus is far from being a "natural" stimulus, and is extremely high in contrast. Nevertheless, these conditions were necessary in order to create a controllable environment, in which it was possible to link the evoked spiking activity to the presented stimuli and at the same time produce high quality multi-unit recordings with high signal-to-noise ratios. This was feasible due to individually adjustable electrodes, which cannot be implanted chronically or used in the freely moving animal.

With the applied measures, it is expected that the observed effects can be highly dependent on the specific neurons that are picked up by the recording electrode. When recording spiking activity, there is a strong dependency on the layer that spiking activity is recorded from, because spikes are typically picked up in a radius of up to 140 μm (**Buzsáki**, 2004). The cat cortex has a thickness of about 2 mm (see **Mitzdorf and Singer** (1978)), so the recording radius of a single electrode will not cover all laminae. The positioning of the electrode is more relevant for spikes than for the LFP signal, which stems from a larger area around the electrode tip, although the exact spatial scales of the LFP are unclear (**Kajikawa and Schroeder**, 2011). The exact placement of the electrode is thus expected to have a considerable impact on the recorded spiking activity. Layer-specific connectivity, especially the feedback connections – and likewise the lack of feedback – might become more visible in the feedback-receiving supragranular layers. In this study, the electrodes were moved from the top layers down, however, clear layer-dependent effects could not be observed. The fact that these layer-dependent connectivity patterns did not clearly show in the results of this study could again have multiple reasons. The observed spiking activity is strongly dependent on the stimulation that is applied, a fact that is backed up by the results obtained for spike rates and tunings, and also visible in the correlation analysis approaches. The presented stimulus directions may have been optimal for a large proportion, but not all of the recorded cells, and the response of the cells will differ accordingly. Also, the overall results will be sensitive to whether the recorded units behave similarly ("choristers“) or not ("soloists", terms adapted from **Okun et al.** (2015)): a high proportion of soloists may hamper the discovery of population effects.

4.2.6 Spike detection and spike sorting

The manual detection of spikes is extremely time-consuming, but bears the advantage that all data are inspected visually so that conspicuous irregularities can be spotted easily. For the multi-units, the thresholds were manually set such that spikes were also detected for the phase of spontaneous activity, in order to enable a comparison between deactivation conditions also for this phase. This partly led to rather low thresholds, which in turn increased the resulting spike rates. Hence, in contrast to the selection of the single-units, which was approached in a rather conservatively way, the spikes for the multi-unit data were detected with a more generous approach. For the preparation of single-unit data, thresholds were set automatically. This is justified, since in this situation, units which are not clearly identified as a separated cluster in the first place, can be excluded later in the process.

Overlapping spikes, background noise, varying amplitudes of spikes of the same cell and signals from axonal fibre bundles that look very much like action potentials make spike sorting a highly complex problem (**Lewicki**, 1998). The high number of spike sorting methods and their different methodological approaches show that there is no "go-to" method for spike sorting, and with none of the available methods it is possible to avoid false positives and negatives. In addition to sparse firing and small injuries caused by electrode penetration, deficits of current spike sorting methods (including WaveClus) contribute to the problem that fewer neurons are detected than should actually be detected, taking the density of neurons in the cortex into account (**Pedreira et al.**, 2012). Validating whether the result of the spike sorting is optimal requires knowledge of the "ground truth" (**Harris et al.**, 2000; **Schulz et al.**, 2015). Since this knowledge is not available, it is not possible to conclusively determine whether all spikes have been assigned correctly.

Here, WaveClus (**Quian Quiroga et al.**, 2004) was chosen because the WaveClus algorithm is automatic, unsupervised, and fast. Moreover, it is widely used (**Wild et al.**, 2012) and has been shown to outperform several other conventional spike sorting methods (**Quian Quiroga et al.**, 2004; **Wild et al.**, 2012): Quian Quiroga and colleagues compared the feature extraction procedures using wavelets against principal component analysis (PCA), the whole spike shape and a set of features. In addition, superparamagnetic clustering (SPC) and K-means clustering were carried out using wavelets and PCA. Superparamagnetic clustering is based on ideas from statistical mechanics, focusing on nearest-neighbour interactions. Since SPC is a stochastic clustering method, the repeated application of the algorithm to the same dataset might yield slightly different results. Clusters found by SPC do not need to have a well-defined mean or low variance, they do not have to be normally distributed and are allowed to overlap (**Quian Quiroga et al.**, 2004). SPC with wavelets led to the fewest classification errors and thus the best performance (**Quian Quiroga et al.**, 2004). Wild and colleagues compared WaveClus to KlustaKwik (**Harris et al.**, 2000) and OSort (**Rutishauser**, 2006) and found WaveClus to be "the most accurate spike sorting algorithm" (**Wild et al.**, 2012).

Hence, in general, the selected spike sorting approach performs well, also in comparison with other spike sorting approaches. However, the above-mentioned limitations still hold.

Temperatures for the SPC algorithm were automatically set by WaveClus, but adjusted manually in order to achieve a clear separation of the clusters. With this, the applied sampling rate of 20 kHz can be viewed as high enough to describe the spike waveforms in sufficient detail.When selecting the temperature, a rather conservative approach was taken, meaning that spikes that could not clearly be assigned to a cluster were rejected and not considered in the analysis. This can again lead to lower spike rates, because spikes that are in any way distorted, e.g. by overlapping with other spikes, or showing slightly different waveforms due a burst, will be excluded from further analysis.

Also, different spike waveforms were observed throughout the experiments. An example is visible in Fig. 2.6: while clusters 2 and 3 exhibit a rather typical action potential shape, the waveform of cluster 1 has a lower amplitude and is much more symmetrical to its peak. This could have several reasons: the distance and position of the neuron(s) to the electrode matters, as well as the shape of the tip itself. Other confounding parameters are non-stationarity of the background noise and electrode drift: the thresholds were set for a whole session, i.e. selected for a timespan of at least 30 minutes of the recording. It is unlikely that the background noise is stationary for this complete time interval, so that with the reliable detection of spikes, there is a bias high-amplitude spikes, while low-amplitude spikes might sometimes have dropped below the threshold. When an electrode drifts towards or away from a certain neuron, this might also alter the recorded waveform, so that these altered spike shapes are excluded from the respective cluster. The signal-to-noise ratio (SNR) was best for experiment 121007 on average, but also differed between different electrodes and sessions for all experiments. Sessions and electrodes with stable background activity and higher SNRs thus will have led to sorting results that are closer to the "ground truth" than for sessions with low SNRs.

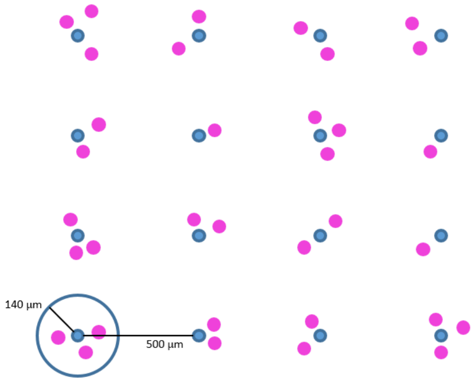

Figure 4.4.: Network topology. The figure shows a schematic of the distribution of units around the electrode tips. It is assumed that spike signals are picked up in a radius of around 140 μm around the electrode tip (Buzsáki, 2004). Distance between the electrodes was 500 μm. Neurons cluster around the electrodes, while the space between the electrodes is not sampled. Note that this is a projection on the 2-dimensional plane, although in reality the networks were 3-dimensional and the electrode tips were placed at slightly different depths. (blue dots: electrode tips, pink dots: single units, circle: radius around electrode tip in which single units are detected)

The electrode constellation and sorting also has an impact on the network topology: the detected units group around the electrode tips, so that, assuming a detection radius of 140 μm around the tip, and a distance of electrodes of at least 500 μm, physical distances between the units of the same electrode are much shorter than between units of different electrodes (see Fig. 4.4).

On the other hand, this also means that it is unlikely that two separate electrodes picked up the spike signal from the same neuron.

4.2.7 Computational aspects

In the field of computational neuroscience, computing time is a very important issue. For this study, the main limiting factor on the amount of analyzed data and the variety of applied methods and parameters was computing time.

To give an example for the impact of long computing times: on a 3.00 GHz computer with 8.00 GB of RAM and an Intel(R) Core(TM)2 Duo CPU, the computations for the GLM method for one session took up to 16 days without interruption. Note that this is only one session with one fixed choice of parameters. Of course, computations were performed in parallel and on faster machines in order to speed up the process. Still, computing time was a major constraint in the analyses that were utilized in this study.

The integration windows for the correlation analyses, for example, were carefully chosen, but this value was set to one fixed value and could not be varied for reasons of computation time. Further variation of these values would certainly be extremely valuable, as the coding of information is likely to be dynamic and there might not even exist one optimal value. The windows relevant for information integration could change in size for different situations.

4.3 Insights into Neural Coding

With the applied methods, the focus was set on synchronous spiking activity (CC, NX) and (one type of) temporal patterns (GLM). From the results, the following conclusion can be drawn:

Finding:
Rates, "assembly-like" structures (CC/NX analysis) and temporal patterns (GLM analysis) all hold information about the deactivation effects on the probed timescales.

4.3.1 Implications on coding strategy

The analysis approaches for NeuroXidence and GLMs assume that synchrony and temporal patterns play a crucial role in information transmission. With the NeuroXidence algorithm (see section 2.7.1), a method that "was designed to test rate against assembly hypothesis" (**Pipa et al.**, 2008) was applied. Thus, all the effects that are found with this method are potential assembly effects. Changes in spike rate were assessed separately to be compared with the effects found in synchrony in order to test the hypotheses. Hence, the effects in rate and temporal patterns can be interpreted separately. As discussed in sections 4.1.3 and 4.1.5, both rates and coordinated activity were affected by the pMS deactivation.

In the cat visual cortex, neurons have been found to engage in synchronous, oscillating firing (**Gray and Singer**, 1989; **Gray et al.**, 1989), and synchronisation and desynchronisation can appear and switch on very short timescales (**Gerstner et al.**, 1996). This supports the idea that those neurons are indeed able to precisely coordinate their firing (**Singer**, 1999b), and that this coordination could play a relevant role in neural information processing.

One issue in detangling the problem of which coding strategy is applied by the brain is that one might be able to find neuronal correlates of certain cognitive functions, but cannot directly link this information to a particular neuronal process. If one does not know what is encoded, there is a risk that one might reach wrong conclusions from observed correlations. Hence, it is important to have an idea about the task(s) the respective brain area has to fulfil. This is especially important because the strategy used to encode information could differ between brain areas: "We anticipate that coding strategies may differ across brain regions, even within a single 'system'" (**Victor** (2006); see also **Jacobs et al.** (2009)). Coding strategies might also change with brain state, and multiple codes might be present simultaneously.

The claim that the spike rate alone is able to carry all the information that is transmitted seems to be refuted: while the spiking rate seems to be proven to carry some information, the receiving neuron is – like the scientist – faced with the question on how to determine the relevant width of the integration window. In any case, the neuron will have to wait for more than one spike to arrive to be able to sense the rate at which the presynaptic neuron(s) is/are firing. Since time constants can vary and external stimuli can also have very different time courses, this does not create an efficient way to extract information from incoming spikes.

In addition, a rigid discrimination between rate coding and temporal coding might be counterproductive, as it is possible to think about the two schemes as the two extremes of the same spectrum, depending on the observation window, such that "the same spike sequence may be interpreted differently (or evoke a different behaviour) later in the day" (**Eggermont**, 1998). In that sense, the code itself is proposed to be unstable and in consequence less significant than the dynamic switching between brain states. However, some studies argue against this notion, stressing the biological relevance of a rigorous distinction of the two schemes (**Theunissen and Miller**, 1995).

Having said this, the variability in the ongoing processes in the brain are one thing, while the measurements of them pose additional obstacles: since in a physiological situation, the rate is unlikely to be stationary, it is extremely difficult to separate contributions of rate and temporal coding (**Gerstner and**

Kistler, 2002), also because correlation between neural spike trains actually does increase with firing rate (**de la Rocha et al.**, 2007).

In summary, the questions of encoding and decoding of information in the brain are still far from being satisfactorily resolved. In order to provide a contribution to the discussion of this issue, for the present study it was decided to probe synchronous and millisecond-precise spiking activity of pairs of neurons and evaluate changes in the correlated activity between these pairs and the changes in experimental parameters. A correlation between neuronal activity and experimental variables is seen as an indication of the observed correlation structure being relevant for the processing of stimulus information in the brain.

4.3.2 Pairwise couplings vs. higher order correlations

There is no physiologically supported reason to assume that neurons are solely coupled in pairs. In fact, neurons typically form synapses with thousands of other neurons. Still, within a recorded subset, patterns of higher order might be extremely sparse, and therefore difficult to detect, but may be all the more crucial if they occur. Therefore, the fact that only pairwise couplings are considered in this study could be considered a major drawback. However, because neurons are connected to such a large number of other neurons, a mere extension to the analysis of triplets or quadruplets would also fail to completely disclose all functional assemblies. Likewise, in order to differentiate between real triplets and the possible pairwise sub-patterns, all these possible patterns must be tested. This attempt would lead to an unmanageable number of patterns to be analyzed, and also require a larger amount of data than the number of recordings that were available for this study. At the same time, the assumption that the brain differentiates between pairs, triplets, quadruplets, and so on, means that the brain would have to distinguish these patterns and separate all hypotheses, which seems highly unlikely because of the complexity of the required computations. In addition, and very importantly so, many graph theoretical analysis methods are only applicable if edges can be described as defined in section 2.8: as the present or absent connection between two nodes. Therefore, a computation of higher order correlations, as for example allowed for by NeuroXidence (**Pipa et al.**, 2008), would require very different subsequent analyses, which contradicts the purpose of this study, where the graph theoretical analysis of the observed networks was intended.

Since plausible effects could be extracted from the data based on solely pairwise interaction, and these findings are also in line with previous findings, I would like to draw the following conclusion:

Finding:
Pairwise correlations **do** hold meaningful information.

4.3.3 Local horizontal networks

The observed local networks are built based on principles of the cortical microcircuitry. The pathways between layers follow a fixed wiring diagram (the *canonical microcircuit*, **Douglas and Martin** (1991)), but the exact micro-anatomical connectivity is unknown. With multi-electrode recordings, it is possible to pick up activity at different sites of the circuit(s), but it is not possible to obtain a complete physiological image of all synaptic events in the circuit. Nevertheless, for the interpretation of the results, knowledge about the underlying circuit can still be advantageous. One drawback in the current study, however, is that there is a lack of information about the exact recording depths, so that the layer that was recorded from could only be estimated, which impedes the interpretation. From the estimation of recording depths (Fig. 3.21) it can be deducted that the recordings did most probably cover multiple layers at the same time. With the electrode matrix as it was applied here, primarily, intrinsic networks between columns were probed. Connectivity within a column, i.e. perpendicular to the surface, cannot be picked up by the recordings, so that a comparison between the two types of connectivity – within a column vs. horizontally – is not possible.

Local horizontal connectivity has mostly been examined within 250 μm around the respective cell, but also up to 1500 μm (see **Boucsein et al.** (2011)). In the present study, the range is considerably larger (500-2121 μm). With the Eckhorn electrode matrix it was not possible to assess local connectivity below the range of 500 μm. The division of connections into „local“ and „remote“ links according to equation 3.1 (p. 56) led to the following distances within the groups (distances in x-y plane): local connections were those reaching up to 707.1 μm, which approximately fits the range of local connections as proposed by Charles Gilbert (750 μm, see **Nelson** (2002)). Remote connections are known to span up to 8 mm (**Galuske and Singer**, 1996). In our study, we could only investigate connections that spanned from 1000 μm up to 2121 μm (limited by the maximum distance between electrodes in the array), thus spanning 2-3 orientation columns (size of a column approx. 400-600 μm (**Kisvarday et al.**, 1997)).

With this, the strongest deactivation effects could actually be observed for sessions 9 and 10 in experiment 121007, namely two sessions in which all electrodes were estimated to be at a similar depth, i.e. possibly within the same layer. In these sessions, data were recorded from supragranular layers, which have been found to exhibit denser horizontal connections as compared to deeper layers (**Lund et al.**, 1993).

Horizontal connectivity becomes particularly crucial if it is assumed that temporal precision is key for neural signal transmission. Although neurons in the visual cortex respond with high firing rates if they are stimulated with an optimal stimulus, it has been hypothesized that the visual cortex actually uses a sparse code, which is observed under natural scenes stimulation (**Olshausen and Field**, 1996). This sparse code would render the temporal precision of inputs and outputs pivotal and horizontal connections could be the means to control this precision. If these connections are now disturbed, for example by missing input from higher regions as observed in the current study, the temporal interaction of the signals gets impaired, which has an effect on temporal codes and assembly coding. This, again, speaks for temporal precision to be crucial in neural signal processing.

4.4 Brain States, Feedback, and Neglect

Considering the initial brain state before pMS deactivation, one important conclusion can be drawn:

Finding:
The extent of the deactivation effects showed a strong dependency on overall brain state.

More precisely, the three "Gamma groups" show different effects: in general, the High Initial Gamma group showed the highest activity, and also the strongest deactivation effects, and turned out to be the most dynamic, for both rates and connectivity measures. For Low and Medium Initial Gamma, the effects were more diffuse. The differences in the scaling of the effects and overall activity level were also traceable in the LFP signal (Figs. 3.15-3.17). This supports the selection of the analysis methods, since it rules out the possibility that the differences were introduced by the selected analysis methods.

It is important to note that the behavioural experiments prior to the recordings showed that in all three experiments, a neglect could be induced by unilateral deactivation of the pMS cortex and bilateral pMS deactivation led to a restitution of behaviour.[2] Hence, the behavioural situation in the awake state was the same in all animals. Despite these similarities, the electrophysiological data revealed noticeable differences in neuronal activity between the recording sessions, as described below. Different manifestations of a disturbance of neuronal activity could thus lead to a similar behavioural outcome.

Payne and Rushmore (2004) explained the phenomenon of neglect by an interhemispheric imbalance that leads to a hyperexcitability of the "healthy", non-impaired hemisphere. However, more recently, **Ptak and Fellrath** (2013) suggested a new model for neglect, based on a disturbance of attentional priority map. This idea was further supported by studies by **Müller** (2017), which indicated that there is no mutual inhibition and no "push-pull" pattern, at least not in the awake behaving animal.

Barnes (2014) assessed the difference between anaesthetized and awake preparations and found that the interhemispheric imbalance that is observed in the anaesthetized cat disappears in the awake animal. In addition, in the anaesthetized animals, alpha power was reduced as compared to the awake state. Assuming that lower frequencies mainly support long-distance communication, this matches the notion that general anaesthesia disconnects brain areas, while local connectivity is less affected (**Casali et al.**, 2013), especially in primary sensory areas. Nevertheless, when global connectivity changes significantly, this will have an immense impact on the timing of signals and, as a consequence, will also alter local connectivity patterns, as observed in the present study.

For all three experiments, the observed brain networks showed differing profiles in their LFP power, absolute spike rates, and variability in spike rates and correlations, with the Low Initial Gamma Power group exhibiting the lowest rates and lowest variabilities. The local network in these sessions could thus be described as less variable and less dynamic. This could reflect a difference in the overall brain state, which, amongst other factors, is dependent on the depth of the anaesthesia (see section 4.4.2). As a consequence, the network might be defragmented from the start, with local activity probably still intact, at least partly, while the global network is disturbed. In this situation, feedback signals are either not generated at all or not passed on to hierarchically lower areas properly. The deactivation of the feedback-sending area thus has a minor additional effect on the lower area.

In general, we expect the following effects when looking at the three different deactivation conditions:

- ipsilateral pMS deactivation → input of contralateral pMS becomes more relevant
- contralateral pMS deactivation → input of ipsilateral pMS becomes more relevant
- bilateral pMS deactivation → the input of other areas than pMS cortex becomes more relevant.

These different inputs are mediated via the corpus callosum, but also via the intercollicular commissure.

The drop in direction selectivity was found to be strongest for bilateral deactivation (see Fig. 3.27). If pMS is required for manifestation of direction selectivity (**Galuske et al.**, 2002), during unilateral deactivation, the contralateral pMS can still support the creation of direction selectivity, while with bilateral pMS deactivation, the signal from pMS is completely extinguished. In this situation, other areas do not seem to be able to take over the missing function of pMS, and the exhibition of direction selectivity cannot be maintained.

---

[2] Note: bilateral deactivation was not performed in experiment 112807.

Interestingly, in the awake, behaving animal, a restitution in behaviour (meaning the neglect disappears) can be observed when both pMS sulci – or both superior colliculi, for that matter – are thermally deactivated (**Lomber and Payne**, 1996). This observation gives rise to the question whether activity levels possibly return to a state of equilibrium during bilateral deactivation in the anaesthetized animal. However, the equilibrium between hemispheres could not directly be assessed here, because bilateral recordings were not performed.

There is one main caveat with studying neglect in the anaesthetized animal: with no attention present during anaesthesia, attention deficits cannot be investigated. Since the system is passively presented with the stimulus, it is rather the neuronal activity and the resulting connectivity patterns rather than the neglect phenomenon as such that can be studied. In the anaesthetized preparation, the sensory input likely outweighs any internal processing, since there is no conscious processing governed by attention, expectation, or prioritisation. This could mean that the system under anaesthesia is more feedforward-based. Following this thought further, the Low Initial Gamma group would be the one where the network is most highly disconnected, with little feedback control. The higher the gamma power gets, the more connected the network gets in turn, enabling proper signal propagation.

Although the separation into groups was based on the power of higher oscillation frequencies in the gamma band, it becomes apparent that there are sessions that also exhibit a higher power in other frequency ranges, while the Low Initial Gamma group shows lower power for almost all frequency bands (Fig. 3.18). This hints at a generally heightened or lowered level of arousal, respectively, which indicates that in the more active situation, communication in all frequency bands is present, i.e. in feedforward and feedback direction, connecting hierarchically higher as well as lower regions.

Altogether, there seems to be a spectrum from wide awake via a drowsy state and light anaesthesia to deep anaesthesia. The spectrum of substates within the state of anaesthesia might be reflected in the different "Gamma groups" that were separated here.

With this, it is not clear whether the main issue in the interplay between anaesthesia and feedback deactivation arises from the disturbance of thalamic activity, cortical activity, other structures, or rather the interactions between multiple brain structures.

In conclusion, it can be stated that a certain level of activity seems to be required for the brain to be able to generate and process feedback signals altogether. With this, the High Initial Gamma Power group seems to be the one most dynamic and active, and thus probably the most promising when it comes to trying to explain healthy brain function.

4.4.1 Criticality

The analysis has shown that different neuronal states can lead to the same behavioural deficit, which supports the idea that there is an optimal state that allows "normal" brain function, which is deviated from in all analyzed individuals during pMS deactivation (though possibly not in the exact same way). The concept of *criticality* (**Beggs and Timme**, 2012) could be a useful framework for the interpretation of the data.

Meaningful communication in the brain requires a certain degree of synchrony, or temporally coordinated activity, but at the same time it requires a certain degree of variability to be able to dynamically process information. At the *critical point*, also referred to as *phase transition point*, coupling and variability are at optimal proportion, and long-distance communication is enabled. Dynamic correlation is strongest, and "neurons can communicate most strongly and over the largest number of synapses" (**Beggs and Timme**, 2012).

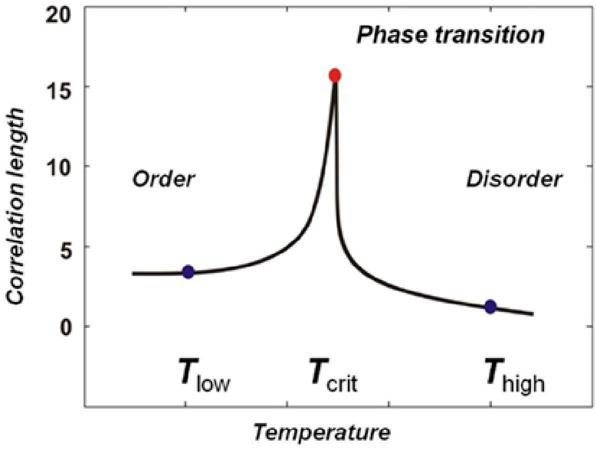

Figure 4.5.: Phase transition. Simulation of the Ising model (for an introduction of the Ising model see Cipra (1987)) in order to illustrate the nature of phase transition. From Beggs and Timme (2012).

Several studies have indicated that the brain operates at a critical state (for a review see **Beggs and Timme** (2012)). In these studies, multiple signals were assessed, including LFP, EEG, MEG, and BOLD[3] data. However, a recent study was not able to confirm criticality for spiking data, but rather found that spiking networks operate at a slightly subcritical state (**Priesemann et al.**, 2014). Advantages of a below-criticality regime might be faster processing and a safety margin that buffers the system from a supercritical state (**Priesemann et al.**, 2014). Even though it has been described that communication, information storage, computational power, dynamic range, and phase synchrony are optimal at the critical point (see summary in **Beggs and Timme** (2012)), the dissociation from a possible supercritical state – which has been associated with epilepsy, as an extreme case of synchronous discharges – might be of even greater importance.

In the analyzed experiments it seems like during neglect the brain state deviates from this optimal, slightly subcritical state. With small network sizes, due to spatial and temporal undersampling of neuronal network activity, systems might be misclassified as being sub- or super-critical, respectively (**Priesemann et al.**, 2009). Still, it could be interesting to analyse the set of networks with respect to criticality.

The hypothesis could be that the crucial difference in the separate groups may have been that, while the networks in the High Initial Gamma Power group operated at a critical or subcritical level, long-range communication in the Low and Medium Initial Gamma groups was disturbed prior to the thermal deactivation – be it by a deeper level of anaesthesia, or other factors – leading to the system being pushed beyond the safety margin and towards a supercritical state.

4.4.2 Effects of anaesthesia

During the course of the experiment, the animals were kept under global anaesthesia. Unarguably, this is a rather artificial situation and it is very likely that several cellular mechanisms are altered as compared to the awake brain. Here, within the "state of anaesthesia" different substates were observed, i.e. although there was one behavioural state – namely quiet unconscious – there seemed to be a gradation in neural state, with state transitions occuring in both a continuous and a discrete fashion. These a priori alterations in activity in the primary visual cortex, as well as in the pMS cortex, could be present

---

[3] BOLD = blood oxygen level dependent

in addition to the effects of thermal deactivation. Although the concentration of halothane was densely monitored and kept at around 0.8 %, the effects of the anaesthetic cannot be fully controlled. Fluctuations in halothane concentration could thus have had considerable effects on the level of activity in area 18 and subsequently on the correlation measures. In combination with the constitution of the animal and its brain before the experiment and the individual metabolic rate, this might have led to different manifestations of the state of narcosis.

Halothane is known to decrease the amount of spikes emitted, when its concentration is increased (**Villeneuve and Casanova**, 2003). Under anaesthesia, figure-ground segregation (**Lamme et al.**, 1998) and the integration of local motion signals (**Pack et al.**, 2001) are impaired, while many functional features in the primary visual areas, such as response amplitude and direction selectivity, are preserved (**Mikami et al.**, 1986; **Pack et al.**, 2001). This preservation of direction selectivity could actually mean that pMS feedback is still in place, since pMS is believed to be necessary for the manifestation of direction selectivity (**Galuske et al.**, 2002).

It has been suggested that potentiation of $GABA_A$ receptors during general anaesthesia might increase inhibition and disrupt oscillatory networks (**Thompson and Wafford**, 2001). A more recent idea, based on results by **Rosner et al.** (1971), suggests that anaesthesia disrupts spike-timing-dependent coding, but leaves rate-coded brain functions largely unaffected (**Swindale**, 2003). It is argued that anaesthesia alters conduction velocity in axonal fibres and thus renders formerly synchronous inputs imprecise. In this situation, a rate code could prove to be more robust than a timing-dependent code, and rate effects might appear stronger in comparison to temporal coding effects than would be the case in the awake animal.

However, many studies about synchrony and temporal patterns have been performed in the anaesthetized animal, and the observed synchronization windows are similar to those in awake recordings (see (**Engel and Singer**, 2001)). In the present study, both effects on the spike rate, as well as on synchrony and temporal patterns were observed. This contradicts the above notion that synchronous inputs are already disrupted by the anaesthesia, and shows that, while synchronous activity might be affected by anaesthesia, it by no means becomes extinct.

General anaesthesia with propofol has been described to lead to a disruption of network connectivity, especially in the parietal network (**Lee et al.**, 2011; **Lewis et al.**, 2012). Under isoflurane and halothane anaesthesia, cortical connectivity has been found to be disrupted, with feedback connections being affected first (**Imas et al.**, 2005).

Alkire et al. (2008) argue that small-world networks, such as the corticothalamic network, might be prone to be strongly affected by anaesthesia since the disconnection from a hub by the disruption of a few long-range connections could lead to a disconnection of the network as a whole.

Liang et al. (2012) found that the disturbance of long-distance connections on average is not more pronounced than for shorter distances, however, the disruption of a few crucial connections could still have a large effect. The same study showed that topological principles (based on clustering coefficient, characteristic path length, small-world-ness and modularity; the latter two also described by **Bullmore and Bassett** (2011)) of the large-scale brain network are not altered under anaesthesia. However, these topological principles become reorganized and the strength of connectivity is reduced.

It has also been proposed that anaesthesia alters activity at much earlier processing stages, such as the thalamus (**Mukherjee and Kaplan**, 1995). **Liang et al.** (2012) also reported an impaired relay in the thalamus with anaesthesia (see also **Boveroux et al.** (2010)). This seems plausible since the thalamus has been referred to as the "gateway to consciousness" (**Crick and Koch**, 2003), and the loss of consciousness is one of the purposes of general anaesthesia. However, it doesn't seem to be clear whether the disturbances in the thalamus are a consequence of disturbances in cortical activity or vice versa (**Boveroux et al.**, 2010).

Since in the present study, variable, stimulus-dependent cortical activity could still be observed in the Low and Medium Initial Gamma groups, it is possible that the driving feedforward stream via LGN might not be strongly affected by the anaesthetic, but other parts of the thalamus are. One candidate for this is the pulvinar: the pulvinar is one of the key players in visual attention (**Shipp**, 2004) and forms connections with multiple areas that are relevant in the study of neglect, such as the primary visual cortex, the pMS cortex and the superior colliculi (**Hughes**, 1980). If this structure gets impaired, so will the whole thalamocortical network, and the extent of this impairment could account for the differences in the Low, Medium, and High Initial Gamma groups.

Ketamine, which was administered at the beginning of the final experiment, has also been described to alter high-level functional networks (**Scheidegger et al.**, 2012; **Lv et al.**, 2016; **Rao et al.**, 2017). However, it only has a short period of effect of approximately 10-20 minutes. Since the recordings were only started several hours after the administration of ketamine, a contribution to the network perturbance by ketamine is not likely.

In summary, it can be stated that within anaesthesia, like within the awake state, there are many different substates to be observed, depending on internal processes and the task to be performed: "anesthetized and awake preparations do not form a dichotomy, but include a range of states with potential similarities and differences in correlations depending on the specific comparison at hand" (**Kohn et al.**, 2009).

With this, the depth of anaesthesia is one candidate for the differences in the frequency profiles, but it is not necessarily the primary one: circadian rhythms – albeit disturbed – might still be present in the anaesthetized animal (**Kärkelä et al.**, 2002; **Brainard et al.**, 2015; **Poulsen et al.**, 2018), while "up" and "down" states might play a role on shorter timescales (**Luczak et al.**, 2007).

4.5 Conclusion

With the methods introduced in this thesis, results were obtained by investigating the dataset on multiple temporal and spatial scales, increasing the granularity: LFP, multi-unit spike rates, correlated activity amongst multi-units, single-unit spike rates, effective connectivity amongst single-units, and tuning properties were assessed. The same general trends, which also match results of previous studies, could be observed throughout the analyses. Therefore, it is concluded that the methods are applicable and valid, since with their application one is able to replicate previous findings, even with small datasets.

With respect to the subsets of data that were analyzed in this study, the observations indicate that, for the Low Initial Gamma and Medium Initial Gamma groups, the global network is already disconnected during the "warm" condition and therefore not very adaptive to changes, which reflects in the local activity. A situation in which the cortical network is already defragmented would mean that the communication between area 18 and pMS is already impaired prior to the pMS deactivation. As a consequence, the deactivation of the pMS then has little or no effect on the ongoing activity. This would also be in line with the low rates and the low overall LFP power that were observed during these recording sessions.

The cortical activity profile of the High Initial Gamma sessions thus, on the spectrum of possible brain states, might be closer to that of the awake state, while the Medium and Low Initial Gamma sessions might be more similar to (slow-wave) sleep (see **Alkire et al.** (2008)).

In conclusion, the initial network state, i.e. the global level of (dis-)connectedness affects neural processing and a certain level of connectivity seems to be an indispensable presupposition for the generation, transmission, and meaningful processing of feedback signals. This seems even more reasonable in the light of the idea that the very basis of consciousness is integration of information (**Engel and Singer**, 2001; **Tononi**, 2008).

Thus, in line with **McGinley et al.** (2015) and **Schölvinck et al.** (2015), it seems strongly advisable to take changes in brain state into account with every assessment of neuronal activity, in both awake and anaesthetized recordings.

4.6 Outlook

The variability in the datasets and the consequent challenges have pushed the utilization of multiple analysis approaches forward. Still, there are many directions in which the research questions could be addressed at a deeper level. Regarding the biological interpretation of the results, the dataset under investigation posed a challenge, especially pertaining to the statistical power due to small sample sizes. Some ideas on how these obstacles could be mended and which following steps could be taken for both the experimental and the analytical methods shall be given in this section.

Electrophysiological recordings

In general, an increase in the number of experiments and sessions would be benefitial to increase the statistical power. Electrode positions were changed so that less repetitions with the same configuration were available. An increase in the number of trials per electrode position would be useful since, for example, the NeuroXidence algorithm needs a certain number of trials so that the significant excess of joint spike events can be determined. These trials could then not be separated in the subsequent anaylsis steps in order to compare the network structure in these trials.

Subsampling occurred on several levels in this study: measurements were only taken in one brain area, although it is evident that multiple areas play a role in the manifestation of neglect as parts of a larger network. Likewise, many thousands of cells are involved in the processing of information and with the relatively small number of electrodes only a few of these neurons were picked up. In addition to these restrictions in the recording of the signals, stimulation conditions were also limited to eight moving directions of a whole-field grating. Furthermore, manipulation of brain function was only performed in one area. Although it is impossible to extend recording and manipulation to all involved areas, it would be desirable to expand the sampled space in all the dimensions mentioned above.

Since it was possible to move the electrodes separately, stable signals could be obtained on almost every electrode by actively searching for suitable cells. However, especially for spike sorting algorithms, tetrode data would have given the advantage of a more precise separation of units. The use of larger arrays, ideally using laminar probes spanning all layers of the cortex, would enable the assessment of not only horizontal networks, but also of laminar interactions inside the recorded area.

Parallel recordings from Area 18 and pMS ipsilateral, but also Area 18 contralateral, pMS contralateral, and other areas – as e.g. performed in the study of **Hofmann** (2020) – would enable the assessment of the information flow between these areas. In this context, recordings from the thalamus might be of particular interest, ideally from both LGN and pulvinar. Bilateral recordings in area 18, especially during bilateral deactivation, would also be valuable in order to assess the disequilibrium between hemispheres. Also, due to the movement of electrodes (and the whole electrode matrix) and the use of different positions, the two corresponding bilateral recording datasets currently cannot be compared. In addition, datasets obtained during deactivation of the superior colliculus could be analyzed in a similar fashion to the present study and compared to the pMS deactivation results.

Another potential experimental approach in this context might be optogenetics (**Boyden et al.**, 2005; **Fenno et al.**, 2011), which could be applied to switch neuronal activity on and off in order to achieve finely targeted reversible deactivation. Optogenetic methods have been applied in cats (see e.g. **Ni et al.** (2016, 2017)). However, in order to achieve deactivation of a whole area, the area must be uniformly transfected and illuminated, which is not trivial to achieve, so that, in comparison, thermal deactivation might still be the better-suited method for similar research questions.

Awake recordings / Aspects of attention

Since the level of anaesthesia is one possible factor in the manifestation of different brain states, it should be aimed at keeping the anaesthesia as light as possible, while at the same time ensuring that the animal is not put in distress. Applying similar analysis approaches to data that were obtained in the awake animal would be even more desirable. The effects of anaesthesia, circadian rhythms, and other possible factors would be removed, while at the same time enabling the study of attention effects on the level of synchrony with passive viewing, but also more elaborate tasks. With this, a comparison of awake and anaesthetized recordings in the same animal could also be of interest.

Awake recordings with reversible thermal deactivation have proven experimentally challenging, but first insights have been obtained (**Rieder**, 2008; **Barnes**, 2014). One of the challenges is to obtain high-quality spike data, because in these setups – at least if the animal is meant to move around and fulfil a task – the electrodes need to be implanted beforehand and cannot be adjusted individually to retrieve a strong and robust signal. In future setups, wireless recording systems could facilitate experiments with freely moving animals.

Classification of brain states

Looking at the results of the present study, within the "Gamma groups", especially within the Medium Initial Gamma group, several states might be mingled into one. Here, it could also be benefitial to perform a more granular analysis and possibly separate the groups even further. For a more precise categorization of brain states, clustering algorithms such as PCA could be applied to better differentiate between brain states, similar to the study of **Stitt et al.** (2017). Instead of the gamma power in the LFP, other criteria for the separation of groups could be probed in order to find the appropriate regressors, such as other frequency bands, initial rate, or laminar position of the electrodes. Coherence between the concerned areas could be studied and utilized as an indicator of the level of integration of the brain network and a comparison of these measures between the awake and anaesthetized state(s). Also, it would be interesting to obtain a more dynamic view of the changes in state in order to evaluate whether state transitions are discrete or continuous. To this end, the size of the temporal analysis windows would have to be decreased and moved over the trial for a sliding window analysis in order to be able to detect changes in states on smaller temporal scales. Another aspect that has not been looked into further is that the LFP spectra indicate that cooling seems to shift the "characteristic gamma" (**van Pelt et al.**, 2012) to higher frequencies (see Fig. 3.15). This could be worthwhile looking into in future studies.

Analysis methods

Regarding the sampling issues (see section 4.2.4), methods like "subsampling scaling" (**Levina and Priesemann**, 2017), which comprises a calculation of the underlying network properties, could be applied to compensate for (sub)sampling effects.

The networks only provide snapshots in time, but they change over the course of the trial. Thus, as an expansion of the connectome, the *dynome*, a dynamic version of the connectome, as introduced by **Kopell et al.** (2014), promises help to better understand the temporal structure of information signalling and enable to link the connectome to the underlying physiological processes in more detail.

Reference networks

Depending on the structure of the graphs to be analyzed, a reference model other than that of random Erdös-Rényi graphs could provide better results. However, it is the first option one should test, as one should exclude randomness of the networks. As an outlook, the random graph model, should, subsequently, also be replaced by other models. Possible alternatives are small-world or scale-free networks, or even more complex models that could be based on the known functional properties of local neuronal networks.

Another limitation of the study is that only measurements of synchrony between pairs of (multi-unit) signals were included. Including higher-order correlations could be very valuable for the thorough investigation of the connectivity patterns and should be accomplished in the future, together with the examination of network motifs.

At the same time, more comprehensive toolboxes for graph theoretical analyses, such as `GraphVar` (**Kruschwitza et al.**, 2015), are being developed and extended and could be utilized in future studies.

Model complexity

An idea that might be worth investigating further is the following: an initial high-dimensional state space with many priors is reduced by a) deactivation and b) stimulation. This reduction in priors would be due to the fact that there are less internal variables caused by a smaller set of possible outcomes; deactivation could reduce the ability to create these priors while stronger stimulation would reduce the uncertainty of the input. Hence, both these factors could change the internal model to one with less principal components.

Interestingly, for the PARAFAC model applied to the dataset in this study, the opposite was the case: the number of components of the PARAFAC model increased with stronger stimulation and was highest for the High Initial Gamma group (see Fig. 3.3). Hence, the networks seem to get more complex with higher initial integration and stronger stimulation. This, however, could again be due to disconnectedness in the initial phase for the Low and Medium Initial Gamma networks.

Hence, further investigation could be useful and first steps towards addressing this question have been taken (**Barnes et al.**, in preparation).

The future of connectomics

The computation of functional brain networks depends on the experimental setup and the parameters used for the computation of connectivity. For this reason, the networks can only be an abstraction, a mere model of the real underlying structures. Heterogeneity, dynamics, and variability of the physiological basis are, to a large extent, neglected. However, with the experimental and analytical methods that are available at present, there is currently no universal remedy in order to solve all these problems.

Many collaborations dedicated to brain networks, supported by millions of dollars, have been founded over the past years and have also received a lot of public attention, such as the Human Brain Project (https://www.humanbrainproject.eu/[4]), the Brain Activity Map Project (or BRAIN Initiative, http://www.kavlifoundation.org/brain-activity-map-project), the Human Connectome Project (**van Essen et al.**, 2013), and the Human Cell Atlas (https://www.humancellatlas.org/). Although some of these approaches have been criticized as over-ambitious or not to focus on the right reserach questions (see e.g. **Frégnac and Laurent** (2014)), these projects could potentially contribute a great deal to the understanding of processing in the brain.

Nevertheless, the results of this thesis show that the applied methods provide a practical approach to the assessment of network structures, in the brain and elsewhere.

---

[4] websites all viewed on 16 December 2018

A Appendix

This appendix gives an overview on the dataset that was analyzed in the present study and lists the number of recording sessions with deactivation condition and recorded hemisphere for each session.

Note: in experiment 101007, session 8 does not exist due to misnumbering. Session 6 was excluded from the analysis because the eyes were not aligned during the recording.

🟩 left hemisphere

🟦 right hemisphere

experiment 101007, "Bob"

	dataset no.	condition	session no.	block no.
warm	001-003		1B	**1**
cooling	004-006	ipsi		
rewarm	007-009			
warm	008-010		2B	
cooling	011-013	contra		
rewarm	5-017 (014-016)			
warm	015-017		3B	
cooling	018-020	bilateral		
rewarm	021-023			
warm	025-027		4B	**2**
cooling	028-030	ipsi		
rewarm	031-033			
warm	032-034		5B	
cooling	035-037	contra		
rewarm	038-040			
warm	039-041		6B	
cooling	042-044	bilateral		
rewarm	045-048			
warm	049-051		7B	**3**
cooling	052-054	ipsi		
rewarm	055-057			
warm	056-058		8B	
cooling	059-061	contra		
rewarm	062-064			
warm	063-065		9B	
cooling	066-068	bilateral		
rewarm	069-071			
warm	072-074		10B	**4**
cooling	075-077	ipsi		
rewarm	078-080			
warm	079-081		11B	
cooling	082-084	contra		
rewarm	085-087			
warm	085-087		12B	
cooling	088-090	bilateral		
rewarm	091-093			
warm	094-096		13B	**5**
cooling	097-099	contra		
rewarm	100-102			
warm	101-103		14B	
cooling	104-106	bilateral		
rewarm	107-109			
warm	110-112		15B	**6**
cooling	113-115	contra		
rewarm	116-118			
warm	117-119		16B	
cooling	120-122	bilateral		
rewarm	123-125			

warm	126-128		17B	**7**
cooling	129-131	contra		
rewarm	132-134			
warm	133-135		18B	
cooling	136-138	bilateral		
rewarm	139-141			
warm	140-142		19B	
cooling	143-145	ipsi		
rewarm	146-148			
warm	149-151		20B	**9**
cooling	152-154	ipsi		
rewarm	155-157			
warm	156-158		21B	
cooling	159-161	contra		
rewarm	162-164			
warm	163-165		22B	
cooling	166-168	bilateral		
rewarm	169-171			
warm	172-174		23B	**10**
cooling	175-177	contra		
rewarm	178-180			
warm	179-181		24B	
cooling	182-184	bilateral		
rewarm	185-187			
warm	188-190		25B	**11**
cooling	191-193	bilateral		
rewarm	194-196			
warm	195-197		26B	
cooling	198-200	contra		
rewarm	201-203			
warm	204-206		27B	**12**
cooling	207-209	contra		
rewarm	210-212			
warm	211-213		28B	
cooling	214-216	bilateral		
rewarm	217-219			
warm	220-222		29B	**13**
cooling	223-225	contra		
rewarm	226-228			
warm	227-229		30B	
cooling	230-231	ipsi		
rewarm	233-235			
warm	234-235		31B	
cooling	237-239	bilateral		
rewarm	240-242			
warm	243-245		32B	**14**
cooling	246-248	contra		
rewarm	249-251			
warm	250-252		33B	
cooling	253-255	ipsi		
rewarm	256-258			
warm	260-262		34B	
cooling	263-265	bilateral		
rewarm	266-268			

experiment 121007, "Timon"

	dataset no.	condition	session no.	block no.
warm	001-003		1T	**1**
cooling	004-006	ipsi		
rewarm	007-009			
warm	008-010		2T	
cooling	011-013	contra		
rewarm	014-016			
warm	015-017		3T	
cooling	018-020	bilateral		
rewarm	021-023			
warm	024-026		4T	**2**
cooling	027-029	contra		
rewarm	030-032			
warm	031-033		5T	
cooling	034-036	bilateral		
rewarm	037-039			
warm	040-042		6T	**3**
cooling	043-045	contra		
rewarm	046-048			
warm	047-049		7T	
cooling	050-052	ipsi		
rewarm	053-055			
warm	054-056		8T	
cooling	057-059	bilateral		
rewarm	060-062			
warm	063-065		9T	**4**
cooling	066-068	ipsi		
rewarm	069-071			
warm	070-072		10T	
cooling	073-075	contra		
rewarm	076-078			
warm	077-079		11T	
cooling	080-082	bilateral		
rewarm	083-085			
warm	086-088		12T	**5**
cooling	089-091	bilateral		
rewarm	092-094			
warm	095-097		13T	**6**
cooling	098-100	bilateral		
rewarm	101-103			
warm	104-106		14T	**7**
cooling	107-109	contra		
rewarm	110-112			
warm	110-112		15T	
cooling	113-115	ipsi		
rewarm	116-118			
warm	117-119		16T	
cooling	120,121,123	bilateral		
rewarm	124-126			
warm	127-129		17T	**8**
cooling	130-132	ipsi		
rewarm	133-135			

warm	136-138		18T	**9**
cooling	139-141	ipsi		
rewarm	142-144			
warm	143-145		19T	
cooling	146-148	contra		
rewarm	149-151			
warm	150-152		20T	
cooling	153-155	bilateral		
rewarm	156-158			
warm	159-161		21T	**10**
cooling	162-164	ipsi		
rewarm	165-167			
warm	166-168		22T	
cooling	169-171	contra		
rewarm	172-174			
warm	173-175		23T	
cooling	176-178	bilateral		
rewarm	179-181			
warm	182-184		24T	**11**
cooling	185-187	contra		
rewarm	188-190			
warm	189-191		25T	
cooling	192-194	bilateral		
rewarm	195-197			
warm	198-200		26T	**12**
cooling	201-203	contra		
rewarm	204-206			
warm	205-207		27T	
cooling	208-210	ipsi		
rewarm	211-213			
warm	212-214		28T	
cooling	215-217	bilateral		
rewarm	218-220			
warm	221-223		29T	**13**
cooling	224-226	ipsi		
rewarm	227-229			
warm	228-230		30T	
cooling	231-233	bilateral		
rewarm	234-236			
warm	237-239		31T	**14**
cooling	240-242	ipsi		
rewarm	243-245			
warm	243-245		32T	
cooling	246-248	contra		
rewarm	249-251			
warm	250-252		33T	
cooling	253-255	bilateral		
rewarm	256-258			

experiment 112807, "Sancho"

	dataset no.	condition	session no.	block no.
warm	001-003		1S	**1**
cooling	004-006	ipsi		
rewarm	007-009			
warm	010-012		2S	**2**
cooling	013-015	ipsi		
rewarm	016-018			
warm	019-021		3S	**3**
cooling	022-024	ipsi		
rewarm	025-027			
warm	028-030		4S	**4**
cooling	031-033	ipsi		
rewarm	034-036			
warm	037-039		5S	**5**
cooling	040-042	ipsi		
rewarm	043-045			
warm	046-048		6S	**6**
cooling	049-051	ipsi		
rewarm	052-054			
warm	055-057		7S	**7**
cooling	058-060	ipsi		
rewarm	061-063			
warm	064-066		8S	**8**
cooling	067-069	ipsi		
rewarm	070-072			
warm	073-078		9S	**9**
cooling	079-081	contra		
rewarm	082-084			
warm	085-087			
warm	088-090		10S	**10**
cooling	091-093	contra		
rewarm	094-096			
warm	097-102		11S	**11**
cooling	103-105	contra		
rewarm	106-108			
warm	109-111		12S	**12**
cooling	112-114	contra		
rewarm	115-117			
warm	118-120		13S	**13**
cooling	121-123	contra		
rewarm	124-126			
warm	127-129		14S	**14**
cooling	130-132	contra		
rewarm	133-135			

Bibliography

Achacoso, T. B. and Yamamoto, W. S. (1991), AY's Neuroanatomy of C. elegans for Computation (CRC Press, Taylor & Francis, Boca Raton, FL)

Adrian, E. D. and Zotterman, Y. (1926), The impulses produced by sensory nerve endings: Part ii: The response of a single end-organ, *J Physiol.*, 61, 151–171

Ahrens, M. B., Orger, M. B., Robson, D. N., Li, J. M., and Keller, P. J. (2013), Whole-brain functional imaging at cellular resolution using light-sheet microscopy, *Nature Methods*, 10, 413–420

Ainsworth, M., Lee, S., Cunningham, M. O., Traub, R. D., Kopell, N. J., and Whittington, M. A. (2012), Rates and rhythms: a synergistic view of frequency and temporal coding in neuronal networks, *Neuron*, 75, 572–583

Akam, T. and Kullmann, D. M. (2014), Oscillatory multiplexing of population codes for selective communication in the mammalian brain, *Nat. Rev. Neurosci.*, 15, 111–122

Albert, R., Jeong, H., and Barabási, A.-L. (1999), Diameter of the world-wide web, *Nature*, 401, 130–131

Albus, K. and Beckmann, R. (1980), Second and third visual areas of the cat: interindividual variability in retinotopic arrangement and cortical location, *J Physiol.*, 299, 247–276

Alivisatos, A. P., Chun, M., Church, G. M., Greenspan, R. J., Roukes, M. L., and Yuste, R. (2012), The brain activity map project and the challenge of functional connectomics, *Neuron*, 74, 970–974

Alkire, M. T., Hudetz, A. G., and Tononi, G. (2008), Consciousness and anesthesia, *Science*, 322, 5903, 876–880

Amaral, L. A. N., Scala, A., Barthélémy, M., and Stanley, H. E. (2000), Classes of small-world networks, *Proc. Natl. Acad. Sci. USA*, 97, 21, 11149–11152

Andersson, C. A. and Bro, R. (2000), The N-way toolbox for MATLAB, *Chemom. Intell. Lab. Syst.*, 52, 1, 1–4

Arieli, A., Sterkin, A., and Grinvald, A. (1996), Dynamics of ongoing activity: explanation of the large variability in evoked cortical responses, *Science*, 273, 1868–1871

Bal, T., Debay, D., and Destexhe, A. (2000), Cortical feedback controls the frequency and synchrony of oscillations in the visual thalamus, *J. Neurosci.*, 20, 19, 7478–7488

Banks, D. (1994), Metric inferences for social networks, *Journal of Classification*, 11, 121–149

Barabási, A. (2009), Scale-free networks: a decade and beyond, *Science*, 325, 5939, 412–413

Barabási, A.-L. and Albert, R. (1999), Emergence of scaling in random networks, *Science*, 286, 509–512

Barnes, W. H. (2014), Reversible Visual Hemineglect: the Role of Neural Oscillations in Primary Visual Cortex, Ph.D. thesis, Technische Universität Darmstadt

Bartolomeo, P. (2007), Visual neglect, *Curr Opin Neurol*, 20, 4, 381–386

Bassett, D. S. and Bullmore, E. (2006), Small-world brain networks, *The Neuroscientist*, 12, 512–523

Bastos, A. M. and Schoffelen, J.-M. (2016), A tutorial review of functional connectivity analysis methods and their interpretational pitfalls, *Front. Syst. Neurosci.*, 9, 175, 1–23

Bastos, A. M., Vezoli, J., Bosman, C. A., Schoffelen, J.-M., Oostenveld, R., Dowdall, J. R., et al. (2015), Visual areas exert feedforward and feedback influences through distinct frequency channels, *Neuron*, 85, 390–401

Bean, B. P. (2007), The action potential in mammalian central neurons, *Nat. Rev. Neurosci.*, 8, 6, 451–65

Bear, M. F., Connors, B. W., and Paradiso, M. A. (2008), Neurowissenschaften - Ein grundlegendes Lehrbuch für Biologie, Medizin und Psychologie (Spektrum Akademischer Verlag, Heidelberg), 3 edition

Beggs, J. M. and Timme, N. (2012), Being critical of criticality in the brain, *Frontiers in Physiology*, 3, 163, 1–14

Berg, J. and Lässig, M. (2004), Local graph alignment and motif search in biological networks, *Proc. Natl. Acad. Sci. USA*, 101, 41, 14689–14694

Berger, H. (1929), Ueber das Elektroenkephalogramm des Menschen, *Archiv für Psychiatrie und Nervenkrankheiten*, 87, 1, 527–570

Bi, G. and Poo, M. (1998), Synaptic modifications in cultured hippocampal neurons: Dependence on spike timing, synaptic strength, and postsynaptic cell type, *J. Neurosci.*, 18, 24, 10464–10472

Bisiach, E., Capitani, E., Luzzatti, C., and Perani, D. (1981), Brain and conscious representation of outside reality, *Neuropsychologia*, 19, 4, 543–551

Blatt, M., Wiseman, S., and Domany, E. (1996), Super-paramagnetic clustering of data, *Phys. Rev. Lett.*, 76, 3251–3254

Boucsein, C., Nawrot, M. P., Schnepel, P., and Aertsen, A. (2011), Beyond the cortical column: abundance and physiology of horizontal connections imply a strong role for inputs from the surround, *Frontiers in Neuroscience*, 5, 32

Boveroux, P., Vanhaudenhuyse, A., Bruno, M. A., Noirhomme, Q., Lauwick, S., Luxen, A., et al. (2010), Breakdown of within- and between-network resting state functional magnetic resonance imaging connectivity during propofol-induced loss of consciousness, *Anesthesiology*, 113, 5, 1038–1053

Boyden, E., Zhang, F., Bamberg, E., Nagel, G., and Deisseroth, K. (2005), Millisecond-timescale, genetically targeted optical control of neural activity, *Nat. Neurosci.*, 8, 9, 1263–1268

Brainard, J., Gobel, M., Bartels, K., Scott, B., Koeppen, M., and Eckle, T. (2015), Circadian rhythms in anesthesia and critical care medicine: Potential importance of circadian disruptions, *Semin Cardiothorac Vasc Anesth*, 19, 1, 49–60

Braitenberg, V. and Schüz, A. (1998), Statistics and Geometry of Neuronal Connectivity (Springer, Berlin)

Bro, R. (1997), PARAFAC. Tutorial and applications, *Chemometrics and Intelligent Laboratory Systems*, 38, 149–171

Bro, R. (1998), Multi-way analysis in the food industry: Models, algorithms, and applications, Ph.D. thesis, University of Amsterdam

Bro, R. and Kiers, H. A. L. (2003), A new efficient method for determining the number of components in PARAFAC methods, *Journal of Chemometrics*, 17, 274–286

Brooks, V. B. (1983), Study of brain function by local, reversible cooling, volume 95 (Springer, Berlin Heidelberg)

Bullmore, E. and Sporns, O. (2009), Complex brain networks: graph theoretical analysis of structural and functional systems, *Nature Reviews Neuroscience*, 10, 186–198

Bullmore, E. T. and Bassett, D. S. (2011), Brain graphs: Graphical models of the human brain connectome, *Annu. Rev. Clin. Psychol.*, 7, 113–140

Buschman, T. J. and Miller, E. K. (2007), Top-down versus bottom-up control of attention in the prefrontal and posterior parietal cortices, *Science*, 315, 5820, 1860–1862

Butts, C. T. and Carley, K. M. (2005), Some simple algorithms for structural comparison, *Computational & Mathematical Organization Theory*, 11, 291–305

Buzsáki, G. (2004), Large-scale recording of neuronal ensembles, *Nat. Neurosci.*, 7, 5, 446–51

Buzsáki, G. (2005), Theta rhythm of navigation: link between path integration and landmark navigation, episodic and semantic memory, *Hippocampus*, 15, 7, 827–840

Buzsáki, G. (2006), Rhythms of the brain (Oxford University Press, Inc., New York)

Buzsáki, G. and Moser, E. I. (2013), Memory, navigation and theta rhythm in the hippocampal-entorhinal system, *Nat. Neurosci.*, 16, 130–138

Calabresi, P., Centonze, D., Pisani, A., Cupini, L., and Bernardi, G. (2003), Synaptic plasticity in the ischaemic brain, *Lancet Neurol.*, 2, 10, 622–629

Carandini, M. (2012), Area V1, *Scholarpedia*, 7, 7, 12105

Carroll, J. D. and Chang, J. (1970), Analysis of individual differences in multidimensional scaling via an N-way generalization of an 'Eckart-Young' decomposition, *Psychometrika*, 35, 3, 283–319

Casali, A. G., Gosseries, O., Rosanova, M., Boly, M., Sarasso, S., Casali, K. R., et al. (2013), A theoretically based index of consciousness independent of sensory processing and behavior, *Sci Transl Med*, 5, 198, 198ra105

Cipra, B. A. (1987), An introduction to the Ising model, *Am. Math. Mon.*, 94, 937–959

Cohen, M. R. and Kohn, A. (2011), Measuring and interpreting neuronal correlations, *Nat. Neurosci.*, 14, 7, 811–819

Crick, F. and Koch, C. (2003), A framework for consciousness, *Nat. Neurosci.*, 6, 119–126

Daley, D. J. and Vere-Jones, D. (2003), An introduction to the theory of point processes. Vol. I: Elementary theory and methods. 2nd ed (Springer-Verlag, New York)

de Costa, N. M. and Martin, K. A. C. (2013), Sparse reconstruction of brain circuits: Or, how to survive without a microscopic connectome, *NeuroImage*, 80, 27–36

de la Rocha, J., Doiron, B., Shea-Brown, E., Josić, K., and Reyes, A. (2007), Correlation between neural spike trains increases with firing rate, *Nature*, 448, 802–807

de Nó, R. L. (1949), Cerebral cortex: architecture, intracortical connections, motor projections, in J. F. Fulton, ed., Physiology of the Nervous System (Oxford University Press, New York, NY), 288–312

Destexhe, A. and Bedard, C. (2013), Local field potential, *Scholarpedia*, 8, 8, 10713

Douglas, R. J. and Martin, K. A. C. (1991), A functional microcircuit for cat visual cortex, *J Physiol.*, 440, 735–769

Ebisch, B. (2007), Studien zur Funktionalität kortikaler Rückprojektionen. Dissertation, Ph.D. thesis, Technische Universität Darmstadt / Max-Planck-Institut für Hirnforschung

Efron, B. and Tibshirani, R. J. (1993), An Introduction to the Bootstrap (Chapman & Hall, New York)

Eggermont, J. J. (1998), Is there a neural code?, *Neuroscience & Biobehavioral Reviews*, 22, 2, 355–370

Eguíluz, V. M., Chialvo, D. R., Cecchi, G. A., Baliki, M., and Apkarian, A. V. (2005), Scale-free brain functional networks, *Phys. Rev. Lett.*, 94, 018102

Elsegai, H., Shiells, H., Thiel, M., and Schelter, B. (2015), Network inference in the presence of latent confounders: the role of instantaneous causalities, *J. Neurosci. Methods*, 245, 91–106

Engel, A. K., Fries, P., and Singer, W. (2001), Dynamic predictions: Oscillations and synchrony in top-down processing, *Nature*, 2, 10, 704–716

Engel, A. K., König, P., Gray, C. M., and Singer, W. (1990), Stimulus-dependent neuronal oscillations in cat visual cortex: Inter-columnar interaction as determined by cross-correlation analysis, *European J Neurosci.*, 2, 588–606

Engel, A. K. and Singer, W. (2001), Temporal binding and the neural correlates of sensory awareness, *Trends in Cognitive Sciences*, 5, 1, 16–25

Erdös, P. and Rényi, A. (1959), On random graphs, *Publ. Math. Debrecen*, 6, 290–297

Fee, M. S., Mitra, P. P., and Kleinfeld, D. (1996), Variability of extracellular spike wave-forms of cortical neurons, *J. Neurophysiol.*, 76, 3823–3833

Felleman, D. and van Essen, D. C. (1991), Distributed hierarchical processing in the primate cerebral cortex, *Cerebral Cortex*, 1, 1–47

Fenno, L., Yizhar, O., and Deisseroth, K. (2011), The development and application of optogenetics, *Annu. Rev. Neurosci.*, 34, 389–412

Field, A. S. and Graupe, D. (1991), Topographic component (parallel factor) analysis of multichannel evoked potentials: practical issues in trilinear spatiotemporal decomposition, *Brain Topogr.*, 3, 4, 407–423

Fino, E. and Yuste, R. (2011), Dense inhibitory connectivity in neocortex., *Neuron*, 69, 6, 1188–1203

Frégnac, Y. and Laurent, G. (2014), Neuroscience: Where is the brain in the human brain project?, *Nature*, 513, 7516, 27–29

Fries, P. (2005), A mechanism for cognitive dynamics: neuronal communication through neuronal coherence, *TRENDS in Cognitive Sciences*, 9, 10, 474–480

Fries, P. (2015), Rhythms for cognition: communication through coherence, *Neuron*, 88, 1, 220–235

Galán, R. F., Ermentrout, B., and Urban, N. N. (2008), Optimal time scale for spike-time reliability: Theory, simulations, and experiments, *J. Neurophysiol.*, 99, 277–283

Galuske, R. A. W., Schmidt, K. E., Goebel, R., Lomber, S. G., and Payne, B. (2002), The role of feedback in shaping neural representations in cat visual cortex, *Proc. Natl. Acad. Sci. USA*, 99, 26, 17083–17088

Galuske, R. A. W. and Singer, W. (1996), The origin and topography of long-range intrinsic projections in cat visual cortex: A developmental study, *Cerebral Cortex*, 6, 3, 417–430

Galvani, A. (1894), Abhandlung über die Kräfte der Electricität bei der Muskelbewegung (Comm. Bonon. Sc. et Art. Inst. et Acad. T. 7; 1791, Originaltitel: De viribus electricitatis in motu musculari commentarius) (Engelmann, Leipzig)

Gansel, K. (2014), A new perspective on the organization of neuronal activity in neocortex and its implications for neuronal information processing and coding, Ph.D. thesis, Carl von Ossietzky Universität Oldenburg

Geider, K. (2008), Einfluss von kortikalen Feedback-Signalen auf die Informationsverarbeitung im primären visuellen Kortex, Diplomarbeit, Technische Universität Darmstadt

Georgii, H.-O. (2007), Stochastik (de Gruyter, Berlin), 3rd edition

Gerhard, F., Pipa, G., Lima, B., Neuenschwander, S., and Gerstner, W. (2011), Extraction of network topology from multi-electrode recordings: is there a small-world effect?, *Frontiers in Computational Neuroscience*, 5, 4

Gerstein, G. L., Bedenbaugh, P., and Aertsen, A. M. H. J. (1989), Neuronal assemblies, *IEEE Transactions on Biomedical Engineering*, 36, 1, 4–14

Gerstner, W., Kempter, R., van Hemmen, J. L., and Wagner, H. (1996), A neuronal learning rule for sub-millisecond temporal coding, *Nature*, 383, 76–78

Gerstner, W. and Kistler, W. (2002), Spiking Neuron Models: Single Neurons, Populations, Plasticity (Cambridge University Press, Cambridge)

Gervasoni, D., Lin, S. C., Ribeiro, S., Soares, E. S., Pantoja, J., and Nicolelis, M. A. (2004), Global forebrain dynamics predict rat behavioral states and their transitions, *J. Neurosci.*, 24, 11137–11147

Gilbert, C. D. and Sigman, M. (2007), Brain states: Top-down influences in sensory processing, *Neuron*, 54, 677–696

Gilbert, C. D. and Wiesel, T. N. (1989), Columnar specificity of intrinsic horizontal and corticocortical connections in cat visual cortex, *J. Neurosci.*, 9, 7, 2432–2442

Golledge, H. D., Hilgetag, C. C., and Tovée, M. J. (1996), Information processing: A solution to the binding problem?, *Current Biology*, 6, 9, 1092–1095

Granger, C. W. J. (1969), Investigating causal relations by econometric models and cross-spectral methods, *Econometrica*, 37, 3, 424–438

Gray, C. M., König, P., Engel, A. K., and Singer, W. (1989), Oscillatory responses in cat visual cortex exhibit inter-columnar synchronisation which reflects global stimulus properties, *Nature*, 338, 334–337

Gray, C. M. and Singer, W. (1989), Stimulus-specific neuronal oscillations in orientation columns of cat visual cortex, *Proc. Natl. Acad. Sci. USA*, 86, 5, 1698–1702

Grinvald, A., Arieli, A., Tsodyks, M., and Kenet, T. (2003), Neuronal assemblies: Single cortical neurons are obedient members of a huge orchestra, *Biopolymers*, 68, 422–436

Grossberg, S. (1976), Adaptive pattern classification and universal recoding: II. Feedback, expectation, olfaction, illusions, *Biological Cybernetics*, 23, 4, 187–202

Hamming, R. W. (1950), Error detecting and error correcting codes, *The Bell System Technical Journal*, 26, 2, 147–160

Harris, K. D., Henze, D. A., Csicsvari, J., Hirase, H., and Buzsáki, G. (2000), Accuracy of tetrode spike separation as determined by simultaneous intracellular and extracellular measurements, *J. Neurophysiol.*, 84, 401–414

Harshman, R. A. (1970), Foundations of the PARAFAC procedure: Model and conditions for an 'explanatory' multi-mode factor analysis, *UCLA Working Papers in phonetics*, 16, 1–84

Harshman, R. A. and Lundy, M. E. (1994), PARAFAC: Parallel factor analysis, *Computational Statistics and Data Analysis*, 18, 39–72

Hasselmo, M. E. (2005), What is the function of hippocampal theta rhythm? - linking behavioral data to phasic properties of field potential and unit recording data, *Hippocampus*, 15, 7, 936–949

Hebb, D. O. (1949), The organization of behavior: A neuropsychological theory (John Wiley Sons, New York)

Henß, L. C. (2012), Untersuchungen zu Feedback-Einflüssen auf neuronale Antworten im visuellen Kortex der Katze - Feedback influence on neuronal responses in cat visual cortex, Bachelor's thesis, Technische Universität Darmstadt

Hildago, C. A. and Barabási, A.-L. (2008), Scale-free networks, *Scholarpedia*, 3, 1, 1716

Hitchcock, F. L. (1927), The expression of a tensor or a polyadic as a sum of products, *Journal of Mathematics and Physics*, 6, 164–189

Hochstein, S. and Ahissar, M. (2002), View from the top: Hierarchies and reverse hierarchies in the visual system, *Neuron*, 36, 5, 791–804

Hoeffding, W. (1963), Probability inequalities for sums of bounded random variables, *J. Amer. Statist. Assoc.*, 58, 13–30

Hofmann, D. (2020), Interareale raumzeitliche Dynamiken und Variabilität der Akivität neuronaler Populationen im visuellen Kortex der Katze, Ph.D. thesis, Technische Universität Darmstadt

Hubel, D. H. and Wiesel, T. N. (1959), Receptive fields of single neurones in the cat's striate cortex, *J Physiol.*, 148, 3, 574–591

Hubel, D. H. and Wiesel, T. N. (1962), Receptive fields, binocular interaction and functional architecture in the cat's visual cortex, *J Physiol.*, 160, 106–154

Hubel, D. H. and Wiesel, T. N. (1965), Receptive fields and functional architecture in two nonstriate visual areas (18 and 19) of the cat, *J. Neurophysiol.*, 28, 229–289

Hughes, H. C. (1980), Efferent organization of the cat pulvinar complex, with a note on bilateral claustrocortical and reticulocortical connections, *J. Comp. Neurol.*, 193, 937–963

Hupé, J. M., James, A. C., Payne, B. R., Lomber, S. G., Girard, P., and Bullier, J. (1998), Cortical feedback improves discrimination between figure and background by V1, V2 and V3 neurons, *Nature*, 394, 6695, 784–787

Imas, O. A., Ropella, K. M., Ward, B. D., Wood, J. D., and Hudetz, A. G. (2005), Volatile anesthetics disrupt frontal-posterior recurrent information transfer at gamma frequencies in rat, *Neurosci. Lett.*, 387, 3, 145–150

Isaacson, J. S. and Scanziani, M. (2011), How inhibition shapes cortical activity, *Neuron*, 72, 2, 231–243

Jacobs, A. L., Fridman, G., Douglas, R. M., Alam, N. M., Latham, P. E., Prusky, G. T., et al. (2009), Ruling out and ruling in neural codes, *Proc. Natl. Acad. Sci. USA*, 106, 14, 5936–5941

Jolliffe, I. (2002), Principal Component Analysis (Springer, New York)

Kaiser, M., Hilgetag, C. C., and Kötter, R. (2010), Hierarchy and dynamics of neural networks, *Frontiers in Neuroinformatics*, 4, 112

Kajikawa, M. and Schroeder, C. E. (2011), How local is the local field potential?, *Neuron*, 72, 847–858

Kandel, E. R., Schwartz, J. H., and Jessel, T. M. (2000), Principles of Neural Science (McGraw-Hill, New York), 4. edition

Kayser, C., Logothetis, N. K., and Panzeri, S. (2010), Millisecond encoding precision of auditory cortex neurons, *Proc. Natl. Acad. Sci. USA.*, 107, 39, 16976–16981

Kenet, T., Bibitchkov, D., Tsodyks, M., Grinvald, A., and Arieli, A. (2003), Spontaneously emerging cortical representations of visual attributes, *Nature*, 425, 954–956

Kiers, H. A. L. (1991), Hierarchical relations among three-way models, *Psychometrika*, 56, 3, 449–470

Kisvarday, Z., Toth, E., Rausch, M., and Eysel, U. (1997), Orientation-specific relationship between populations of excitatory and inhibitory lateral connections in the visual cortex of the cat, *Cereb Cortex*, 7, 605–618

Kohn, A., Zandvakili, A., and Smith, M. A. (2009), Correlations and brain states: from electrophysiology to functional imaging, *Current Opinion in Neurobiology*, 19, 434–438

Kopell, N., Kramer, M. A., Malerba, P., and Whittington, M. A. (2010), Are different rhythms good for different functions?, *Frontiers in Human Neuroscience*, 4, 187, 1–9

Kopell, N. J., Gritton, H. J., Whittington, M. A., and Kramer, M. A. (2014), Beyond the connectome: the dynome, *Neuron*, 83, 1319–1328

Kärkelä, J., Vakkuri, O., Kaukinen, S., Huang, W.-Q., and Pasanen, M. (2002), The influence of anaesthesia and surgery on the circadian rhythm of melatonin, *Acta Anaestesiol Scand*, 46, 30–36

Kroonenberg, P. M. and de Leeuw, J. (1980), Principal component analysis of three-mode data by means of alternating least squares algorithms, *Psychometrika*, 45, 1, 69–97

Kruschwitza, J., Lista, D., Walleraa, L., Rubinov, M., and Walter, H. (2015), GraphVar: a user-friendly toolbox for comprehensive graph analyses of functional brain connectivity, *J. Neurosci. Methods*, 245, 107–115

Kruskal, J. B. (1989), How 3-MFA data can cause degenerate PARAFAC solutions, among other relationships, in R. Coppi and S. Bolasco, eds., Multiway data analysis (Elsevier, Amsterdam), 115–122

Lamme, V. A., Supèr, H., and Spekreijse, H. (1998), Feedforward, horizontal, and feedback processing in the visual cortex, *Current Opinion in Neurobiology*, 8, 529–535

Lee, U., Müller, M., Noh, G.-J., Choi, B., and Mashour, G. A. (2011), Dissociable network properties of anesthetic state transitions, *Anesthesiology*, 114, 872–881

Levina, A. and Priesemann, V. (2017), Subsampling scaling, *Nature Communications*, 8, 15140, 1–9

Lewicki, M. S. (1998), A review of methods for spike sorting: the detection and classification of neural action potentials, *Network*, 9, 4, R53–78

Lewis, L. D., Weiner, V. S., Mukamel, E. A., Donoghue, J. A., Eskandar, E. N., Madsen, J. R., et al. (2012), Rapid fragmentation of neuronal networks at the onset of propofol-induced unconsciousness, *Proc. Natl. Acad. Sci. USA*, 109, 49, E3377–E3386

Liang, Z., King, J., and Zhang, N. (2012), Intrinsic organization of the anesthetized brain, *J. Neurosci.*, 32, 30, 10183–10191

Lisman, J. (2010), Working memory: The importance of theta and gamma oscillations, *Current Biology*, 20, 11, R490–R492

Lomber, S. (2001), Behavioral cartography of visual functions in cat parietal cortex: areal and laminar dissociations, in C. Casanova and M. Ptito, eds., Visions: From Neurons to Cognition (Elsevier Science B. V., Amsterdam)

Lomber, S. G. (1999), The advantages and limitations of permanent or reversible deactivation techniques in the assessment of neural function, *J. Neurosci. Methods*, 86, 109–117

Lomber, S. G. and Payne, B. R. (1996), Removal of two halves restores the whole: reversal of visual hemineglect during bilateral cortical or collicular inactivation in the cat, *Vis. Neurosci.*, 13, 1143–1156

Lomber, S. G. and Payne, B. R. (2000), Contributions of cat posterior parietal cortex to visuospatial discrimination, *Vis. Neurosci.*, 17, 701–709

Lomber, S. G., Payne, B. R., and Horel, J. A. (1999), The cryoloop: an adaptable reversible cooling deactivation method for behavioral or electrophysiological assessment of neural function, *J. Neurosci. Methods*, 86, 179–194

Luczak, A., Barthó, P., Marguet, S. L., Buzsáki, G., and Harris, K. D. (2007), Sequential structure of neocortical spontaneous activity in vivo, *Proc. Natl. Acad. Sci. USA*, 104, 1, 347–352

Lund, J. S., Yoshioka, T., and Levitt, J. (1993), Comparison of intrinsic connectivity in different areas of macaque monkey cerebral cortex, *Cereb Cortex*, 3, 2, 148–162

Lv, Q., Yang, L., Li, G., Wang, Z., Shen, Z., Yu, W., et al. (2016), Large-scale persistent network reconfiguration induced by ketamine in anesthetized monkeys: relevance to mood disorders, *Biol Psychiatry*, 79, 765–775

Maldonado, P., Babul, C., Singer, W., Rodriguez, E., Berger, D., and Grün, S. (2008), Synchronization of neuronal responses in primary visual cortex of monkeys viewing natural images, *J. Neurophysiol.*, 100, 1523–1532

Mao, B. Q., Hamzei-Sichani, F., Aronov, D., Froemke, R. C., and Yuste, R. (2001), Dynamics of spontaneous activity in neuronal slices, *Neuron*, 32, 5, 883–898

Markov, N. T. and Kennedy, H. (2013), The importance of being hierarchical, *Current Opinion in Neurobiology*, 23, 187–194

Markov, N. T., Vezoli, J., Chameau, P., Falchier, A., Quilodran, R., Huissoud, C., et al. (2014), Anatomy of hierarchy: feedforward and feedback pathways in macaque visual cortex, *J Comp Neurol.*, 522, 1, 225–259

Masquelier, T., Albantakis, L., and Deco, G. (2011), The timing of vision – how neural processing links to different temporal dynamics, *Frontiers in Psychology*, 2, 151

Massey, F. J. J. (1951), The Kolmogorov-Smirnov Test for Goodness of Fit, *American Statistical Association*, 46, 253, 68–78

McCullagh, P. and Nelder, J. (1989), Generalized linear models (Chapman & Hall, London)

McGinley, M. J., Vinck, M., Reimer, J., Batista-Brito, R., Zagha, E., Cadwell, C. R., et al. (2015), Waking state: Rapid variations modulate neural and behavioral responses, *Neuron*, 87, 1143–1161

Michalareas, G., Vezoli, J., van Pelt, S., Schoffelen, J.-M., Kennedy, H., and Fries, P. (2016), Alpha-beta and gamma rhythms subserve feedback and feedforward influences among human visual cortical areas, *Neuron*, 89, 384–397

Mignard, M. and Malpeli, J. G. (1991), Paths of information flow through visual cortex, *Science*, 251, 4998, 1249–1251

Mikami, A., Newsome, W. T., and Wurtz, R. H. (1986), Motion selectivity in macaque visual cortex. II. Spatiotemporal range of directional interactions in MT and V1, *J. Neurophysiol.*, 55, 1328–1339

Miller, R. G. J. (1991), Simultaneous Statistical Inference (Springer, New York)

Milner, P. M. (1974), A model for visual shape recognition, *Psychological Review*, 81, 6, 521–535

Mitzdorf, U. and Singer, W. (1978), Prominent excitatory pathways in the cat visual cortex (A 17 and A 18): A current source density analysis of electrically evoked potentials, *Exp. Brain Res.*, 33, 371–394

Miwakeichi, F., Martínez-Montes, E., Valdés-Sosa, P. A., Nishiyama, N., Mizuhara, H., and Yamaguchi, Y. (2004), Decomposing EEG data into space-time-frequency components using Parallel Factor Analysis, *NeuroImage*, 22, 1035–1045

Müller, M. C. (2017), Visual hemineglect and lesion-induced changes of top-down activity in the primary visual cortex, Ph.D. thesis, Technische Universität Darmstadt

Mountcastle, V. B. (1997), The columnar organization of the neocortex, *Brain*, 120, 4, 701–722

Mukherjee, P. and Kaplan, E. (1995), Dynamics of neurons in the cat lateral geniculate nucleus: in vivo electrophysiology and computational modeling, *J. Neurophysiol.*, 74, 1222–1243

Nelder, J. A. and Wedderburn, R. W. M. (1972), Generalized linear models, *J. R. Statist. Soc. A.*, 135, 370–384

Nelson, S. (2002), Cortical microcircuits: diverse or canonical?, *Neuron*, 36, 1, 19–27

Ni, J., Lewis, C. M., Wunderle, T., Jendritza, P., Diester, I., and Fries, P. (2017), Gamma-band resonance of visual cortex to optogenetic stimulation, *bioRxiv*

Ni, J., Wunderle, T., Lewis, C. M., Desimone, R., Diester, I., and Fries, P. (2016), Gamma-rhythmic gain modulation, *Neuron*, 92, 240–251

Okatan, M., Wilson, M. A., and Brown, E. N. (2005), Analyzing functional connectivity using a network likelihood model of ensemble neural spiking activity, *Neural Computation*, 17, 1927–1961

Okun, M., Steinmetz, N. A., Cossell, L., Iacaruso, M. F., Ko, H., Barth'o, P., et al. (2015), Diverse coupling of neurons to populations in sensory cortex, *Nature*, 521, 7553, 511–515

Olshausen, B. A. and Field, D. J. (1996), Emergence of simple-cell receptive field properties by learning a sparse code for natural images, *Nature*, 381, 607–609

Oppenheim, A. V., Willsky, A. S., and Nawab, S. H. (1997), Signals & Systems (Prentice-Hall, Inc., Upper Saddle River, NJ, USA)

Orban, G. A., Kennedy, H., and Maes, H. (1981a), Response to movement of neurons in areas 17 and 18 of the cat: velocity selectivity, *J. Neurophysiol.*, 45, 6, 1043–1058

Orban, G. A., Kennedy, H., and Maes, H. (1981b), Velocity sensitivity of areas 17 and 18 of the cat, *Acta Psychologica*, 48, 303–309

Ostojic, S., Brunel, N., and Hakim, V. (2009), How connectivity, background activity, and synaptic properties shape the cross-correlation between spike trains, *J. Neurosci.*, 29, 33, 10234–10253

Otsuka, B. and Hassler, R. (1962), Über Aufbau und Gliederung der corticalen Sehsphäre bei der Katze, *Archiv für Psychiatrie und Zeitschrift f. d. ges. Neurologie*, 203, 212–234

Pack, C. C., Berezovskii, V. K., and Born, R. T. (2001), Dynamic properties of neurons in cortical area MT in alert and anaesthetized macaque monkeys, *Nature*, 414, 905–908

Papo, D., Zanin, M., and Buldú, J. M. (2014), Reconstructing functional brain networks: have we got the basics right?, *Frontiers in Human Neuroscience*, 8

Park, H.-J. and Friston, K. (2013), Structural and functional brain networks: From connections to cognition, *Science*, 342, 6158, 1238411

Payne, B. R. (1990), The representation of the ipsilateral visual field in the transition zone between areas 17 and 18 of the cat's cerebral cortex, *Vis. Neurosci.*, 4, 445–474

Payne, B. R. and Lomber, S. G. (2003), Quantitative analyses of principal and secondary compound parietooccipital feedback pathways in cat, *Experimental Brain Research*, 152, 4, 420–433

Payne, B. R., Lomber, S. G., Geerarts, S., van der Gucht, E., and Vandenbussche, E. (1996), Reversible visual hemineglect, *Procl. Natl. Acad. Sci. USA*, 93, 290–294

Payne, B. R. and Peters, A. (2001), The Cat Primary Visual Cortex (Academic Press, San Diego)

Payne, B. R. and Rushmore, R. J. (2004), Functional circuitry underlying natural and interventional cancellation of visual neglect, *Exp Brain Res*, 154, 127–153

Pedreira, C., Martinez, J., Ison, M. J., and Quian Quiroga, R. (2012), How many neurons can we see with current spike sorting algorithms?, *J. Neurosci. Methods*, 211, 58–65

Pipa, G. and Munk, M. H. J. (2011), Higher order spike synchrony in prefrontal cortex during visual memory, *Frontiers in Computational Neuroscience*, 1–13

Pipa, G., Wheeler, D., Singer, W., and Nikolic, D. (2008), Neuroxidence: Reliable and efficient analysis of an excess or deficiency of joint-spike events, *Journal of Computational Neuroscience*, 25, 64–88

Poulsen, R. C., Warman, G. R., Sleigh, J., Ludin, N. M., and Cheeseman, J. F. (2018), How does general anaesthesia affect the circadian clock?, *Sleep Medicine Reviews*, 37, 35–44

Priesemann, V., Munk, M. H. J., and Wibral, M. (2009), Subsampling effects in neuronal avalanche distributions recorded *in vivo*, *BMC Neuroscience*, 10, 40

Priesemann, V., Wibral, M., and Triesch, J. (2013), Learning more by sampling less: subsampling effects are model specific, *BMC Neuroscience*, 14, Suppl 1, P414

Priesemann, V., Wibral, M., Valderrama, M., Pröpper, R., Quyen, M. L. V., Geisel, T., et al. (2014), Spike avalanches *in vivo* suggest a driven, slightly subcritical brain state, *Front. Syst. Neurosci.*, 8, 108, 1–17

Ptak, R. and Fellrath, J. (2013), Spatial neglect and the neural coding of attentional priority, *Neurosci. Biobehav. Rev.*, 37, 4, 705–722

Quian Quiroga, R., Nadasdy, Z., and Ben-Shaul, Y. (2004), Unsupervised spike detection and sorting with wavelets and superparamagnetic clustering, *Neural Computation*, 16, 1661–1687

Quinn, C. J., Coleman, T. P., Kiyavash, N., and Hatsopoulos, N. G. (2011), Estimating the directed information to infer causal relationships in ensemble neural spike train recordings, *J Comput Neurosci*, 30, 17–44

Rafal, R. D. (1994), Neglect, *Current Opinion in Neurobiology*, 4, 231–236

Raichle, M. E. (2015), The restless brain: how intrinsic activity organizes brain function, *Phil. Trans. R. Soc. B*, 20140172, 370

Rao, J. S., Liu, Z., Zhao, C., Wei, R. H., Zhao, W., Tian, P. Y., et al. (2017), Ketamine changes the local resting-state functional properties of anesthetized-monkey brain, *Magn Reson Imaging*, 43, 144–150

Rao, R. P. and Sejnowski, T. J. (2002), Predictive coding, cortical feedback, and spike-timing dependent plasticity, in R. P. Rao, B. A. Olshausen, and M. S. Lewicki, eds., Probabilistic Models of the Brain: Perception and Neural Function (MIT Press, Cambridge, MA), 297–316

Rao, R. P. N. and Ballard, D. H. (1999), Predictive coding in the visual cortex: a functional interpretation of some extra-classical receptive-field effects, *Nature Neuroscience*, 2, 1, 79–87

Redner, S. (1998), How popular is your paper? An empirical study of the citation distribution, *The European Physical Journal B - Condensed Matter and Complex Systems*, 4, 2, 131–134

Reijneveld, J. C., Ponten, S. C., Berendse, H. W., and Stam, C. (2007), The application of graph theoretical analysis to complex networks in the brain, *Clinical Neurophysiology*, 118, 11, 2317–2331

Rieder, M. (2008), Elektrophysiologische Untersuchungen zur aufmerksamkeitsabhängigen Modulation der Aktivität im visuellen Kortex von Katzen, Diplomarbeit, Technische Universität Darmstadt

Rosner, B. S., Clark, D. L., and Beck, C. (1971), Inhalational anesthetics and conduction velocity of human peripheral nerve, *Electroenceph. Clin. Neurophysiol.*, 31, 109–144

Rubinov, M. and Sporns, O. (2010), Complex network measures of brain connectivity: Uses and interpretations., *NeuroImage*, 52, 1059–69

Rushmore, R. J., Valero-Cabre, A., Lomber, S., Hilgetag, C. C., and Payne, B. (2006), Functional circuitry underlying visual neglect, *Brain*, 129, 7, 1803–1821

Rutishauser, U. (2006), Online detection and sorting of extracellularly recorded action potentials in human medial temporal lobe recordings, *J. Neurosci. Methods*, 154, 204–224

Salin, P. A. and Bullier, J. (1995), Corticocortical connections in the visual system: structure and function, *Physiol Rev.*, 75, 1, 107–154

Salinas, E. and Sejnowski, T. J. (2001), Correlated neuronal activity an the flow of neural information, *Nature*, 2, 539–550

Sandell, J. and Schiller, P. (1982), Effect of cooling area 18 on striate cortex cells in the squirrel monkey, *J. Neurophysiol.*, 48, 1, 38–48

Scheidegger, M., Walter, M., Lehmann, M., Metzger, C., Grimm, S., Boeker, H., et al. (2012), Ketamine decreases resting state functional network connectivity in healthy subjects: implications for antidepressant drug action, *PLOS One*, 7, e44799

Schmitz, S. K. (2009), Statistische Untersuchungen von Konnektivitäts-Matrizen, Diplomarbeit, Technische Universität Darmstadt

Schmitz, S. K., Hasselbach, P. P., Ebisch, B., Klein, A., Pipa, G., and Galuske, R. A. W. (2015), Application of Parallel Factor Analysis (PARAFAC) to electrophysiological data, *Front. Neuroinform.*, 8, 84

Schölvinck, M. L., Saleem, A. B., Benucci, A., Harris, K. D., and Carandini, M. (2015), Cortical state determines global variability and correlations in visual cortex, *J. Neurosci.*, 35, 170–178

Schreiber, T. (2000), Measuring information transfer, *Phys. Rev. Lett.*, 85, 461–464

Schulz, D. P. A., Sahani, M., and Carandini, M. (2015), Five key factors determining pairwise correlations in visual cortex, *J. Neurophysiol.*, 114, 2, 1022–1033

Schwabe, L., Obermayer, K., Angelucci, A., and Bressloff, P. C. (2006), The role of feedback in shaping the extra-classical receptive field of cortical neurons: A recurrent network model, *J. Neurosci.*, 26, 36, 9117–9129

Seasholtz, M. B. and Kowalski, B. (1993), The parsimony principle applied to multivariate calibration, *Analytica Chimica Acta*, 277, 165–177

Segraves, M. A. and Innocenti, G. M. (1985), Comparison of the distributions of ipsilaterally and contralaterally projecting corticocortical neruons in cat visual cortex using two flourescent tracers, *J. Neurosci.*, 5, 8, 2107–2118

Seung, S. H. (2009), Reading the book of memory: sparse sampling versus dense mapping of connectomes, *Neuron*, 62, 1, 17–29

Shadlen, M. N. and Movshon, J. A. (1999), Synchrony unbound: A critical evaluation of the temporal binding hypothesis, *Neuron*, 24, 67–77

Shannon, C. E. and Weaver, W. (1949), The mathematical theory of communication (University of Illinois Press, Urbana, Illinois)

Shatz, C. J. (1992), The developing brain, *United States: Scientific American*, 267, 3, 60–67

Shipp, S. (2004), The brain circuitry of attention, *Trends Cogn. Sci.*, 8, 223–230

Singer, W. (1999a), Neuronal synchrony: A versatile code for the definition of relations?, *Neuron*, 24, 49–65

Singer, W. (1999b), Time as coding space?, *Current Opinion in Neurobiology*, 9, 189–194

Singer, W. (2009), Distributed processing and temporal codes in neuronal networks, *Cogn Neurodyn*, 3, 189–196

Smilde, A. K. and Doornbos, D. A. (1991), Three-way methods for the calibration of chromatographic systems: Comparing PARAFAC and three-way PLS, *Journal of Chemometrics*, 5, 345–360

Smith, M. A. and Kohn, A. (2008), Spatial and temporal scales of neuronal correlation in primary visual cortex, *J. Neurosci.*, 28, 48, 12591–12603

Sporns, O. (2006), Small-world connectivity, motif composition, and complexity of fractal neuronal connections, *Biosystems*, 85, 1, 55–64

Sporns, O. (2011), Networks of the brain (MIT Press, Cambridge, MA)

Sporns, O. and Honey, C. J. (2006), Small worlds inside big brains, *Proc. Natl. Acad. Sci. USA*, 103, 19219–19220

Sporns, O. and Zwi, J. D. (2004), The small world of the cerebral cortex, *Neuroinformatics*, 2, 145–162

Sprague, J. (1966), Interaction of cortex and superior colliculus in mediation of visually guided behavior in the cat, *Science*, 153, 1544–1547

Stein, E. S., Itsekson-Hayosh, Z., Aronovich, A., Reisner, Y., Bushi, D., Pick, C. G., et al. (2015), Thrombin induces ischemic LTP (iLTP): implications for synaptic plasticity in the acute phase of ischemic stroke, *Scientific reports*, 5, 7912

Stitt, I., Hollensteiner, K. J., Galindo-Leon, E., Pieper, F., Fiedler, E., Stieglitz, T., et al. (2017), Dynamic reconfiguration of cortical functional connectivity across brain states, *Sci Rep.*, 7, 1, 8797

Strogatz, S. H. (2001), Exploring complex networks, *Nature*, 410, 268–276

Stumpf, M. P. H., Wiuf, C., and May, R. M. (2005), Subnets of scale-free networks are not scale-free: Sampling properties of networks, *Proc. Natl. Acad. Sci. USA*, 102, 12, 4221– 4224

Sullivan, L. M. (2008), Essentials of Biostatistics in Public Health (Jones & Bartlett Learning, Sudbury, MA)

Swindale, N. V. (2003), Neural synchrony, axonal path lengths, and general anesthesia: A hypothesis, *The Neuroscientist*, 9, 6, 440–445

Symonds, L. L. and Rosenquist, A. C. (1984), Corticocortical connections among visual areas in the cat, *Journal of Comparative Neurology*, 229, 1, 1–38

Tetzlaff, C., Kolodziejski, C., Markelic, I., and Wörgötter, F. (2012), Time scales of memory, learning, and plasticity, *Biol Cybern*, 106, 715–726

Theunissen, F. and Miller, J. P. (1995), Temporal encoding in nervous systems: A rigorous definition, *Journal of Computational Neuroscience*, 2, 149–162

Thompson, S.-A. and Wafford, K. (2001), Mechanism of action of general anaesthetics — new information from molecular pharmacology, *Current Opinion in Pharmacology*, 1, 1, 78–83

Tononi, G. (2008), Consciousness as integrated information: a provisional manifesto, *Biol Bull*, 215, 216–242

Treisman, A. (1996), The binding problem, *Curr. Opin. Neurobiol.*, 6, 171–178

Treisman, A. (1999), Solutions to the binding problem: progress through controversy and convergence, *Neuron*, 24, 105–110

Tretter, F., Cynader, M., and Singer, W. (1975), Cat parastriate cortex: a primary or secondary visual area, *J. Neurophysiol.*, 38, 1099–1113

Truccolo, W., Eden, U. T., Fellows, M. R., Donoghue, J. P., and Brown, E. N. (2005), A point process framework for relating neural spiking activity to spiking history, neural ensemble, and extrinsic covariate effects, *J. Neurophysiol.*, 93, 1074–1089

Tucker, L. R. (1966), Some mathematical notes on three-mode factor analysis, *Psychometrika*, 31, 3, 279–311

Tusa, R. J., Palmer, L. A., and Rosenquist, A. C. (1981), Multiple cortical visual areas: Visual field topography in the cat, in C. N. Woolsey, ed., Cortical sensory organisation, volume 2 (Humana Press, Clifton, NJ, USA), volume 2

Tusa, R. J., Rosenquist, A. C., and Palmer, L. A. (1979), Retinotopic organization of areas 18 and 19 in the cat, *J Comp Neurol*, 185, 4, 657–678

Uhlhaas, P., Pipa, G., Lima, B., Melloni, L., Neuenschwander, S., Nikolic, D., et al. (2009), Neural synchrony in cortical networks: history, concept and current status, *Front. Integr. Neurosci.*, 3–17

van den Heuvel, M. P. and Sporns, O. (2013), An anatomical substrate for integration among functional networks in human cortex, *J. Neurosci.*, 33, 36, 14489–14500

van Essen, D. C. and Maunsell, J. H. R. (1983), Hierarchical organization and functional streams in the visual cortex, *Trends in NeuroSciences*, 6, 9, 370–375

van Essen, D. C., Smith, S. M., Barch, D. M., Behrens, T. E., Yacoub, E., and for the WU-Minn HCP Consortium, K. U. (2013), The WU-Minn Human Connectome Project: an overview, *NeuroImage*, 80, 62–79

van Kerkoerle, T., Self, M. W., Dagnino, B., Gariel-Mathis, M.-A., Poort, J., van der Togt, C., et al. (2014), Alpha and gamma oscillations characterize feedback and feedforward processing in monkey visual cortex, *Proceedings of the National Academy of Sciences*, 111, 40, 14332–14341, doi:10.1073/Proc.Natl.Acad.Sci.USA.1402773111

van Pelt, S., Boomsma, D. I., and Fries, P. (2012), Magnetoencephalography in twins reveals a strong genetic determination of the peak frequency of visually induced gamma-band synchronization, *J. Neurosci.*, 32, 10, 3388–3392

van Rullen, R., Guyonneau, R., and Thorpe, S. J. (2005), Spike times make sense, *TRENDS in Neurosciences*, 28, 1, 1–4

Vanduffel, W., Payne, B., Lomber, S., and Orban, G. (1997), Functional impact of cerebral connections, *Proc. Natl. Acad. Sci. U. S. A.*, 94, 7617–7620

Vögler, S. (2014), Raumzeitliche Dynamik der Aktivität neuronaler Populationen im visuellen Kortex der Katze, Ph.D. thesis, Technische Universität Darmstadt

Vicente, R., Gollo, L. L., Mirasso, C., Fischer, I., and Pipa, G. (2008), Dynamical relaying can yield zero time lag neuronal synchrony despite long conduction delays, *Proc. Natl. Acad. Sci. USA*, 105, 44, 17157–17162

Vicente, R., Wibral, M., Lindner, M., and Pipa, G. (2011), Transfer entropy–a model-free measure of effective connectivity for the neurosciences, *J. Comput. Neurosci.*, 30, 1, 45–67

Victor, J. D. (2006), Approaches to information-theoretic analysis of neural activity, *Biol Theory*, 1, 3, 302–316

Villeneuve, M. Y. and Casanova, C. (2003), On the use of isoflurane versus halothane in the study of visual response properties of single cells in the primary visual cortex, *J. Neurosci. Methods*, 129, 1, 19–31

Volgushev, M., Vidyasagar, T., Chistiakov, M., Yousef, T., and Eysel, U. (2000), Membrane properties and spike generation in rat visual cortical cells during reversible cooling, *J Physiol.*, 522 Pt 1, 59–76

von der Malsburg, C. (1981), The correlation theory of brain function, *Internal report 81-2, Max-Planck-Institut für Biophysikalische Chemie, Göttingen*

Watts, D. and Strogatz, S. H. (1998), Collective dynamics of 'small world' networks, *Nature*, 393, 440–442

Waxman, S. G. (1980), Determinants of conduction velocity in myelinated nerve fibers, *Muscle Nerve*, 3, 2, 141–150

White, J. G., Southgate, E., Thomson, J. N., and Brenner, S. (1986), The structure of the nervous system of the nematode Caenorhabditis elegans, *Philos Trans R Soc Lond B Biol Sci.*, 314, 1165, 1–340

Wild, J., Prekopcsak, Z., Sieger, T., Novak, D., and Jech, R. (2012), Performance comparison of extracellular spike sorting algorithms for single-channel recordings, *J. Neurosci. Methods*, 203, 369–376

Wilting, J. and Priesemann, V. (2018), Inferring collective dynamical states from widely unobserved systems, *Nature Communications*, 9, 2325, 1–7

Yu, S., Huang, D., Singer, W., and Nikolic, D. (2008), A small world of neuronal synchrony, *Cereb Cortex.*, 18, 12, 2891–2901

Zagha, E. and McCormick, D. A. (2014), Neural control of brain state, *Current Opinion in Neurobiology*, 29, 178–186

Zhang, S., Xu, M., Kamigaki, T., Do, J. P. H., Chang, W.-C., Jenvay, S., et al. (2014), Selective attention. long-range and local circuits for top-down modulation of visual cortex processing, *Science*, 345, 660–665

Zucker, R. S. and Regehr, W. G. (2002), Short-term synaptic plasticity, *Annu. Rev. Physiol.*, 64, 355–405

Lebenslauf

PERSÖNLICHE DATEN

Name:	Sarah Katharina Schmitz
Geburtsdatum & -Ort:	25.09.1982, Groß-Gerau

AUSBILDUNG

05/2009 - heute	Promotion, Fachbereich Biologie, Systemische Neurophysiologie Technische Universität Darmstadt
10/2002 - 04/2009	Diplomstudium Mathematik, Technische Universität Darmstadt
06/2002	Abitur, Bertha-von-Suttner-Schule, Mörfelden-Walldorf

BERUFSERFAHRUNG

09/2019 - heute	Head of Automator Solutions, LORENZ Life Sciences GmbH, Frankfurt am Main
01/2019 - 08/2019	Senior Solution Engineer, LORENZ Life Sciences GmbH, Frankfurt am Main
09/2015 - 12/2018	Technical Consultant, LORENZ Life Sciences GmbH, Frankfurt am Main
05/2013 - 09/2014	Wissenschaftliche Hilfskraft Fachbereich Biologie, Systemische Neurophysiolgie Technische Universität Darmstadt
05/2011 - 04/2013	Wissenschaftlicher Mitarbeiter Fachbereich Biologie, Systemische Neurophysiolgie Technische Universität Darmstadt
05/2008 - 04/2009	Studentische Hilfskraft Max-Planck-Institut für Hirnforschung, Abteilung Neurophysiologie Frankfurt am Main
10/2006 - 03/2007	Studentische Hilfskraft Fachbereich Mathematik Technische Universität Darmstadt
09/2005 - 06/2006	Werkstudentin Fujitsu Siemens Computers, Bad Homburg

STIPENDIEN

05/2009 - 04/2011	Doktoranden-Stipendium, Frankfurt Institute for Advanced Studies, Frankfurt

PUBLIKATIONEN & KONFERENZBEITRÄGE

Schmitz SK, Hasselbach PP, Ebisch B, Klein A, Pipa G and Galuske RA (2015). Application of Parallel Factor Analysis (PARAFAC) to Electrophysiological Data. Front. Neuroinform. 8:84. doi: 10.3389/fninf.2014.00084

Schmitz K, Hasselbach PP, Ebisch B, Nakano Daniel M, Pipa G, Klein A, Galuske RAW (2010). Application of parallel factor analysis to electrophysiological data. Neuroscience 2010; Supported by a DAAD travel grant

Schmitz K, Pipa G, Ebisch B, Geider K, Galuske RAW (2010). Graph theory analysis of local functional networks in cat visual cortex. FENS Abstr. vol 5, 130.73, 2010, Federation of European Neuroscience Societies (FENS) Forum Amsterdam

Schmitz K, Pipa G, Galuske RAW (2009). Applying graph theory to the analysis of functional network dynamics in visual cortex. Frontiers in Computational Neuroscience. Conference Abstract: Bernstein Conference on Computational Neuroscience. doi: 10.3389/conf.neuro.10.2009.14.071
Bernstein Conference on Computational Neuroscience, Frankfurt am Main; Begleitender Vortrag beim Studenten-Symposium am 3. Oktober 2009

thank you.

First of all I would like to thank **Prof. Dr. Ralf Galuske** for the supervision of my doctorate. Thank you, Ralf, for inviting me into the field of neuroscience, giving me the opportunity to work in the stimulating environment of a Max Planck Institute, and supporting my interest in exploring the (neuroscience) world. I would like to thank **Prof. Dr. Gordon Pipa** for the co-supervision of my thesis, for providing the NeuroXidence code, supporting the implementation of the GLM procedure, and for many fruitful discussions.

I am very grateful to **Prof. Dr. Wolf Singer** for the opportunity to conduct part of my work at the Max Planck Institute for Brain Research.

I highly appreciate the financial support I received for my studies, workshops, and travel expenses from **FIAS**, **TU Darmstadt** and its equal opportunities office, the **DAAD**, the **Max Planck Society**, **Minerva FemmeNet**, and **GRADE**.

I would like to thank **Dr. Philipp Hasselbach** and the team of **AG Klein** from the ETIT department at TU Darmstadt for the enjoyable and productive collaboration in the PARAFAC project.

Thank you to everybody in the **Systemic Neuroscience Group** at the biology department at **TU Darmstadt** and at **MPIH/ESI** for all the fun times and support, especially to everyone who contributed to the recording of the data that built the fundament of my thesis.

A very special thank you goes to **Dr. Miriam Müller** for proofreading of parts of the thesis and so many valuable discussions, but generally for being the best office mate I could have wished for, and for sharing fun, frustration, and gin! Thank you, **Dr. Will Barnes**, for all your support, especially with the LFP analysis, proofreading of the thesis, and many helpful discussions on neglect as well as liquid computing. Thank you, **Dr. Klaus von Wangenheim**, for your thoughts, interest, and advice, which made a tremendous contribution towards my perseverance. Thank you for many scientific discussions and proofreading of parts of the thesis, but also for the encouragement to discover heaven and the underwater world. Thank you, **Dr. Mathias Peter**, for the continuous motivation and regular pep talks on the last steps of the way.

Thank you also to all **LORENZians** for the support.

Danke an alle meine Freunde, ganz besonders an **Dr. Kirsten Santelmann** und **Dr. Maria Scherf**. Ich bin sehr froh, Euch zu haben. Danke für Euren unermüdlichen Zuspruch und Eure Motivation!

Ein riesengroßes Dankeschön an meine **Lieblingsnachbarn** und an meine gesamte **Familie**. Danke für alles! Ihr seid die Besten.

Ehrenwörtliche Erklärung

Ich erkläre hiermit ehrenwörtlich, dass ich die vorliegende Arbeit entsprechend den Regeln guter wissenschaftlicher Praxis selbstständig und ohne unzulässige Hilfe Dritter angefertigt habe.

Sämtliche aus fremden Quellen direkt oder indirekt übernommenen Gedanken sowie sämtliche von Anderen direkt oder indirekt übernommenen Daten, Techniken und Materialien sind als solche kenntlich gemacht. Die Arbeit wurde bisher bei keiner anderen Hochschule zu Prüfungszwecken eingereicht.

Darmstadt, den ....

....
Sarah Katharina Schmitz